An amplitude analysis of the four body decay $D^0 \to K^+K^-\pi^+\pi^-$ and a study on the $\pi^+\pi^-$ S wave for the decay $D^0 \to K_S^0\pi^+\pi^-$

Lauren Martin

Christ Church College, Oxford

A thesis submitted for the degree of Doctor of Philosophy at the University of Oxford

Michaelmas Term, 2011

An amplitude analysis of the four body decay $D^0 \to K^+K^-\pi^+\pi^-$ and a study on the $\pi^+\pi^-$ S wave for the decay $D^0 \to K^0_S\pi^+\pi^-$

Lauren Martin
Christ Church College, Oxford

submitted for the degree of Doctor of Philosophy
at the University of Oxford

Michaelmas Term, 2011

ABSTRACT

The angle γ, with an uncertainty of approximately 10° is the least well constrained angle of the unitary triangle. Better experimental constraints on this parameter are required in order to provide a consistency check on the standard model description of CP violation. A promising strategy for measuring γ involves exploiting interference effects present in $B^\pm \to DK^\pm$ decays where the D subsequently decays to a three or four body final state. The three body decay $D \to K^0_S\pi^+\pi^-$ and the four body decay $D^0 \to K^+K^-\pi^+\pi^-$ are suitable candidates for making such a measurement. However independent knowledge of the decay structure of these decays is required.

The impact of the model, used to describe the $\pi^+\pi^-$ S wave, in the $D^0 \to K^+K^-\pi^+\pi^-$ decay, on the uncertainty in the measurement of gamma is estimated via a simulation study. It is determined that the uncertainty on a γ measurement would be compromised by this model uncertainty within one year of LHCb data running.

The four body decay $D^0 \to K^+K^-\pi^+\pi^-$ also provides a candidate for making a γ measurement. This decay is expected to display a rich resonant structure. An understanding of this decay may also provide an insight into low energy QCD in addition to allowing a search for CP violation. Only one previous amplitude analysis has been performed on this decay.

Using data collected at the CLEO-II.V, CLEO-III and CLEO-c experiments an amplitude model is developed for the $D^0 \to K^+K^-\pi^+\pi^-$ decay. This model is qualitatively similar to that produced in the previous analysis although the model presented in this thesis considers higher orbital angular momentum states and distinguishes between conjugate states that the previous model did not. A search for CP violation is also carried out using the $D^0 \to K^+K^-\pi^+\pi^-$ decay data. A positive confirmation of CP violation at the level of sensitivity provided by this decay data would provide evidence for a level of CP violation which could not be accounted for within the standard model. No significant evidence for CP violation is observed in this decay.

A toy MC study was carried out in order to determine the sensitivity to γ which may be achieved using this decay. In this study, sets of 1000 B^+ and B^- events are generated and the decay model developed for the $D \to K^+K^-\pi^+\pi^-$ decay is used to describe the D decay. The sensitivity to γ determined in this study is 11°.

Preface

CLEO was a symmetrical e^+e^- experiment located at Cornell university and operated between 1979 and 2008. It was originally designed to study the Υ and B meson properties but the centre of mass energies were later reduced to around that of the charm threshold in order to make precision charm measurements. The data used in the analysis described in this thesis were taken at centre of mass energies between 3 and 11 GeV.

Resonant decays of charmed mesons to three or more particles dominantly proceed through a variety of resonant two and three body decays. The Dalitz plot technique is often used to describe the amplitudes of these sub processes and we therefore make great use of this method in this thesis.

In chapter 1 the theoretical background for the work in the proceeding thesis is introduced. The standard model and the description of CP violation is described. The unitary matrix and the angle γ, which is of particular pertinence to the following analysis is introduced together with the methods used to measure γ. CP violation as it occurs in the charm sector is then described in more detail. The techniques of Dalitz analyses which will be employed in the following analysis are then discussed as they apply to both three and four body decays.

In Chapter 2 an overview of the CLEO detector is given. The various components of the detector and the accelerator are described in detail. The differences between the newer and older versions of the experiment are also explained in this chapter.

In Chapter 3 the problems in describing the $\pi^+\pi^-$ S wave model for the $D^0 \rightarrow K^0_S\pi^+\pi^-$ decay are described. This decay provides access to γ via the B decays $B^\pm \rightarrow D(K^0_S\pi^+\pi^-)$ where D is either D^0 or $\overline{D}^0$. Such a decay is a good candidate for making a measurement of γ at the LHCb detector. The uncertainty on a measurement of γ due to the uncertainty on the description of the $\pi^+\pi^-$ S wave model is determined in this chapter. My contribution to this work was implimenting the K-matrix formulation in the existing fitter framework. I was then able to estimate the model error on γ which would be introduced as a result of the $\pi^+\pi^-$ S wave model.

The remaining chapters deal with the four body decay $D^0 \to K^+K^-\pi^+\pi^-$.

Chapter 4 begins with a review of the previous studies conducted into this decay. The selection of $D^0 \to K^+K^-\pi^+\pi^-$ events for each detector configuration and decay topology are described. Finally the estimations of the fractions of backgrounds and misidentified events are also described. The work described in this chapter was carried out by other members of the UK Dalitz group.

Chapter 5 covers the background necessary for conducting an amplitude fit. We first give a description of the particular form of the amplitude model for the four body decay used in this analysis. The framework of the fitter used to perform the amplitude fit is presented together with a consistency check on the fitter. The development of models to describe backgrounds to the signal sample and the manner in which the acceptance and efficiency effects are taken into account are also discussed. In addition to helping with the implimentation and testing of the fitter, I was responsible for determining the best models for each of the background components given background samples provided by other members of the UK Dalitz group.

In chapter 6 the central results of this thesis are presented. First the model used to describe the CP tagged datasets is introduced, followed by a discucssion of the development of the final amplitude model for the $D^0 \to K^+K^-\pi^+\pi^-$ decay. The results of the amplitude fit are then presented together with the estimations of systematic uncertainties. Finally a robustness test on the final model is carried out. The work in this chapter was entirely my own (although the data samples required to carry it out were provided by other members of the Dalitz group).

In chapter 7 the final model is discussed and compared to the model produced in a previous analysis of this decay mode. A search for CP violation via the amplitude analysis of this decay is described. Finally a study is presented in which the amplitude model is used to determine the sensitivity to the parameter γ which may be achieved using this decay. Again the work in this chapter is entirely my own. The work presented in the final four chapters of this thesis has now been published [1].

Acknowledgments

I wish to thank the Science and Technology Facilities Council (STFC)[1] for funding my four year studentship and enabling me to work on location at both CERN and the CLEO-c experiment.

I would particularly like to thank my supervisors Jim Libby, Mat Charles and Guy Wilkinson for their tremendous encouragement and persistence both during the analysis and particularly the write up stage, which was absolutely vital for the completion of this thesis.

I would also like to thank Jonas Rademacker for his time and patience in helping me to use the MINT software package which was so important to this thesis.

I am also very grateful for the help of many other colleagues. In particular Paras Naik for endless help with the CLEO software system, his infectious upbeat attitude and our many motivational tea breaks. I would also like to thank Andrew Powell for so much technical and practical help and encouragement over the last five years, which was of so much help to my work, moving to America and actually handing this thesis in. I am very grateful! I would also like to thank Sneha Malde for her encouragement during the final stages of my thesis.

I must also thank those I worked with in Ithaca for all of their help with setting up my work and for making my time there so enjoyable. Special thanks must go to Brian Moziak, Eric White, Pete Zwebber and Paras Naik.

I must also thank all of the other Oxford CLEO-c and LHCb students which have all offered help and made the time spent at work much more enjoyable. I would especially like to thank Funai Xing, Phil Hunt, Chris Thomas, Daniel Johnson and Sean Brisbane for their help and company at various times over the last five years.

I would also like to thank all of my friends both in and outside of Oxford who have provided me with so much fun and distraction. I would also like to thank my family, especially my parents and brother for all of their endless support. Finally I would like to thank Max for helping and supporting me in too many ways to mention here.

Contents

List of Figures

List of Tables

Chapter 1

CP Violation and Multi-body Charm Decays

1.1 Introduction

Despite the enormous success of the Standard Model in correctly describing the fundamental particles and their interactions, there are indications that further physics will be required to account properly for observed phenomena. For example the "hierarchy problem"; this describes the disparate electroweak and Planck energy scales. In the Standard Model quantum corrections to the Higgs mass become divergent at high energies. In order to maintain the consistency of the theory these corrections would have to undergo a "fine-tuned" cancellation [2], which appears unsatisfactory.

Other areas of the Standard Model remain poorly constrained by experiment. CP violation has been observed and may be accounted for in the Standard Model. However, it has yet to be established whether the form of CP violation predicted by the Standard Model is sufficient to describe the level and structure of CP violation that occurs in nature. In addition to CP violation which has already been observed in the kaon system [3], many CP violating effects are expected in the decays of B mesons and such effects have recently been observed at the B factory experiments Babar and Belle [4, 5]. These observations included time dependent analyses of neutral B^0 decays (in both flavour and CP eigenstates), in addition to studies of the decays of B_S^0 decays and analyses of $B^{\pm}$ systems. These provide an opportunity for independently testing the predictions of the Standard Model. It is possible that redundant measurements of Standard Model parameters may produce results which are inconsistent; this would indicate the need for a richer theory in order to describe properly CP violation. There is particular reason to believe that the Standard Model description of CP violation is incomplete as it cannot adequately explain the matter anti-matter asymmetry in the universe [6].

1.2 CP Violation and The Standard Model

1.2.1 Symmetries and Symmetry Violations

Symmetries are fundamental to our understanding of physical systems. In particular Noether's theorem [7] illustrates that any differentiable symmetry of a physical system will have an associated conserved quantity. For example, from the invariance of a system under space time translations the conservation of energy and momentum in that system may be inferred. Similarly the conservation of angular momentum is related to rotational invariance. The Standard Model itself is based on a gauge field theory (where each field has an associated gauge symmetry).

CPT Symmetries

In addition to continuous symmetries there are discrete transformations under which a field theory Lagrangian may be symmetric. Three such discrete symmetries are:

1. **P**: The parity transformation, corresponds to an inversion of the spacial coordinates ($\mathbf{r} \to -\mathbf{r}$). Thus changing the "handedness" of space.

2. **T**: The time reversal operator corresponds to an inversion in the direction of time.

3. **C**: Charge conjugation corresponds to the change in sign of the charge and of all other internal additive quantum numbers associated with each particle.

It can be shown that in any local Lagrangian field theory the combined **CPT** transformation must be an exact symmetry of the Lagrangian [8]. Furthermore **C**, **P** and **T** are each symmetries of electromagnetic and strong interactions. Weak interactions are known to violate **C**, **P** and **T** [9]. Although **CP** may be considered an approximate symmetry of weak interactions, **CP** violation has nonetheless been unambiguously observed in weak interactions involving both strange and beauty hadrons [3], [10].

1.2.2 Direct and Indirect CP Violation

CP violation can be divided into two broad categories, which are independent of the model used to describe them:

1. **Direct CP Violation.** This occurs when the magnitude of the amplitude of a decay to a final state is not equal to that of the conjugate decay.

2. **Indirect CP violation** occurs in neutral meson mixing and may also manifest itself in the interference between mixing and decays.

Direct CP Violation Consider decays to a final state f, and define $A_f = \langle f|H|B^0\rangle$ and $\overline{A}_{\overline{f}} = \langle \overline{f}|H|\overline{B}^0\rangle$. It is useful to consider the physically meaningful and convention independent quantity $\left|\frac{\overline{A}_{\overline{f}}}{A_f}\right|$. If complex terms in the Lagrangian contribute to these decay amplitudes they will occur with opposite signed phases in A_f and $\overline{A}_{\overline{f}}$. The only possible source of such terms in the Standard Model is in the electroweak sector as a result of complex terms in the CKM matrix (The CKM matrix describes mixing of quark flavour in the standard model and will be described later in this chapter) [11]. These "weak" phases may be denoted by ϕ_i. Another phase may occur in A_f and $\overline{A}_{\overline{f}}$ as a result of contributions from rescattering (predominantly via the strong interaction) of on-shell intermediate states. These "strong phases" are denoted by δ_i, and appear with the same sign in both A_f and $\overline{A}_{\overline{f}}$. If several processes contribute to the transition $B_0 \to f$ then A_f will be given by the sum of all such contributions. In this case:

$$
\begin{aligned}
A_f &= \Sigma_i |A_i| e^{i(\delta_i+\phi_i)}, \\
\overline{A}_{\overline{f}} &= \Sigma_i |A_i| e^{i(\delta_i-\phi_i)}.
\end{aligned}
\tag{1.1}
$$

where A_i represents the amplitude of the individual process. If multiple processes contribute which each have unique non zero weak and strong phases then $\left|\frac{A_f}{\overline{A}_{\overline{f}}}\right| \neq 1$ and therefore there will be direct CP violation present in the decay.

Indirect CP violation Mixing occurs in the neutral meson sector since the flavour eigenstates of the neutral mesons are not also the mass eigenstates of the system. It is the mass eigenstates which must be considered in order to describe the time evolution of these particles, and therefore the flavour eigenstates will be mixed as they propagate. If the CP eigenstates do not coincide with the mass eigenstates CP violation will exist in the neutral meson sector. CP violation can also occur in the interference of decays with and without mixing when both of the neutral mesons decay to the same CP eigenstates. Indirect CP violation has been observed in both the neutral kaon and B meson systems, but has only recently been seen in the D^0 system [13].

1.2.3 The Standard Model

The Standard Model of particle physics [14] is based around an $SU(3)_C \otimes SU(2)_L \otimes U(1)_Y$ gauge field theory. The theory comprises three generations of fermions (quarks and leptons). Interactions within this theory occur via the exchange of gauge bosons. In the case of the weak interactions (described by the (SU(2) group) these gauge bosons are the massive, spin-1 $W^{\pm}$ and Z^0 bosons, whereas one massless photon and eight massless gluons are associated with the electromagnetic (U(1)) and strong (SU(3)) interactions respectively.

1.2.4 The Higgs Mechanism and Quark Mass

Since the weak interaction couples only to left handed fermions, different SU(2) representations are required for left and right handed fermions. The left handed fermions are described by SU(2) doublets of isospin $\pm\frac{1}{2}$ and the right handed fermions are described by SU(2) singlets with weak isospin 0. Mass terms of the form $m(\overline{\psi}_L\psi_R+\overline{\psi}_R\psi_L)$ may not be included in the Standard Model Lagrangian since this combination of an SU(2) doublet and singlet would violate gauge invariance. The spontaneous symmetry breaking of the electroweak group $SU(3)_C \otimes SU(2)_L \otimes U(1)_Y \rightarrow SU(3)_C \otimes U(1)_{QED}$ occurs via the "Higgs Mechanism". Gauge invariant mass terms may then be introduced into the Standard Model Lagrangian via Yukawa couplings between the scalar Higgs field and fermion fields.

The Yukawa interaction of the quarks may be written as [15]:

$$\mathcal{L}_{\text{Yukawa}} = -Y^d_{ij}\overline{Q}_{Li}\phi d_{Rj} - Y^u_{ij}\overline{Q}_{Li}\epsilon\phi^* u_{Rj} + h.c. \tag{1.2}$$

where: $Y^{u,d}$ are complex matrices specifying the Yukawa couplings, ϕ is an $SU(2)$ doublet of complex scalar Higgs fields ($\phi = (\phi^+, \phi^0)$), ϵ is the (dimension 2) anti-symmetric tensor, Q_{Li} represents the left handed quark doublet, and d_{Rj} and u_{Rj} represent the down and up type right handed quark singlets in the weak eigenstate basis and $h.c.$ refers to the hermitian conjugate of the first part of the expression. The labels i and j refer to the quark generation. Under a suitable potential, $V(\phi)$, the Higgs field may acquire a non zero vacuum expectation value, given in the "unitary gauge" by $\langle\phi\rangle = \frac{1}{\sqrt{2}}(0, v)$. Equation 1.2 will then give rise to mass terms for up and down type quarks of the form:

$$\frac{v}{\sqrt{2}}Y^d_{ij}\overline{d}_{Li}d_{Rj}, \tag{1.3}$$

$$\frac{v}{\sqrt{2}}Y^u_{ij}\overline{u}_{Li}u_{Rj}. \tag{1.4}$$

1.2.5 CP Violation via Complex Yukawa Couplings

The first term of equation 1.2 will change under the CP transformation as follows:

$$Y^d_{ij}\overline{Q}_{Li}\phi d_{Rj} \rightarrow_{CP} Y^d_{ij}\phi^\dagger Q_{Li}d_{Rj}. \tag{1.5}$$

Therefore in the case that the Yukawa couplings are real ($Y^d_{ij} = (Y^d_{ij})^*$) this term would transform under CP into its hermitian conjugate. The same is true of the second term of equation 1.2. Therefore in the case that the Yukawa couplings are real the Lagrangian is unchanged under the CP transformation and so CP violation would not occur in the Standard Model. Thus CP violation requires the Yukawa couplings to be complex.

1.2.6 The CKM Matrix and Flavour Mixing

The mass matrices for eigenstates of quark flavour as illustrated by equation 1.4 are: $M^u = \frac{v}{\sqrt{2}}Y^u$ and $M^d = \frac{v}{\sqrt{2}}Y^d$. In order to move basis from flavour to mass eigenstates the mass matrix must be diagonalized:

$$U^{u,d}_L M^{u,d} U^{u,d\dagger}_R = \mathrm{diag}(m_{u,d}, m_{c,s}, m_{t,b}) \tag{1.6}$$

where the masses $m_{u,d}$, $m_{c,s}$ and $m_{t,b}$ are real and $U_L^{u(d)}$ and $U_R^{u(d)}$ are unitary matrices. Due to the unitarity of the matrices $U_L^{u(d)}$ the transformation from flavour to mass eigenstates has no affect on neutral current processes [15]:

$$\overline{u}_i^{\text{weak}} u_i^{\text{weak}} = \overline{u}_i^{\text{mass}} u_i^{\text{mass}}. \tag{1.7}$$

However charged current interactions are modified by the product $V_{\text{CKM}} \equiv (U^u)^\dagger U^d$:

$$\overline{u}_i^{\text{weak}} d_i^{\text{weak}} \rightarrow \overline{u}_i^{\text{mass}} (U^u)^\dagger U^d d_i^{\text{mass}} \tag{1.8}$$

The "CKM Matrix", V_{CKM}, therefore defines the likelihood of decays between d type and u type quarks:

$$V_{\text{CKM}} = \begin{pmatrix} V_{ud} & V_{us} & V_{ub} \\ V_{cd} & V_{cs} & V_{cb} \\ V_{td} & V_{ts} & V_{tb} \end{pmatrix}. \tag{1.9}$$

As the product of unitary matrices, V_{CKM}, must also be unitary. In general a 3×3 unitary matrix may be defined by three angles and six complex phases. However in the case of the CKM matrix five complex phases correspond to relative phases between quark fields and may be factored out without physical consequence. However one complex phase remains and it is this phase which enables the Standard Model to accommodate CP violation.

1.2.7 Parametrization of the CKM Matrix

The Chau and Keung parametrization

By choosing a particular parametrization of the CKM matrix its unitary nature may be displayed manifestly. One of the commonly used parametrization is the "Chau and Keung" parametrization [16]. This is obtained from the product of three rotation matrices characterized by Euler angles θ_{12}, θ_{13} and θ_{23} in addition to a complex phase, δ. The matrix under this parametrization is given by:

$$V_{\text{CKM}} = \begin{pmatrix} c_{12}c_{13} & s_{12}c_{13} & s_{13}e^{-i\delta_{13}} \\ -s_{12}c_{23} - c_{12}s_{23}e^{i\delta_{13}} & c_{12}c_{23} - s_{12}s_{23}s_{13}e^{i\delta_{13}} & s_{23}c_{13} \\ s_{12}c_{23} - c_{12}s_{23}e^{i\delta_{13}} & -c_{12}c_{23} - s_{12}s_{23}s_{13}e^{i\delta_{13}} & c_{23}s_{13} \end{pmatrix} \tag{1.10}$$

where $c_{ij} = \cos(\theta_{ij})$ and $s_{ij} = \sin(\theta_{ij})$ and $\delta = \delta_{13}$.

The Wolfenstein Parametrization

The Wolfenstein parametrization [17] is another common parametrization of the CKM matrix. This parametrization is inspired by the experimental observation that a hierarchy exists between the mixing angles such that $\theta_{13} << \theta_{23} << \theta_{12}$. Expressed in terms of the small quantity $\lambda \approx |V_{us}| \approx 0.23$, the order of magnitude of the CKM elements is given by:

$$\begin{pmatrix} 1 & \lambda & \lambda^3 \\ \lambda & 1 & \lambda^2 \\ \lambda^3 & \lambda^2 & 1 \end{pmatrix}. \tag{1.11}$$

In addition to the expansion term λ this parametrization uses three real parameters A, η and ρ which are all of order 1. The expansion of the CKM matrix up to terms $\mathcal{O}(\lambda^3)$ is given by:

$$V_{\mathrm{CKM}} = \begin{pmatrix} 1-\frac{1}{2}\lambda^2 & \lambda & A\lambda^3(\rho - i\eta) \\ -\lambda & 1-\frac{1}{2}\lambda^2 & A\lambda^2 \\ A\lambda^3(1-\rho-i\eta) & -A\lambda^2 & 1 \end{pmatrix}. \tag{1.12}$$

It may be noted from equation 1.12 that the parameter η quantifies the imaginary component of V_{CKM} and hence the level of CP violation.

1.2.8 The Unitary Triangle and Angles α , β and γ

Unitarity Triangles

The unitarity of the CKM matrix imposes nine complex linear relations on its elements: $\Sigma_k V^*_{ik} V_{kj} = \delta_{ij}$. Six of these relations (those for which $i \neq j$) can be represented as triangles in the complex plane. The fact that V_{CKM} may be parametrized by one complex phase rather than the six of a general unitary matrix leads to the further constraint that the six unitary triangles all have the same area in the complex plane. The area of each triangle may be written as $\frac{1}{2}|J|$ where J is the "Jarlskog invariant" [18]. The Jarlskog invariant is defined in terms of the CKM elements by:

$$J = \mathrm{Im}(V_{ij} V_{kl} V^*_{il} V^*_{kj}) \qquad (k \neq l, j \neq i). \tag{1.13}$$

The area of the unitary triangles provides a measure of the level of CP violation in the Standard Model; in the limit of no CP violation the unitary triangles tend to straight lines in the complex plane. Switching from one parametrization to another equates to rotating the triangles in the complex plane, therefore the angles and lengths of the triangles provide a convenient convention independent method of describing the Standard Model description of CP violation.

Of the six unitary triangles, four are difficult to access experimentally since they have two sides which are very much longer than the third. The remaining two, which both have all sides of length $\mathcal{O}(\lambda^3)$, are listed below:

$$V_{ub}^* V_{ud} + V_{cb}^* V_{cd} + V_{tb}^* V_{td} = 0 \tag{1.14}$$

$$V_{ud}^* V_{td} + V_{us}^* V_{ts} + V_{ub}^* V_{tb} = 0 \tag{1.15}$$

By convention equation 1.14 alone is referred to as the Unitary Triangle. The three angles associated with the Unitary Triangle are α, β, γ (also refereed to as ϕ_2, ϕ_1, ϕ_3 respectively) and are defined as:

$$\alpha \equiv \arg\left(-\frac{V_{td}V_{tb}^*}{V_{ud}V_{ub}^*}\right), \quad \beta \equiv \arg\left(-\frac{V_{cd}V_{cb}^*}{V_{td}V_{tb}^*}\right), \quad \gamma \equiv \arg\left(-\frac{V_{ud}V_{ub}^*}{V_{cd}V_{cb}^*}\right). \tag{1.16}$$

The Unitary triangle is illustrated in figure 1.1.

1.2.9 Experimental Constraints

One of the main goals of flavour physics is to over-constrain the parameters of the Unitary Triangle. With this aim measurements have been made to give information on the magnitudes of all relevant elements of the CKM matrix and all angles of the Unitary Triangle. Any deviation from unitarity would provide a clear indication of new physics beyond the Standard Model. To date there is no strong experimental evidence of any such deviation. The current (at the time of writing) constraints on the unitarity triangle are displayed graphically in figure 1.2.

Measurements on the Magnitude of CKM elements

A summary of the measurements of the magnitudes of the CKM elements relevant to the Unitary Triangle is given by 1.17. All of these (global averaged) measurements are provided by [19].

$$|V_{ud}| = 0.97394 \pm 0.00089,$$

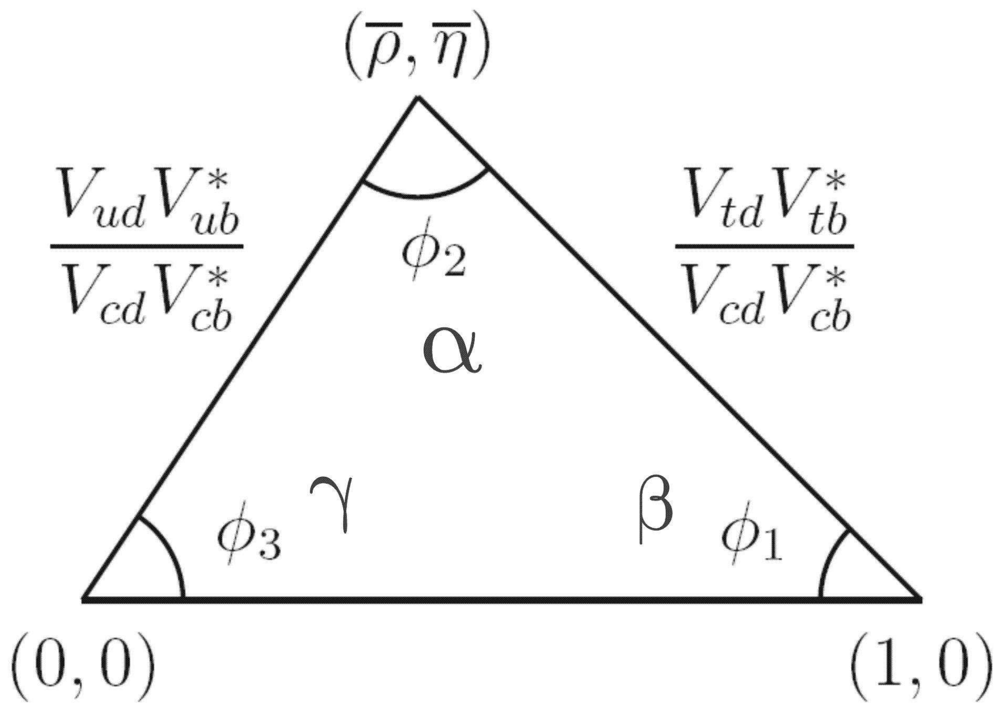

Figure 1.1: The Unitary Triangle. It is conventional that the horizontal side of the triangle is given unit length.

$$\begin{aligned}
|V_{cd}| &= 0.224 \pm 0.014, \\
|V_{cb}| &= 40.75 \pm 2.0 \times 10^{-3}, \\
|V_{ub}| &= 3.48 \pm 0.59 \times 10^{-3}, \\
|V_{td}| &= 8.1 \pm 0.6 \times 10^{-3}, \\
|V_{tb}| &= 0.99 \pm 0.15.
\end{aligned} \tag{1.17}$$

The knowledge of $|V_{ud}|$ comes from measurements of neutron decays, in addition to super allowed nuclear β decay. $|V_{cd}|$ measurements are obtained from measurements of dimuon production in deep inelastic neutrino-neutron scattering. $|V_{cb}|$ information is obtained from both the inclusive and exclusive semi-leptonic decays of B mesons to charm. $|V_{ub}|$ has been measured via semi-leptonic B decays. $|V_{td}|$ is obtained from measurements of B meson oscillations; this allows determination of the oscillation frequencies of B^0 and B_s, $\triangle m_s$, $\triangle m_d$ respectvely and from this information along with the relevant form factors $|V_{td}|$ is constrained. The measurement of $|V_{tb}|$ is obtained from the ratios of the branching fraction of the top quark decays $t \to Wb$ to the branching fractions of $t \to Wq$, where q is either d or s quark.

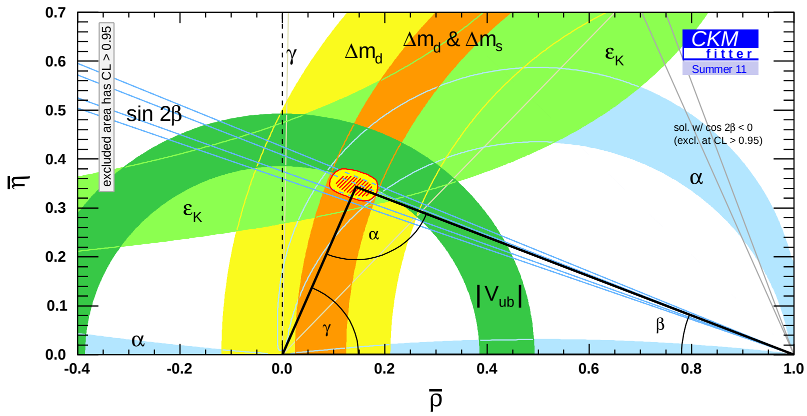

Figure 1.2: Current experimental constraints on the parameters of the CKM triangle. Taken from reference [19]

Measurements on the angles of the Unitary Triangle

Direct measurements can also be made of the angles of the Unitary Triangle. The current best world averages of the angles α, β and γ are given by [19]:

$$\begin{aligned} \alpha &= (89.0^{+4.4}_{-4.2})^\circ \\ \beta &= (21.38^{+0.79}_{-0.77})^\circ \\ \gamma &= (68^{+10}_{-11})^\circ \end{aligned} \tag{1.18}$$

The β measurement comes from a time dependent analysis of $B^0 \to J/\psi K_S$ and related decays. The measurements of α comes primarily from measurements of the $B^0 \to \rho\rho$ decay mode.

The angle γ is currently the least well constrained parameter of the Unitary Triangle. In order to provide a rigorous test of unitarity the precision on the measurement of γ must be improved. A precision measurement of γ is particularly important since it has no dependence on CKM elements involving the top quark. This distinguishes γ as the only CP violation parameter which may be accessed via tree level decay processes. Since such tree level processes are not expected to suffer possible significant contributions from new physics, measurements thus made would provide a Standard Model "standard candle" against which measurements of γ that are made involving loop processes (which are sensitive to possible contributions from new physics) may be compared.

1.2.10 γ Measurements from $B \to DK$ Decays

As described in section 1.2.9, γ is currently the least well constrained angle of the Unitary Triangle. It is possible to measure γ through only tree level processes by studying the decay $B^{\pm} \to DK^{\pm}$, where D refers to D^0 or $\overline{D}^0$, and both the D^0 and $\overline{D}^0$ decay to the same final state. The Feynman diagrams for the $B^- \to DK^-$ decays are illustrated in Fig. 1.3 and 1.4. As first noted in [20] and [21] it is possible to

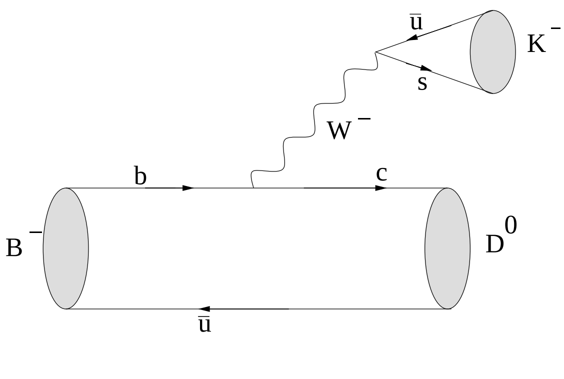

Figure 1.3: Feynman Diagram for $B^- \to D^0 K^-$. This amplitude will depend on $V_{cb}V_{us}^*$

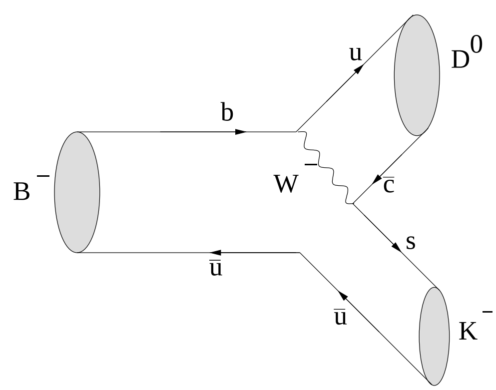

Figure 1.4: Feynman Diagram for $B^- \to \overline{D}^0 K^-$. This amplitude will depend on $V_{ub}V_{cs}^*$ which introduces the weak phase.

access γ using these decays as a result of interference between the quark transitions $b \to u\bar{c}s$ and $b \to c\bar{u}s$. Since it is the interference between the D^0 and $\overline{D}^0$ decays which provide access to γ it is useful to consider the following ratios:

$$\frac{A(B^- \to \overline{D}^0 K^-)}{A(B^- \to D^0 K^-)} = r_B e^{i(\delta_B - \gamma)}, \tag{1.19}$$
$$\frac{A(B^+ \to D^0 K^+)}{A(B^+ \to \overline{D}^0 K^+)} = r_B e^{i(\delta_B + \gamma)}.$$

Here r_B gives the ratio of the magnitudes of the $B \to D^0 K$ and $B \to \overline{D}^0 K$ decays. Due to colour suppression the decay $B^- \to D^0 K^-$ is favoured compared to $B^- \to$

$\overline{D}^0 K^-$ and therefore r_B is small; the current world averaged measurement is given by $r_B = 0.103^{+0.017}_{-0.023}$ [19]. δ_B is a CP invariant "strong phase". Such phases relate to processes associated with the strong and electromagnetic force. The $B^\pm \to DK^\pm$ decay may be considered in terms of two sets of processes:

1. The weak decay of the initial state, $i \to f'$,
2. The strong or electromagnetic scattering of the product of the weak interaction into the final state, $f' \to f$,

where f' is an intermediate state (which results from the flavour changing weak interaction and so must have the same quark content as the final state) and f is the final state (which results from scattering of the particles due to strong and electromagnetic processes). The scattering of the particles into the final state will be dominated by the strong force, and gives rise to the "strong phase", δ_B referred to in equation 1.19. The average of all current measurements give δ_B as $135 \pm 26°$ [22]. Including the decay of the D^0 and $\overline{D}^0$ into the final state, f_D, the amplitude for the full decay chain may be written as:

$$\frac{A(B^- \to D(f_D)K^-)}{A(B^- \to D^0 K^-)} = A_D + r_B e^{i(\delta_B - \gamma)} \bar{A}_D, \tag{1.20}$$

$$\frac{A(B^+ \to D(f_D)K^+)}{A(B^+ \to \bar{D}^0 K^+)} = \bar{A}_D + r_B e^{i(\delta_B + \gamma)} A_D. \tag{1.21}$$

Here A_D and $\bar{A}_D$ are the amplitudes for the decays of D^0 and $\overline{D}^0$, respectively, into the final state f_D. Several experimental strategies have been proposed for the extraction of γ and the other free parameters involved in the $B \to DK$ decays, which differ according to the decay mode of the D^0 or $\overline{D}^0$.

The GGSZ Method

The GGSZ method (first proposed by Giri, Grossman, Soffer and Zupan) [34] involves studying a final state of the D decay, f_D, which involves three or more particles. When the D decays to such a multi-body final state, the momenta of the final state particles may vary continuously and the decay is expected to proceed predominantly via a variety of intermediate resonant states [35]. This is in contrast to two body final states for which the decay is governed by a single quantum mechanical amplitude [34]. Each point within the final state phase space corresponds to a specific combination of the intermediate resonances, and may be considered as a unique final state [36]. Considering a particular point, x, in the f phase space the amplitude of the decay $B^{\pm} \rightarrow D(f_{D,x})K^{\pm}$ may be written as [34]:

$$A(B^{+} \rightarrow D(f_{D,x})K^{+}) = A_D(x) + \overline{A}_D(x) r_B e^{i(\delta_B+\gamma)}, \tag{1.22}$$

$$A(B^{-} \rightarrow D(f_{D,x})K^{-}) = \overline{A}_D(x) + A_D(x) r_B e^{i(\delta_B-\gamma)}, \tag{1.23}$$

where $A_D(x)$ corresponds to the amplitude of the decay $D^0 \rightarrow f_D(x)$ and similarly $\overline{A}_D(x)$ corresponds to the amplitude $\overline{D}^0 \rightarrow f_D(x)$. Note that the interference terms in 1.22 and 1.23 are dependent on both the D decay (x) and B decay parameters (δ_B, r_B and γ). Therefore the observed distribution of final states of the decays $B^{\pm} \rightarrow D(f(x))K^{\pm}$ is not simply that seen in inclusive D decays but is modified in a way that depends on the B decay parameters. Since γ transforms to $-\gamma$ under CP, while the strong phase δ_B is unchanged it is possible to make a measurement of γ (in addition to the parameters δ_B and r_B) from a single final state of the D decay, if the amplitude structure ($A_D(x)$, $\overline{A}_D(x)$) of the D decay is known. This analysis may be applied to any D decay with three or more particles in the final state.

In order to make γ measurements from 3 or 4 body D decays (in $B^{\pm} \rightarrow D(f_D)K^{\pm}$) it is vital to have a detailed independent knowledge of the amplitude structure of the D^0 and $\overline{D}^0$ decays. This may be obtained from independent flavour tagged $D \rightarrow f_D$ decay samples. The GGSZ method has been used to make γ measurements at the B-factories using the decay $D^0 \rightarrow K_S\pi^+\pi^-$, this is discussed in more detail in chapter 3.

It has also been proposed that in order to parametrize the D decays in a model independent manner, the phase space of the final state of the D decay may be divided into bins and the population of events in each bin and the bin averaged strong phase may be measured [23]. These parameters would then provide an input in a fit to data collected from the same D decay in which the D resulted from the decay $B^{\pm} \rightarrow DK^{\pm}$, so that a measurement of γ could be made.

The GLW Method The first strategy that proposed using $B^{\pm} \to DK^{\pm}$ decays to measure γ is the so-called GLW (Gronau, London, Wyler) method, [20]. In this method final states of the D decays which are CP eigenstates are considered. These can be even, for example $D^0 \to K^+K^-$ or odd, for example $D^0 \to K_S\pi^0$. The relative rates of the decays can be measured using a simple counting experiment. However γ does not appear at leading order in the decay rates to CP eigenstates so sensitivity to γ using this method is limited.

The ADS method In the case of the ADS (Atwood, Dunietz, Soni) method [21] D decays to non-CP eigenstates are used. Maximum interference and therefore maximum sensitivity to γ is achieved when a favoured (suppressed) $B^{\pm} \to DK^{\pm}$ decay is followed by a suppressed (favoured) $D \to f_D$ decay, for example $B^{\pm} \to (K^{\mp}\pi^{\pm})_D K^{\pm}$. Combining two GLW final states with four ADS final states provides a sufficient number of observables for a measurement of γ to be made.

1.3 CP Violation In Charm Decays

Of particular pertinence to the work presented in this thesis is CP violation as it may occur in the charm sector. Measurements of CP violation in the charm sector provide promising channels with which to search for new physics since the Standard Model predictions for CP violation are very small (of the order of 10^{-3}) where as new physics contributions can generate larger effects [24].

The small predictions of CP violation in the Standard Model can be understood since only the first two generations of quarks are present in the initial and final states of the charm meson decays and the processes are dominated by tree level amplitudes in which a quark undergoing a $c \to (s, d)$ transition emits a W boson which converts to a quark-antiquark pair. Within the Standard Model a process involving only the first two quark generations is CP conserving, therefore CP violation in charm decays requires contributions from virtual b quarks which may be introduced only via penguin or box diagrams. These contributions however are suppressed by a factor $V_{cb}V_{ub}^*$, therefore any observations of larger CP violating effects in this sector would require contributions from physics beyond the Standard Model. In particular charm decays probe new physics scenarios in which the up type quarks play important roles. These include certain supersymmetric models and models in which the quark mixing is generated in the up sector [25].

1.3.1 CP Violation in Singly Cabibbo Suppressed D decays

Singly Cabibbo suppressed (SCS) decays of D mesons (those involving a $|\Delta C| = 1$ quark transition where C is the quantum number associated with the number of charm quarks) may occur through charge current quark transitions ($c \to s\bar{s}u$ or $c \to d\bar{d}u$) or the transition $c \to uq\bar{q}$ which is represented by a penguin diagram. The tree level and penguin Feynman diagrams in the example of the SCS $D^0 \to K^+K^-$ decay are shown in figures 1.5 and 1.6, respectively. The interference between penguin

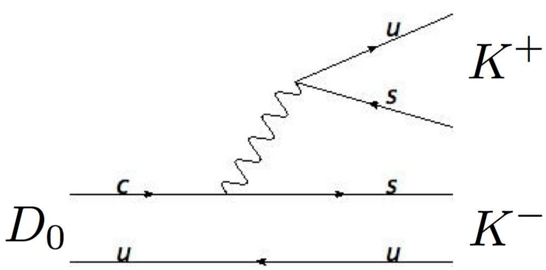

Figure 1.5: Feynman diagram for tree level $D^0 \to K^+K^-$ singly Cabibbo suppressed decay.

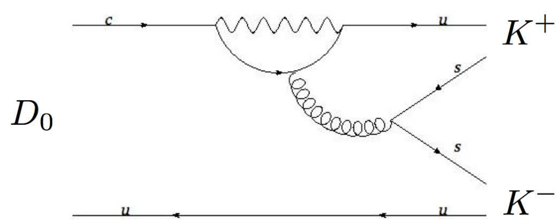

Figure 1.6: Feynman diagram for penguin contribution to the $D^0 \to K^+K^-$ singly Cabibbo suppressed decay.

and tree level processes is able to generate CP violation for SCS decays. The quark transitions $c \to uq\bar{q}$ are sensitive to new physics interactions which can generate direct CP violation. There are possible contributions from tree level interactions in some beyond the Standard Model theories (for example flavour changing Z or Z' couplings) however these are bounded to offer contributions well below the currently observable level [24]. However some one loop effects from QCD penguin or dipole operators are able to generate CP violating effects that reach levels of order 10^{-2} which could be observed with current experiments [24].

No such contribution is possible for either Cabibbo favored decays (which involve the quark transition $c \rightarrow sd\overline{u}$) or doubly Cabibbo suppressed decays (involving the quark transition $c \rightarrow d\overline{s}u$) since these decays proceed via processes that share the same weak phase therefore no direct CP violation is expected in the Standard Model for these decays.

Experimental Searches

Several methods exist by which a search for CP violation can be performed in SCS D decays.

Decay Rate Measurements In one strategy a measurement of the branching fraction of the D decay to a final state f ($\Gamma(D \rightarrow f)$) and the corresponding branching fraction for the conjugate decay ($\Gamma(\overline{D} \rightarrow \overline{f})$) is made. The CP asymmetry for such a decay is defined as a_f:

$$a_f = \frac{\Gamma(D \rightarrow f) - \Gamma(\overline{D} \rightarrow \overline{f})}{\Gamma(D \rightarrow f) + \Gamma(\overline{D} \rightarrow \overline{f})}, \tag{1.24}$$

where D may represent a D^0, D_s^+, D^+ or a charmed baryon and $\overline{D}$ represents a $\overline{D}^0$, D_S^- or D^-, respectively. In the case of charged D decays no mixing is possible so only direct CP violation may contribute to a CP asymmetry. In the case of D^0 and $\overline{D}^0$ decays three categories of CP violation)via mixing, via the interference between mixing and decay and direct CP violation) may all, in principle, contribute to an observed asymmetry. However the contribution to CP violation via mixing is expected to be unobservably small, in the standard model, so any measurable CP asymmetry is likely to be dominated by direct CP violation.

Many measurements of this nature have been made. For example studies which made measurements on the decays $D^0 \rightarrow K^+K^-$ and $D^0 \rightarrow \pi^+\pi^-$, were carried out at Babar [26] and Belle [27], numerous other measurements on a variety of charged and neutral D decays have also been made and no definitive CP asymmetry has only recently been observed [28], [13].

T-odd Moments Measurements An alternative method of measuring CP violation is to observe T violation and infer CP violation by assuming the validity of the CPT theorem. The relevant T asymmetry parameter, A_T is defined as:

$$\mathcal{A}_T \equiv \frac{1}{2}(A_T - \overline{A}_T), \tag{1.25}$$

where:

$$A_T = \frac{\Gamma(\vec{\nu}_1 \cdot (\vec{\nu}_2 \times \vec{\nu}_3) > 0) - \Gamma(\vec{\nu}_1 \cdot (\vec{\nu}_2 \times \vec{\nu}_3) < 0)}{\Gamma(\vec{\nu}_1 \cdot (\vec{\nu}_2 \times \vec{\nu}_3) > 0) + \Gamma(\vec{\nu}_1 \cdot (\vec{\nu}_2 \times \vec{\nu}_3) < 0)}, \tag{1.26}$$

where $\vec{\nu}_i$ is either the momentum or spin of the final state particle in the D rest frame. The vector $\vec{\nu}_i$ changes sign under the T operation therefore products containing three factors of $\vec{\nu}_i$ are odd under the T operation.

The observable A_T alone is not sufficient to establish T violation since final state interactions may introduce asymmetries. The T violating phase changes sign for the conjugate decay while the strong phases introduced by the final state interactions are unchanged. Therefore a non zero value of $\mathcal{A}_T$ is required in order to provide an unambiguous indication of T violation. This analysis has been carried out at FOCUS (a fixed target heavy flavour experiment located at Fermilab [29]) [30] and more recently at Babar [31] for the four body SCS decay $D \to K^+K^-\pi^+\pi^-$ using the momentum of the final state particles in expression 1.26. No evidence for T asymmetry was observed in this channel.

Amplitude Analyses A further method of measuring CP violation which is particularly pertinent to the work presented in this thesis involves studying the intermediate states via which a multibody decay proceeds. This technique requires the development of a model to describe the intermediate states of the decay. Asymmetries in the model describing the decay of the D^0 and that of the $\overline{D}^0$ can provide an indication of CP violation. Such a technique has the advantage of being sensitive to small CP asymmetries in localised areas of phase space rather than requiring a large global CP asymmetry. This technique will be described in further detail in chapter 7.

1.4 Amplitude Analysis of D decays

Consider a D meson decay to a final state of N pseudoscalar particles. The four-momenta of the final state particles provides $4N$ degrees of freedom. The fixed masses of the daughter particles removes N degrees of freedom, and four momentum conservation removes a further four degrees of freedom. Since the D is a spin zero particle a further three degrees of freedom describing the rotational orientation of the decay are also removed leaving $3N - 7$ independent degrees of freedom which are required to describe completely the decay kinematics.

1.4.1 Three Body Decays and the Dalitz-plot Analysis Technique

In the case of D decays to final states of three pseudo-scalar particles (for example $D \to K_S^0 \pi^+ \pi^-$), the decay kinematics may be completely described by two variables. These variables may be chosen from combinations of invariant masses of pairs of the final state particles, $s_{23} = m_{23}^2 = (p_2 + p_3)^2$ and $s_{13} = m_{13}^2 = (p_1 + p_3)^2$, where the final state particles are labeled from 1 to 3 and p_i gives the four momentum of the i^{th} particle. The Lorentz invariant variables s_{23} and s_{13} therefore contain all the unique information about the decay. These variables are referred to as Dalitz variables. A scatter plot of the Dalitz variables s_{13} against s_{23} is referred to as a Dalitz plot. This technique was first proposed by Richard Dalitz when studying the three body decays of charged kaons [32].

In general the decay rate of a spin zero particle to three pseudo scalar particles is given by:

$$\Gamma = \frac{1}{(2\pi)^3 32 M^3} |\mathcal{M}|^2 ds_{13} ds_{23} \tag{1.27}$$

where M is the mass of the decaying particle and $\mathcal{M}$ is the amplitude containing all the dynamics of the decay. An advantage of using Dalitz variables to describe the decay is that in the absence of any internal decay structure (such that $\mathcal{M}$ is constant) the kinematically allowed region of the Dalitz plot is evenly populated with events. Therefore any variation over the Dalitz plot may be attributed to the resonant dynamics of the decay.

For example if a decay to three pseudoscalars P_1, P_2, P_3 proceeds through an intermediate resonance R: $D \rightarrow P_1 R(\rightarrow P_2 P_3)$ the resonance R will be visible in the Dalitz plot as a band perpendicular to the s_{23} axis, centered around the nominal mass squared of resonance R. Similarly if the decay proceeds via an intermediate resonance $R^{'}$: $D \rightarrow P_3 R^{'}(\rightarrow P_1 P_2)$ the resonance $R^{'}$ will appear as a band with gradient -1 in the Dalitz plot. This is illustrated for the example of the decay $D^0 \rightarrow K_S \pi^+ \pi^-$ in figure 1.7. The band in the Dalitz plot corresponding to each

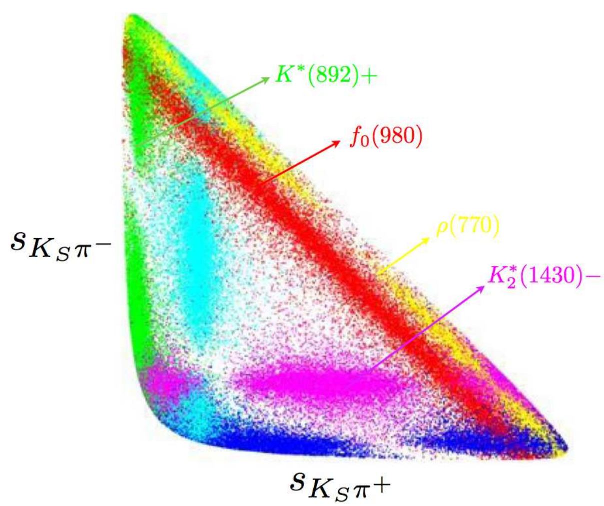

Figure 1.7: A Dalitz plot using simulated data for the decay $D^0 \rightarrow K_S \pi^+ \pi^-$. Several resonant components are illustrated in different colours. Along the horizontal axis the blue verticle band is centred around 891.7 MeV. Similarly the pink horizontal band intersects the vertical axis at 1429 MeV. The bounds of the triangle are determimed by the allowed phase space for the decay. (Image produced by Tom Lathan).

resonance also provides information about the angular momentum of the resonance. Considering the example of a spin-1 resonance, there is a dependence on the angle between the momentum vector of the resonant particle and that of the other daughter which is given by the spherical harmonic Y_1^0 ($\propto \cos\theta$). In the Dalitz plane this dependence manifests itself as an absence of entries around the center of the resonant band corresponding to the spin-1 resonance. This behavior can be observed for the $\rho(770)$ resonance in figure 1.7. Similarly a spin-2 resonance has an angular dependence given by the Y_2^0 spherical harmonic ($\propto 3\cos^2\theta - 1$) which gives rise to two regions of depletion in the band. An example of this may be observed in the Dalitz plane for the $K_2^*(1430)$ resonance in figure 1.7. A spin-0 resonance which has no angular dependence will appear as a featureless band in the Dalitz plot, as occurs for the $f_0(980)$ resonance in figure 1.7.

The relative density of each band gives an indication of the level of contribution of the corresponding resonance to the decay amplitude. The Dalitz plot also gives information about interference between resonances. For example, underpopulated regions of the Dalitz plot indicate regions of negative interference between intermediate resonance states.

A Dalitz plot therefore provides a useful, frame independent, visual representation of the internal structure of a three body decay and by analyzing such a plot, quantitative information about the various intermediate resonant states and their relative contributions and interference may be obtained.

1.4.2 The Isobar Model

In order to parametrize the dynamics of the decay, represented by $\mathcal{M}$ in expression 1.27, a model for the D decay may be developed. A common model used to parametrize such a multi body decay is called the "isobar model". In general the isobar model amplitude for a resonant decay is given by a coherent sum of resonant amplitudes:

$$\mathcal{M} = c_0 + \Sigma_{i>0} c_i A_i \tag{1.28}$$

where c_i is a complex number which parametrizes the contribution of the resonance i and describes its relative phase. Each term A_i gives the amplitude corresponding to a single resonance. The first term of expression 1.28 represents a non resonant contribution to the decay. This non resonant contribution is assumed to take the form of a flat S-wave, although in general it could display more complicated structure.

Consider the general case of a particle P decaying via an intermediate resonance r to a final state abc: $P \to ar(\to bc)$. The amplitude for this individual process is given by [33]:

$$\begin{aligned} \mathcal{A}_r &= \sum_{\lambda} \langle ab|r_\lambda\rangle T_r(m_{ab}) \langle cr_\lambda|P\rangle && (1.29) \\ &= Z(L, l, \vec{p}, \vec{q}) B_L^R(|\vec{p}|) B_L^r(|\vec{q}|) T_r(m_{ab}), && (1.30) \end{aligned}$$

where L is the orbital angular momentum between r and c, l is the spin of resonance r, $\vec{q}$ and $\vec{p}$ are the momenta of a and b in the r rest frame, Z is a function which describes the angular distribution of final state particles, B_L^R and B_L^r are barrier factors for the processes $P \to rc$ and $r \to ab$ respectively and $T_r(m_{ab})$ is a function which describes the resonance r. The sum in equation 1.30 is over the helicity states of r, denoted by λ.

No unique parameterizations exist for the functions Z, B_L and T_{ab} but the most commonly used choices are discussed in the following.

The Barrier Factors, B_L

The barrier factors are spin dependent terms which account for effects due to the non-zero spatial extent of the interacting particles. The most common method for accounting for this behavior is by using a "Blatt-Weisskopf penetration factor", F_l^r [71]. For values of angular momentum $l = 1, 2, 3$, for a resonance of mass M decaying into particles i and j with invariant mass m_{ij}, F_l^r is given by:

$$F_0^r = 1 \tag{1.31}$$

$$F_1^r = \sqrt{\frac{1 + z_q(M)}{1 + z_q(m_{ij})}} \tag{1.32}$$

$$F_2^r = \sqrt{\frac{9 + 3z_q(M) + z_q^2(M)}{9 + 3z_q(m_{ij}) + z_q^2(m_{ij})}} \tag{1.33}$$

where:

$$z_q(m_{ij}) = r^2 q^2(m_{ij}) \tag{1.34}$$

and r is the radius of the decaying particle and the "breaking momentum" $q(s)$ is given by:

$$q(m_{ij}) = \sqrt{\frac{((m_{ij}^2 - (m_i - m_j)^2)(m_{ij}^2 - (m_i + m_j)^2))}{(m_{ij}^2)}}. \tag{1.35}$$

The Angular Distribution term, Z_L

The term Z_L in 1.30 describes the behavior arising from the angular momentum of the decay. This function is dependent on the spin and angular momentum of the resonance. Both the "Lorentz invariant amplitudes" [37] and "helicity amplitudes" [38] are commonly used to account for these spin dependent effects. These terms are equivalent for all zero spin particles. In the study presented in this thesis Lorentz invariant spin amplitudes, s_l, are used. These terms are calculated by describing the decay in terms of a sequence of pseudo two body decays. The particles which make up these intermediate two body states may be either resonant states or non resonant states where the non resonant particles combine to form a partial wave. A spin amplitude for each vertex is calculated from the polarisation vectors and four momenta of the incoming and two outgoing particles. The total spin amplitude is finally given by the product of the terms corresponding to the vertex of each intermediate sub process.

The Breit-Wigner Formalism

The term T_r in 1.30 represents the lineshape of the resonant decay and may be modeled with a relativistic Breit-Wigner function, BW, which is given by [73]:

$$BW = \frac{1}{M^2 - m_{ij}^2 - iM\Gamma} \tag{1.36}$$

where Γ is the momentum dependent width of the resonance which is itself given by:

$$\Gamma = \Gamma_{measured}(\frac{q_{m_{ab}}}{q_{m_r}})^{2l+1}(\frac{m_r}{m_{ij}})(F_l^r)^2 \tag{1.37}$$

where $\Gamma_{measured}$ is the measured fixed width of the resonance. The Breit Wigner formalism is used extensively in the study presented in this thesis. The masses and measured widths of all resonances are taken as detailed in [22].

If the threshold for the decay $r \to ab$ is close to the resonance the shape of the lineshape may become distorted. In this situation the "Flatte" lineshape [41] provides a better description of the resonant decay. The Flatte formula is given by:

$$T_{ij} = \frac{1}{m_r^2 - m_{ij}^2 - i(\rho_1 g_1^2 + \rho_2 g_2^2)}, \tag{1.38}$$

where $g_1^2 + g_2^2 = 1$ and $\rho_{1,2}$ are phase space factors.

The Breit-Wigner formulation is in fact an approximation, corresponding to the first term in a Taylor expansion about a pole in the operator describing the interaction [40]. This is a good approximation when it is used to describe narrow resonances which do not significantly overlap, however when used to describe broad overlapping resonances the Breit-Wigner formulation can violate unitarity. This point is elaborated on in chapter 3.

1.4.3 Four Body Decays

Almost all of what has been said regarding the amplitude analysis of three body decays may also be applied to four body decays (although strictly the term Dalitz plot refers specifically to three body final states). However there are some notable differences when dealing with four body decays. In order to parametrize fully the final state, five (rather than two) independent parameters are required. These may be chosen from invariant masses of final state particles: s_{234}, s_{12}, s_{23}, s_{34}, s_{123}. Using the convention $t_{ij} \equiv (p_i - p_j)^2$ it may be noted that $t_{01}(p_0 - p_1) \equiv s_{234}(p_2 + p_3 + p_4)$ where the index 0 refers to the initial decay particle.In contrast to three-body final states the four body final state phase space is not flat in these variables. For a four-body decay the phase space density is given by the square root of the inverse of the Grahm determinant [69]

$$\frac{d^4\phi}{dt_{01}ds_{12}ds_{23}ds_{34}dt_{04}} = \frac{\pi^2}{32m_0^2}(-\Delta_4)^{-\frac{1}{2}} \tag{1.39}$$

where Δ_4 is the 4-dimensional Grahm determinant. The Grahm determinant may be written, for a general n-dimensional decay as [69]:

$$\Delta_n \equiv \begin{vmatrix} p_1.p_1 & p_1.p_2 & \dots & p_1.p_n \\ p_2.p_1 & p_2.p_2 & \dots & p_2.p_n \\ . & . & . & . \\ . & . & . & . \\ . & . & . & . \\ p_n.p_1 & p_n.p_2 & \dots & p_n.p_n \end{vmatrix}. \tag{1.40}$$

In contrast to the flat three body phase space density the four body phase space density is not bounded. The specifics of the four body amplitude analysis is explained in further detail in chapter 5.

1.5 Summary

CP violation provides good opportunities to test the standard model and provides a potential source of evidence for new physics. A number of avenues exist to investigate CP violation within the charm sector. In particular measurements of the CP violating parameter γ are important to increase knowledge of CP violation, and analysis of decays of the type $B^{\pm} \to D(f(x))K^{\pm}$ will make an important contribution towards this goal.

Chapter 2

The CLEO Detector

2.1 Introduction

The CLEO detector was located at Cornell university, USA (see figure 2.1) and collected data from e^+e^- collisions at centre of mass energies ranging from 3 to 11 GeV between 1979 and 2008 when it was decommissioned. During this time major contributions were made to many areas of charm and B physics. The colliding beams were provided by the Cornell Electron Storage Ring, CESR.

2.2 CLEO and CESR: an overview

CLEO originally studied the Υ system and B meson properties. It was upgraded numerous times during its lifetime; to CLEO II in 1989, CLEO II.V in 1995, CLEO III in 1999, and finally in 2003 to CLEO-c when the running energy was reduced to 4 GeV (around the charm threshold) in order to make precision charm measurements. The CLEO detector was able to provide an almost 4π solid angle coverage around the collision region.

2.2.1 CESR

CESR, illustrated in figure 2.2, is a symmetric e^+e^- collider, located 12m underground on the Cornell campus. The accelerator is comprised of three main components:

1. Linear Accelerator (Linac)

2. Synchrotron

Figure 2.1: A photograph illustrating the location of the CESR accelerator and CLEO detector under the Cornell campus in Ithaca, NY

3. Storage ring

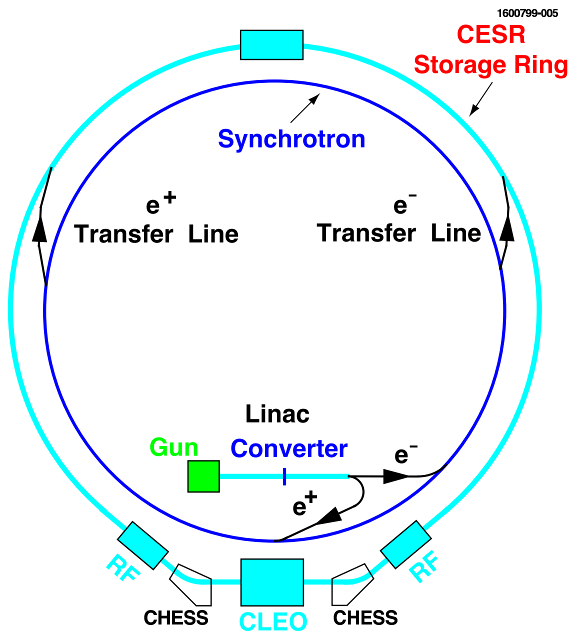

Figure 2.2: Diagram of the CESR accelerator complex.

Electrons are produced from the heated filament of an electron gun, they are then compressed into packets and accelerated by an electric field in the linac to energies of 300 MeV. Positrons are produced by colliding some of the accelerated electrons (at energies of 150 MeV) on a fixed tungsten target. This produces a shower of particles from which the positrons may be extracted and accelerated down the remaining length of the Linac, reaching energies of 150 MeV.

The synchrotron is located in the tunnel, at a smaller radius than the storage ring. Acceleration here is achieved through a series of four radio frequency cavities. The dipole magnets used to contain the bunches of accelerated particles continuously ramp their magnetic field as the particles are accelerated. Finally after acceleration the particles are injected into the storage ring. Here the bunches of particles are focused by quadrupole and sextuple magnets. Electrostatic separators are used to provide the (minimal) deviation required to the electron and positron paths, to prevent collisions of the particles other than at the interaction point. This is illustrated in figure 2.2.

2.3 CLEO III Detector

The data in this thesis were collected with several configurations of the CLEO detector. The CLEO-III detector, shown in figure 2.3, is described first, as the earlier CLEO-II.V and later CLEO-c detectors can be best understood in terms of how they differed from CLEO-III.

The CLEO III detector was optimised for studying the decays of B mesons around the threshold of production at the $\Upsilon(4S)$ resonance. The detector consisted of an inner silicon vertex detector, surrounded by a wire drift chamber, a RICH (Ring Imaging Cherenkov) detector, a crystal calorimeter, a superconducting solenoid magnet (which provided the magnetic field of 1.5 T parallel to the beam pipe, in order to curve the paths of charged particles in a direction perpendicular to the beam), and finally muon chambers.

2.3.1 Tracking System

For the purposes of tracking cylindrical co-ordinates are used, the z axis is defined parallel to the beam direction, the co-ordinate r defines the perpindicular distance from the centre of the beam pipe, and the angle θ is defined relative to the vertical direction. The silicon vertex detector was designed to perform an accurate measurement of the z vertex and the angle $\cot\theta$ of a heavy meson decay, in particular those of b-hadrons. The information from the drift chamber dominated the momentum measurement, while both the silicon vertex detector and the drift chamber contributed to the measurement of ϕ and of the impact parameter [42]. Together the charged particle tracking system allowed for measurements of charged particles in the range $|\cos\theta| < 0.93$ and over the full azimuthal range so that 93% of the solid angle was covered. The silicon vertex detector was particularly important for z measurements since the first z measurement of the drift chamber did not occur until $r = 37$ cm. The silicon detector also increased the accuracy with which charged tracks could be extrapolated into outer detectors, such as the RICH. In conjunction with the inner layers of the drift chamber, particles with a transverse momentum of less than 100 MeV could be reconstructed. Excellent momentum resolution was important for establishing the $D^{*+} - D^0$ "mass difference", in the decay $D^{*+} \to D\pi^+$

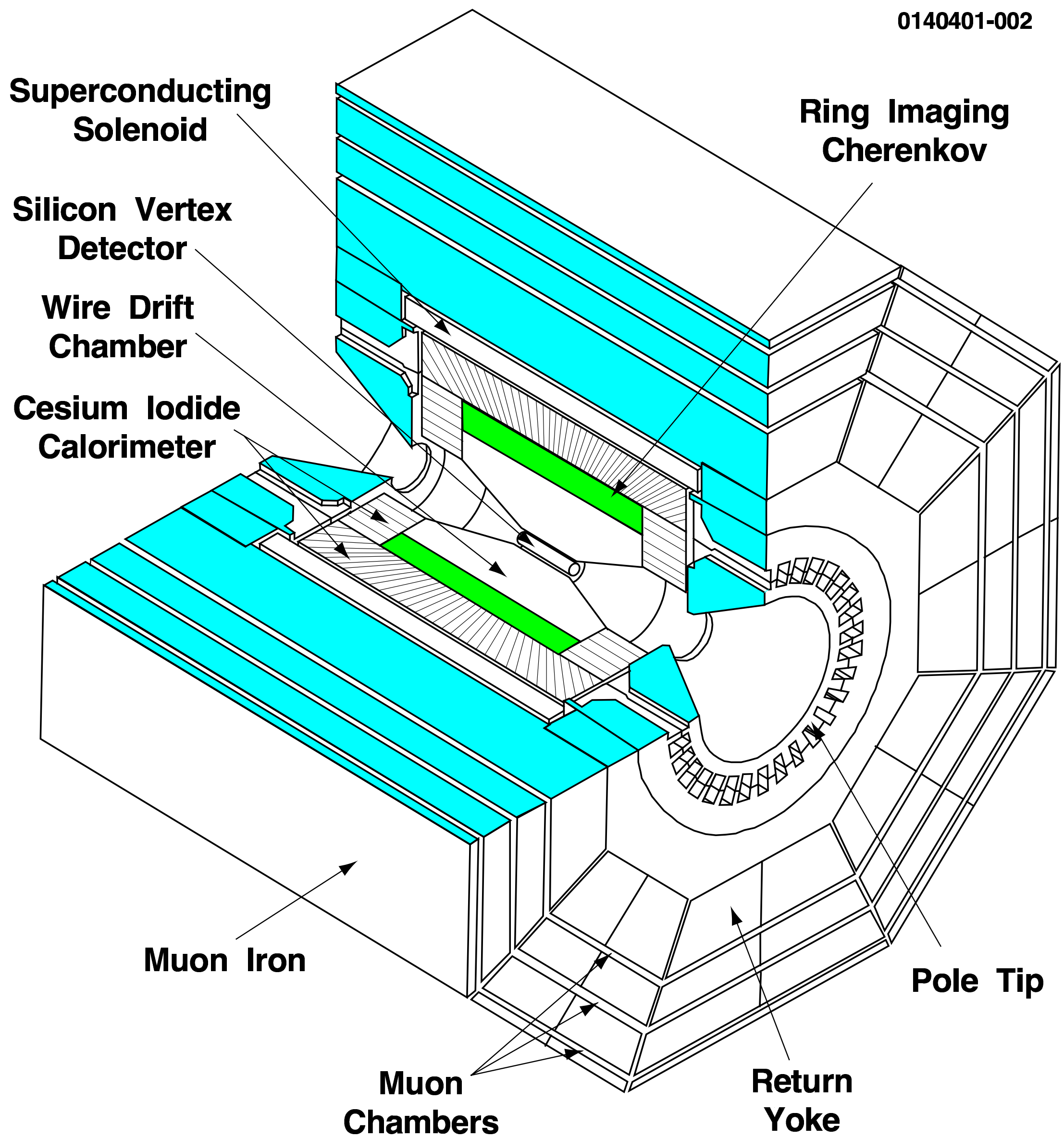

Figure 2.3: A 3 dimension view of the CLEO-III detector.

(and the conjugate decay), which is an important criterion in the selection for the analysis presented in this thesis. With precision information about the direction of the pion provided by the silicon vertex detector and the momentum resolution provided by the drift chamber (a momentum resolution of 40 MeV at a momentum of 5.3 GeV) a mass difference resolution of 0.19 MeV/c^2 was achieved [43].

Silicon Vertex Detector The silicon vertex detector, as illustrated in figure 2.4, consisted of four layers of double-sided silicon strip detectors, spanning a radial distance of 2.5 to 10 cm from the centre of the beam pipe. Each layer was comprised of silicon detectors of dimensions 5 cm$\times$ 2.7 cm$\times$ 300 μm. The n-side of the detector was used to measure the $r-\phi$ coordinate and had silicon strips every 50 μm. The p-side had silicon strips orientated in the z direction with silicon strips every 100 μm. There were a total of 447 silicon detectors with proportionally more detectors in each layer [44].

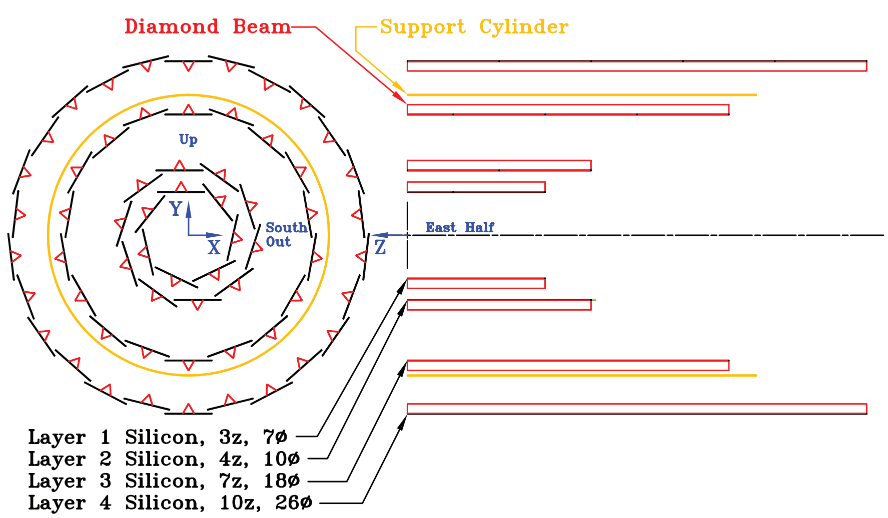

Figure 2.4: Schematic of the CLEO-III Silicon Vertex Detector.

The Drift Chamber (DR) The drift chamber, shown in figure 2.5, consisted of 47 layers and a total of 9796 cells, spanning a radial distance of 13 to 82 cm from the beamline. The detector consisted of a single volume of gas, a 60% : 40% mixture of helium and propane. Each cell formed an approximate 14 mm $\times$ 14 mm square, at the centre of which was a sense wire anode made of gold-plated tungsten. Each sense

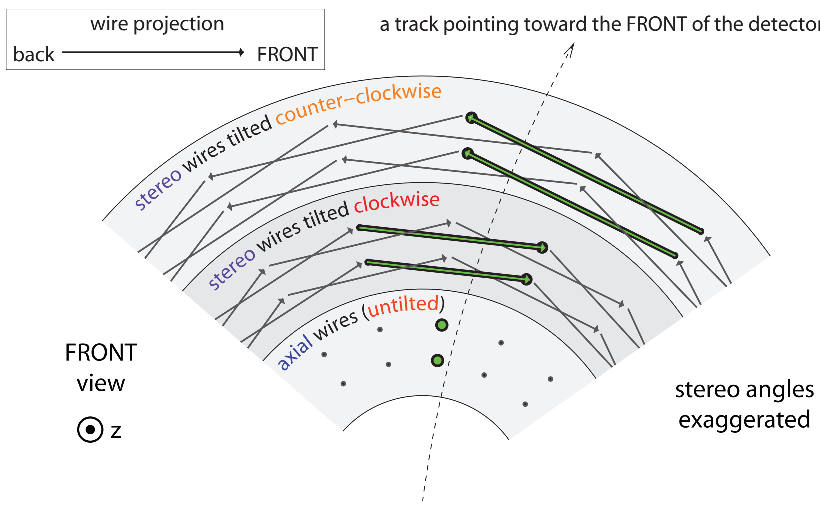

Figure 2.5: Schematic of the Drift Chamber, DR used in the CLEO-III detector.

wire was surrounded by eight parallel "field wires" made of gold-plated aluminium. The electric field in each cell was produced by a 2.1kV potential difference which was applied between the sense and field wires. This provided sufficient field strength close to the sense wire to produce an avalanche of electrons, as electrons from ionised atoms travel towards the sense wire and in turn ionise further atoms. This process is illustrated in figure 2.6. The timing of this pulse in the sense wire allowed a calculation of the closest approach of the trajectory of the charged particle to the sense wire.

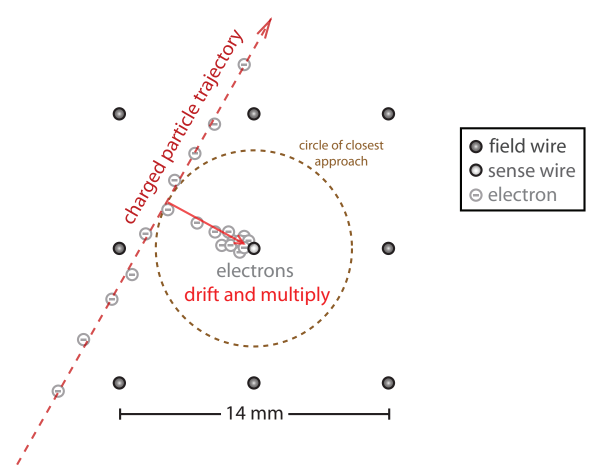

Figure 2.6: Illustration of charge collection as a charged particle traverses the drift chamber volume.

The small radius section of the drift chamber end-plate allowed space for the

CESR focusing magnets. In this small layer the 16 sense wire layers were all parallel to the beam line. The 31 remaining layers of sense wires in the outer section were divided into groups of four layers, with each group alternating the stereo angle with respect to the detector axis. This allowed some z information about the particle tracks to be provided. The variation of stereo angles with respect to the beam axis was 0.021 to 0.028 rad. Furthermore the ϕ angle of each sense wire was offset by a small amount from one end of the wire to another in order to provide some ϕ information.

2.3.2 Particle Identification

$\mathrm{d}E/\mathrm{d}X$ Information The drift chamber provided a measurement of the energy loss per unit length, $\mathrm{d}E/\mathrm{d}X$, of a charged particle via an analysis of the heights of the electrical pulses along the sense wires as the particle traversed this region. At sufficiently high energies $\mathrm{d}E/\mathrm{d}X$ depends only on the velocity of the particle, therefore within this appropriate energy range the Bethe Bloche formula [22] may be used to determine the particle's velocity. Combining this velocity measurement with the momentum measurement provided by the tracking system allowed a determination of the particle's mass and hence the identification of the particle [45]. Figure 2.7 illustrates $\mathrm{d}E/\mathrm{d}X$ as a function of momentum for various reconstructed kaon, pion and proton tracks. Regions of overlap of this figure correspond to the range of momenta for which $\mathrm{d}E/\mathrm{d}X$ information is not effective in providing particle identification. Pion and kaon separation is not possible above 700 MeV. In order for a positive particle identification to be made it was required that the particle hypothesis did not overlap, within three standard deviations, with that of another particle.

The RICH System The Ring Imaging CHerenkov (RICH) system [47] was located immediately outside of the drift chamber and within the detector calorimeters. The CLEO-III RICH system was able to cover 83% of the 4π solid angle of the detector. The principle of a RICH system relies on the Cherenkov effect. Relativistic particles which traverse a dense medium will radiate photons when they travel faster

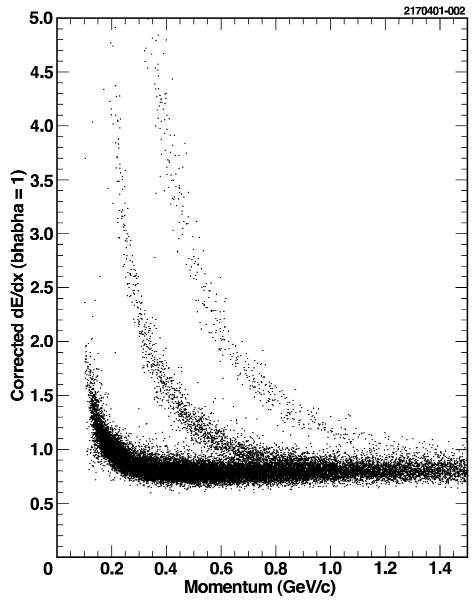

Figure 2.7: Resolution of $\mathrm{d}E/\mathrm{d}X$ as a function of momentum in the CLEO-III drift chamber. From left to right the π, K and p bands are shown.

than light travels in that medium. The angle at which this Cherenkov radiation is emitted, θ_c, is given by:

$$\cos\theta_c = \frac{c}{vn} \tag{2.1}$$

where n is the value of the refractive index of the dielectric medium. The maximum angle (saturated Cherenkov angle) θ_c^{max} for a given medium is therefore given by $\cos\theta_c^{max} = \frac{1}{n}$. Furthermore the number of Cherenkov photons, N_γ, of energy, E, emitted per unit length, l is given by the Frank Tramer equation:

$$\frac{dN_\gamma}{dldE} = \frac{\alpha}{\hbar c} Z^2 \sin^2(\theta_c(E)) \tag{2.2}$$

where Z is the particle charge and α the fine structure constant [48].

In CLEO-III the RICH radiator consisted of a 10 mm thick layer of lithium fluoride crystals. Cherenkov photons produced in the radiator traveled through a volume of nitrogen gas of 16 cm thickness; this enabled the cone of Cherenkov light to expand so that it could be resolved by the detector. A thin calcium window contained the volume of nitrogen, beyond which was the Cherenkov photon detector. This was formed of a mixture of methane and triethylamine gas. As photons enter the region of this photosensitive gas electrons were released via the photo-electric effect, this electric current was amplified via a series of spatially segmented multi-wire proportional chambers as illustrated in figure 2.8. The charge induced on the rectangular array of cathode pads then enabled determination of a two dimensional image of the Cherenkov ring in the detector plane.

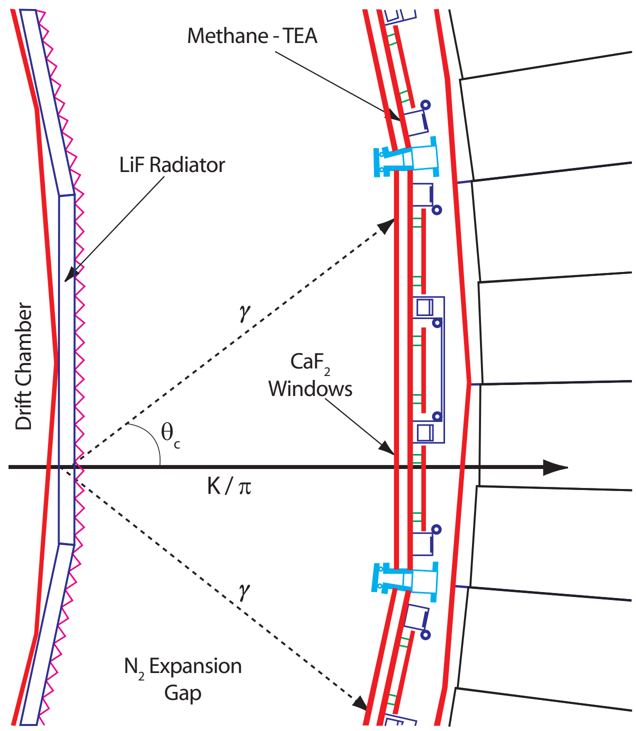

Figure 2.8: Cherenkov photons in the CLEO RICH detector.

The refractive index of lithium fluoride is 1.5, therefore the saturated Cherenkov angle in the lithium fluoride radiator is 48°. The critical angle of the radiator and gas expansion boundary is 42°, therefore for particles with trajectories normal to this boundary it would be possible for the entire ring of emitted Cherenkov photons to be totally internally reflected back into the radiator volume. For this reason the boundary of the radiator crystal region immediately surrounding the interaction region was designed in a "saw-tooth" shape. Further from the interaction region the surface was flat as total internal reflection would only affect part of the ring here.

From equation 2.1 it is clear that the velocity of the particle may be deduced from the Cherenkov angle of the photons emitted by a particle which travels above the threshold velocity in the radiator volume. Since the refractive index of lithium fluoride is 1.5, particles must travel at velocities greater than $\frac{2}{3}c$ within the radiator in order to emit Cherenkov photons. Therefore given momentum information the rest mass of the particle may be deduced. The RICH information was therefore used in conjunction with momentum information to determine the likelihood of a given particle hypothesis. This was calculated from the number of Cherenkov photons that were detected within five standard deviations of the expected ring size for a particular particle hypothesis. However the quality of the likelihood determination was calculated from the number of photons detected within three standard deviations of the expected ring radius. It was usual for at least three photons to be required to be within three standard deviations for a given track in order to provide reliable particle identification.

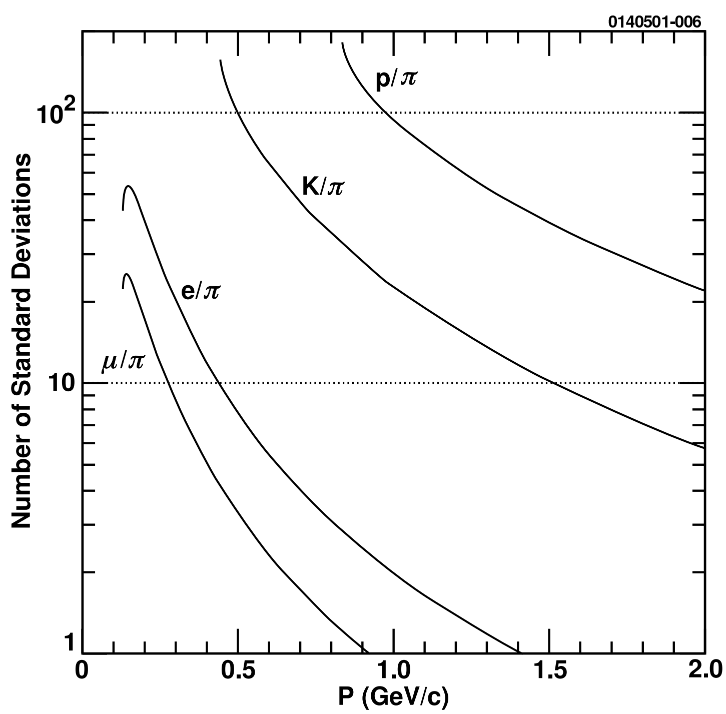

Figure 2.9: The resolution of the RICH detector as a function of momentum.

As can be seen in figure 2.9 the RICH $K-\pi$ separation was not reliable below 500MeV/c because kaons do not radiate Cherenkov photons below this momentum. By comparing figures 2.9 and 2.7 it is clear that the RICH information complements the particle identification provided by the ionisation per unit length, allowing particles to be identified over a broad momentum range.

The information from the RICH and dE/dX may be combined to give a difference in χ^2 value:

$$\Delta\chi^2 = -2\ln(L_K) - (-2\ln(L_\pi)) + \sigma_K^2 - \sigma_\pi^2 \tag{2.3}$$

where L_K, L_π are the RICH likelihood for a kaon or pion respectively and σ_K^2 and σ_π^2 are the number of standard deviations squared away from the expected kaon or pion dE/dX track respectively. Particles for which $\Delta\chi^2 < 0$ are therefore more likely to be kaons than pions.

Crystal Calorimeter The crystal calorimeter was made up 7784 Thallium doped CsI scintillating crystals. These were distributed between a cylindrical barrel section consisting of 6144 tapered crystals arranged with only a small tilt away from the interaction point and the two end caps which were made up of 820 rectangular crystals. The layout is illustrated in figure 2.10. The crystal calorimeter covered in total 93% of the full 4π solid angle. The crystals in the barrel region optimally covered particles with a trajectory satisfying $|\cos\theta| < 0.8$. The endcap crystals provided optimal coverage for particles with trajectories satisfying $0.85 < |\cos\theta| < 0.93$. The narrow "transition region" ($0.8 < |\cos\theta| < 0.85$ had substantially worse energy resolution.The crystals in both the barrel and end cap sections were of similar dimensions with a 5×5 cm face and were 30 cm in length.

Charged particles and photons entering the calorimeter ionised atoms in the scintillator material. Electrons were promoted from the valence to the conduction band of the crystal. The presence of the Thallium doping led to the existence of energy states that lie between the CsI conductance and valence bands, therefore electrons which were promoted to the conduction band would cascade back to the valence band via these additional states, thereby preventing re-absorption of the released photons.

The radiation length of the doped CsI was 1.83 cm with a Moliere radius (the radius of the cylinder containing 90% of the shower energy) of 3.8 cm. Therefore the energy deposited from a shower was well localised to a small "cluster" of neighboring crystals.

Four silicon photodiodes were mounted on the rear face of each crystal in order to collect the scintillation light. The resulting electrical signal was then shaped and amplified by a separate integrating preamplifier for each photodiode. This information was able to provide a determination of the energy of a shower.

The crystal calorimeter provided the primary means of identifying electrons and detecting photons. π^0 mesons, which decay with a branching fraction of 99% via $\pi^0 \to \gamma\gamma$, were also identified primarily by reconstructing these two photons.

The photon energy resolution provided by the calorimeter was 1.5% at 5 GeV rising to 7% at 30 MeV. This gave a pion mass resolution of $5-7\%$ depending on the energy and location of the photons [46].

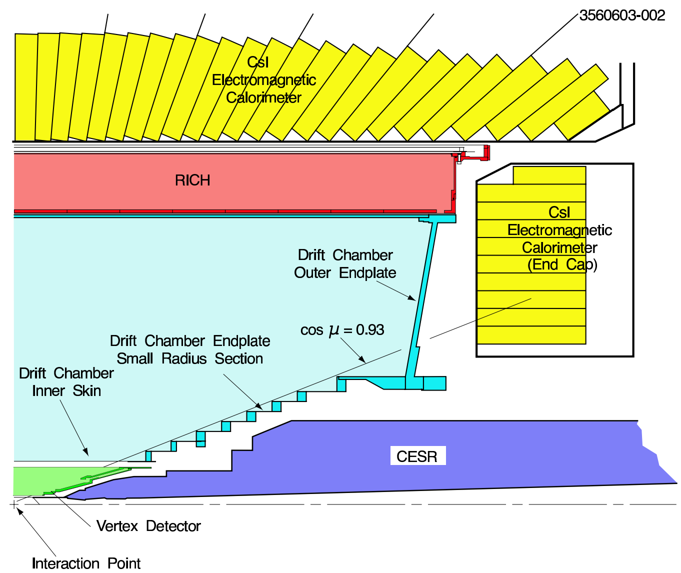

Figure 2.10: Layout of the CLEO-III Crystal Calorimeter.

Muon Detectors Although this analysis did not require information from the muon detectors a brief description is included here for completeness. The muon detectors were comprised of three layers of plastic proportional tubes which operated in a similar manner to the drift chamber and were embedded within the magnetic iron yoke. Muons, which penetrate the iron, produce a detectable electrical signal. The muon detector covered 85% of the solid angle of the detector.

2.3.3 The Trigger System

The trigger was responsible for the task of identifying bunch crossings which contained interesting physics and determining at which time these bunch crossings occurred. The trigger system combined the information provided by both the drift chamber and the shower energy topology in the crystal calorimeter. This information was processed independently by dedicated electronics boards and was then combined in the global level 1 trigger stage in order to determine whether to accept the event.

Tracking Trigger The tracking trigger was separated into information from the axial tracking and stereo tracking. The axial tracking trigger considered each of the 1696 axial wires separately. Since there were too many (8100) stereo wires to be read out individually these were grouped into 4×4 blocks for consideration by the trigger. The tracking triggers stored events which contained tracks consistent with particle trajectories with transverse momentum greater than 200 MeV/c and impact parameters of up to 5 mm. The stereo and axial information was then correlated in order to form tracks which were fed into the global level 1 trigger.

Calorimeter Trigger The calorimeter provided information about how much energy had been deposited at a specific location in the calorimeter. The trigger needed to allow for low energy showers which may be spread over a number of adjacent crystals in the calorimeter. To avoid missing such events in the trigger crystals were grouped into 64 “tiles”. The tiles were composed of 8×8 blocks of crystals with some overlap since each tile shared the corner 4×4 block of crystals with its diagonal neighbour; this is illustrated in figure 2.11. In practice a shower was spread over no more than a 5×5 block of crystals, therefore the majority of the energy of a shower was always deposited in one tile.

Level 1 Trigger Information from the tracking and calorimeter triggers was provided to the level 1 global trigger. Since tracking information was available in 2μs and calorimetry information was available in 2.5μs this information was passed through variable depth pipelines in order to provide time aligned information. The

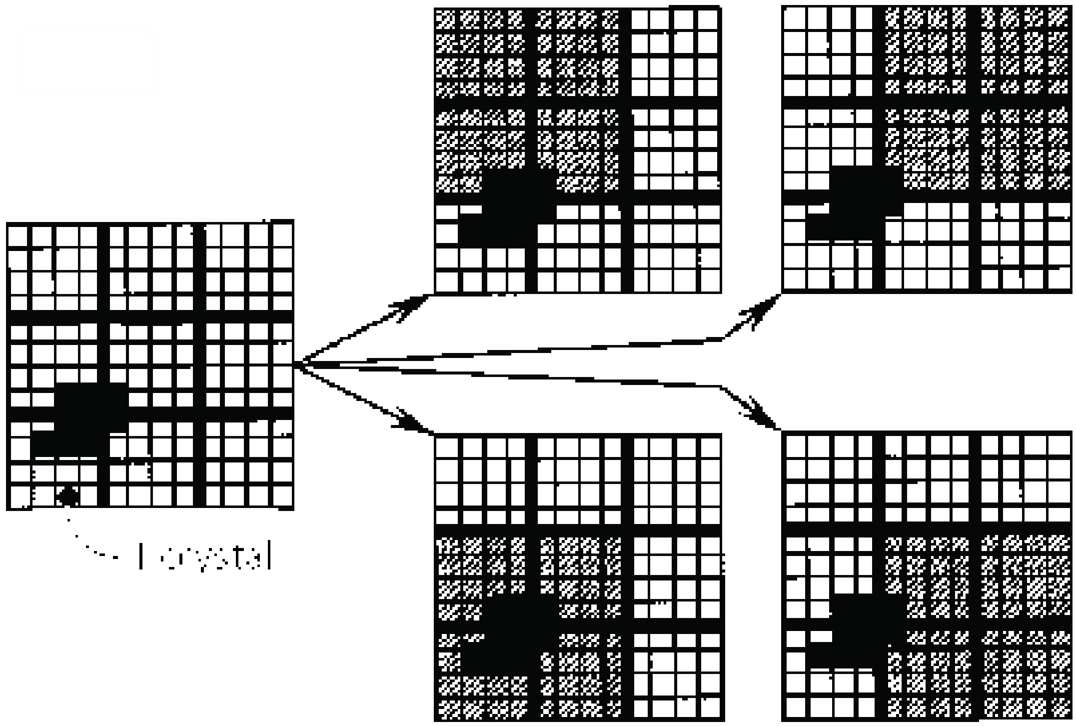

Figure 2.11: Layout of the "Tiles' used by the CLEO-III Calorimeter trigger.

combined track and shower information was then compared to 8 predefined trigger conditions or "trigger lines". If any of these conditions were satisfied the event information was passed onto the DAQ (Data Acquisition system).

DAQ The DAQ was responsible for writing the events that passed one or more of the trigger lines to the mass storage device for analysis and for data quality control. If a new event passed the trigger condition while a previous event was still being recorded by the DAQ the new event would be lost. It was therefore advantageous to minimise this "dead time" by minimising the time taken to record an event. The dead time for the CLEO-III DAQ was less than 3% of the total read out time.

2.4 The CLEO-II.V Detector

The above description applies to the CLEO-III detector. A small portion of the data in this analysis was collected from an older incarnation of the CLEO detector: CLEO-II.V. CLEO-II.V was commissioned in 1989 as an upgrade to the existing

CLEO-II detector and collected data until it was upgraded again to CLEO-III in 1995 in response to the improved luminosity capabilities of the CESR accelerator.

The muon detectors and the superconducting solenoids were as described for the CLEO-III detector and the crystal calorimeter was also almost identical to that of CLEO-III, but all the other systems were updated. The differences between the CLEO-II.V and CLEO-III detector are listed below.

- The CLEO-II.V silicon vertex system was made up of three, rather than four, layers [49].

- The central drift chamber of CLEO-II.V was shorter and less narrow than that of CLEO-III and it also had a larger lever arm.

- The CLEO-II.V detector had no RICH system. Instead CLEO-II.V had a Time Of Flight (TOF) detector consisting of 64 counters which were located immediately beyond the drift chamber and inside the crystal calorimeter. The scintillating material (bricon) emitted photons when charged particles traversed the detector. These photons were collected by Lucite light pipes at the end of each scintillator which channeled the light to a phototube which recorded the pulse. The system was able to provide a time of flight measurement to within 150 ps. This information was combined with momentum measurements in order to provide a mass measurement for particle identification. This particle identification system was significantly less effective than that of CLEO-III.

- The barrel section of the crystal calorimeter was the same as for CLEO-III however the end caps of the outer drift chamber were much thicker in CLEO-II.V so that there was more material obstructing the barrel. In the CLEO-II.V detector the region of the barrel for which energy resolution was optimal was 14% less than that of CLEO-III.

2.5 The CLEO-c Detector

A large proportion of the data used in this thesis was acquired from the CLEO-c detector. In 1995 the running energy of CLEO was reduced from that of the $\Upsilon(4S)$

(10 GeV), to energies at or just above the threshold for charm production (3.77 GeV – 4.170 GeV). The CLEO-c detector, illustrated in figure 2.12, was largely unchanged from that of CLEO-III.

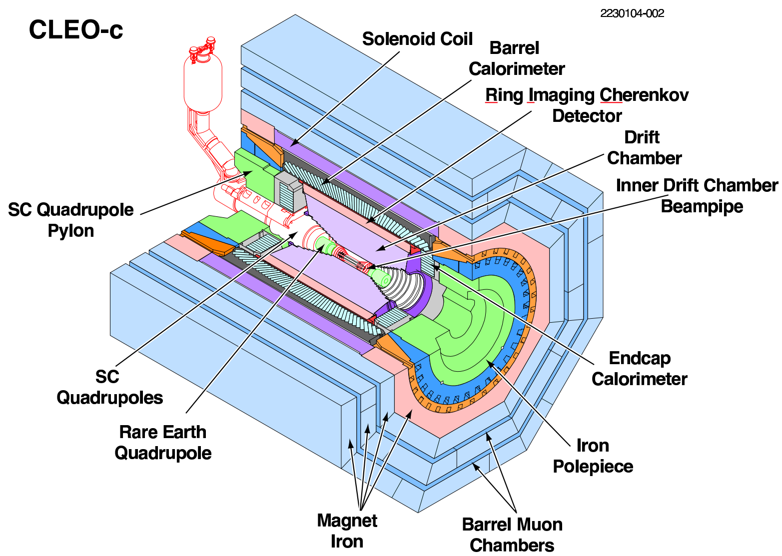

Figure 2.12: The CLEO-c Detector

The lower running energy resulted in a lower mean momentum for the particles produced in the subsequent decays. In the case of charged particles produced by D_s^+ decays the mean momentum was reduced from 530 MeV to 396 MeV [46]. A similar shift occurred for the decays of D^{*+} which are relevant to this analysis. In order to optimize tracking performance for this new energy regime the magnetic field strength was reduced from 1.5 T to 1.0 T at the time of the upgrade to CLEO-c. The lower field strength had the advantage that tracks with low transverse momentum ($\approx$ 60 MeV/c) reached further into the drift chamber and so had improved reconstruction efficiency.

The CLEO tracking trigger functioned with the same algorithms as for CLEO-III and was most efficient for tracks with a curvature of greater than 55 cm, which corresponded to tracks with transverse momentum of greater than 250 MeV/c. The reduction in magnetic field during the CLEO-c stage compensated for the lower transverse momentum of interesting tracks and therefore maintained the trigger efficiency.

At lower momentum it was advantageous to reduce the quantity of material that made up the body of the detector in order to reduce multiple scattering which would dominate momentum resolution at the energies of CLEO-c.

The average flight path was also reduced at lower centre of mass energies. For example at the $\psi(3770)$ resonance the average flight distance of a D^0 would be 18 μm compared to flight distances of > 100 μm at 10.6 GeV. Since the resolution achievable from the silicon vertex detector was > 70 μm this device would no longer prove useful in the CLEO-c regime. For this reason and to reduce the material in the experiment the silicon vertex detector was replaced by a smaller inner wire drift chamber, the ZD detector.

2.5.1 The ZD detector

Located within the CLEO-III drift chamber (DR), the ZD occupied a radius of 4.1 to 11.7 cm from the beamline and was made up of a single gas volume (60% helium, 40% propane) which encased six layers of axial anode wires. Each anode wire was surrounded by eight parallel field wires which together formed a single cell. The ZD drift chamber worked on the same principles as the DR and had cells of the same dimensions.

The ZD was designed to minimise the quantity of material which would impede the trajectory of low momentum particles. It had a 1 mm aluminium inner wall and an outer wall constructed of mylar which was 127 μm thick. It was comprised of 300 drift cells with a potential difference of 1.9 kV applied between the sense and field wires. A photo of the ZD is shown in figure 2.13.

The ZD provided vital z information close to the interaction point; in the case of particles with transverse momentum less than 70 MeV/c it provided the only source of z information. The cells were arranged in large stereo angles of $11-15°$ in order to give sufficient resolution. The ZD had an angular coverage of $|\cos\theta| < 0.93$.

2.5.2 Reconstruction and Monte-Carlo

Reconstruction As an event was read out a software process, "Pass1", was carried out on the raw event information. This was done primarily to perform quality

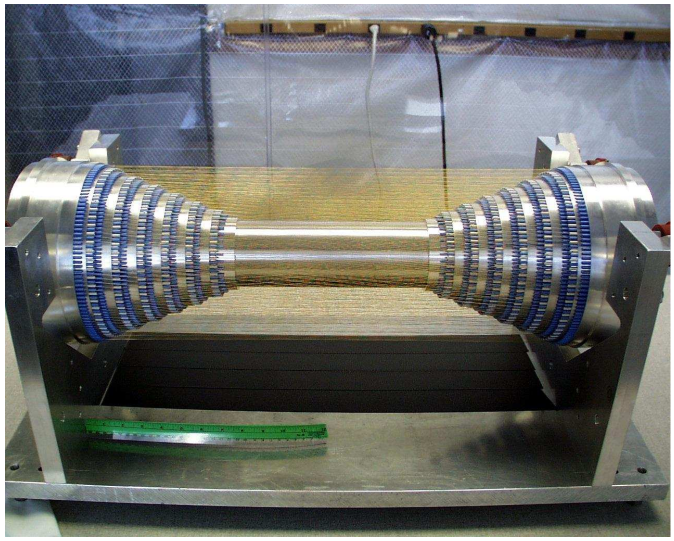

Figure 2.13: A photo of the CLEO-c ZD detector.

control of the data. The reconstruction was carried out later, to provide output for offline anaylsis, in a step called "Pass2", performed when all calibration information was available. This software package reconstructed and fit the tracks from the raw detector information (from either real or simulated Monte Carlo events) and produced a set of physical quantities which could be used for analysis.

Monte-Carlo Generation The CLEO software packages were able to generate Monte Carlo events and simulate the interaction of these events with the detector. The software separated the information which was specific to the accelerator from the physics generation of decays. Information provided by CESR was used in order to simulate the conditions of beam collisions. This information was then passed on to the physics generators which generated the subsequent interactions.

The CLEO Monte Carlo physics generators first generated the initial e^+e^- collision followed by the primary decays of the daughters resulting from this initial collision. The event generators responsible for this initial stage were the EvtGen [50] and QQ [51] software packages for CLEO-c and CLEO-III respectively.

In each case it was possible for the user to define a "decay file" which specified the branching fractions of the decay required and the specific model which would be used to describe the decay. These parameters defined the probability function which the generator used to generate the decay. Furthermore it was possible for the user to insert decays generated outside of the CLEO framework into the EvtGen or QQ generated decay chain at this stage. Any unstable particles which are produced would then decay according to predefined decay tables. In this way decays were generated according to simulated beam conditions and a user defined physics model.

These generated four vectors provided the input for the GEANT software package [52] which modelled the interaction of these particles with the detector and the detector response to the particles. Detector resolution and noise were also simulated in this routine. This stage was dependent on the particular detector material and geometry and therefore needed to be calibrated according to the appropriate CLEO detector. The resultant output which could be passed on to Pass2 was of the same form as data with the addition of "truth information" which is stored from the initial event generation.

2.6 Conclusions

In this chapter the main aspects of the acceleration and detection at the CLEO experiment have been outlined. In its lifetime CLEO operated over a range of centre of mass energies, and the detector has been adapted over time to accomodate these changes. The analysis in this thesis makes use of collisions from the CLEO-II.V, CLEO-III and CLEO-c experiments.

Chapter 3

An investigation of the $\pi\pi$ S-wave model for measurements of γ with $B^{\pm} \to (K^0_S\pi^+\pi^-)_D K^{\pm}$ at LHCb

3.1 Preamble

The analysis described in this chapter is a stand alone study which has been published as an LHCb note [53]. It descibes the first implementation of an alternative model (the K-matrix model) for the $\pi^+\pi^-$ S-wave. The use of the K-matrix has been a significant contribution to the pushing down the model uncertainty in the *final* Babar measurement of γ to three degrees [54].

3.2 Introduction

As described in chapter 1 a measurement of γ can be made from the decays $B^- \to D^0K^-$ and $B^+ \to D^0K^+$ where D^0 is either a D^0 or a $\overline{D}^0$. The Feynman diagrams for these decays are illustrated in Fig. 1.3 and 1.4. The weak-phase difference between these two amplitudes is $-\gamma$, which is the relative phase between V_{cb} and V_{ub}. Therefore when D^0 and $\overline{D}^0$ both decay to a common final state, a simultaneous fit to the B^+ and B^- decay will allow a measurement of γ to be made. A suitable decay for the measurement of γ is: $B^{\pm} \to D^0(K^0_S\pi^+\pi^-)K^{\pm}$ [55] . The amplitude for the $B^{\pm}$ decays are given by:

$$\mathfrak{A}_{B^+} = f(m_+^2, m_-^2) + r_b e^{i(\delta_B+\gamma)} f(m_-^2, m_+^2), \quad (3.1)$$

$$\mathfrak{A}_{B^-} = f(m_-^2, m_+^2) + r_b e^{i(\delta_B-\gamma)} f(m_+^2, m_-^2) \quad (3.2)$$

where $m^2_{+,-}$ refers to the square of the invariant mass of the $K^0_S\pi^{\pm}$, $f(m^2_-, m^2_+)$ is the D^0 decay amplitude in terms of the Dalitz variables, r_b gives the ratio of the magnitudes of the amplitudes (as a consequence of color suppression and the magnitudes of the relevant CKM elements r_b is found to be $r_b \simeq 0.1$) and δ_B gives the strong phase difference between the two amplitudes. The Dalitz plots for 2500 simulated B^+ and B^- decay events taken from [60] are shown in Fig.3.1. The B^- distribution is more densely populated than the B^+ around $m^2_- \simeq 1.4\ GeV^2$, $m^2_+ \simeq 0.8$ GeV^2 and less densely populated around $m^2_- \simeq 2.7$ GeV^2, $m^2_+ \simeq 0.6$ GeV^2.

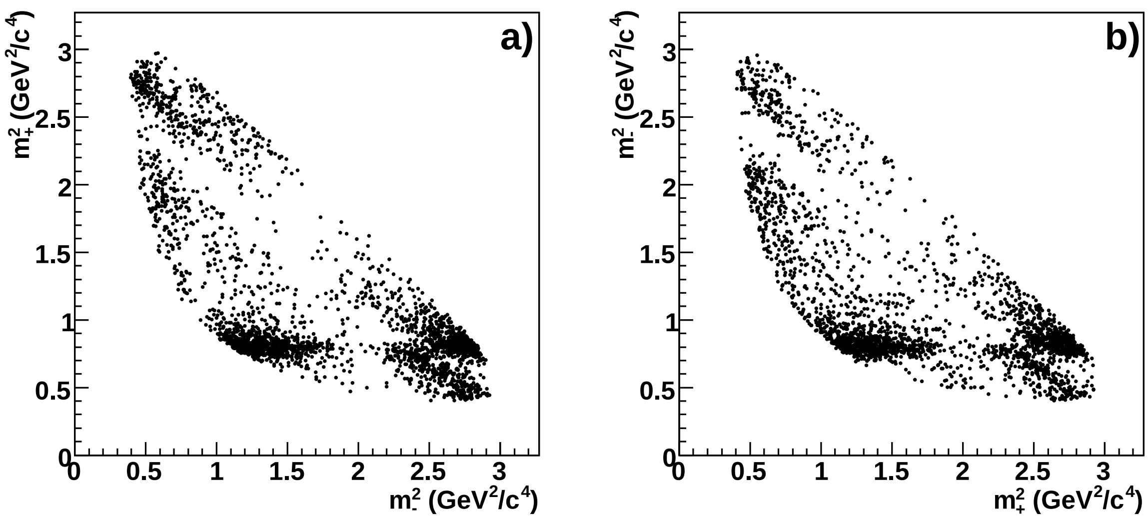

Figure 3.1: Distributions of a) m^2_+ against m^2_- for $B^+ \to D^0(K^0_S\pi^+\pi^-)K^+$ and b) m^2_- against m^2_+ for $B^- \to D^0(K^0_S\pi^+\pi^-)K^-$ [60].

The current measurements of γ using this method are $(78.4 \pm 10.8 \pm 3.6 \pm 8.9)^\circ$ and $(68 \pm 14 \pm 4 \pm 3)^\circ$ from Belle [56] and Babar [54] respectively and the errors are statistical, experimental systematic and model errors respectively. Here, the model error refers to the uncertainty associated with the D^0 decay amplitude, $f(m^2_-, m^2_+)$. Extracting the parameter γ from this decay requires assumptions to be made about the D^0 decay amplitude model. A model independent measurement of γ has already been made at Belle [57], however the vast majority of the statistics are derived from model dependent methods. Due to the large statistical uncertainty the model error does not dominant the precision on γ. The Belle collaboration do not use the K-matrix model and so pick up a larger contribution to the model uncertainty due to the S-wave parameterisation. The sensitivity from LHCb within one nominal year is expected to be $(7-12)^{\circ}$ [60] therefore the model uncertainty on γ will represent a relatively large contribution to the total error.

3.3 The Isobar Model

Since the decay under consideration has three particles in the final state the amplitude may have contributions from intermediate resonances, in addition to a non-resonant component. The most common model used is the isobar model.

According to the isobar formalism the decay amplitude is written as a coherent sum of the three-body non-resonant amplitude and two-body Breit-Wigner amplitudes:

$$f(m_+^2, m_-^2) = a_0 e^{i\phi_0} + \Sigma_r a_r e^{i\phi_r} A_{spin}. \tag{3.3}$$

Here A_{spin} are the spin-dependent Breit-Wigner terms [61] and the first term models the non-resonant part of the amplitude, the parameters a_r and ϕ_r give the amplitude and phase of the resonance r, while a_0 and ϕ_0 are the amplitude and phase of the non-resonant contribution.

In general the isobar model works well for describing processes involving narrow well isolated resonances, however when describing broad overlapping resonances an amplitude written as a sum of Breit-Wigner resonances may violate unitarity which is an indication that the isobar model is not appropriate for this situation. The isobar model has been described in general in section 1.4.2. The parameters for this decay model have been obtained from a fit to flavour tagged $D^0 \to K_S\pi^+\pi^-$ decays, [65] as shown in Table 3.1.

	K-matrix			Isobar		
Component	$\mathrm{Re}(a_r e^{i\phi_r})$	$\mathrm{Im}(a_r e^{i\phi_r})$	Fit Fraction(%)	$\mathrm{Re}(a_r e^{i\phi_r})$	$\mathrm{Im}(a_r e^{i\phi_r})$	Fit Fraction(%)
$K^*(892)^-$	-1.159±0.027	1.361 ± 0.020	58.9	-1.223±0.011	1.346 ± 0.010	58.1
$K_0^*(1430)^-$	2.482±0.075	-6.53 ± 0.033	9.1	-1.698±0.022	-0.576 ± 0.024	6.7
$K_2^*(1430)^-$	0.852±0.042	-0.729 ± 0.051	3.1	-0.834±0.021	0.931 ± 0.022	3.6
$K^*(1410)^-$	-0.402±0.076	0.050 ± 0.072	0.2	-0.248±0.038	-0.108 ± 0.031	0.1
$K^*(1680)^-$	-1.00±0.29	1.69 ± 0.28	1.4	-1.285±0.014	0.205± 0.013	0.6
$K^*(892)^+$	0.133 ± 0.008	-0.132 ± 0.007	0.7	0.0997 ± 0.0036	-0.1271 ± 0.0034	0.5
$K_0^*(1430)^+$	0.375 ± 0.06	-0.143 ± 0.066	0.2	-0.027 ± 0.016	-0.076 ± 0.017	0.0
$K_2^*(1430)^-$	0.088 ± 0.037	0.057 ± 0.38	0.0	0.019 ± 0.017	0.177 ± 0.018	0.1
$\rho(770)$	1.0 (fixed)	0 (fixed)	22.3	1.0 (fixed)	0 (fixed)	21.6
$\omega(782)$	-0.0182 ± 0.0019	0.0367 ± 0.0014	0.6	-0.02194 ± 0.00099	0.03942 ± 0.00066	0.7
$f_2(1270)$	0.787 ± 0.039	0.0397 ± 0.049	2.7	-0.699 ± 0.018	0.0387 ± 0.018	2.1
$\rho(1450)$	0.405 ± 0.079	-0.458 ± 0.116	0.3	0.253 ± 0.038	0.036 ± 0.055	0.1
β_1	-3.78 ± 0.13	1.23 ± 0.16	-	-	-	-
β_2	9.55 ± 0.2	3.43 ± 0.40	-	-	-	-
β_4	12.97 ± 0.67	1.27 ± 0.66	-	-	-	-
f_{11}^{prod}	-10.22 ± 0.32	6.35 ± 0.39	-	-	-	-
m of $\pi\pi$ S-Wave	-	-	16.2	-	-	-
Non-resonant	-	-	-	-0.99 ± 0.19	3.82 ± 0.13	8.5
$f_0(980)$	-	-	-	0.4465 ± 0.0057	0.2572 ± 0.0081	6.4
$f_0(1370)$	-	-	-	0.95± 0.11	-1.619 ± 0.011	2.0
σ	-	-	-	1.28 ± 0.02	0.273 ± 0.024	7.6
σ'	-	-	-	0.290 ± 0.010	-0.0655 ± 0.0098	0.9

Table 3.1: Parameters for the decay model with the $\pi\pi$ S-wave component modeled with K-matrix and isobar formalism. The fit fraction is defined as $\int\int \frac{dm_+^2 dm_-^2 |a_r A(K_S^0\pi\pi|r)|^2}{|\sum_j a_j A(K_S^0\pi\pi|j)|^2} \times 100\%$. These parameters have been obtained in a fit to flavour tagged decays [65]. This model was state of the art at the time at which this study was carried out but has now been superseded

For the D^0 decays the $\pi\pi$ S-wave component is composed of four scalar resonances ($f_0(980)$, $f_0(1370)$, σ, σ') in addition to a non-resonant contribution. The σ and σ' resonances must be included in order to correctly describe the data using the isobar model, however the existence of the σ is controversial and has not yet been confirmed, while σ' is believed not to exist and is included empirically in order to describe the data. These four resonances are also sufficiently broad so as to overlap with each other significantly. Therefore it is necessary to investigate alternative models for the $\pi\pi$ S-wave component of the decay, while still using a sum of Breit-Wigner amplitudes to model the $K\pi$ and higher spin $\pi\pi$ resonances.

3.4 The K-Matrix Formulation

In contrast to the isobar model the more general K-matrix formalism [61], [62] is well suited to describing the interplay between broad overlapping resonances. The K-matrix formalism was originally formulated to describe two particle scattering.

Two particle scattering is described using the scattering matrix, which is given by

$$S = I + 2i\rho^{\frac{1}{2}}T\rho^{\frac{1}{2}}. \tag{3.4}$$

Here the scattering matrix is separated into the identity which describes the probability that the particles do not interact at all and the second term which describes the scattering interaction. For multi-channel scattering ρ represents a diagonal matrix whose elements are given by the phase space factor for the relevant channel. The scattering matrix must respect analycity ($S^\dagger S = SS^\dagger = I$) which places a constraint on the transition matrix, T:

$$T - T^\dagger = 2iT^\dagger\rho T. \tag{3.5}$$

For a general transition matrix ensuring that equation 3.5 is obeyed would involve solving a complicated set of non-linear equations. However if the transition matrix is expressed in terms of the 'K-matrix':

$$T = (1 - iK\rho)^{-1}K. \tag{3.6}$$

It can be shown, without loss of generality, that the K-matrix may be chosen to be real and symmetric, thus ensuring that equation 3.5 is obeyed.

In the K-matrix formalism resonances are not summed directly into the transition matrix as in the isobar model, but rather appear as a sum of poles in the K-matrix itself. This therefore negates the need to consider the existence of the σ and σ' resonances. In the case of well isolated resonances it may be shown that the K-matrix and Breit-Wigner formalisms are equivalent. However in the case of broad overlapping resonances the two formulations are distinct and result in different expressions for the physical transition matrix.

3.4.1 Parametrization for the Scattering Process

The most common parametrization of the K-matrix is given by:

$$\begin{aligned} K_{ij} &= [\Sigma_\alpha \frac{g_i^\alpha g_j^\alpha}{m_\alpha^2 - m^2} + f_{ij}^{scatt} \frac{1 - s_0^{scatt}}{m^2 - s_0^{scatt}}] \\ &\times \frac{(1 - s_{A0})}{(m^2 - s_0^{scatt})}(m^2 - s_A \frac{m_\pi^2}{2}) \end{aligned} \tag{3.7}$$

where m represents the $\pi\pi$ invariant mass. The first term in this expression, involving a sum over poles represents the resonant contribution with the factors g_i^α giving the coupling of the i^{th} channel to the α pole. The parameters f_{ij}^{scatt} and s_0^{scatt} appearing in the second term describe the non-resonant contribution to the amplitude while the parameters s_{A0} and s_A, appearing in the third (multiplicative) factor, are required to suppress an unphysical kinematic singularity near the $\pi\pi$ threshold. The parameters of (3.7) are taken from a global fit to all the available $\pi\pi$ scattering data [63]. Five poles are considered for five different scattering channels ($1 = \pi\pi$, $2 = KK$, $3 = 4\pi$, $4 = \eta\eta$, $5 = \eta\eta'$) in which the integer corresponds to the channel number. The phase space factors for the two particle channels are defined such that $\rho \rightarrow I$ as $m \rightarrow \infty$. The scattered $\pi\pi$ S-wave amplitude is shown in Fig.3.2 from which it is apparent that the amplitude differs from the standard Breit-Wigner shape. Figures 3.3-3.4 illustrate that the K-matrix parameterisation as implimented respects unitarity and is consistent with that presented in the original publication [63].

The Argand diagram is shown in Fig. 3.3, the amplitude remains within the unitarity circle illustrating the fact that the scattering description respects analycity as required. The elasticity is defined as the amplitude for which no new particles

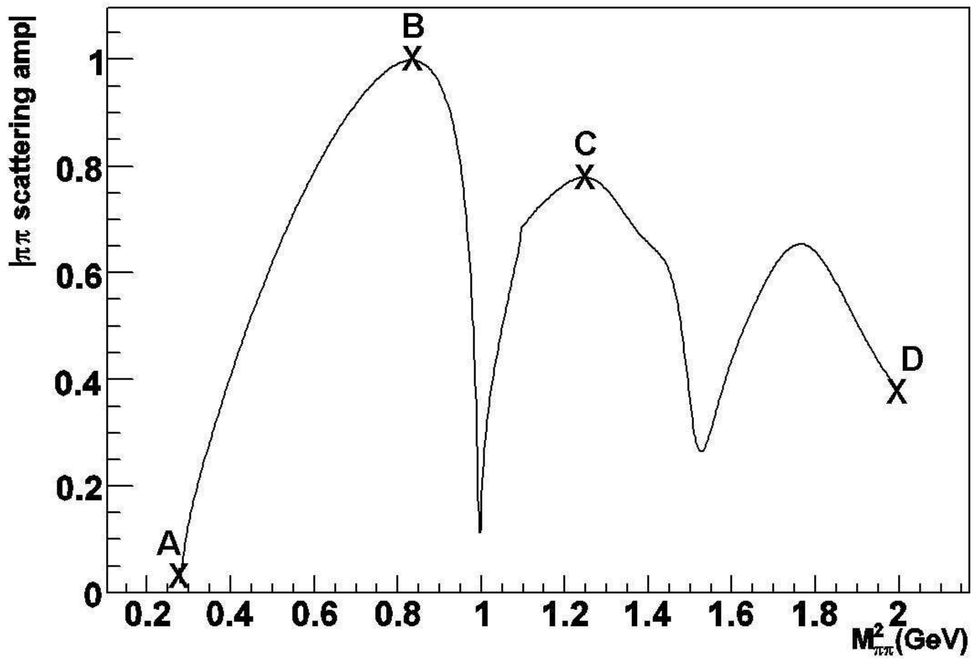

Figure 3.2: Amplitude for $\pi\pi$ scattered S-wave.

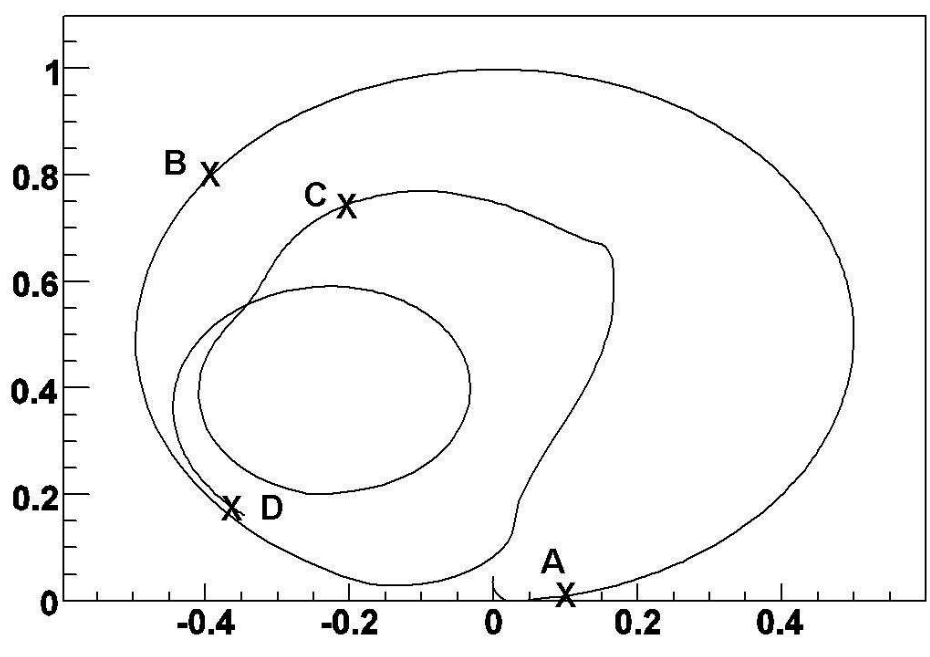

Figure 3.3: Argand diagram for $\pi\pi$ scattered S-wave with points A, B, C, D corresponding to those in Fig. 3.2.The horizontal axis gives the real part and the vertical axis the imaginary part of the complex amplitude.

are produced and is plotted in Fig. 3.4.2. The scattering is almost elastic until $\simeq 1$ GeV where the threshold for scattering into the $K\overline{K}$ channel is reached.

3.4.2 Generalisation to a Production Process

In order to describe the D^0 decays the K-matrix approach must be generalized to describe a production process, this has been carried out in [64]. The T-matrix must be replaced by the 'F-vector' which is given by

$$F = (I - iK\rho)^{-1}P, \tag{3.8}$$

where each element of the F-vector gives the amplitude of scattering into the relevant channel. This expression also involves the 'P-vector' which describes the coupling to each of the intermediate channels at the production process (the D^0 decay in this case), this is illustrated schematically in figure 3.4.

The most common parametrization of the P-vector [61] is given by

$$P_j = [\Sigma_\alpha \frac{\beta_\alpha g_j^\alpha}{m_\alpha^2 - m^2} + f_{1j}^{prod} \frac{1 - s_0^{prod}}{m^2 - s_0^{prod}}]. \tag{3.9}$$

The poles m_α^2 in the P-vector must match those of the K-matrix in order to avoid unphysical singularities in the amplitude. The (complex) β_α factors carry the information about the resonance production. The non-resonant parameters f_{1j}^{prod} and s_0^{prod} also appear only in the P-vector and must be fit for the particular production process. The parameters of equation (3.9) for the $\pi\pi$ S-wave, in addition to the isobar parameters of the decay, have been obtained from a flavour tagged fit to $215,000$ $D^0 \to K_s^0\pi^+\pi^-$ decays [65] (orignally based on the analysis presented in [63] and are given in Table 3.1).

The amplitude for the $\pi\pi$ S-wave in the D^0 decay is plotted in Fig. 3.6(a) and may be compared to the equivalent plot in the Breit-Wigner model shown in Fig. 3.6(b), where it can be seen that while the two formalisms give the same general features there are distinct differences between the two. It may be noted from Fig. 3.6(a) that at $m_{\pi\pi}^2 \approx 1.2\text{GeV}^2$ the K-matrix formalism predicts a small peak which to some extent replicates the controversial σ resonance (as described by the model used in [65]).

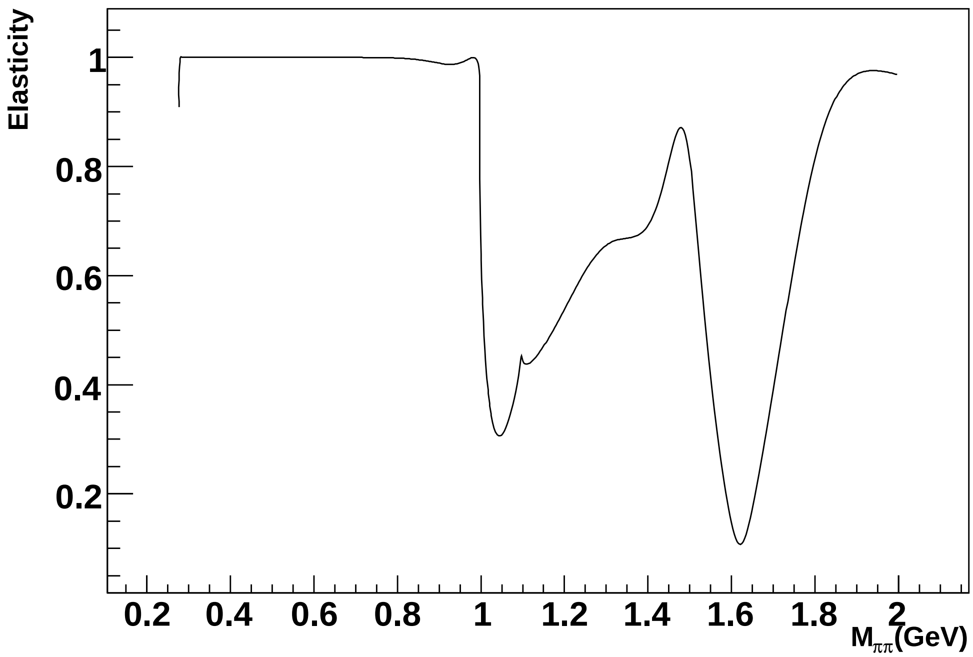

Figure 3.4: Elasticity for $\pi\pi$ scattered S-wave.

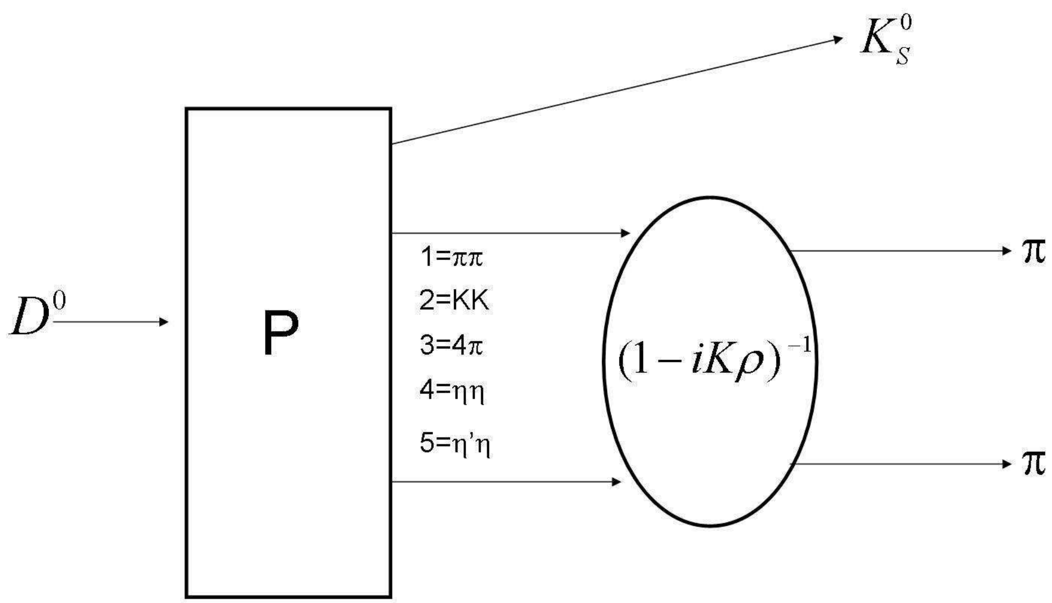

Figure 3.5: Schematic of the role of the P-vector in relating the K-matrix derived for production to $D^0 \to K_S^0\pi^+\pi^-$ decay.

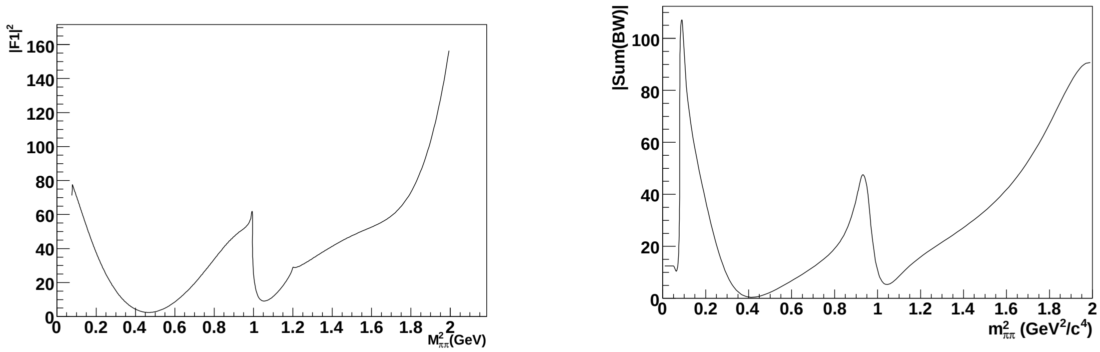

Figure 3.6: "$\pi\pi$ S-wave in $D^0 \to K^0_S\pi^+\pi^-$ decay described by (a) the K-matrix and (b) isobar formalisms. The x-axis illustrates the $\pi^+\pi^-$ invariant mass, $m_{\pi\pi}$.

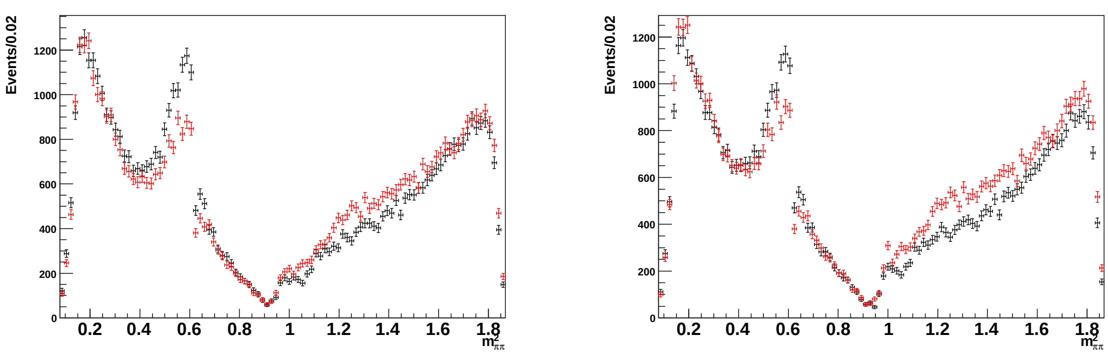

(a) Generated using the isobar model.

(b) Generated using the K-matrix model

Figure 3.7: $\pi\pi$ projections for B^+ (red) and B^- (black) decays.

3.5 Model Error on γ

The aim of this study was to use this previous work [65] which has been carried out on the K-matrix formalism in order to determine the impact of the model choices (isobar or K-matrix) for the $\pi\pi$ S-wave on the model error on a measurement on γ made via this method. When the $\pi\pi$ S-wave models are incorporated into the full $B^\pm$ decay model, the Dalitz plot projections of events along the $\pi\pi$ invariant mass squared are shown in Fig. 3.7 for the $\pi\pi$ S-wave component modeled with both the K-matrix and isobar parameterisation . The values of γ, δ_B and r_b were taken as: 60°, 130° and 0.1, respectively. These values are compatible with the current world averages [66]. The two formulations result in noticeable differences to the decays particularly above 1 GeV.

In order to determine the effect of the $\pi^+\pi^-$ S-wave description on γ, B^+ and B^- events were generated according to the isobar model and then fit back for the parameters γ and δ to the K-matrix model. This was then compared to the case where the data was both generated and fitted using the isobar model. For each fit 5000 B^+ and B^- events (corresponding to two years of LHCb data taking) were generated, 200 experiments were generated in total. The parameters for γ, r_b and δ_B were floated in the fit and given input values of 60° and 130° respectively, all other parameters were fixed. For each of the 200 experiments fitted values for γ, r_b and δ_B were returned for both the K-matrix and isobar parameterizations.. The fitted values for γ are illustrated in Fig. 3.8 and 3.9, fitted using the isobar and K-matrix model respectively. The distributions of $gamma$ are fitted to a guassian. In the case of the fits generated and fitted using the isobar model the mean of the guassian is consistent with the input value of 60°, in the case of the fits fitted using the K-matrix parameterization the mean of the guassian is $62.4° \pm 0.7$. The average shift introduced by the K-matrix model with respect to the isobar model is therefore seen to be $2.4° \pm 0.7$ which is in agreement with the shift quoted in [58] (when scaled to take account of the value of r_b).

3.6 Conclusions

The K-matrix parameterisation of the $\pi^+\pi^-$ S-wave component of the $D^0 \to K^0_S\pi^+\pi^-$ decay has been implemented. The effect of an incorrect description of the $\pi^+\pi^-$ S-wave has been investigated for determining γ from $B^- \to D^0(K^0_S\pi^+\pi^-)K^-$ decays for sample sizes currently being accumulated at LHCb. The shift is of the order of the model uncertainty quoted by other experiments from this source [59]. The K-matrix formulation will be used by LHCb to reduce the model error as has been done by BABAR [54]. However, ultimately model-independent determinations will be most effective in reducing the systematic uncertainty on γ.

It should be noted that the K-matrix formulation is not used further in this thesis due to the small size of the flavour-tagged sample of $D^0 \to K^+K^-\pi^+\pi^-$ decays collected at CLEO-c (Chapter 4) compared to the $D^0 \to K^0_S\pi^+\pi^+$ samples collected by the B factories. However, in future high-statistics amplitude fits to $K^+K^-\pi^+\pi^-$ data this parameterisation should be utilised.

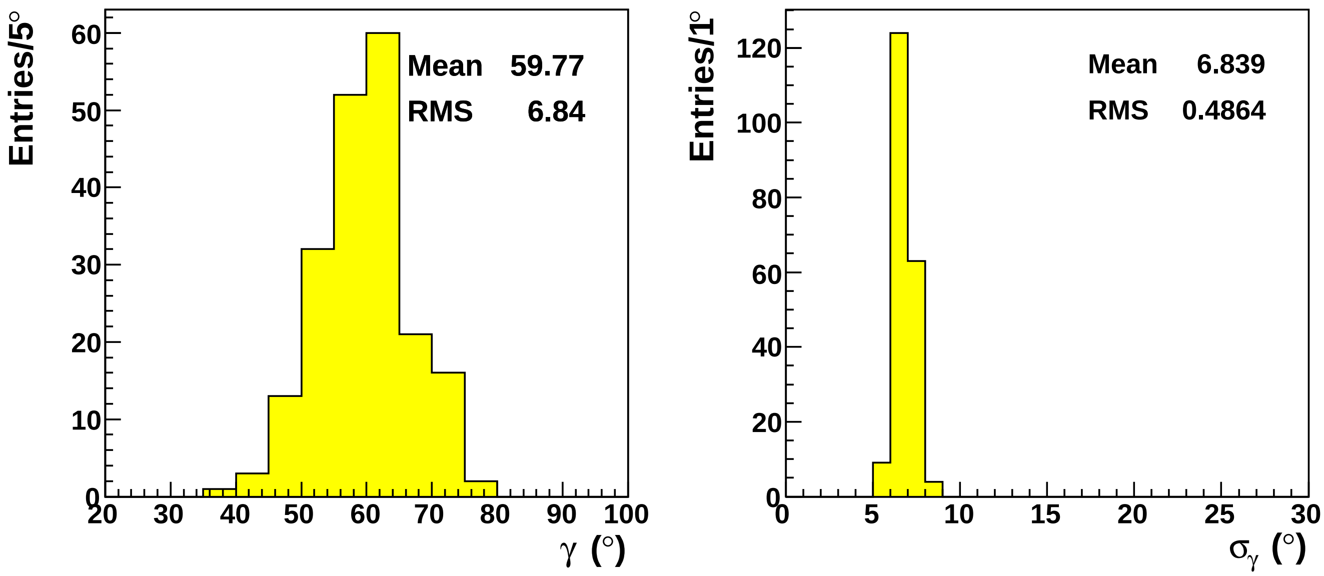

Figure 3.8: Results for γ generated and fitted using isobar model.

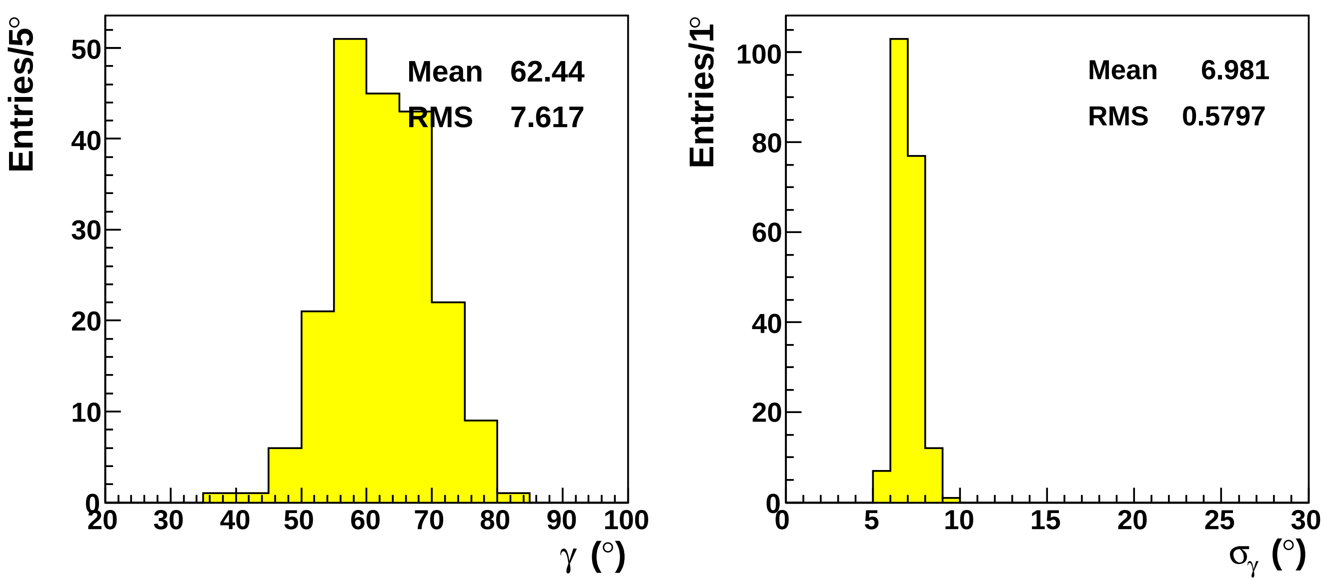

Figure 3.9: Results for γ fitted using K-matrix model.

Chapter 4

Selection of $D \to K^+K^-\pi^+\pi^-$ Datasets at CLEO

4.1 Introduction

In this chapter the selection of $D \to K^+K^-\pi^+\pi^-$ events is described in detail. This work was largely carried out by other members of the UK CLEO-c group. In determining optimal selection cuts for this decay extensive use was made of the MC system (where background events can be identified) and the cuts were chosen which maximised the ratio of the number of signal to background events. This procedure was carried out seperately for each CLEO dataset since the environments were significantly different in each case.

4.2 The Signal Decay

As discussed in chapter 1, in order to access γ via $B^{\pm} \to D(f)K^{\pm}$ it is necessary to obtain a model for the decay of the D into its final state, f. The decay $D \to K^+K^-\pi^+\pi^-$ is singly Cabibbo suppressed and is expected to display a rich resonant sub structure. This decay presents a possible candidate for a γ measurement. The decay is also interesting in its own right as it allows a study of QCD at low energy and provides an opportunity to search for CP violation. The final state of the D decay contains all charged particles which is advantageous for studying in hadronic colliders such as LHCb.

4.2.1 Previous Studies

The most recent study published describing a model for this decay was carried out using 1300 $D \to K^+K^-\pi^+\pi^-$ events selected at the FOCUS experiment [77]. This study considered ten resonant contributions and found that the dominant contributions to the decay were from the $D \to AP$ decays, in particular: $D \to K_1^+(1270)K^-$. They also reported a large contribution from the $D \to VV$ decay: $D \to \phi(1020)\rho(770)$. (Where A, V and P refer to axial vector, vector and pseudoscalar particles respectively). This study made no distinction between the decays of a particle via a state S and its conjugate state $\overline{S}$ (for example the decays $D \to K_1^+(1400)K^-$ and $D \to \overline{K}_1^-(1400)K^+$).

The only previous study made on this decay mode was conducted at the $E791$ fixed target experiment at Fermilab [78]. This study was unable to distinguish between D^0 and $\overline{D}^0$ decays due to limited statistics. This study reported six resonant and a non-resonant component, with the dominant contribution deriving from the non-resonant component and the $D \to VPP$ decay $D \to \rho(770)K^+K^-$.

It is the aim of the study presented in this thesis to produce a full model to describe the resonant sub structure of the $D \to K^+K^-\pi^+\pi^-$ decay using data collected at the CLEO detector. In order to maximise statistics data are analysed from CLEO II.V, CLEO-III and CLEO-c. These data span a range of centre of mass energies arising from different production mechanisms.

4.3 Flavour Tagged Data Sets

Flavour tagged datasets refer to datasets consisting of $D \to K^+K^-\pi^+\pi^-$ events where the flavour of the mother D is known. In total four distinct flavour tagged datasets were used in this analysis: those from the CLEO-II.V, CLEO-III experiments and the CLEO-c experiment at centre of mass energies of 3770 MeV and 4170 MeV (which will be referred to as the 3770 and 4170 datasets respectively). The number of selected events from each flavour tagged dataset is given in table 4.1.

Data Set	**Number of Selected Events**
CLEO-II.V	279
CLEO-III	1225
3770	1396
4170	739
Total	**3639**

Table 4.1: Number of selected flavour tagged events in each dataset.

4.3.1 CLEO-II.V and CLEO-III datasets

Relevant events were selected from data at CLEO-II.V and CLEO-III, at centre of mass energies well above the threshold for charm production. The CLEO-II.V data was collected at the $\Upsilon(4S)$ resonance. The integrated luminosity of this dataset was 9 fb^{-1}. The integrated luminosities and centre of mass energies of the CLEO-III sample are presented in table 4.2.

At these higher centre of mass energies, in order to control the background levels and to be able to "tag" the flavour of the D accurately, the D^0 or $\overline{D}^0$ was required to originate from a D^{*+} or D^{*-} in the decay topology: $D^{*+} \to D^0\pi_s^+$ or $D^{*-} \to \overline{D}^0\pi_s^-$ respectively. Due to the relatively small mass difference between the D^* and the D^0, the charged pion, $\pi_s^\pm$, was expected to have a low momentum in the centre of mass frame of the D^*. The charge of this "slow" pion enabled the flavour of the $D^0(\overline{D}^0)$ to be tagged.

$\sqrt{s}$ (GeV)	$\mathcal{L}$ (pb^{-1})
7.0	2.8
7.4	8.9
8.4	7.7
9.46	1513
10.02	1925
10.36	1723
10.58	8965
10.87	460
11.2	722

Table 4.2: Centre of mass energies and corresponding integrated luminosities for CLEO-III datasets used in the analysis.

Event Selection

The primary selection involved limits on the slow pion momentum ($150 \leq p_{\pi_s} \leq 500$ MeV/c for CLEO-III and $100 \leq p_{\pi_s} \leq 500$ MeV/c for CLEO-II.V) and cuts to suppress pion pairs originating from a K_S^0 (an event with two pions with invariant mass consistent with a K_S^0 was rejected if either pion had an impact parameter greater than 1.5 mm or if the flight distance of the candidate K_S^0 was greater than two assigned errors from the interaction point). This suppresses the $D \rightarrow K_S^0 K^+ K^-$ background. (Since the K_S^0 decays to $\pi^+\pi^-$ wih a branching fraction of 70% it represented a significant background to this study). There were also requirements that all D^0 decay products originated from a single vertex and that the D^0 and π_s candidates also originate from a single vertex.

In the case of kaons with momentum $\geq$ 500MeV/c information from the RICH detector was required in order to satisfy the selection criterion (at least three photons must be associated with the kaon in the RICH detector). In the case of CLEO-II.V no RICH information was available and so this selection criteria was not applied. Kaons for which this information was not available, or lower momentum kaons and pions, were identified via their energy loss in the drift chamber. Kaons were required to have a recorded dE/dX within 2.1 σ of that expected of a true kaon. Similarly a positive pion identification required the candidate to have a dE/dX within 2.5 σ for CLEO-II.V and 3.2 σ for CLEO-III of that expected of a true pion. When time of flight information was available it was required to lie within 2.5 σ of that expected for both pions and kaons.

In order to perform the final selection on candidates, cuts were made on the D^* momentum, $p_{D^*} \geq \frac{1}{2}\sqrt{\frac{E^2_{beam}}{c^2} - M^2_{D^*}c^2}$ (the momentum was required to be at least half the maximum kinematically allowed momentum), in order to suppress combinatoric backgrounds and to suppress secondary D^* candidates which originated from B decays. The mass of the D^0, m_{D^0}, and the D^*, D^0 “mass difference”, ΔM, ($\Delta M = m_{D^*} - m_{D^0}$), were computed for each candidate. A signal region was then defined in the m_{D^0}, ΔM plane in order to select appropriate candidates. The signal region was defined to be within $\pm$11.22 MeV of the world average of the D^0 mass and within $\pm$1 MeV of the world average for the $D^* - D^0$ mass difference, this corresponds to mass windows of approximately 3σ.

4.3.2 CLEO-c datasets

This analysis uses also data collected by CLEO-c at centre of mass energies of 3770 MeV and 4170 MeV. In order to select $D \to K^+K^-\pi^+\pi^-$ events at these centre of mass energies the standard procedures for CLEO-c event selection [79] were employed.

$\psi(3770)$ resonance dataset

In total 818 pb^{-1} of data were available at the centre of mass energy of the $\psi(3770)$ resonance. This resonance decays to $D^0\overline{D}^0$ and D^+D^- with a ratio of 57 : 43 [80]. D^0 and $\overline{D}^0$ pairs produced in this way were used in this analysis. With this production process the only way to tag the flavour of the meson responsible for the $K^+K^-\pi^+\pi^-$ decay is to determine the flavour of the other D-meson in the event. The flavour of the "other side" D was determined from its inclusive decay to kaons, under the assumption that the decay was Cabibbo favoured. (A certain proportion of these decays would have been "mis-tagged" and this was accounted for when fitting this dataset). Events were selected in which the decay products of the other side D contained a single kaon and in order to improve the sample purity and minimise the level of mis-tagging a minimum momentum restriction of 400 MeV/c was placed on this kaon.

A tighter K_S^0 veto was required compared to the CLEO-III and CLEO-II.V datasets. This is because the D^0 mesons and any daughter K_S^0 particles had energy, and so the K_S^0 had in general a shorter flight distance before decaying. Events containing pion pairs with an invariant mass consistent with a K_S^0 were rejected if the flight distance normalised by the assigned uncertainty of the candidate K_S^0 was greater than 1 or if either pion had an impact parameter of greater than 1 mm.

In order to determine a signal region for the events the beam constrained mass of a candidate event, m_{bc} was defined: $m_{bc} \equiv \sqrt{\frac{E_{CM}^2}{4c^4} - \frac{\vec{P}_D^2}{c^2}}$ where $\vec{P}_D$ is the momentum of the signal D^0 candidate. A further variable $\Delta E \equiv E_D - \frac{E_{CM}}{2}$ was also defined, where E_D is the sum of the energies of the candidate D^0 daughter particles. The distribution of both variables peaks at the nominal D^0 mass. Selection windows of ± 5 MeV and ± 15 MeV were then defined for the variables m_{bc} and ΔE respectively.

A kinematic fit was carried out on selected events by constraining the invariant mass of the candidate D^0 particle to the D^0 mass in order to improve the resolution of the particle's momenta.

4170 **Resonance dataset**

A further 600 pb^{-1} of data was available at the CLEO-c experiment from e^+e^- collisions at a centre of mass energy of 4170 MeV. At this centre of mass energy pairs of charmed mesons (for example $D^*\overline{D}$, $D^*\overline{D}^*$, $D^*\overline{D}\pi$ and $D_s^{+*}D_S^-$) may be produced and there are various ways in which a daughter D^0 or $\overline{D}^0$ may result from the decays of these initial states. The different production processes populate different regions of the $m_{bc} - \Delta E$ space.

The primary meson pairs which gave the greatest purity in the signal sample and were therefore used in this study were: $D^{*+}D^{*-}$ and $D^{*0}\overline{D}^{*0}$. Events of interest were selected from the decay topologies $D^{*+} \to D^0\pi^+$ and $D^{*0} \to D^0\gamma$ and similarly for the conjugate decays. No attempt was made to reconstruct the accompanying pion or photon, rather only the D^0 was reconstructed and the events selected according to their position in $m_{bc} - \Delta E$ space. The flavour of the D^0 was tagged via the decay of the other side D^{*0} or $D^{*\pm}$ which was tagged via its inclusive decay to kaons as for the 3770 sample. However the minimum momentum restriction on the kaon used for tagging in this case was increased to 600 MeV/c due to the higher level or background in this sample.

The variable ΔE_{sig} was defined as $E_{sig} \equiv 2.112\text{GeV} - 1.12 m_{bc}/c^2$ (where the coefficients were determined in a fit to the distribution of signal events which were simulated using the Monte Carlo system). A signal region was then defined as: $2.005 < m_{bc} < 2.040$ GeV and $|\Delta E - \Delta E_{sig}| < 10$ MeV. The background was further suppressed by requiring the momentum of the D^0 candidate to be greater than 450 MeV.

4.4 Flavour Tagged Backgrounds

The level and shape of the background contamination of the signal samples needed to be accounted for when fitting each flavour tagged dataset.

4.4.1 Background Estimations

In order to account for background (non $D \to K^+K^-\pi^+\pi^-$) events which passed the selection criteria, it was necessary to estimate both the number of events in each sample which corresponded to background and the shape of this background within the signal phase space. Background samples and background fractions for each background type were provided by other members of the UK CLEO-c group.

As has previously been described, for the D^0 decays originating from D^* mesons, the variables ΔM and m_{D^0} for event candidates were used in the event selection. The distribution of these two variables for all potential candidates were each fitted to the sum of two bifurcated Gaussians plus a background shape. In the case of m_{D^0} the background shape was flat and in the case of ΔM a shape was used which modeled the phase space of the $D^{*+} - D^0$ invariant mass distribution. The level of this flat background was allowed to float during the fit to these variables. It was then possible to determine the proportion of true signal events expected within the signal region, by integrating the signal fit within the signal region and dividing this by the integral of the combined signal and background fit. The result of this fit to the CLEO-III data candidates is illustrated in figure 4.4.1. It was then necessary to establish a description of the background events which occur within this signal region. In order to do this events were selected from "sideband regions" of the ΔM, m_{D^0} plane. The same analysis was carried out on the CLEO-II.V data sample. Data collected from these sideband regions enabled a fit to be performed which models the shape of the "flat background"; this refers to background of the type that is flat in the variables ΔM and m_{D^0}.

In the case of CLEO-c datasets the signal window was defined in the $m_{bc} - \Delta E$ plane. In the case of the 3770 sample the background sidebands were defined as the regions $-5 < m_{bc} < 5$ MeV and $|\Delta E \pm 45| < 30$ MeV. In the case of the 4170 dataset the background sidebands are defined as $2.005 < m_{bc} < 2.040$ GeV and $|(\Delta E - \Delta E_{sig}) \pm 45| < 20$ MeV.

Simulation studies confirmed that the sideband data suffered minimal contamination from signal events and mimicked accurately the background present in the signal region in the case of all four datasets. The proportion of each flavour tagged dataset which was comprised of flat background is illustrated in table 4.3.

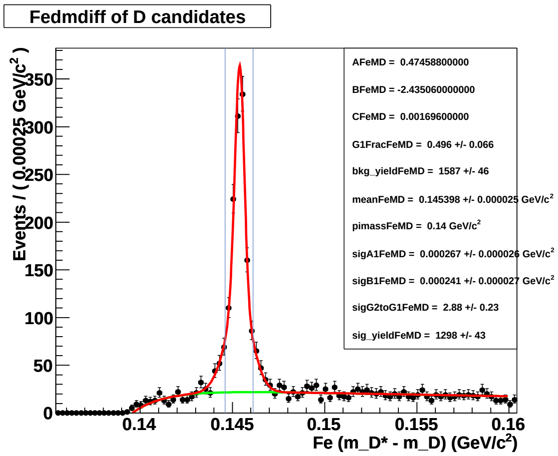

(a) The distribution of ΔM for events which pass all other selection criteria.

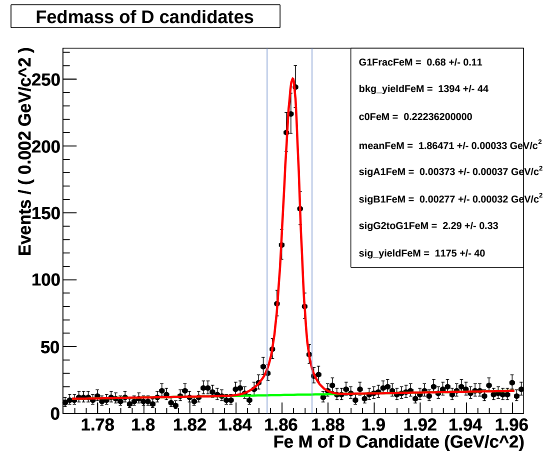

(b) The distribution of m_{D^0} for events which pass all other selection criteria.

Figure 4.1: The ΔM and m_{D^0} distributions for the CLEO-III dataset. The red curves illustrate the fitted results for the combined signal and background for each distribution while the green curve illustrates the fitted background contribution. The signal regions are indicated on each distribution.

The data collected from these sideband regions were used to model the flat background for each dataset. Backgrounds which peaked within the signal region were considered separately.

Data Set	Proportion flat background
CLEO-II.V	$26.0 \pm 3.0\%$
CLEO-III	$10.8 \pm 0.4\%$
3770	$13.5 \pm 0.5\%$
4170	$33 \pm 1.1\%$

Table 4.3: Proportion of each flavour tagged dataset which was made up of flat background.

4.4.2 Peaking Background

In addition to the flat background which has been described in the preceding section the datasets also suffered a contribution from background which peaked within the signal region. Monte Carlo studies revealed that this background was made up almost entirely of $K_S^0 K^+ K^-$ events. Other sources of background such as misidentified $K^\pm \pi^\mp \pi^+ \pi^-$ events were negligible. The level of this peaking background was allowed to float as a free parameter in the fit.

4.5 Mistagging in Flavour Tagged Samples

For each dataset there is a certain probability per event that the flavour of the D^0 in the decay of interest was incorrectly tagged. This effect is largest for the CLEO-c datasets. As previously explained, the flavour of the D^0 in these cases is tagged according to the decay of the "other side" D^0 to kaons. The main contribution to mistagging results from pions from the "other side" D^0 being misidentified as kaons. So many pions are produced in D decays that they have almost no correlation with the flavour of the mother D particle. Therefore a pion misidentified as a kaon can results in an incorrect flavour tag.

In order to quantify the mistag rate in the CLEO-c data set, events were selected containing apparent decays of the category,$D^0 \to K^+\pi^+\pi^-\pi^-$ and the charge conjugate decays. These events were flavour tagged using the same method as was used for the $D \to K^+K^-\pi^+\pi^-$ sample. The outcome of this tag was then compared to the tagging of the event via the charge of the kaon in the signal decay (assuming a Cabibbo favoured decay a negative kaon would imply that the mother particle was a D^0 and vice versa) in order to determine if the original tag was correct. A small correction is applied to account for genuine doubly Cabibbo suppressed decays. The mistag rate for the CLEO-c samples was measured to be $(3.4 \pm 0.4\%)$ for the 3770 sample and $(7.5 \pm 0.7\%)$ for the 4170 sample. The larger mistag rate for the 4170 sample can be attributed to the fact that in some cases for this sample the other side D was charged. The inclusive branching fraction of charged D to kaons is only around half that of the neutral D decays. Therefore a larger proportion of the other side tags were likely to correspond to background in this case.

The same method was applied in order to measure the mistag rate for the CLEO-III and CLEO-II.V samples. The mistag rate for these samples was estimated as $(0.64 \pm 0.05\%)$.

4.6 CP Tagged Datasets

As discussed in chapter 2 the CLEO-c experiment collected 818 pb^{-1} of its data at the centre of mass energy of the $\psi(3770)$ resonance. $D^0\overline{D}^0$ pairs are produced at this centre of mass energy via a virtual photon. The system $e^+e^- \rightarrow \psi(3770) \rightarrow D^0\overline{D}^0$ is a quantum correlated system [83] with definite CP quantum number $\mathbf{C} = -1$. Therefore, assuming the absence of CP violation, if one D is reconstructed in a state of definite CP the other D must necessarily decay into a state with the opposite CP. In addition to $D \rightarrow K^+K^-\pi^+\pi^-$ decays in which the D is of a specified flavour, data have been used in this study where the D is known to be in a particular CP state, since the accompanying D in the event has been reconstructed in the opposite CP state. The CP even tags which are practical to use were; $\pi^+\pi^-$, K^+K^-, $K^0_S\pi^0\pi^0$, $K_L\pi^0$ and $K_L\omega(\pi^+\pi^-\pi^0)$. The available CP odd tags were; $K^0_S\pi^0$, $K^0_S\omega(\pi^+\pi^-\pi^0)$, $K^0_S\phi(K^+K^-)$, $K^0_S\eta(\gamma\gamma)$, $K^0_S\eta(\pi^+\pi^-\pi^0)$ and $K^0_S\eta'(\pi^+\pi^-\eta)$.

Data were collected using $D \rightarrow K^+K^-\pi^+\pi^-$ decays in which the "other side" D was tagged as decaying to both purely CP even and CP odd states. In addition decays of the other side D to states consisting of an "admixture" of CP odd and CP even states have been considered. In particular signal $D \rightarrow K^+K^-\pi^+\pi^-$ decays tagged against the decays $D \rightarrow K^0_S\pi^+\pi^-$ and $D \rightarrow K^0_L\pi^+\pi^-$ were selected.

In the case of the admixture CP tagged states, the decay rate is dependent both on the region of $K^+K^-\pi^+\pi^-$ phase space and the region of $K^0_{L,S}\pi^+\pi^-$ phase space of the event. In order to make use of the $D \rightarrow K^0_{L,S}\pi^+\pi^-$ decay, information on the strong phase variation is required. This is available in bins of Dalitz space as determined in a previous CLEO analysis [82]. Therefore for the $K_{L,S}\pi^+\pi^-$ vs $D \rightarrow K^+K^-\pi^+\pi^-$ data collected for this study, in addition to the $K^+K^-\pi^+\pi^-$ kinematic parameters, the corresponding Dalitz bin: n into which the other side $K_{L,S}\pi^+\pi^-$ fell was also recorded for each event.

Although the CP tagged data offer only a relatively small increase in statistics the improvement in precision is more significant than would be the case for the equivelant flavour tagged dataset, this is explained in more detail in chapter 6.

4.6.1 Event Selection

Of particular note to the selection of CP tagged data was the difficulty in selecting K^0_L particles. The long lifetime of the K_L particle makes it very likely to decay outside of the detector volume. Therefore the K_L particles were selected inclusively using a missing mass technique, which requires all other particles in the event to have been reconstructed. In this technique the presence of the K_L is inferred by the missing energy. This was in contrast to the K_S^0 particles which were selected exclusively via the decay: $K_S^0 \to \pi^+\pi^-$.

The selection criteria for the pure CP tagged data in the analysis presented here were identical to those of [81], and those of the ad-mixture CP tagged data were identical to those in [82].

The number of selected events for both the pure CP tags and the admixture can be seen in table 4.4.

Tag	**Mode**	**Number of Selected Events**
CP Even	$\pi^+\pi^-$	8
	K^+K^-	11
	$K_S^0\pi^0\pi^0$	7
	$K_L\pi^0$	9
	$K_L\omega(\pi^+\pi^-\pi^0)$	14
	Total	**49**
CP odd	$K_S^0\pi^0$	15
	$K_S^0\omega(\pi^+\pi^-\pi^0)$	12
	$K_S^0\phi(K^+K^-)$	1
	$K_S^0\eta(\gamma\gamma)$	2
	$K_S^0\eta(\pi^+\pi^-\pi^0)$	1
	$K_S^0\eta^{'}(\pi^+\pi^-\eta)$	1
	Total	**32**
Admixture	$K_S^0\pi^+\pi^-$	63
	$K_L\pi^+\pi^-$	87
	Total	**155**
All CP Data	**Total**	**231**

Table 4.4: Number of selected CP tagged events in each mode.

4.6.2 CP Tagged Backgrounds

The backgrounds to the CP tagged samples can be divided into six categories:

1. Flat tagged background

2. Peaking tagged background

3. Flat signal background

4. Peaking signal background

5. D^+D^- background

6. Continuum production background

The "tag background" refers to background comprised of genuine $D \to K^+K^-\pi^+\pi^-$ events but for which the other side D decay has an incorrectly reconstructed CP tag. This can be further sub categorized into "flat" and "peaking" tagged background. Flat tagged background describes background which is evenly distributed across the signal and sideband region of the D from which the CP mode was reconstructed so falls into box B in addition to the signal box, S in figure 4.2 . This background is equivalent to the flat flavour tagged background described in section 5.6.1, except that it occurs for the other side D (rather than the D which decays to $K^+K^-\pi^+\pi^-$). Similarly peaking tagged background refers to background which peaks within the signal region of the CP mode so only appears in box S.

The "Signal" background refers to events for which the decay $D \to K^+K^-\pi^+\pi^-$ was incorrectly identified. Again this background can be divided into peaking and flat signal backgrounds in the same way that was described for flavour tagged backgrounds. Monte Carlo studies revealed that there was no significant contribution from a flat signal type background and so this contribution was not considered further.

Another possible source of background which was considered occurred due to decays resulting from D^+D^- which had been incorrectly reconstructed as the $D^0\overline{D}^0$ decays of interest.

The sixth possible background resulted from "continuum production" that did not result from a $\psi(3770)$, this background will appear in box C in addition to box S in figure4.2 .

The different selection technique employed for the K_L particles necessitated by its long lifetime, significantly affected the background distributions for the CP tags involving K_L particles. The CP tagged modes involving K_L particles were therefore

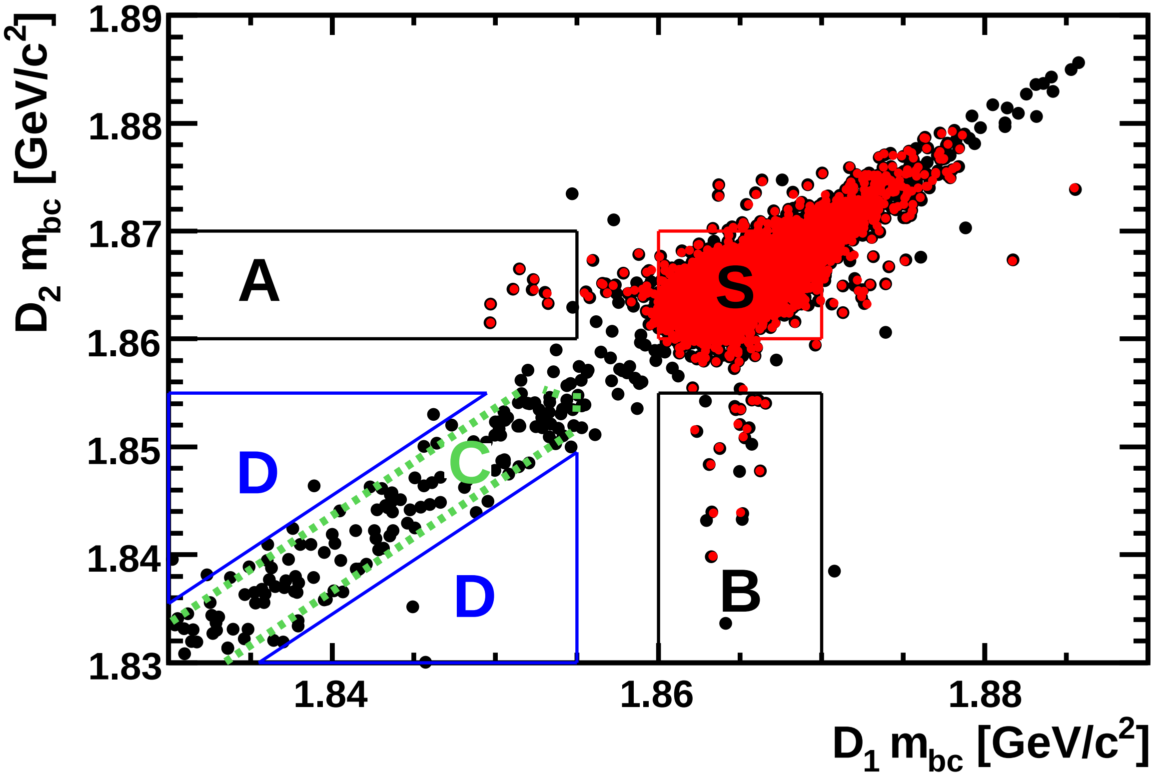

Figure 4.2: Signal and sideband boxes for a Monte Carlo sample of double tagged neutral D mesons. The red data points illustrate events which were fully reconstructed candidates which have full association with a Monte Carlo decay. The black points refer to background data.D_1 refers to the D particle which decays to the signal decay while D_2 refers to the particle decaying to the relevant tag.

treated separately from the other modes when considering background contamination.

In order to determine the shape and level of each background category within the signal region both Monte Carlo and genuine data were used. In particular the "generic Monte-Carlo" sample was used in this study. This was a simulation of $\psi(3770) \to D\overline{D}$ decays in the CLEO-c detector. Two separate generic Monte Carlo samples were available, corresponding to 20 and 30 times the integrated luminosity which was available in the corresponding data samples. "Continuum Monte-Carlo" samples were also used for background studies for the CP samples. This Monte Carlo sample consisted of continuum e^+e^- events and corresponded to a luminosity 5 times greater than the corresponding data samples.

4.6.3 Background Levels

It was then necessary to establish the proportion of events likely to be made up of each background type within each signal sample.

In the case of the flat tagged background in order to determine the expected fraction of this type of background expected in the signal sample the ratio, R_{TF} was calculated, where R_{TF} is the ratio of the number of this category of MC events in the signal box to the number of MC events in sideband A (which is comprised entirely of tagged flat background):

$$R_{TF} = \frac{\text{Number of tagged flat MC events in S}}{\text{Number of MC events in A}}. \tag{4.1}$$

The case is more complicated for the D^+D^- and continuum backgrounds since these backgrounds are simulated in separate MC samples of separate sizes and both occur in sideband C of the signal sample. The number of D^+D^- events present in the generic MC sample is expected to be 22.22 times greater than that present in data, where as the continuum Monte Carlo is five times larger than the data sample. w is defined as the weight which must be applied to the continuum Monte Carlo sample in order to account for its smaller size compared to the D^+D^- events generated in the generic MC sample, and has the value $w = \frac{22.22}{5} = 4.444$. It was then possible to calculate the ratios $R_{D^+D^-}$ and R_{cont}:

$$R_{D^+D^-} = \frac{\text{Number of } D^+D^- \text{ MC events in S}}{\text{Number of } D^+D^- \text{ MC events in C} + w \times \text{Number of continuum MC events in S}} \tag{4.2}$$

$$\tag{4.3}$$

$$R_{cont} = \frac{w \times \text{ Number of continuum MC events in S}}{\text{Number of } D^+D^- \text{ MC events in C} + w \times \text{Number of continuum MC events in S}}. \tag{4.4}$$

In order to scale between the Monte Carlo and data samples, the scale factor s is calculated:

$$s = \frac{\Sigma_{sidebands} \text{ Number of data events}}{\Sigma_{sidebands} \text{ Number of Monte Carlo events}}. \tag{4.5}$$

The number of expected events of these background categories in a particular CP tagged sample, i, is then given by:

$$N_{D^+D^-}(i) = s \times R_{D^+D^-} \tag{4.6}$$

$$
\begin{aligned}
&\times \big(\text{Number of } D^+D^- \text{ MC events in C in sample } i \\
&+ w \times \text{Number of continuum MC events in S in sample } i\big) \\
N_{cont}(i) &= s \times R_{cont} \qquad (4.7)\\
&\times \big(\text{Number of } D^+D^- \text{ MC events in C in sample } i \\
&+ w \times \text{Number of continuum MC events in S in sample } i\big) \\
N_{TF}(i) &= s \times R_{TF} \times \big(\text{Number of MC events in A in sample } i\big) \qquad (4.8)
\end{aligned}
$$

In the case of the peaking backgrounds, which do not occur in the sidebands, the number of expected events of each category is estimated simply by scaling the number of Monte Carlo events which occur in the signal box of a particular CP tagged sample to the luminosity of the data sample. The number of neutral DD pairs produced in the combined generic MC samples is expected to equal 22.78 times that of the data. Therefore the estimated number of signal peaking, $N_{SP}(i)$ and tag peaking, $N_{TP}(i)$ events in a particular CP tagged sample, i, is estimated by:

$$
\begin{aligned}
N_{SP}(i) &= \frac{\text{Number of Signal Peaking MC events in S in sample } i}{22.78} \qquad (4.9)\\
N_{TP}(i) &= \frac{\text{Number of Tag Peaking MC events in S in sample } i}{22.78}. \qquad (4.10)
\end{aligned}
$$

A separate background fraction was calculated in this way for each category of background for each of the CP even and odd data samples and also for each of the 16 bins in both the $K^0_S\pi^+\pi^-$ and $K_L\pi^+\pi^-$ samples. The background estimations were carried out separately for the tagged modes which involved a K_L particle. In the case of the CP even data both K_L and non K_L background sources were present. The background fractions involving K_L particles are listed in table 4.6 and the background from tags not involving K_L particles are listed in table 4.6.

In the final fit the fractions of each distribution were fixed to the values described in tables 4.5 and 4.5. Plots of the background distributions for the CP tagged data are shown in appendix A.

	D^+D^-	**Continuum**	**Tagged Flat**	**Tag Peaked**	**Signal Peaked**	**Total**
CP Even	0.028±0.002	0.126±0.011	0.006±0.001	0.002±0.001	0.059±0.007	**0.221±0.014**
CP Odd	0.002±0.001	0.008±0.002	0.004±0.001	0.03±0.006	0.115±0.013	**0.16±0.014**
$K_S^0\pi^+\pi^-$ **Bin 1**	0.014±0.005	0.062±0.021	0.002±0.002	0.009±0.009	0.263±0.048	**0.349±0.053**
$K_S^0\pi^+\pi^-$ **Bin 2**	0.009±0.003	0.041±0.015	0.0±0.0	0.0±0.0	0.099±0.032	**0.149±0.036**
$K_S^0\pi^+\pi^-$ **Bin 3**	0.004±0.004	0.018±0.017	0.004±0.004	0.0±0.0	0.132±0.044	**0.157±0.048**
$K_S^0\pi^+\pi^-$ **Bin 4**	0.006±0.004	0.026±0.019	0.0±0.0	0.015±0.015	0.0±0.0	**0.046±0.024**
$K_S^0\pi^+\pi^-$ **Bin 5**	0.004±0.002	0.017±0.007	0.0±0.0	0.005±0.006	0.082±0.02	**0.109±0.022**
$K_S^0\pi^+\pi^-$ **Bin 6**	0.001±0.001	0.003±0.003	0.0±0.0	0.0±0.0	0.033±0.019	**0.037±0.02**
$K_S^0\pi^+\pi^-$ **Bin 7**	0.001±0.001	0.004±0.004	0.0±0.0	0.015±0.015	0.132±0.043	**0.151±0.046**
$K_S^0\pi^+\pi^-$ **Bin 8**	0.005±0.002	0.024±0.008	0.0±0.0	0.009±0.009	0.22±0.044	**0.258±0.046**
$K_S^0\pi^+\pi^-$ **Bin -1**	0.014±0.003	0.065±0.016	0.0±0.0	0.015±0.015	0.19±0.051	**0.284±0.056**
$K_S^0\pi^+\pi^-$ **Bin -2**	0.013±0.006	0.061±0.029	0.0±0.0	0.0±0.0	0.439±0.137	**0.513±0.14**
$K_S^0\pi^+\pi^-$ **Bin -3**	0.003±0.002	0.015±0.01	0.0±0.0	0.0±0.0	0.037±0.016	**0.055±0.019**
$K_S^0\pi^+\pi^-$ **Bin -4**	0.0±0.0	0.0±0.0	0.0±0.0	0.044±0.025	0.073±0.033	**0.117±0.041**
$K_S^0\pi^+\pi^-$ **Bin -5**	0.003±0.001	0.015±0.005	0.0±0.0	0.0±0.0	0.114±0.033	**0.132±0.034**
$K_S^0\pi^+\pi^-$ **Bin -6**	0.019±0.007	0.085±0.03	0.0±0.0	0.0±0.0	0.395±0.133	**0.499±0.136**
$K_S^0\pi^+\pi^-$ **Bin -7**	0.009±0.005	0.04±0.023	0.0±0.0	0.044±0.024	0.22±0.058	**0.312±0.067**
$K_S^0\pi^+\pi^-$ **Bin -8**	0.006±0.002	0.027±0.01	0.0±0.0	0.0±0.0	0.073±0.023	**0.106±0.025**

Table 4.5: The background fractions for each of the five background categories. The above numbers apply to the background from CP tags which did not involve K_L particles. The bins referred to here will be described in chapter 5.

	D^+D^-	**Continuum**	**Tagged Flat**	**Tag Peaked**	**Signal Peaked**	**Total**
CP Even	0.02±0.002	0.01±0.001	0.034±0.004	0.008±0.003	0.073±0.008	**0.145±0.01**
$K_L\pi^+\pi^-$ **Bin 1**	0.035±0.005	0.017±0.003	0.059±0.009	0.0±0.0	0.084±0.016	**0.195±0.019**
$K_L\pi^+\pi^-$ **Bin 2**	0.028±0.009	0.013±0.004	0.047±0.014	0.0±0.0	0.121±0.037	**0.208±0.041**
$K_L\pi^+\pi^-$ **Bin 3**	0.011±0.004	0.005±0.002	0.019±0.007	0.0±0.0	0.033±0.013	**0.069±0.016**
$K_L\pi^+\pi^-$ **Bin 4**	0.023±0.008	0.011±0.004	0.038±0.013	0.0±0.0	0.0±0.0	**0.072±0.016**
$K_L\pi^+\pi^-$ **Bin 5**	0.038±0.009	0.018±0.004	0.064±0.015	0.0±0.0	0.158±0.039	**0.279±0.043**
$K_L\pi^+\pi^-$ **Bin 6**	0.025±0.007	0.012±0.003	0.042±0.011	0.0±0.0	0.117±0.03	**0.197±0.033**
$K_L\pi^+\pi^-$ **Bin 7**	0.028±0.008	0.013±0.004	0.047±0.014	0.0±0.0	0.165±0.043	**0.252±0.046**
$K_L\pi^+\pi^-$ **Bin 8**	0.055±0.009	0.026±0.004	0.092±0.015	0.0±0.0	0.1±0.025	**0.273±0.031**
$K_L\pi^+\pi^-$ **Bin -1**	0.028±0.004	0.013±0.002	0.046±0.007	0.0±0.0	0.091±0.016	**0.178±0.018**
$K_L\pi^+\pi^-$ **Bin -2**	0.03±0.009	0.014±0.004	0.051±0.015	0.0±0.0	0.132±0.04	**0.227±0.044**
$K_L\pi^+\pi^-$ **Bin -3**	0.045±0.016	0.022±0.007	0.076±0.026	0.0±0.0	0.088±0.043	**0.231±0.053**
$K_L\pi^+\pi^-$ **Bin -4**	0.0±0.0	0.0±0.0	0.0±0.0	0.0±0.0	0.0±0.0	**0.0±0.0**
$K_L\pi^+\pi^-$ **Bin -5**	0.056±0.017	0.026±0.008	0.093±0.028	0.0±0.0	0.329±0.082	**0.504±0.088**
$K_L\pi^+\pi^-$ **Bin -6**	0.018±0.006	0.009±0.003	0.031±0.01	0.0±0.0	0.07±0.025	**0.128±0.028**
$K_L\pi^+\pi^-$ **Bin -7**	0.05±0.013	0.024±0.006	0.085±0.022	0.0±0.0	0.161±0.05	**0.32±0.056**
$K_L\pi^+\pi^-$ **Bin -8**	0.026±0.007	0.012±0.003	0.044±0.012	0.0±0.0	0.097±0.03	**0.179±0.033**

Table 4.6: The background fractions for each of the five background categories. The above numbers apply to the background from CP tags which involved K_L particles.. The bins referred to here will be described in chapter 5.

4.7 Summary

In this chapter the event selection for the flavour tagged and CP tagged datasets has been described. The background and mistagging levels for each dataset has also been described. This work was carried out by other members of the UK CLEO group but has been included in this thesis for completeness.

Chapter 5

Preparing the Amplitude Fit

5.1 Introduction

In this chapter the procedure required for the four body $D \to K^+K^-\pi^+\pi^-$ amplitude analysis will be described. The details of the isobar model used to describe this decay are explained in addition to the treatment of the backgrounds and acceptances which are unique to this study. The technical details of the fitting framework are also explained in this chapter.

5.2 Four-Body Amplitude Fitting

Four-body amplitude fitting presents additional difficulties compared to three-body Dalitz fits. As described in chapter 1, in order to parametrize fully the final state five independent parameters are required. It is usual to choose these from the combinations of two-body and three-body invariant masses squared of the final state particles. The choice which is made for this study is: $s_{234} \equiv t_{01}$, s_{12}, s_{23}, s_{34}, $s_{123} \equiv t_{04}$, using the convention $s_{ij} \equiv (p_i + p_j)^2$ and $t_{ij} \equiv (p_i - p_j)^2$, where the particles D^0, K^+, K^-, π^+, π^- are labeled 0, 1, 2, 3, 4 respectively. (The fitting procedure actually makes use of the four vectors of each daughter particle, although these variables are not all independent. However when the χ^2 values are calculated and illustrating the plots only the five, Lorentz invariant, Dalitz variables are used.) As described in chapter 1 the phase space for a four-body decay is unbounded. The amplitude structure is also more complicated for a four-body final state, as the decay may proceed via either one or two intermediate resonances. One resonant sequence of decay, which is possible for the four body case, occurs when the decay cascades to the final state via two intermediate two body states. An example of this is the decay: $D \to K^- K_1^+(1270)(\pi^+ K^*(892)(K^+\pi^-))$. In addition to decays such as $D^0 \to K^*(892)(K^+\pi^-)K^-\pi^+$, decays such as $D^0 \to \phi(K^+K^-)\rho(\pi^+\pi^-)$ may also occur. This leads to a probability density function which is more sharply peaking than that for a three body decay since it contains terms which are proportional to $|A_iA_j|^2$ in addition to terms proportional to only one amplitude, $|A_i|^2$. This presents technical difficulties in event generation and fitting.

In this study an isobar model is used to describe the decay. In the isobar model the full decay amplitude, A_{D^0}, is written as a coherent sum of individual resonant terms corresponding to each intermediate state:

$$A_{D^0} = \sum_i a_i A_i(t_{01}, s_{12}, s_{23}, s_{34}, t_{04}) \tag{5.1}$$

where a_i is a complex factor corresponding to the intermediate state i and A_i gives an amplitude term relating to a single resonant or non-resonant intermediate state. It is the real and imaginary parts of a_i which are determined in the amplitude fit. As described in chapter 1, A_i is given by a product of three terms:

$$A_i = F_l \cdot s_l \cdot BW \tag{5.2}$$

where l specifies the relative angular momentum between the decay particles, and s_l is a Lorentz invariant "spin factor" which takes into account overall angular momentum conservation and is dependent on both the spin of the resonance(s) and the orbital angular momentum of the decay. These factors are used as specified in [70] and are listed in appendix B. F_l is the "Blatt Weisskopf" penetration factor [71] which attempts to account for the underlying quark structure of the decaying particle and the intermediate resoances. Finally BW gives the lineshape of the decay with the most common choice being the relativistic Breit-Wigner lineshape [73], although in the case of the $D^0 \to f_0(\pi^+\pi^-)K^+K^-$ decay an alternative lineshape (the Flattè lineshape) is also considered in the analysis presented in this thesis. In the case of non-resonant decays F_l and BW are defined to be one.

In the case of intermediate states with two resonances this amplitude is given by:

$$A_i = s_l \cdot BW_1 \cdot BW_2 \cdot F_{l1} \cdot F_{l2} \tag{5.3}$$

5.3 Introduction to Mint

The MINT framework is a general software package [72] used for generating and fitting decays to multi-body final states.

5.3.1 Event Generation

The highly peaked nature of the probability density function, combined with the non-flat (and unbounded) nature of the phase space distribution for four-body decays presents difficulties for efficient four-body event generation. In particular because there is no upper bound on the phase space density, it is not possible to use an "accept-reject" selection in order to generate phase space distributed events, let alone events distributed according to a sharply peaked resonant model. In order to overcome these problems, events are generated according to a distribution which approximates the peaking nature of the final PDF. These events are then weighted and an accept-reject procedure can be carried out on these events more efficiently.

The generation of events according to the approximate PDF will now be described. It can be shown [74], that the phase space integral for an n-body final state can be written in terms of the integrated two-body phase spaces for intermediate states. In particular the four-body phase space integral, R_4, may be written as:

$$R_4 = \int R_2(M_{D^2}; s_{12}, s_{34}) R_2(s_{12}; m_1^2, m_2^2) R_2(s_{34}; m_3^2, m_4^2) ds_{12} ds_{34} \tag{5.4}$$

where $R_2(M_A^2; m_B^2, m_C^2)$ is the integrated two-body phase space for the decay $A \to BC$. This approach works for all decay sequences but one. The only sequence which must be treated distinctly is for decays of the type $D \to P_4 A(\to P_3 B(\to P_1 P_2))$ (for example the decay: $D \to K^- K_1^+(1270)(\pi^+ K^*(892)(K^+\pi^-)))$. In this case the integrated phase space can be written as:

$$R_4 = \int R_2(M_{D^2}; s_{123}, m_4^2) R_2(s_{123}; s_{12}, m_3^2) R_2(s_{12}; m_1^2, m_2^2) ds_{123} ds_{12}. \tag{5.5}$$

Therefore considering a single intermediate resonant amplitude, the probability, P, of an event with invariant mass squared values between s_{12} and $s_{12} + ds_{12}$ and between s_{34} and $s_{34} + ds_{34}$ is given by:

$$\begin{aligned} P &= |A(s_{12}, s_{34})|^2 ds_{12} ds_{34} R_2(M_{D^2}; s_{12}, s_{34}) \\ &\times R_2(s_{12}; m_1^2, m_2^2) R_2(s_{34}; m_3^2, m_4^2) \end{aligned} \tag{5.6}$$

Considering a simple Breit-Wigner function for particle with mass M and decay width Γ:

$$BW = \frac{1}{M^2\Gamma^2 + (s - M^2)^2} \tag{5.7}$$

and defining the variable ρ such that $s_{ij} = M\Gamma \tan(\rho_{ij}) + M^2 \Rightarrow BW(s)\frac{ds}{d\rho} = \frac{1}{M\Gamma}$, it is then possible to generate a simple Breit-Wigner function by generating flat values of ρ between $-\frac{\pi}{2}$ and $\frac{\pi}{2}$. Therefore expression 5.6 may be rewritten as:

$$P = \frac{1}{M\Gamma} d\rho_{12} d\rho_{34} R_2(M_{D^2}; s_{12}, s_{34}) R_2(s_{12}; m_1^2, m_2^2) R_2(s_{34}; m_3^2, m_4^2) \tag{5.8}$$

where the amplitude has been approximated by the simple Breit-Wigner amplitude of 5.7. Events are therefore generated by generating flat pairs of ρ_{12}, ρ_{34} and then weighting these events by $R_2(M_{D^2}; s_{12}, s_{34}) R_2(s_{12}; m_1^2, m_2^2) R_2(s_{34}; m_3^2, m_4^2)$. The full decay chain may then be generated with the corresponding fixed values of s_{12} and s_{34}. In this way each of the intermediate states are generated separately. The generator probability density function, "generated PDF", is therefore given by an incoherent sum of simplified Breit-Wigner functions:

$$\text{Generated PDF} = \sum_k |BW_k|^2 \frac{d^5\phi}{ds_{ij}}, \tag{5.9}$$

where the sum is over all of the intermediate states. Having generated weighted events according to the distribution 5.9, the (phase-space) weights of events are then multiplied by the factor $\frac{\text{Full PDF}}{\text{Generated PDF}}$.

The maximum weight of the events is then estimated according to the "generalised Pareto distribution" [75]. It can be shown that tails of functions which satisfy certain conditions can be modelled using the generalised Pareto distribution. This is a function which for a particular choice of parameters reduces to an exponential and is able to reproduce a continuous range of shapes. The value of the maximum weight is estimated by fitting the Pareto function to the largest n weights (where n depends on the confidence level required).

Having estimated this maximum value an accept-reject procedure is then carried out on the weighted events. The generator function, though not equal to the full PDF, approximates the peaking structure so that the accept and reject procedure is much more efficient in terms of CPU. This therefore achieves unweighted event generation according to the full probability density function accounting for interference affects, mass dependent widths and any other acceptance or efficiency effects which are included in the full distribution function.

5.3.2 Event Fitting

In addition to the probability density function which describes the signal as given in expression 5.1, background distributions may be added incoherently in order to give the full probability distribution function.

$$PDF = S \times f + B \times (1 - f) \tag{5.10}$$

where S gives the normalised signal distribution, B the normalised background distribution and f the fraction of events which consist of signal. This process can be expanded to include more than one background component:

$$B = B_1 \times b_1 + B_2 \times (1 - b_1). \tag{5.11}$$

Any signal or background component may also include a multiplicative function (of the particles' four momenta) to account for acceptance effects, for example expression 5.1 may include a function, ϵ:

$$S \quad = \quad \epsilon(p_0, p_1, p_2, p_3, p_4) r_4 |\sum_i a_i A_i(t_{01}, s_{12}, s_{23}, s_{34}, t_{04})|^2 \tag{5.12}$$

where r_4 is the four body phase space density ($r_4 = \frac{dR_4}{dp}$). The values of the complex parameters a_i are determined during the fit. These may be fit either in terms of the phase and modulus of each value of a_i or in terms of the Cartesian real and imaginary parts of a_i. One member of the a_i parameter set is fixed to an arbitrary value (by convention $(1, 0)$) during the fit, in order to fix the overall normalization and phase to which the fit is not sensitive. A log-likelihood fit is carried out to all remaining members of the a_i parameter set. The log-likelihood function is defined by:

$$\log(\mathcal{L}) = \sum_{\text{events}} \log(PDF(\text{event})) \tag{5.13}$$

If a number of separate event sets with different efficiency functions, and different background distributions are to be fit simultaneously the log-likelihood function is given by:

$$\log(\mathcal{L}) = \sum_{\text{sample}_i} \sum_{\text{event}_j} \log(PDF_i(\text{event}_{ij})) \tag{5.14}$$

where:

$$\begin{aligned} PDF_i &= \epsilon_i(p_0, p_1, p_2, p_3, p_4) r_4 |\sum_k a_k A_k(t_{01}, s_{12}, s_{23}, s_{34}, t_{04})|^2 \times s_i \qquad (5.15) \\ &+ B_i \times (1 - s_i). \end{aligned}$$

The maximum of the log-likelihood function is found using the MINUIT package [76].

5.3.3 Normalisation

When more than one function is added incoherently as in the case of expression 5.10 the individual functions must be properly normalised. In order to normalize the signal and background PDFs of 5.10 large numbers of weighted Monte Carlo events are generated. The normalisation is then calculated as shown:

$$\begin{aligned} \text{Norm} &= \int |\text{A}(p,x)|^2 \epsilon(p) r_4(p) dp \qquad (5.16) \\ &\simeq \left(\frac{\Phi}{\sum_{events}^{N} \text{Weight}_{event}} \right) \sum_{events}^{N} \frac{\text{Weight}_{event} \times \epsilon(p) \times |\text{A}_{event}|^2}{\text{Gen}_{event}}, \qquad (5.17) \end{aligned}$$

where A represents the amplitude function of expression 5.1, p represents the measured particles four momenta, x represents the fitted parameters, Gen represents the generator PDF relative to phase space, Weight represents the weight of the generated event (if unweighted Monte Carlo events are used for normalisation: Weight = 1 for all events) and Φ represents the total volume of allowed phase space. The number of events required such that expression 5.17 approximates expression 5.16 with sufficient precision is calculated by evaluating the variance of expression 5.17 and ensuring that:

$$\text{precision}^2 \times \text{mean}^2 \quad > \quad \text{variance} \tag{5.18}$$

where "precision" is the specified required precision and "mean" and "variance" are the mean and variance of 5.17 respectively. Events are generated until the requirement of 5.18 is satisfied. In the case of the isobar signal PDF (5.12) the normalisation, as calculated from N unweighted Monte Carlo events is therefore given by:

$$\begin{aligned}
\text{Norm} &= \frac{1}{N}\sum_{events}^{N}[\frac{\epsilon(p_0,p_1,p_2,p_3,p_4)}{Gen}|\sum_i a_i A_i(t_{01},s_{12},s_{23},s_{34},t_{04})|^2] && (5.19)\\
&= \frac{1}{N}\sum_{events}^{N}[\frac{\epsilon(p_0,p_1,p_2,p_3,p_4)}{Gen_{event}} && (5.20)\\
&\times \sum_i\sum_j[a_i^* a_j A_i^*(t_{01},s_{12},s_{23},s_{34},t_{04})A_j(t_{01},s_{12},s_{23},s_{34},t_{04})]]\\
&= \frac{1}{N}\sum_i\sum_j[a_i^* a_j && (5.21)\\
&\times \sum_{events}^{N}[\frac{\epsilon(p_0,p_1,p_2,p_3,p_4)A_i^*(t_{01},s_{12},s_{23},s_{34},t_{04})A_j(t_{01},s_{12},s_{23},s_{34},t_{04})}{Gen_{event}}]].
\end{aligned}$$

Note that the order in which the summation of amplitudes and events is carried out is switched from 5.20 to 5.21, this means that the Hermitian matrix $M_{ij} = \sum_{events}^{N}\epsilon A_i^* A_j$ may be calculated once and then saved. In this way the time consuming sum over a large number of events need not be recalculated each time the values of the parameters a_i are changed during the fitting procedure.

5.3.4 Fit Quality

In order to quantify the quality of the fit, a value of χ^2 is determined. The phase space is enclosed in a five dimensional region. The box in each dimension is divided in half creating 32 equal bins. Each box which has more than a maximum number (100) of data events is divided in the same manner into a further 32 boxes. This process is continued iteratively until all boxes contain less than the maximum number of events. The boxes are then sorted according to the number of events contained in them. Starting from the box containing the fewest events, each box is combined with the box containing the next fewest events until the resulting box has a minimum number (50) of events. This process is repeated until all boxes contain the minimum number of events or more.

The χ^2 per degree of freedom is then calculated in the usual way:

$$\chi^2_{DOF} = \frac{1}{(N_{bins} - N_{parameters} - 1)} \sum_{bin} \frac{(N_{expected,i} - N_{events,i})^2}{N_{expected,i}} \tag{5.22}$$

where $N_{parameters}$ is the number of parameters that were allowed to float during the fit. The number of bins is subtracted by 1 in the denominator of equation 5.22 since the number of events in the final bin is determined by the overall normalisation and so does not represent a degree of freedom. $N_{expected,i}$ gives the number of events in the bin i predicted by the PDF (5.10). In general therefore $N_{expected,i}$ is given by the integral of the PDF function across the ith χ^2 bin. In order to calculate this value a large MC sample is generated according to a PDF, PDF_{gen}. The expected number of events in each bin, i, $N_{expected,i}$ according to PDF is then given by:

$$N_{expected,i} = Norm \times \sum_{\text{MC events in bin } i} MC_{weight}(event) \tag{5.23}$$

$$Norm = \frac{\text{Total number of data events}}{\sum_{\text{all MC events}} MC_{weight}(event)} \tag{5.24}$$

$$\begin{aligned} MC_{weight}(event) &= \frac{PDF(event) \times \text{weight}(event)}{PDF_{gen}(event)} \\ &= \frac{|A|^2 \times \epsilon \times \text{weight}(event)}{Gen_{event}} \end{aligned} \tag{5.25}$$

where weight($event$) gives the weight of the MC event, Gen gives the generator PDF of the MC event, relative to phase space, ϵ represents the factor which accounts for acceptance affects and A represents the D^0 decay amplitude of expression 5.1.

5.3.5 Fit Fraction

The "fit fraction" is also calculated for each resonant component which has been fit. As for three body decays the fit fraction is defined for a resonance r as the value of $|a_r|^2|A_r|^2$ integrated over the entire kinematically allowed region divided by the integrated value of $|A_{D^0}|^2$. This gives a convention independent measurement of the contribution of each resonance to the total decay. The fit fraction is calculated numerically to a specified precision.

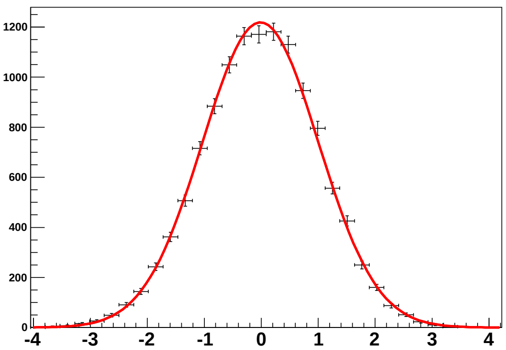

Figure 5.1: Sum of pull distribution of all fitted parameters from MC $D^0 \to K^+\pi^-\pi^+\pi^-$ verification studies.

5.4 Fitter Verification

5.4.1 Self Consistency

In order to verify the self consistency of the MINT four body generation and fitting a pull study was conducted. One thousand sets of 10000 $D_0 \to K^-\pi^+\pi^-\pi^+$ events were generated according to a simple amplitude model, consisting of six resonant and one non resonant component. The complex amplitudes of the generated model were then fit back with one component ($a_1(1260)(\to \rho\pi)K$) fixed to avoid any redundant free parameters. The fitted complex amplitudes were then compared to the input values.

	Parameter	Input Values	Mean Pull Value	Width of Pull Values
1	$K_1(1270)(\to \rho K)\pi$ Real	0.080	-0.053 $\pm$ 0.032	0.98 $\pm$ 0.02
2	$K_1(1270)(\to \rho K)\pi$ Imaginary	0.030	-0.092 $\pm$ 0.033	1.02 $\pm$ 0.03
3	$\overline{K}^*(892)(\to \pi K)\pi\pi$ Real	-1.030	0.057 $\pm$ 0.034	0.98 $\pm$ 0.03
4	$\overline{K}^*(892)(\to \pi K)\pi\pi$ Imaginary	0.180	-0.014 $\pm$ 0.031	0.94 $\pm$ 0.02
5	$\overline{K}^*(892)(\to \pi K)\rho$ Real	-0.010	013 $\pm$ 0.031	0.97 $\pm$ 0.03
6	$\overline{K}^*(892)(\to \pi K)\rho$ Imaginary	0.300	-0.136 $\pm$ 0.033	0.98 $\pm$ 0.03
7	$\overline{K}^*(892)(\to \pi K)\rho$ D-wave Real	-0.060	0.071 $\pm$ 0.032	0.96 $\pm$ 0.02
8	$\overline{K}^*(892)(\to \pi K)\rho$ D-wave Imaginary	0.130	0.009 $\pm$ 0.034	1.00 $\pm$ 0.03
9	Non Resonant Real	0.190	0.005 $\pm$ 0.033	1.02 $\pm$ 0.03
10	Non Resonant Imaginary	-0.290	0.042 $\pm$ 0.033	1.00 $\pm$ 0.02
11	$\rho K\pi$ Real	0.170	-0.049 $\pm$ 0.034	1.02 $\pm$ 0.03
12	$\rho K\pi$ Imaginary	-0.040	-0.005 $\pm$ 0.034	1.02 $\pm$ 0.02
13	$a_1(1260)(\to \rho\pi)K$ Real	1.00	0.0 $\pm$ 0.0	0.0
14	$a_1(1260)(\to \rho\pi)K$ Imaginary	0.00	0.0 $\pm$ 0.0	0.0

Table 5.1: Table of pull results to test self consistency of four body amplitude fitter.

The pull value of each fitted component for each returned fit is calculated in the usual way: pull $= \frac{\text{Fitted Value} - \text{Input Value}}{\text{Error on Fitted Value}}$. The pull values of the 12 fitted variables were fitted to a Gaussian the combined pulls from all variables added together are plotted in figure 5.1. The results for each component are reported in table 5.1. For an unbiased fit with correctly determined uncertainties the pull values are expected to follow a Gaussian distribution centered around 0 with a width of 1.0. The pull results are consistent with a Gaussian of width 1.0. The central values are for the most part consistent with 0, but do have deviations from 0 which are greater than would be expected from a random selection of independent variables. This can be attributed to correlations between the variables. It may be concluded however that the generation and fitting of MINT is at least sufficiently self consistent to analyse the data samples considered in this thesis.

5.5 Combining D^0 and $\overline{D}^0$ Decays

Each of the flavour tagged datasets consisted of both D^0 and $\overline{D}^0$ decays. In order to determine the parameters of the $D^0 \to K^+K^-\pi^+\pi^-$ decay, the $\overline{D}^0 \to K^+K^-\pi^+\pi^-$ decays were "CP flipped" and combined with the $D^0 \to K^+K^-\pi^+\pi^-$ decays. In order to CP flip these decays each particle in the decay was switched with its conjugate particle (i.e. $\pi^+ \leftrightarrow \pi^-$, $K^+ \leftrightarrow K^-$) and its 3-momentum was transformed: $\mathbf{P}_i \to -\mathbf{P}_{-i}$. This operation assumes that CP violation is negligible. This assumption is tested seperately in a later step of this analysis.

5.6 Backgrounds to the Flavour Tagged Datasets

5.6.1 Modelling the Flat Background

Since the conditions under which the signal events were produced was distinct for each dataset, with different experimental configurations and decay topologies, the level and shape of the background is expected to differ for each data set and so was modeled separately. The background characteristics were studied using data collected in the sideband samples selected for each dataset as presented in chapter 4. The sidebands are the regions of phase space which fail the mass cuts but are otherwise consistent with the signal decay such as boxes A and B of figure 4.2.

In order to describe each of these background distributions a model was required. The background was expected to result from random combinations of the four final state particles K^+, K^-, π^+, π^-, in addition to random combinations of resonances and final state particles which decay to the same final state but did not originate from a single D^0. Any resonance which may contribute to the signal was also considered as a possible contribution to the background. The combinations of K^+, K^-, π^+, π^- were assumed to follow a phase space distribution. The resonant contributions were modeled with Breit-Wigner lineshapes with no form factors or angular distribution. The usual angular dependences of the resonant decays were not included in the model since the background particles did not decay from a D^0 but rather from a variety of unknown decay topologies. The various contributions to the background would not interfere and therefore were added incoherently in the background model as shown in equation 5.26:

$$PDF_{background} = r_4(p)\left(a_{nr} + \sum_r a_r|BW_r|^2\right). \tag{5.26}$$

The real numbers a_{nr}, a_r, which determine the contribution of the non resonant component and each resonant component, r, respectively were determined in the fit.

In order to determine which combinations of resonances would best describe the background distribution for each dataset, the χ^2 per degree of freedom was calculated for each fit as described in section 5.9. Combinations of resonances were considered which in each case included a ϕ resonance, a ρ resonance, a $K_1(1270)$ resonance, and a f_0 resonance, in addition to the non resonant component. The five combinations which best described the background sample as indicated by the χ^2 value were then fit again with an additional component included. For each combination of resonances any resonance with a fit fraction of less than 0.5% was removed and another fit was attempted with the remaining components. This process was carried out iteratively for each sample until no further improvement in the χ^2 per degree of freedom was achieved. Of all the attempted configurations the one with the best χ^2 per degree of freedom was selected. The fit fractions of each resonant and non-resonant component in each of the final background models are shown in table 5.2.

The projections of the fitted background samples in the invariant mass squared variables are illustrated in figures 5.2, 5.3, 5.4 and 5.5. These flat background models and the fraction of events in the signal region which result from these backgrounds were then fixed in the final PDF for each flavour tagged sample as described in chapter 5. The background projections show that the background to each dataset has a distinct shape, This is expected because each of the datasets, results from either a significantly different detector configeration, selection procedure or both.

	CLEO-II.V	**CLEO-III**	**CLEO-c** 3770	**CLEO-c** 4170
$\overline{K_1}(1270)^-(\rightarrow \overline{K_0}^*(1430), \pi^-), K^+$	-	-	0.019±0.064	-
$K_1(1270)^+(\rightarrow K^*(892), \pi^+), K^-$	0.053±0.015	-	-	-
$\overline{K_1}(1270)^-(\rightarrow \overline{K_0}^*(892), \pi^-), K^+$	0.006±0.015	0.032±0.015	0.033±0.021	-
$K_1(1270)^+(\rightarrow \rho(770), K^+), K^-$	-	-	0.005±0.013	-
$K_1(1400)^+(\rightarrow K_0^*(892), \pi^+), K^-$	-	0.055±0.014	0.015±0.023	-
$\phi(1020), \pi^+, \pi^-$	-	0.079±0.011	0.143±0.022	0.102±0.013
$K^*(892)\overline{K^*}(892)$	0.007±0.012	0.045±0.014	0.101±0.019	0.01±0.017
$\phi(1020)\rho(770)$	-±0.004	-	-	-
$\overline{K^*}(892), K^+, \pi^-$	-	-	-	0.032±0.023
$f(0)(980), K^+, K^-$	0.033±0.047	0.128±0.049	0.293±0.118	-
K^+, K^-, π^+, π^-	0.899±0.048	0.661±0.046	0.373±0.103	0.516±0.078
$\rho(770)K^+, K^-$	-	-	-	0.243±0.034
$K^*(892), K^-, \pi^+$	-	-	0.017±0.035	0.098±0.025
χ^2 **per DOF**	**1.32**	**1.2**	**1.17**	**2.13**

Table 5.2: The fit fractions of each contribution to the background for each dataset.

5.6.2 Peaking Background: $D^0 \rightarrow K_S^0(\pi^+\pi^-)K^+K^-$

In addition to the flat background described above it was also necessary to consider other backgrounds that did not appear in the sideband regions but instead peaked within the signal box. This type of background is likely to result from other decays of D^0 which pass the selection cuts. Monte Carlo studies were performed in order to evaluate these types of backgrounds. In the case of the CLEO-II.V and CLEO-III samples there was an expected contribution from $D^0 \rightarrow K_S^0(\pi^+\pi^-)K^+K^-$ decays, but the level was sufficiently small that this background could be neglected. However in the case of the lower energy CLEO-c samples, since the K_S^0 did not travel as far before decaying it was not possible to suppress all decays of the type $D^0 \rightarrow K_S^0(\pi^+\pi^-)K^+K^-$ from the signal region and thus these samples did suffer a non negligible contribution from this background.

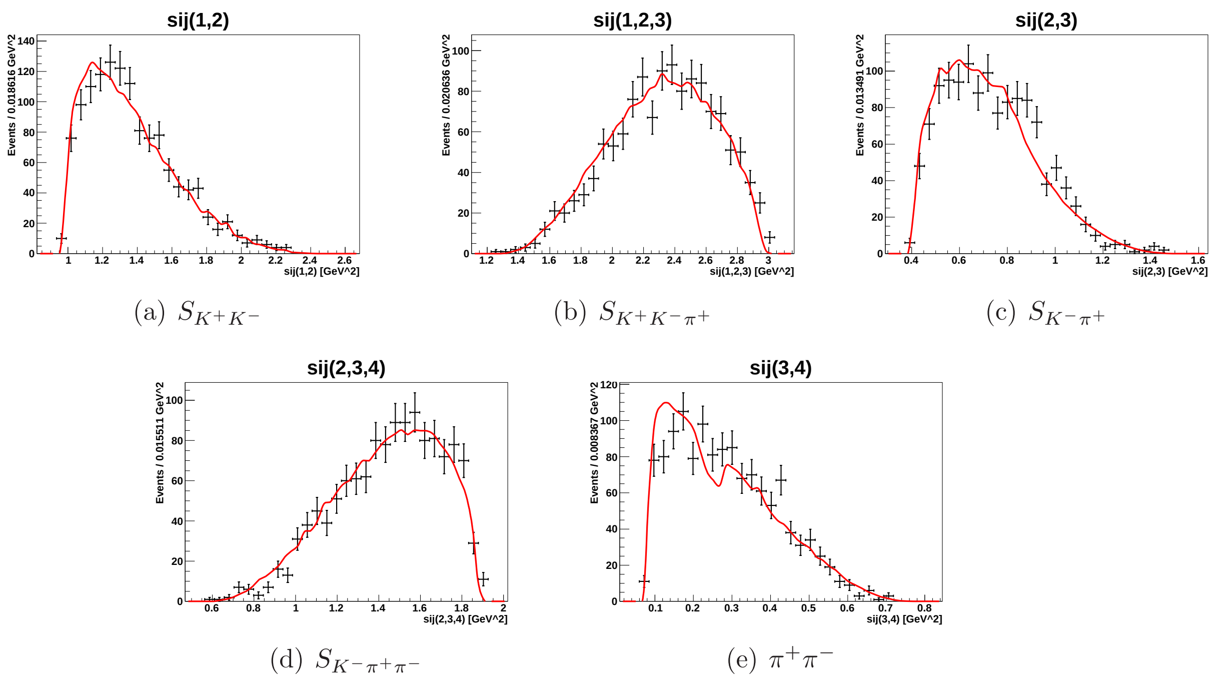

(a) $S_{K^+K^-}$ (b) $S_{K^+K^-\pi^+}$ (c) $S_{K^-\pi^+}$

(d) $S_{K^-\pi^+\pi^-}$ (e) $\pi^+\pi^-$

Figure 5.2: Projections of fitted result(red) against selected data(black) for the background sample from the CLEO-II.V sample.

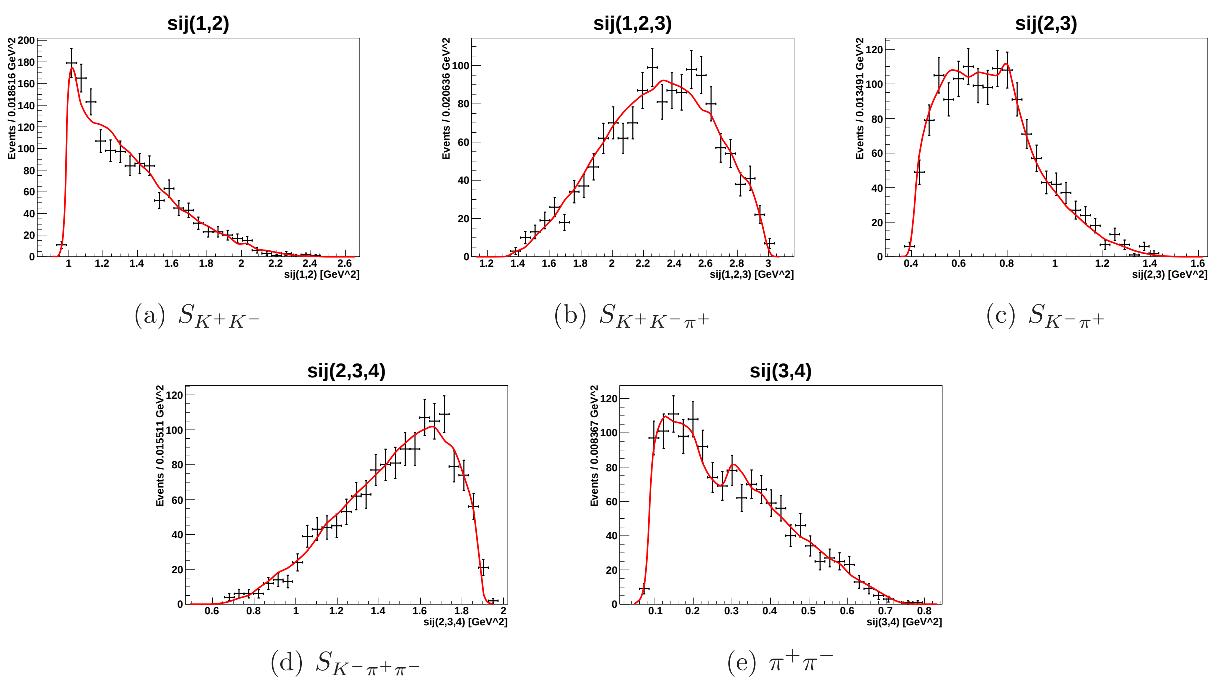

(a) $S_{K^+K^-}$ (b) $S_{K^+K^-\pi^+}$ (c) $S_{K^-\pi^+}$

(d) $S_{K^-\pi^+\pi^-}$ (e) $\pi^+\pi^-$

Figure 5.3: Projections of fitted result(red) against selected data(black) for the background sample from the CLEO-III sample.

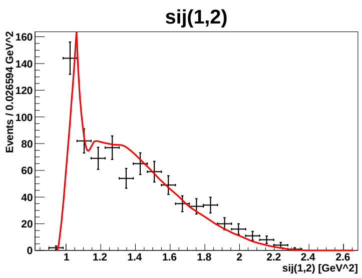

(a) $S_{K^+K^-}$

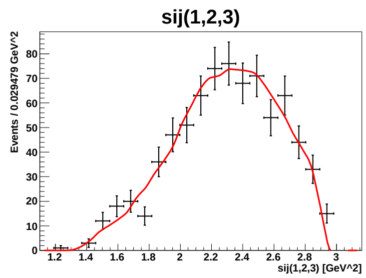

(b) $S_{K^+K^-\pi^+}$

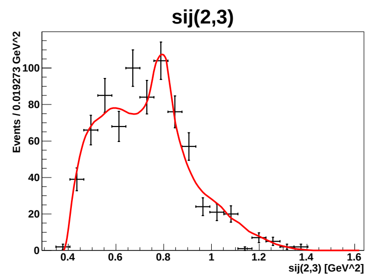

(c) $S_{K^-\pi^+}$

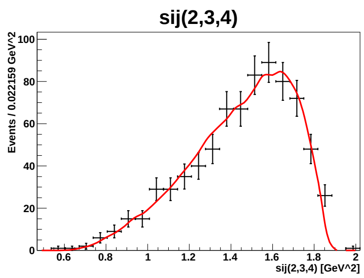

(d) $S_{K^-\pi^+\pi^-}$

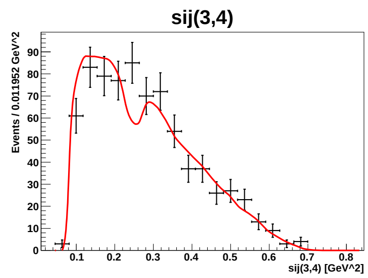

(e) $\pi^+\pi^-$

Figure 5.4: Projections of fitted result(red) against selected data(black) for the background sample from the CLEO-c 3770 sample.

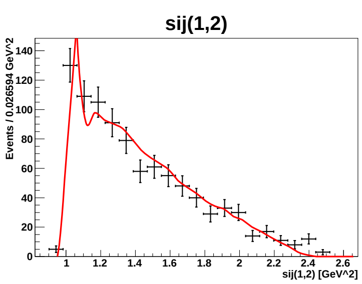

(a) $S_{K^+K^-}$

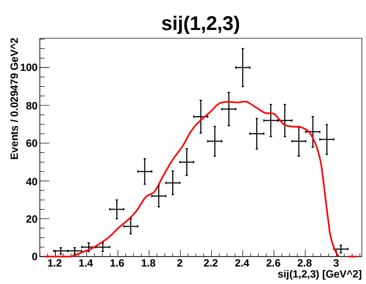

(b) $S_{K^+K^-\pi^+}$

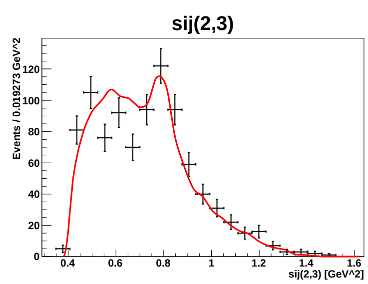

(c) $S_{K^-\pi^+}$

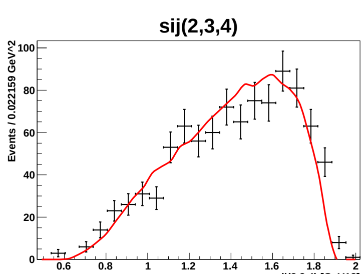

(d) $S_{K^-\pi^+\pi^-}$

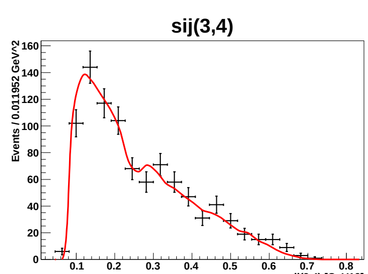

(e) $\pi^+\pi^-$

Figure 5.5: Projections of fitted result(red) against selected data(black) for the background sample from the CLEO-c 4170 sample.

Monte Carlo studies suggested that the level of this background would lie at the 3% level in the case of the 3770 MeV sample, and a little less for the 4170 MeV sample where the K^0_S momentum is higher. However due to the peaking nature of this background it was not possible to measure its level from the sidebands for either CLEO-c dataset. Therefore the level of this peaking background for each sample was allowed to float as a free parameter during the final fit to the signal distributions. The results of these fits are illustrated in section 6.5

In order to determine the shape of this background in the signal region, a sample of events was collected from the signal region of the CLEO-c data samples containing all events which failed the "K^0_S veto" cuts. (These are the cuts which are applied specifically to reduce the $D^0 \to K^0_S(\pi^+\pi^-)K^+K^-$ background).

Although the $D_0 \to K^0_S K^+K^-$ is a three-body decay for which a Dalitz model exists, [22], in the present analysis it is necessary to construct an empirical four body amplitude model to describe how the final state particles are distributed and enter as background to the signal decay. An amplitude model was developed to model this sample. In this model the K^0_S was treated as a resonance with a width of 100 MeV which accounted for the smearing due to the non-zero detector resolution in measuring the K^0_S. The resonant contributions to the $D^0 \to K^0_S K^+K^-$ decay which were considered in order to form the Dalitz model for the full decay were those listed in [22]. In this case the fitted PDF consisted of a coherent sum of all resonant contributions including their angular dependences. The values of the complex amplitudes corresponding to each resonant contribution were obtained during the fit. The best configuration of resonances was then determined by beginning with a pure $K^0_S K^+K^-$ model and adding resonances one at a time, and removing those which had a small fit fraction. The models which had the smallest χ^2 per degree of freedom were then selected. These fits were carried out separately for the 3770 and 4170 CLEO-c samples. The mass projections of the fits to these samples are shown in figures 5.6 and 5.7. The fit fractions are illustrated in 5.3. It may be noted that the sum of fit fractions for these samples are very large, which indicates a large degree of intereference between the components which are included. The χ^2 value in particular for the 4170 sample does not indicate a very good fit for this model. Uncertainties in these models were however considered as a systematic, this is discussed in chapter 6.

Contribution	**Fit Fraction** 3770	**Fit Fraction** 4170
$a_0^+(1450)(\to K_S^0K^+)K^-$	1.15 ± 0.43	0.06 ± 0.09
$a_0(1450)(\to K^+K^-)K_S^0$	2.38 ± 0.78	2.86 ± 0.75
$a_0^+(980)(\to K_S^0K^+)K^-$	0.05 ± 0.03	0.11 ± 0.06
$a_0(980)(\to K^+K^-)K_S^0$	0.22 ± 0.03	0.19 ± 0.03
$\phi(1020)(\to K^+K^-)K_S^0$	0.24 ± 0.12	0.17 ± 0.08
$K_S^0K^+K^-$	4.31 ± 1.72	3.05 ± 1.13
χ^2 **per degree of freedom**	**1.62**	**2.93**

Table 5.3: The fit fractions of components contributing to the $D \to K_S^0K^+K^-$ background.

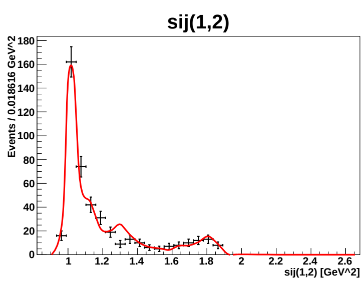

(a) $S_{K^+K^-}$

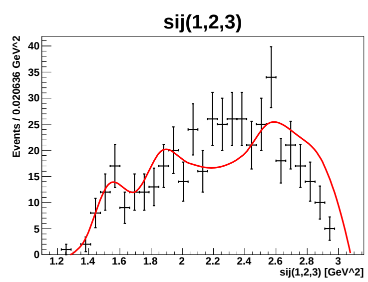

(b) $S_{K^+K^-\pi^+}$

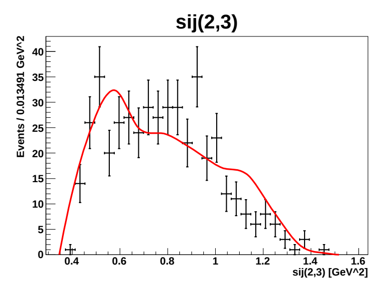

(c) $S_{K^-\pi^+}$

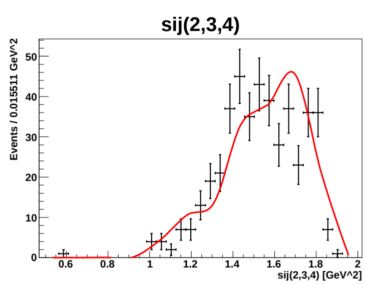

(d) $S_{K^-\pi^+\pi^-}$

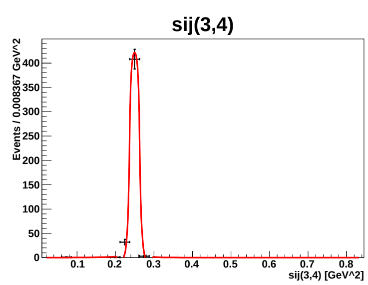

(e) $S_{\pi^+\pi^-}$

Figure 5.6: Projections of fitted result(red) against selected data(black) for the background sample from the $K_S^0K^+K^-$ CLEO-c 3770 sample.

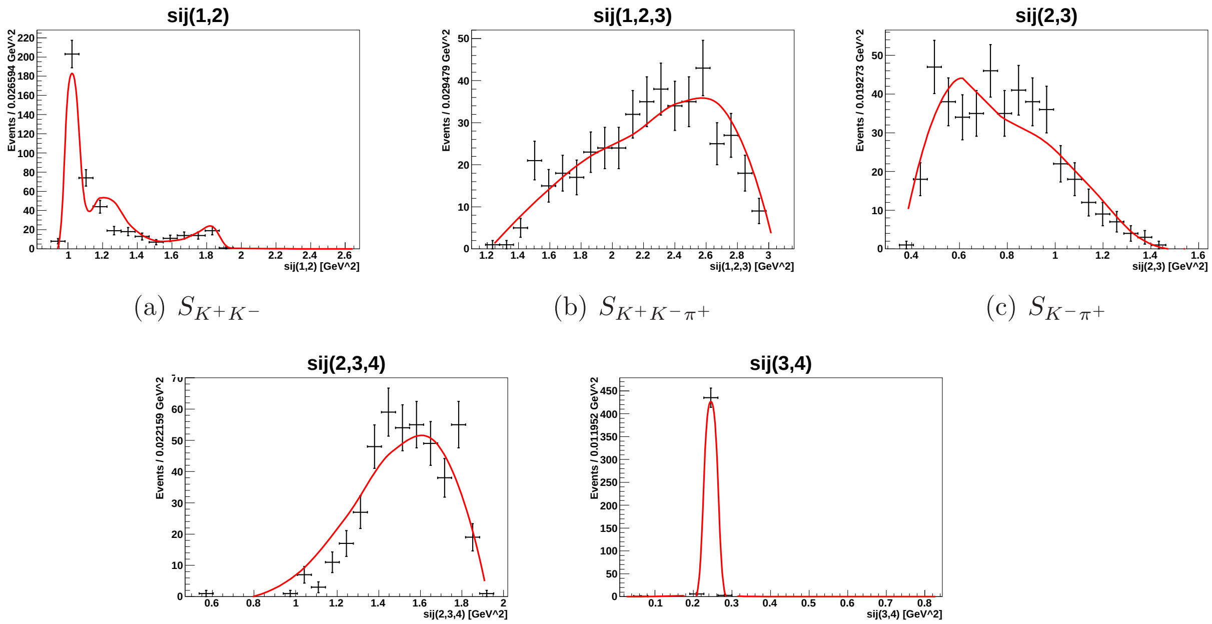

(a) $S_{K^+K^-}$ (b) $S_{K^+K^-\pi^+}$ (c) $S_{K^-\pi^+}$

(d) $S_{K^-\pi^+\pi^-}$ (e) $S_{\pi^+\pi^-}$

Figure 5.7: Projections of fitted result(red) against selected data(black) for the background sample from the $K^0_S K^+ K^-$ sample CLEO-c 4170 sample.

5.7 Backgrounds to the CP-tagged Datasets

The CP-tagged datasets were contaminated by background events which could be divided into categories which have been described in section 4.6.2. Both the generic and continuim Monte Carlo samples (as described in section 4.6.2) and data were used in order to collect background samples from which the shape of each background category was modelled. The full model obtained for each of the CP tagged background models are listed in appendix A but are described more generally here..

5.7.1 Flat Tagged Background

In order to characterise the behaviour of this background, data were selected from the sidebands (of the tagged side D meson) of the generic Monte Carlo and data samples, illustrated by box A of 4.2. The samples were combined and events from each Monte Carlo sample were weighted accordingly (for example those from the 20 times luminosity sample were weighted by 0.05).

Since the events were incorrectly tagged the $D \to K^+K^-\pi^+\pi^-$ events did not have the CP correlations of a tagged CP sample. The $D \to K^+K^-\pi^+\pi^-$ decays were therefore assumed to be comprised of equal proportions of uncorrelated D^0 and $\overline{D}^0$ decays. The PDF used to model this background was therefore an incoherent sum of the D^0 and $\overline{D}^0$ decay amplitudes, A and $\overline{A}$:

$$PDF \;=\; \frac{1}{2}(|A|^2 + |\overline{A}|^2). \tag{5.27}$$

In order to model the amplitude A a coherent amplitude model was used. Since only a small sample was available to fit, it was not possible to calculate a reliable χ^2 value for this background sample. The final model was therefore determined by inspection of the mass projections for each configuration of resonances, in order to determine which configuration best matched the sample. The mass projections from the fit to this background sample are illustrated in figure 5.8 for all modes which do not contain a K^0_L particle and figure 5.9 for modes containing a K^0_L.

5.7.2 Tagged Peaking Background

A sample of this background was collected from the signal box (box S in figure 4.2) of the generic Monte Carlo samples, in this case the truth information available for the Monte Carlo sample enabled these events to be distinguished from genuine signal and other background events. The tagged peaking background, as for the flat tagged background, was assumed to be comprised of equal proportions of uncorrelated D^0 and $\overline{D}^0$ decays, and was therefore modeled with the PDF of expression 5.27. Again a coherent amplitude model was used to describe the D^0 decay amplitude, A. The mass projections for the fits to the tagged peaking background samples with all modes except those involving K^0_L particles are illustrated in figure 5.10 and those modes involving K^0_L particles are illustrated in figure 5.11.

5.7.3 Peaking Signal Background

A peaking signal sample was collected from the signal box of the generic Monte Carlo samples. Monte Carlo studies revealed that the peaking signal background was comprised entirely of $K^0_S K^+K^-$ decays. Therefore this background component was modeled as an incoherent sum of $D^0 \to K^0_S(\pi^+\pi^-)K^+K^-$ and $\overline{D}^0 \to K^0_S(\pi^+\pi^-)K^+K^-$ decays. The PDF which was fit was again that of expression 5.27 where the amplitude A now describes the $D^0 \to K^0_S(\pi^+\pi^-)K^+K^-$ decay. This decay was modeled

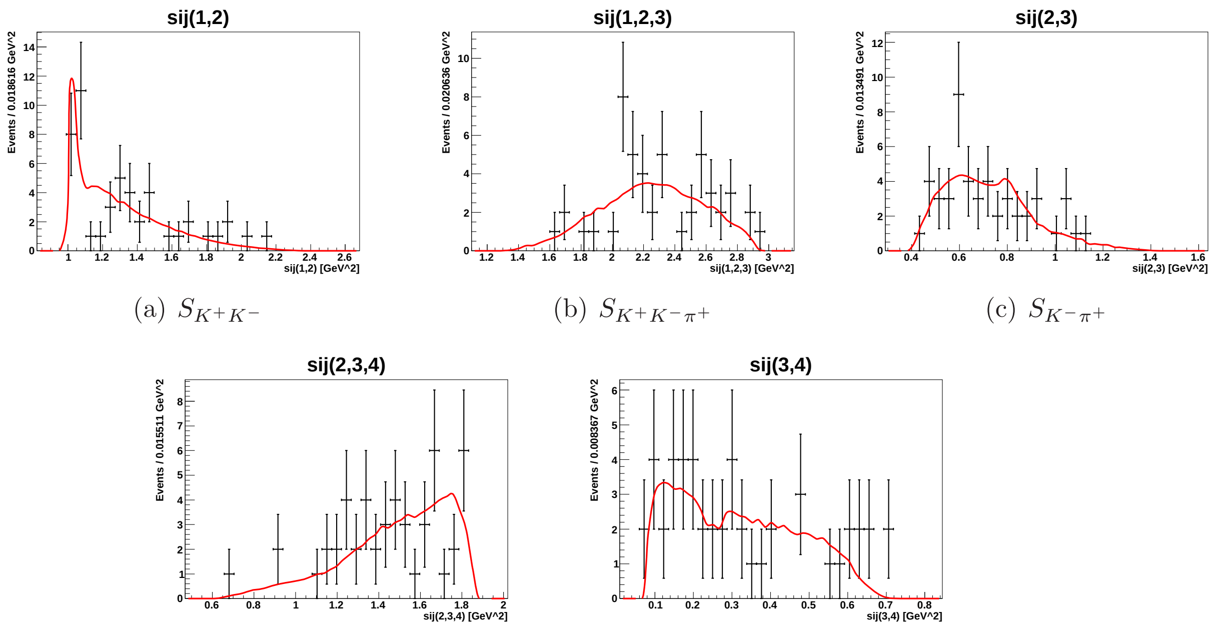

(a) $S_{K^+K^-}$ (b) $S_{K^+K^-\pi^+}$ (c) $S_{K^-\pi^+}$

(d) $S_{K^-\pi^+\pi^-}$ (e) $S_{\pi^+\pi^-}$

Figure 5.8: Projections of fitted result(red) against selected data(black) for the background sample from the "Tagged Flat" sample for all CP modes not involving a K_L particle.

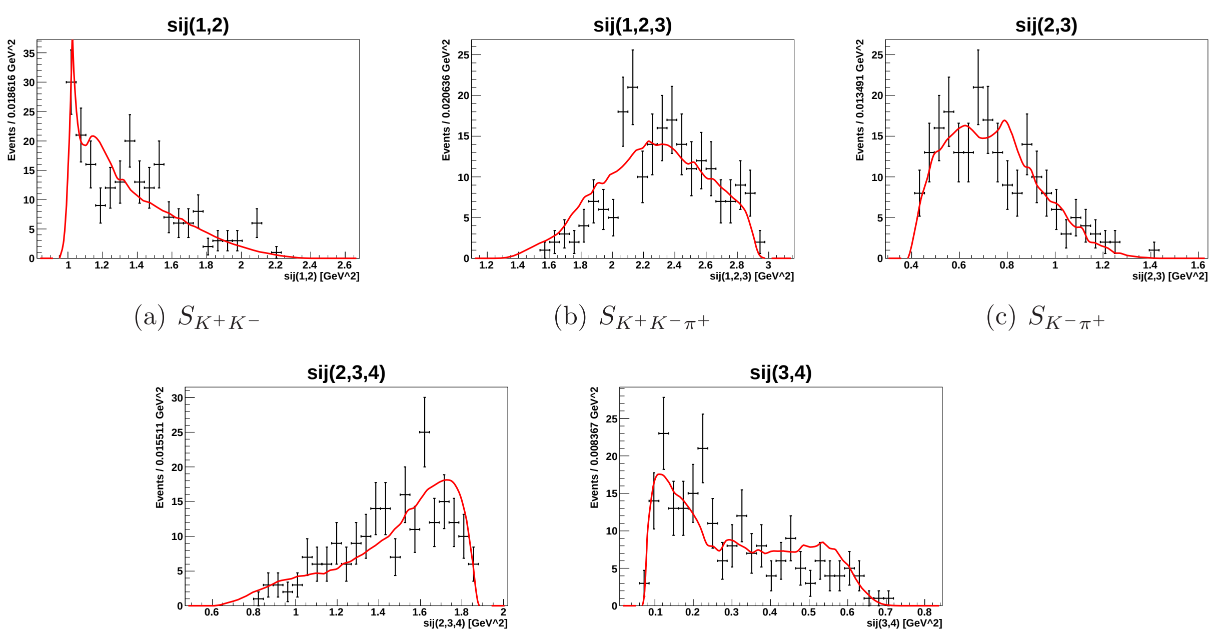

(a) $S_{K^+K^-}$ (b) $S_{K^+K^-\pi^+}$ (c) $S_{K^-\pi^+}$

(d) $S_{K^-\pi^+\pi^-}$ (e) $S_{\pi^+\pi^-}$

Figure 5.9: Projections of fitted result(red) against selected data(black) for the background sample from the "Tagged Flat" sample for all CP modes involving a K_L particle.

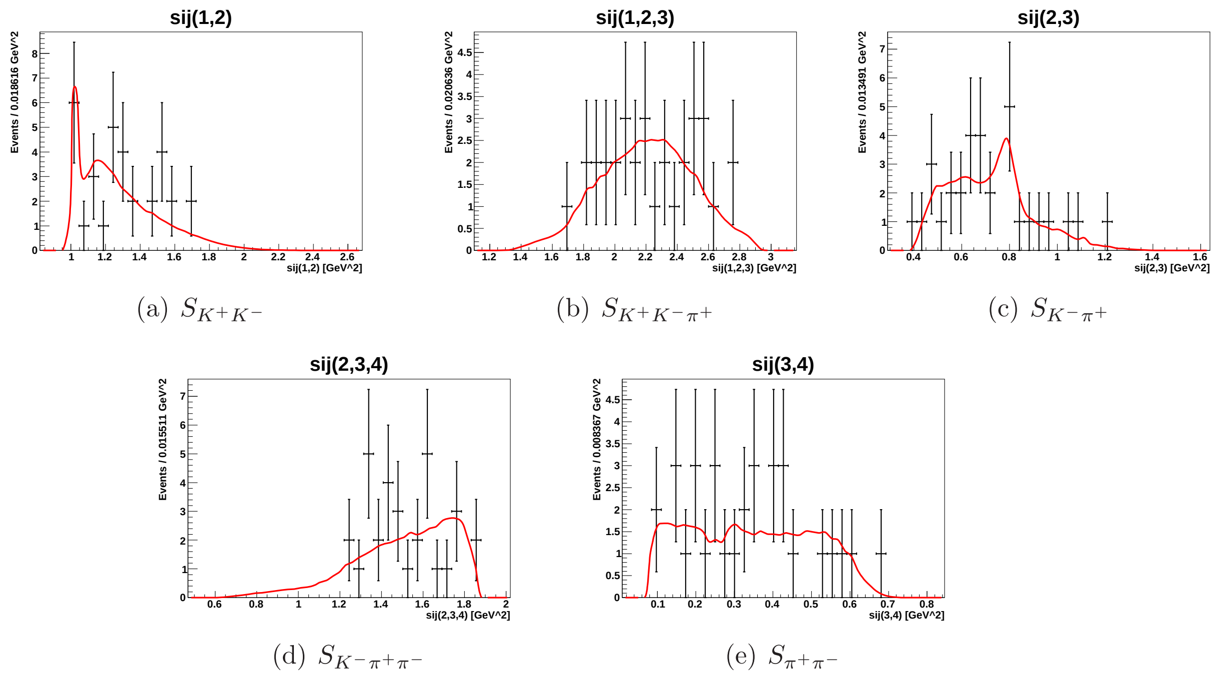

(a) $S_{K^+K^-}$ (b) $S_{K^+K^-\pi^+}$ (c) $S_{K^-\pi^+}$

(d) $S_{K^-\pi^+\pi^-}$ (e) $S_{\pi^+\pi^-}$

Figure 5.10: Projections of fitted result(red) against selected data(black) for the background sample from the "Tagged Peaking" sample for all CP modes not involving a K_L particle.

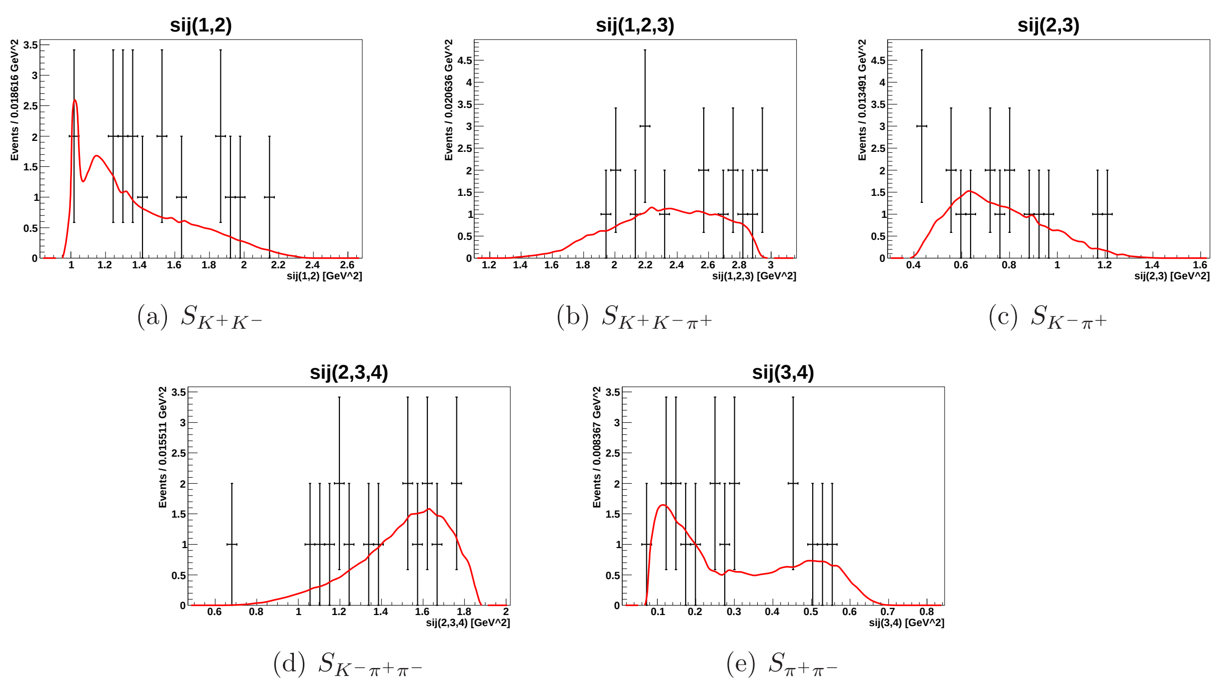

(a) $S_{K^+K^-}$ (b) $S_{K^+K^-\pi^+}$ (c) $S_{K^-\pi^+}$

(d) $S_{K^-\pi^+\pi^-}$ (e) $S_{\pi^+\pi^-}$

Figure 5.11: Projections of fitted result(red) against selected data(black) for the background sample from the "Tagged Peaking" sample for all CP modes involving a K_L particle.

in the same way as was described for the peaking background for the flavour tagged sample. The fitted mass projections are illustrated in figures 5.12 and 5.13.

5.7.4 D^+D^- Background

A sample of D^+D^- background events was collected from the generic Monte Carlo sample. In addition to appearing within the signal box the D^+D^- background also occurs within box C of figure 4.2. The D^+D^- background category was modeled with the PDF of expression 5.27, since it was assumed that the $D^\pm$ decay would follow a similar structure to that of the neutral D decays. A coherent $D^0 \to K^+K^-\pi^+\pi^-$ amplitude model was used to model the decay amplitude, A. The mass projections for the fits to this background sample are illustrated in figures 5.14 and 5.15.

5.7.5 Continuum Background

The continuum Monte Carlo sample was used to collect a sample of events in order to deduce the shape of the continuum background. In addition to appearing within the signal box the continuum background also occurs within box C of figure 5.27. The continuum background was assumed to be comprised of random combinations of K^+, K^-, π^+, π^- and resonant particles and was therefore modeled with an incoherent amplitude model. There was no distinction between different CP tagged modes for the continuum background sample and so the K_L^0 and other modes were not treated separately for this background category. The mass projections for the fits to this background sample are illustrated in figure 5.16.

5.8 Mistagging in Flavour Tagged Samples

In the fit to flavour tagged data in order to account for mistags, the signal PDF was altered to:

$$PDF_{sig} = (1-\omega)|A|^2 + \omega|\overline{A}|^2 \tag{5.28}$$

where A is the amplitude for the $D^0 \to K^+K^-\pi^+\pi^-$ decay, $\overline{A}$ is the corresponding amplitude for the $\overline{D}^0 \to K^+K^-\pi^+\pi^-$ decay and ω is the mis-tag rate. The amplitude for the conjugate decay, $\overline{A}$, is related to that of the D^0 decay, A according to:

$$A(E_{\pi^\pm,K^\pm}, \mathbf{p}_{\pi^+}, \mathbf{p}_{\pi^-}, \mathbf{p}_{K^+}, \mathbf{p}_{K^-}) = \overline{A}(E_{\pi^\mp,K^\mp}, -\mathbf{p}_{\pi^-}, -\mathbf{p}_{\pi^+}, -\mathbf{p}_{K^-}, -\mathbf{p}_{K^+}) \tag{5.29}$$

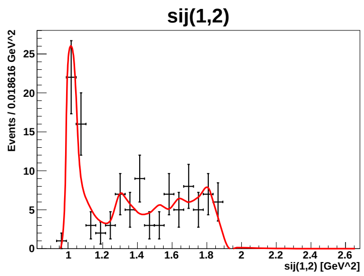

(a) $S_{K^+K^-}$

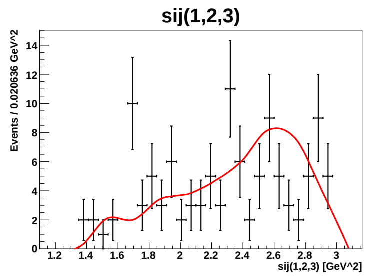

(b) $S_{K^+K^-\pi^+}$

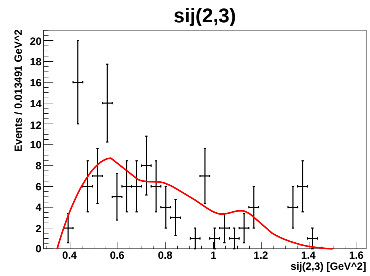

(c) $S_{K^-\pi^+}$

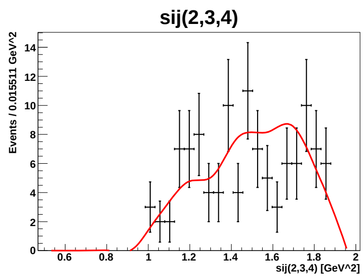

(d) $S_{K^-\pi^+\pi^-}$

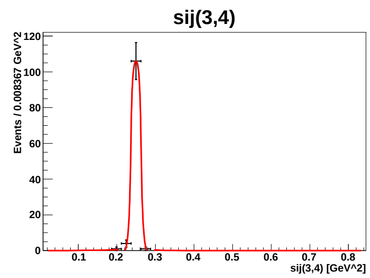

(e) $S_{\pi^+\pi^-}$

Figure 5.12: Projections of fitted result(red) against selected data(black) for the background sample from the "Signal Peaking" sample for all CP modes not involving a K_L particle.

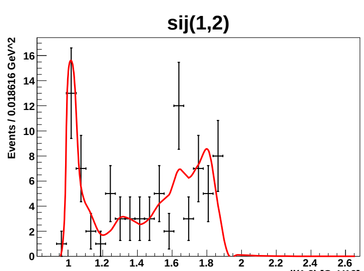

(a) $S_{K^+K^-}$

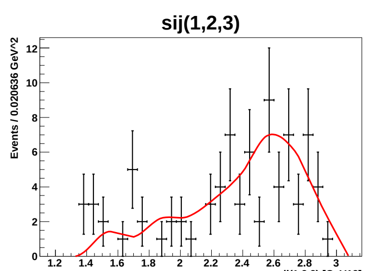

(b) $S_{K^+K^-\pi^+}$

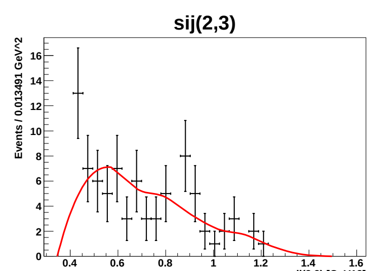

(c) $S_{K^-\pi^+}$

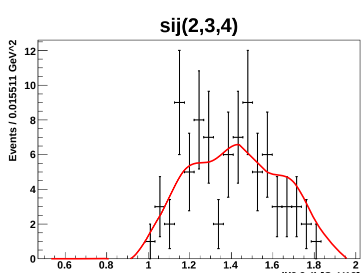

(d) $S_{K^-\pi^+\pi^-}$

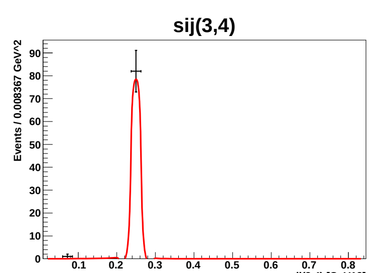

(e) $S_{\pi^+\pi^-}$

Figure 5.13: Projections of fitted result(red) against selected data(black) for the background sample from the "Signal Peaking" sample for all CP modes involving a K_L particle.

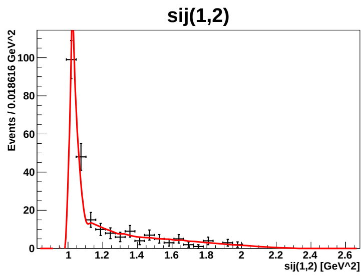

(a) $S_{K^+K^-}$

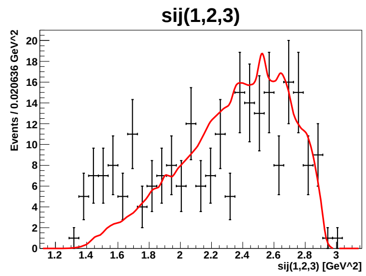

(b) $S_{K^+K^-\pi^+}$

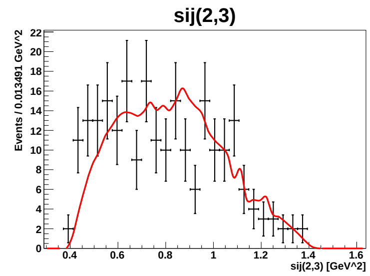

(c) $S_{K^-\pi^+}$

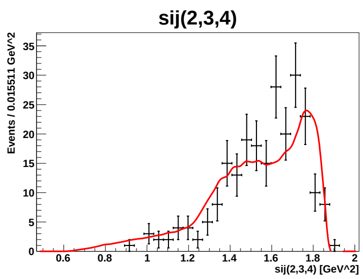

(d) $S_{K^-\pi^+\pi^-}$

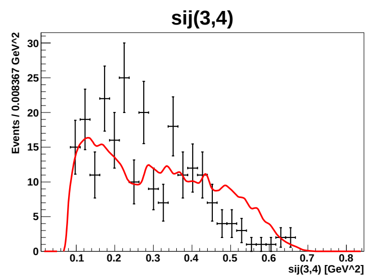

(e) $S_{\pi^+\pi^-}$

Figure 5.14: Projections of fitted result(red) against selected data(black) for the background sample from the D^+D^- sample for all CP modes not involving a K_L particle.

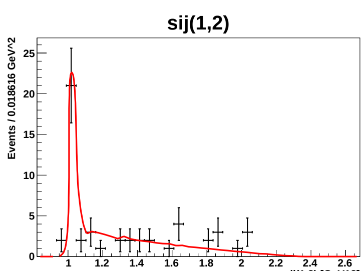

(a) $S_{K^+K^-}$

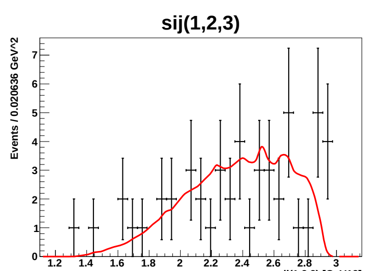

(b) $S_{K^+K^-\pi^+}$

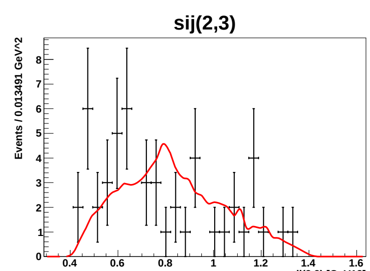

(c) $S_{K^-\pi^+}$

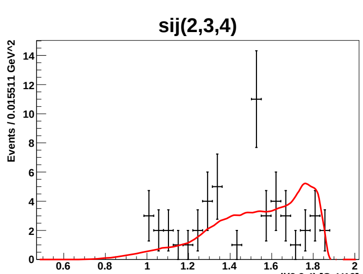

(d) $S_{K^-\pi^+\pi^-}$

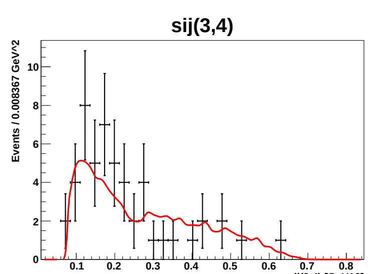

(e) $S_{\pi^+\pi^-}$

Figure 5.15: Projections of fitted result(red) against selected data(black) for the background sample from the D^+D^- sample for all CP modes involving a K_L particle.

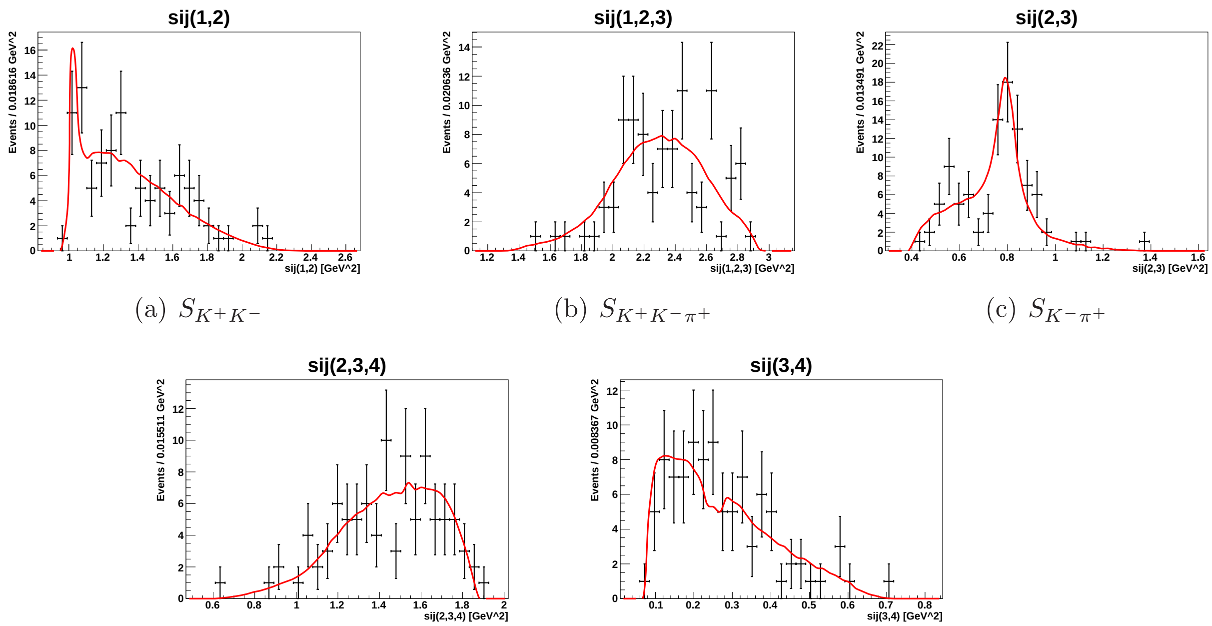

(a) $S_{K^+K^-}$ (b) $S_{K^+K^-\pi^+}$ (c) $S_{K^-\pi^+}$

(d) $S_{K^-\pi^+\pi^-}$ (e) $S_{\pi^+\pi^-}$

Figure 5.16: Projections of fitted result(red) against selected data(black) for the background sample from the “continuum” background sample.

where $E_{\pi,K}$ represents the energies of the daughter particles and $\mathbf{p}_i$ is the three-momentum of particle i.

5.9 Efficiency

It is necessary to account for efficiency and acceptance effects that affect the data distributions. Signal events were not selected with 100% efficiency and there would have been some resolution effects since the momenta of the particles were not measured with perfect accuracy. These effects were likely to vary across the phase space region of signal events and therefore needed to be taken into account when fitting the signal distributions. Two distinct methods were considered in order to account for efficiency effects.

One method for accounting for efficiency effects is to develop an explicit parametrization across the Dalitz space. The explicit efficiency function, may be a function of the four momenta of the mother particle in addition to any of the daughters four momenta. Having established an explicit parametrization for the efficiency function,

ϵ, the signal probability density function which is to be fit is then multiplied by this efficiency function, as detailed in equation 5.12.

An alternative method for accounting for efficiency does not require any explicit parametrization of the efficiency function. From expressions 5.12 and 5.16 the full normalised signal PDF including efficiency is given by:

$$PDF = \frac{\epsilon(p)|A(p,x)|^2 r_4(p)}{\int \epsilon(p)|A(p,x)|^2 r_4(p)dp}, \tag{5.30}$$

where p refers to the four-momenta of the decay particles. However, it is the log-likelihood of the PDF, as given in expression 5.13 which is minimised in terms of the fitted parameters, x. The log-likelihood of equation 5.30 is given by:

$$\begin{aligned} \log(PDF) &= \sum_{events} \Bigg[\log(\epsilon(p)) + \log(r_4(p)) + \log\left(|A(x,p)|^2\right) \qquad (5.31) \\ &- \log\left(\int \epsilon(p)|A(p,x)|^2 r_4(p)dp\right)\Bigg]. \end{aligned}$$

When the derivative of equation 5.31 is taken with respect to the floated parameters, x, the first two terms $\log(\epsilon(p))$ and $\log(r_4(p))$, vanish as they are not dependent on the fit parameters. Thus the efficiency function $\epsilon(p)$ can only affect the fit result through the normalisation term that is the fourth term of expression 5.31.

Therefore in order to account for the efficiency effects the set of Monte Carlo events which are to be used for integrating the signal distribution function have the efficiency function applied to them. This was achieved by passing these generated Monte Carlo events through the detector simulation and reconstruction and applying the selection cuts onto these reconstructed events. The efficiency corrected Monte Carlo events have therefore been generated according to a function relative to phase space, Gen_ϵ which is related to the generating function before acceptance was applied, Gen_b according to:

$$Gen_\epsilon = Gen_b \times \epsilon(p). \tag{5.32}$$

Substituting 5.32 into 5.17 therefore gives the expression:

$$\text{Norm} = \frac{1}{N}\sum_{events}^{N} \frac{\text{Weight}_{event} \times |\text{A}_{event}|^2}{Gen_{b,event}}, \tag{5.33}$$

so that by using the efficiency corrected Monte Carlo events, the efficiency effects are included in the normalisation without requiring an explicit expression for the efficiency function, $\epsilon(p)$ across the Dalitz space.

These efficiency applied Monte Carlo events were then used for the integration of the signal probability density function as given in 5.17. Since the function $\epsilon(p)$ has therefore been included in the normalisation, the factor of ϵ in the numerator of 5.30 may then be omitted without affecting the fit result. This method is advantageous since it does not require any decision as to which variables the efficiency function is most sensitive to and was therefore used in this study.

If the full PDF is comprised of a signal and background as described by equation 5.10 then including normalisation of both signal and background distributions the full PDF may be expressed as:

$$PDF = s \times \frac{\epsilon(p)A(p,x)r_4(p)}{\int \epsilon(p)A(p,x)r_4(p)dp} + (1-s) \times \frac{B(p,x')r_4(p)}{\int B(p,x')r_4(p)dp} \tag{5.34}$$

where x' are the parameters of the background distribution (which are determined prior to the fit to the signal distribution) and $B(p, x')$ is the background distribution. It can be seen that when taking the logarithm of equation 5.34, $\epsilon(p)$ is no longer a common factor to the PDF. Therefore the factor of $\epsilon(p)$ appearing in the numerator of the first expression of 5.34 no longer vanishes in the derivative of the logarithm of 5.34 with respect to the fit parameters x. However it is possible to define the function $B_\epsilon(p, x') = \frac{B(p,x')}{\epsilon}$ so that 5.34 may be rewritten as:

$$\begin{aligned} PDF &= s \times \frac{\epsilon(p)A(p,x)r_4(p)}{\int \epsilon(p)A(p,x)r_4(p)dp} + (1-s) \times \frac{\epsilon(p)B_\epsilon(p,x')r_4(p)}{\int \epsilon(p)B_\epsilon(p,x')r_4(p)dp} && (5.35) \\ &= \epsilon(p)r_4(p) && (5.36) \\ &\times \left[s \times \frac{A(p,x)}{\int \epsilon(p)A(p,x)r_4(p)dp} + (1-s) \times \frac{B_\epsilon(p,x')}{\int \epsilon(p)B_\epsilon(p,x')r_4(p)dp} \right]. \end{aligned}$$

In order to establish a model for the function $B_\epsilon(p, x')$, (as opposed to the function $B(p, x')$), the same efficiency corrected Monte Carlo events were used in order to integrate the background distribution as were used in the integration of the signal distribution function during the fit to the background parameters x'. Once these background parameters, x', have been determined the fit to the signal parameters x may be carried out using the efficiency applied Monte Carlo events to normalise both the background and signal distributions.

This method may trivially be generalised to any number of background distributions. If a number of separate event sets are being fitted such that the log likelihood is given by equation 5.14, the same method may be applied with the appropriate efficiency applied Monte Carlo events used to integrate the PDF corresponding to each event set.

5.9.1 χ^2 Calculation Including the Efficiency Function

It has been explained that the efficiency function, ϵ, of expression 5.37 only impacts the fit result through its occurence in the normalistion factor. Therefore it is possible to use a function $PDF^{'}$, which is related to the true value of the PDF via : $PDF^{'} = PDF/\epsilon$, without affecting the results of the fit. However the value of the PDF is also significant for the χ^2 calculation. In order to account for the efficiency correction when calculating the χ^2 value, the efficiency corrected Monte Carlo events were also used in order to calculate the number of expected events in each χ^2 bin (5.24). These Monte Carlo events were generated with a value relative to phase space of $PDF_{gen,b}$. They were then re-weighted according to the unknown efficiency function, ϵ. Therefore the full generating function of these Monte Carlo events is given by $PDF_{gen,b}\epsilon$. Equation 5.25 may then be rewritten in terms of the functions PDF' and PDF_{gen}:

$$MC_{weight}(event_i) = \frac{|A(event_i)|^2\epsilon(event_i) \times r_4(event) \times \text{Weight}(event)}{PDF_{gen,b}(event_i)\epsilon(event_i)} \quad (5.37)$$

$$= \frac{PDF^{'}(event_i) \times r_4(event) \times \text{Weight}(event)}{PDF_{gen,b}(event_i)}. \quad (5.38)$$

Thus it can be seen that if the efficiency corrected Monte Carlo events are used in order to estimate the number of expected events in each χ^2 bin, then the value of ϵ may again be omitted from the numerator of the expression for the full PDF (5.37) when calculating the χ^2 value. In this manner no explicit function for the efficiency function is required.

5.9.2 Monte Carlo approximation of Efficiency Function

In the case of the CLEO-c and CLEO III data sets, unweighted $D \to K^+K^-\pi^+\pi^-$ events were generated using the MINT generator according to a simple resonant model, which approximated the signal distribution. Using a model which approximated the peaking structure of the signal events ensured that the best precision in efficiency determination was obtained in the regions of phase space in which most of the signal events were concentrated.

These events were then inserted into the CLEO Monte Carlo program for each of the relevant detector configurations and decay chains. In each case the initial decay chain from which the D^0 originated was generated by the CLEO MC system. The MINT generated decay particles were then Lorentz boosted into the frame of this mother D^0 and inserted into the Monte Carlo decay tree prior to the detector simulation, reconstruction and selection. The MINT generator PDF value was stored for each event, as this was required for the normalisation (as shown in equation 5.16).

Having been passed through the detector simulation and reconstruction the events were selected using the same cuts that were applied to the signal events. Approximately one million selected events were collected and used in order to integrate each signal and background distribution for the corresponding data set. The precision obtained for each of the datasets using the one million events for normalisation was 0.003.

It was not possible to follow the same procedure in the CLEO-II.V analysis as the CPU resources of the platforms on which the CLEO-II.V simulation ran were inadaquate to process a sufficient number of events in an acceptable period of time.

Instead it was decided to use CLEO-II.V Monte Carlo only to measure the efficiencies as a function of momentum as this procedure requires many fewer events. The efficiency corrected CLEO-III integration events were then re-weighted on an event by event basis according to:

$$W = \frac{\epsilon_2(p_{\pi^+})\epsilon_2(p_{\pi^-})\epsilon_2(p_{K^+})\epsilon_2(p_{K^-})}{\epsilon_3(p_{\pi^+})\epsilon_3(p_{\pi^-})\epsilon_3(p_{K^+})\epsilon_3(p_{K^-})} \tag{5.39}$$

where W is the applied weight of the event (as appears in expressions 5.16 and 5.38) and $\epsilon_{2,3}(P_{\pi,K})$ is the efficiency ratio as a function of the momentum of the pion or kaon for the CLEO II.V or III dataset respectively. These reweighed events were then used as integration events and in the χ^2 calculation for this data set as previously described.

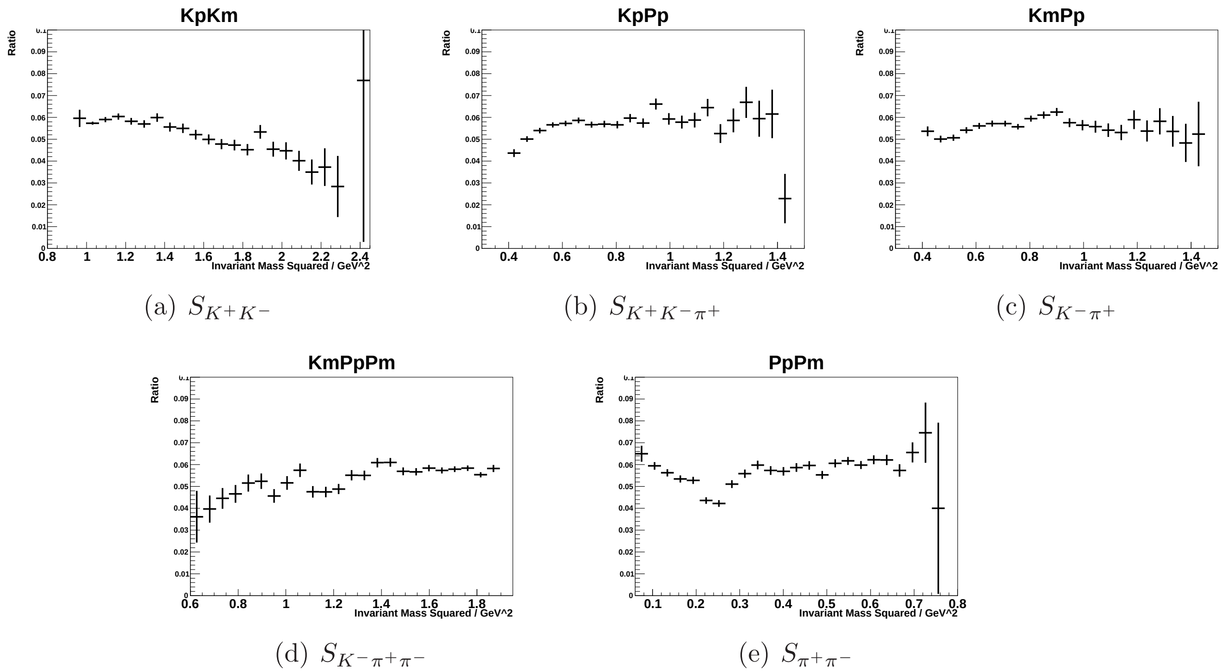

(a) $S_{K^+K^-}$ (b) $S_{K^+K^-\pi^+}$ (c) $S_{K^-\pi^+}$

(d) $S_{K^-\pi^+\pi^-}$ (e) $S_{\pi^+\pi^-}$

Figure 5.17: The event select efficiency in terms of the mass projections for the CLEO-III dataset.

Since the CLEO-II.V and CLEO-III datasets were collected at the same collision energy and with detector configurations that were very similiar the weighting procedure provided only a small correction to the efficiency (the weights, W which were applied had a mean of 0.866 and a standard deviation of 0.036). The efficiency corrected integrated events were also used to integrate the PDF relating to the relevant background samples. The efficiency ratios for the CLEO-III, and CLEO-c datasets, and the ratios $\frac{\epsilon_2(p_i)}{\epsilon_3(p_i)}$ for the CLEO-II.V datasets are illustrated in figures 5.17, 5.18, 5.19 and 5.20.

5.9.3 Summary

In this chapter the model which is going to be used to describe the signal decay is explained. The method for accounting for the backgrounds to each of the datasets is explained, and the final models for each of these background components has been shown. The method for accounting for efficiency has also been described, and the efficiency distributions for each of the flavour tagged datasets are illustrated in figures 5.17, 5.18, 5.19 and 5.20. The method via which this model has been implimented in the fitter has also been described in detail.

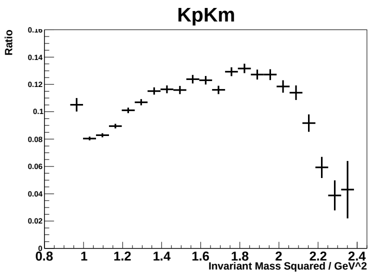

(a) $S_{K^+K^-}$

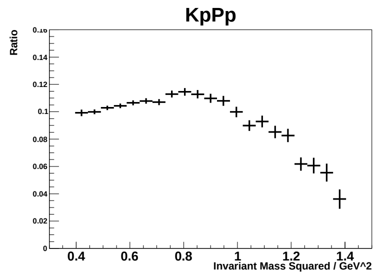

(b) $S_{K^+K^-\pi^+}$

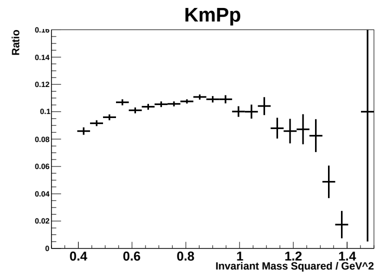

(c) $S_{K^-\pi^+}$

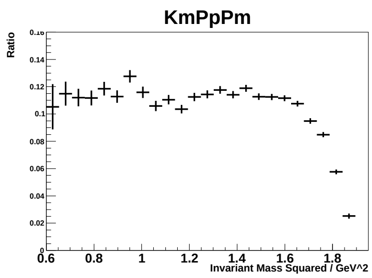

(d) $S_{K^-\pi^+\pi^-}$

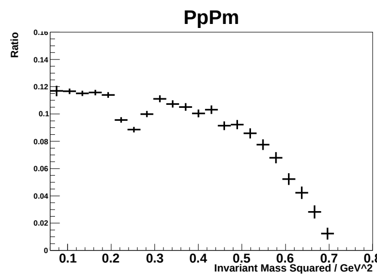

(e) $S_{\pi^+\pi^-}$

Figure 5.18: The event select efficiency in terms of the mass projections for the 3770 dataset.

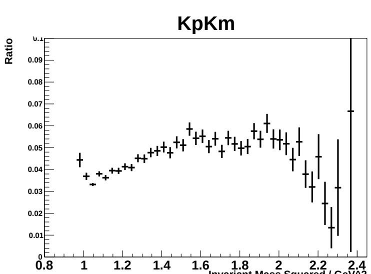

(a) $S_{K^+K^-}$

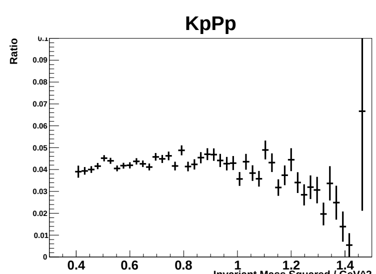

(b) $S_{K^+K^-\pi^+}$

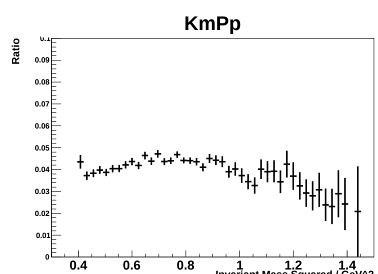

(c) $S_{K^-\pi^+}$

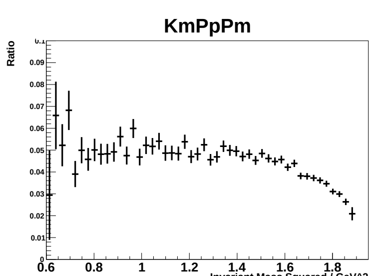

(d) $S_{K^-\pi^+\pi^-}$

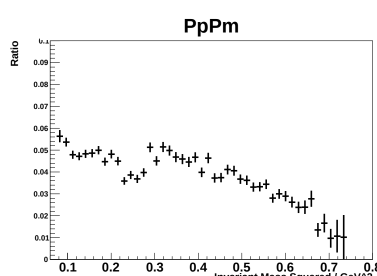

(e) $S_{\pi^+\pi^-}$

Figure 5.19: The event select efficiency in terms of the mass projections for the 4170 dataset.

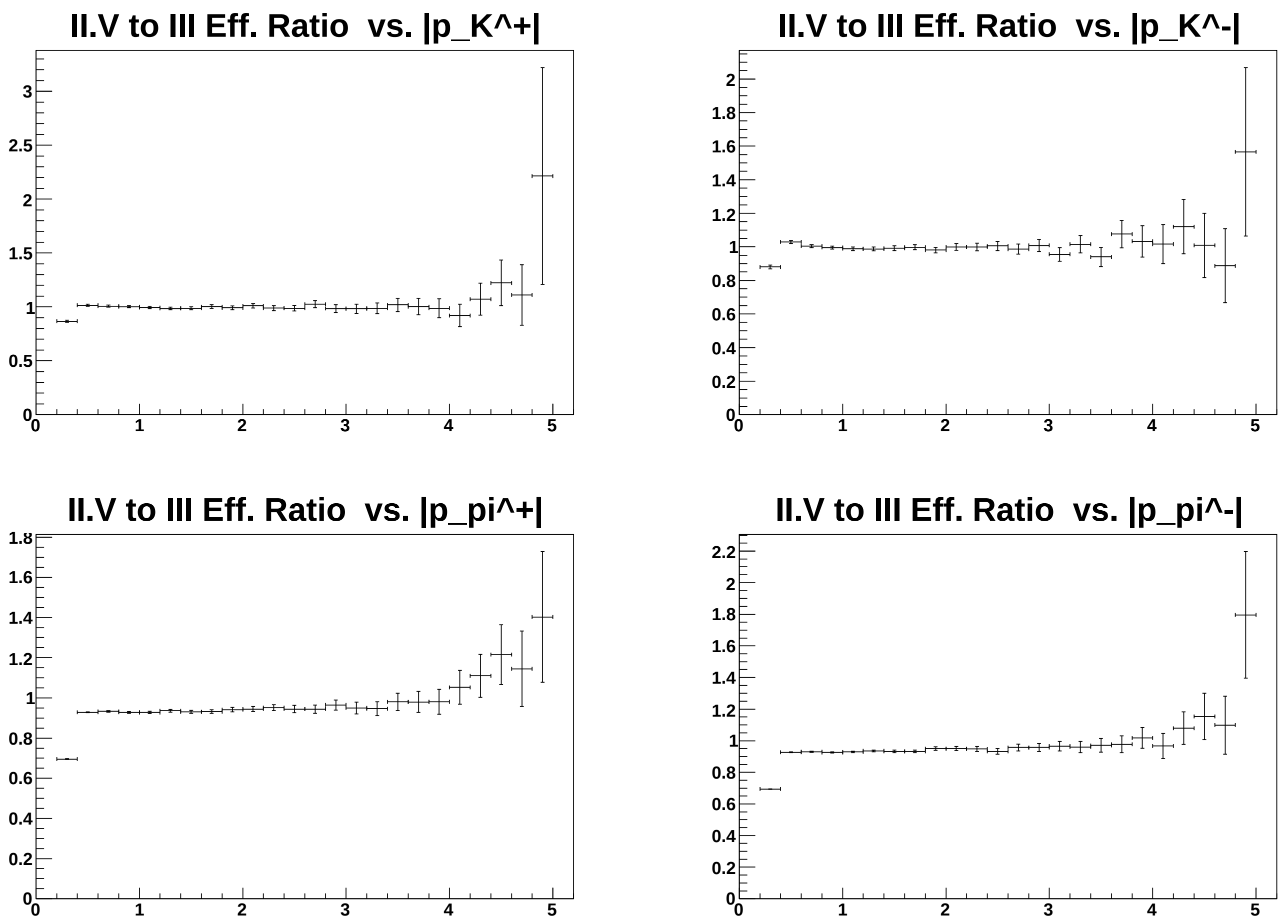

Figure 5.20: The CLEO-II.V dataset: Ratios of CLEO-II.V to CLEO-III selection efficiency ($\frac{\epsilon_2(p)}{\epsilon_3(p)}$) as a function, of particle momentum.The x-axis gives the momentum of the particle in units of $\frac{\mathrm{GeV}^2}{c^2}$ and the y-axis gives the ratios of the efficiency of CLEO-II.V to CLEO-III.

Chapter 6

Building the Amplitude Model

6.1 Introduction

In this chapter the construction of the final model is described. In particular the modelling of the CP tagged datasets is desribed. The various categories of decay topologies which are used to describe the signal decay are described and justified. A validation test of the fitting procedure is provided and the evaluation of the systematic effects is given.

6.2 The Datasets

In total four flavour tagged datasets (described in section 4.1) and four CP tagged data sets (described in section 4.4), totaling 3870 events, are used in this study as summarised in table 6.2.

The signal distribution of each dataset is sensitive to the amplitude, A of the decay $D^0 \rightarrow K^+K^-\pi^+\pi^-$ and the conjugate amplitude $\overline{A}$ for the decay $\overline{D}^0 \rightarrow K^+K^-\pi^+\pi^-$ which is assumed to be related to A via expression 5.29. In the case of the flavour tagged data sets the signal PDF is given by expression 5.28. The signal PDF of the pure CP tagged datasets are given by expressions 6.6 and 6.8 and the "pseudo tagged" dataset have a signal PDF which is modeled by the expression 6.10. The efficiency effects for each dataset are accounted for by using the corresponding efficiency corrected integration events as described in chapter 5. The amplitude A is described by an isobar model as given in expression 5.1. The complex amplitudes a_i as described in 5.1 are determined in a simultaneous fit to all data sets. The complex amplitudes are fitted in terms of their Cartesian components (the real and imaginary parts) as opposed to polar coordinates, since this avoids unwanted "edge effects" for amplitudes with a phase close to zero which may be either positive or negative.

In addition to the complex amplitudes, two additional parameters are included in the fit which determine the proportion of $K_S^0K^+K^-$ peaking background events in the two CLEO-c flavour tagged datasets. The fit uses the MINUIT package to maximize the log likelihood defined by expression 5.14, as described in chapter 5.

Data Set	**Number of Selected Events**	**Purity of Sample**
CLEO-II.V	279	$74.0 \pm 3.0\%$
CLEO-III	1225	$89.2 \pm 0.4\%$
$\psi(3770)$	1396	$83.9 \pm 0.7\%$
$\psi(4170)$	739	$65.1 \pm 1.2\%$
$K_L^0\pi^+\pi^-$	87	$79.8 \pm 2.6\%$
$K_S^0\pi^+\pi^-$	63	$83.1 \pm 6.2\%$
CP Even	49	$63.4 \pm 1.7\%$
CP Odd	32	$84.0 \pm 1.4\%$
Total	**3870**	$\mathbf{80.9 \pm 0.4\%}$

Table 6.1: Number and purity of selected events in each data set.

6.2.1 Fit Quality

In order to provide a measure of the quality of the fit to the combined data sets a χ^2 value is calculated for each of the flavour tagged data sets as described in chapter 5. The average χ^2 value per bin, χ^2_{bin} for each dataset is given by the expression:

$$\chi^2_{bin} = \frac{1}{N_{bins}} \sum_{bin} \frac{(N_{expected} - N_{events})^2}{N_{expected}}. \tag{6.1}$$

In the case of the CP tagged data sets there are not sufficient events to calculate a reliable χ^2 value, therefore only the flavour tagged data sets are used in the χ^2 calculation. The χ^2 value for the combined fit to all data sets is then calculated:

$$\chi^2_{DOF} = \frac{1}{(\sum_i (N_{Bins,i} - 1) - N_{parameters})} \Sigma_i \chi^2_i \times N_{Bins,i} \tag{6.2}$$

where $N_{Bins,i}$ represents the number of χ^2 bins in the data set i, $N_{expected}$ gives the number of events expected in a given bin according to the PDF and N_{events} gives the number of data events which falls within the bin, χ^2_i represents the χ^2 value per bin for data set i and $N_{parameters}$ gives the total number of fitted parameters.

6.3 CP Tagged Rates

As shown in table 6.2, 6% of the data used for this study is comprised of CP tagged data collected at the centre of mass energy of the $\psi(3770)$ resonance. $D^0\overline{D}^0$ pairs are produced at this centre of mass energy via a virtual photon. The system $e^+e^- \rightarrow \psi(3770) \rightarrow D^0\overline{D}^0$ is a quantum correlated system [83] with definite CP quantum number $\mathbf{C} = -1$. The decay rate (Γ_{ij}) of the decay, $D_1 \rightarrow i$,$D_2 \rightarrow j$ of the CP odd $D^0\overline{D}^0$ system may be described by the antisymmetric matrix, $\mathcal{M}_{ij}$ [84]:

$$\Gamma_{ij} = |\mathcal{M}_{ij}|^2 \tag{6.3}$$

$$\mathcal{M}_{ij} = A_i\overline{A}_j - A_j\overline{A}_i \tag{6.4}$$

where A_i gives the amplitude for the $D^0 \rightarrow i$ decay and $\overline{A}_i$ gives the amplitude for the $\overline{D}^0 \rightarrow i$ decay. One may then consider the case where i is the final state of interest, $K^+K^-\pi^+\pi^-$, and j is a particular CP state.

6.3.1 Pure CP Tags

In the case that j is a CP even state so that $A_j = \overline{A}_j$, considering 6.4, the normalised amplitude for the $D \rightarrow K^+K^-\pi^+\pi^-$ decay will then be given by the usual CP odd amplitude:

$$\Gamma_{odd} = |A_{odd}|^2 \tag{6.5}$$

$$A_{odd} = \frac{1}{\sqrt{2}}(A - \overline{A}), \tag{6.6}$$

and for the case in which i is a CP odd state such that $A_j = -\overline{A}_j$ the rate will be given by the usual CP even amplitude:

$$\Gamma_{even} = |A_{even}|^2 \tag{6.7}$$

$$A_{even} = \frac{1}{\sqrt{2}}(A + \overline{A}), \tag{6.8}$$

where A ($\overline{A}$) is the amplitude of the $D^0 \to K^+K^-\pi^+\pi^-$ ($\overline{D}^0 \to K^+K^-\pi^+\pi^-$) decay. This is expected since when the "other side" D is reconstructed in an even (odd) CP state, the decay of interest must be in an odd (even) state, in order to conserve the over all CP odd state of the system.

6.3.2 "Admixture" CP Tags

One may also consider the case where the final state j is a state consisting of an admixture of CP even and CP odd states. In particular the three body states $K^0_S\pi^+\pi^-$ and $K^0_L\pi^+\pi^-$, which have been studied extensively in a previous CLEO measurement [82] . In these cases the decay rate of the decay of interest is dependent on both the region of the $K^+K^-\pi^+\pi^-$ phase space for the signal and the region of the $K_{L,S}\pi^+\pi^-$ Dalitz plane in which the tag decay occurs. Considering equations 6.3 and 6.4 the decay rate to such a state would be given by:

$$\begin{aligned}\Gamma &= |A_i|^2|\overline{A}_j|^2 + |A_j|^2|\overline{A}_i|^2 - (A_i\overline{A}_i^* A_j^*\overline{A}_j + A_j\overline{A}_j^* A_i^*\overline{A}_i) \qquad (6.9)\\ &= \Gamma_j|\overline{A}_i|^2 + \Gamma_{\overline{j}}|A_i|^2 - 2\sqrt{\Gamma_j\Gamma_{\overline{j}}}[\cos\theta_j Re(A_i\overline{A}_i^*) + \sin\theta_j Im(A_i\overline{A}_i^*)]\end{aligned}$$

where Γ_j ($\Gamma_{\overline{j}}$) gives the decay rate of the $D^0 \to K_{L,S}\pi^+\pi^-$ ($\overline{D}^0 \to K_{L,S}\pi^+\pi^-$) decay and θ_j gives the relative argument of the two decays amplitudes: $\theta_j = Arg(\frac{A_j}{\overline{A}_j})$. Therefore in order to use these admixture tagged decays to determine a model for the $D \to K^+K^-\pi^+\pi^-$ decay external information of the $D \to K_{L,S}\pi^+\pi^-$ decay is required.

In this study, in order to account for the $K_{L,S}\pi^+\pi^-$ decay a binned analysis of $K_{L,S}\pi^+\pi^-$ is used, [82]. In [82] the $K_{L,S}\pi^+\pi^-$ Dalitz plane was defined by the variables $m_+^2 = m^2_{K^0_S\pi^+}$ and $m_-^2 = m^2_{K^0_S\pi^-}$. The Dalitz plane was divided in half along the line $m_-^2 = m_+^2$. The upper half of the Dalitz plot ($m_-^2 > m_+^2$) was divided into 8 bins labeled $n = 1$ to $n = 8$. The bins in the lower half of the Dalitz plot, labeled $n = -1$ to $n = -8$ are defined symmetrically, so that if an event with Dalitz variables $(m_+^2, m_-^2) = (x, y)$ fell into bin i an event with $(m_+^2, m_-^2) = (y, x)$ would fall into bin $-i$. This binning is illustrated in figure 6.1.

The expected number of $D^0 \to K_{L,S}\pi^+\pi^-$ events falling into each bin, K_n, in addition to the bin averaged values of $\cos\theta = C_n$ and $\sin\theta = S_n$, were published in this study [82] for both $K^0_S\pi^+\pi^-$ and $K^0_L\pi^+\pi^-$.

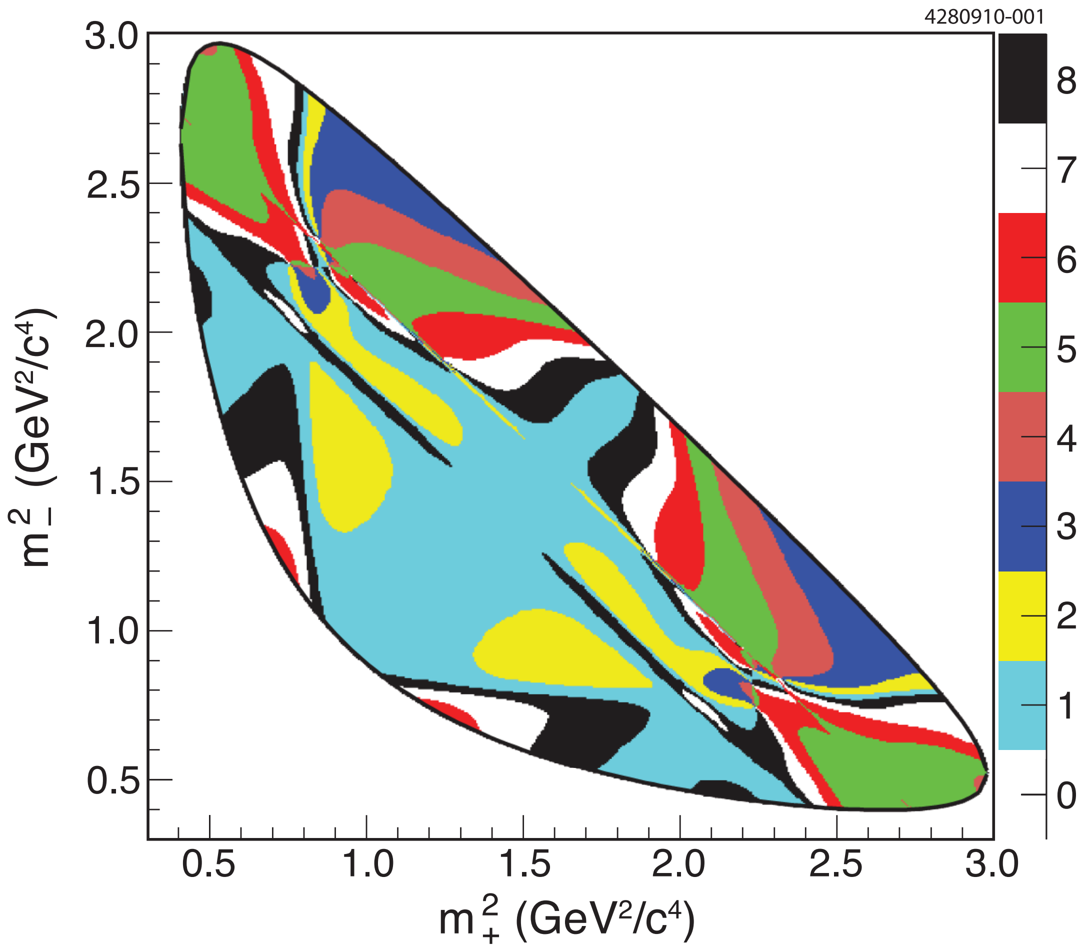

Figure 6.1: Plot illustrating the sixteen bins of the $K^0_{S,L}\pi^+\pi^-$ Dalitz space.

Due to the symmetry of the Dalitz binning it may be noted that $S_{-i} = -S_i$, $C_i = C_{-i}$ and the expected number of $\overline{D}^0 \rightarrow K_{L,S}\pi^+\pi^-$ events expected in bin i is given by K_{-i}.

In reference [82], several choices of bins were considered. The binning used in this thesis is the so called 'equal δ_D' binning, in which the bins in each half the Dalitz plane were chosen such that there is an equal division in strong phase difference across the bins.

Therefore for the $K_{L,S}\pi^+\pi^-$ vs $D \rightarrow K^+K^-\pi^+\pi^-$ data collected for this study the Dalitz bin, n into which the other side $K_{L,S}\pi^+\pi^-$ fell is recorded for each event. The rate equation 6.10 is then approximated with:

$$\Gamma \quad \propto \quad N_n|\overline{A}|^2 + N_{-n}|A|^2 - 2\sqrt{N_n N_{-n}}[C_n Re(A\overline{A}^*) + S_n Im(A\overline{A}^*)] \quad (6.10)$$

where the subscript i has now been dropped and N_n gives the predicted number of

$K_{L,S}\pi^+\pi^-$ events per unit of Dalitz area in a given bin, n (i.e. $N_n = K_n/a_n$, where a_n is the Dalitz area of bin n). The normalisation of expression 6.10 is given by the sum of the normalisations of each of the four terms. Each product of $D \to K^+K^-\pi^+\pi^-$ amplitudes A^*A, $\overline{A}^*\overline{A}$ and $\overline{A}^*A$ may be normalised as illustrated in expression 5.21. In general the product $A\overline{A}^*$ is complex and normalisations of the real and imaginary parts of this product are given by the real and imaginary parts respectively of the normalisation of the complex product.

6.4 The D^0 Decay Model

A large number of intermediate resonances can in principle contribute to the decay and it is the purpose of this analysis is to find that combination that best describes the data.

6.4.1 Angular Momentum States

For some decay topologies there are also a number of different angular momentum states which may occur within a given decay chain. The angular momentum of the final state particles affects the decay amplitude via the spin factor term of expression 5.2.

Three of the possible general resonant and non-resonant decay topologies are as follows:

$$D \;\to\; R_1(P_1P_2)P_3P_4 \tag{6.11}$$

$$D \;\to\; R_1(P_1P_2)R_1^{'}(P_3P_4) \tag{6.12}$$

$$D \;\to\; P_1P_2P_3P_4 \tag{6.13}$$

where $R_1^{(')}$ represents a spin 1 resonance and P_i represent a final state pseudoscalar meson ($K^\pm, \pi^\pm$). An example of decay 6.11 is $D^0 \to \phi(K^+K^-)\pi^+\pi^-$. An example of decay 6.12 is $D^0 \to \phi(K^+K^-)\rho(\pi^+\pi^-)$. The final state particles may exist in a state of relative angular momentum with each other. The relative angular momentum of the final state particles may combine in more than one configuration while satisfying overall angular momentum conservation. In this study relative angular momentum values of up to $l = 2$ between pairs of particles are considered.

For example in the case of configuration 6.11 the particles P_3P_4 may have a relative angular momentum state of $l = 1$ or $l = 2$ while conserving the overall angular momentum in the decay (in the case that the particles P_3P_4 are in a relative angular momentum state $l = 2$ there must be a relative angular momentum of $l = 1$ between the resonance R_1 and the P_3P_4 system). Similarly in the case of the decay 6.12 the resonances R_1 and R_1' may exist in one of three relative angular momentum states (S-wave, P-wave or D-wave). Each of these possible angular momentum states is considered in this study.

In the case of the entirely non resonant decay (6.13) there are three possible configurations in which the final state particles can form pairs. Depending on the relative angular momentum within each pair of particles, the pairs of particles may then have a relative angular momentum between them. This possibility is also considered in the current study.

Several spin two resonances are also considered when building the model. The relative orbital angular momentum of these resonances with other decay particles is allowed for in the same manner as described above.

The full list of resonances and relative angular momentum states which are considered can be found in appendix C.

6.4.2 Converging on a Final Model

With such a large number of possible resonant contributions it is not practical for fits to be carried out using all possible configurations of resonances. It is therefore necessary to develop a strategy for determining the most likely configurations of resonances to produce a good fit to the data. By inspection of the mass projections of the data distributions certain features are sufficiently evident to necessitate including a core set of baseline resonances in most models. In particular, the following resonant features need to be included:

1. A $\phi(1020)$ resonance,

2. A $\rho(770)$ resonance,

3. A $K^*(892)$ resonance,

4. A high mass hadronic state such as a $K_1^-(1270)$, $K_1^-(1400)$ or a $K^-(1680)$ resonance.

These features are illustrated in the example of the flavour tagged 3770 sample in figures 6.2, 6.3, 6.4 and 6.5.

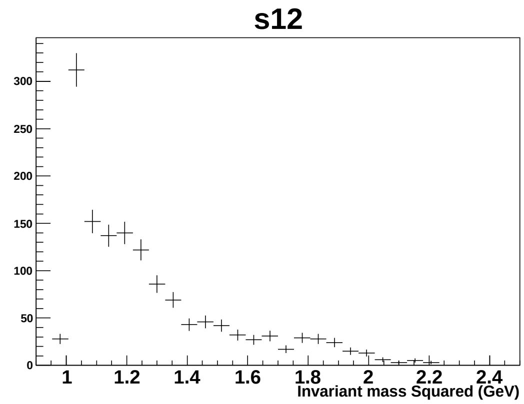

Figure 6.2: Flavour tagged 3770 sample. K^+K^- invariant mass squared projection. A clear ϕ peak is visible at $s_{12} \approx 1$ GeV^2.

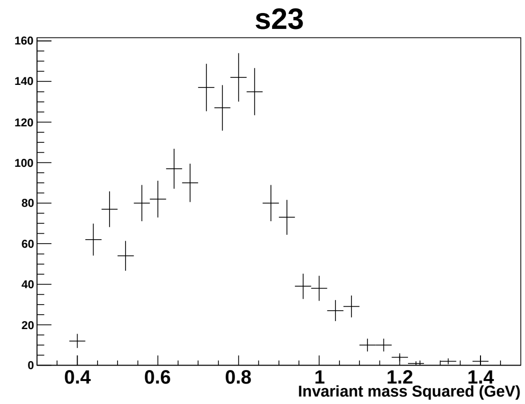

Figure 6.3: $K^-\pi^+$ invariant mass squared projection. A clear $K^*(892)$ peak is visible at $s_{23} \approx 0.8$ GeV^2.

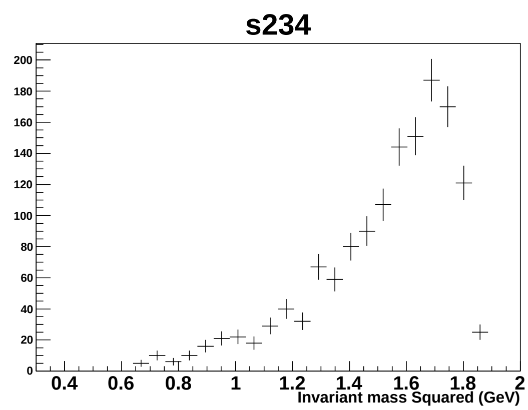

Figure 6.4: $K^-\pi^+\pi^-$ invariant mass squared projection. A peak is visible towards the upper edge of the phase space, this may be due to a $K_1^-(1270)$, a $K_1^-(1400)$ or a $K^-(1680)$ resonance.

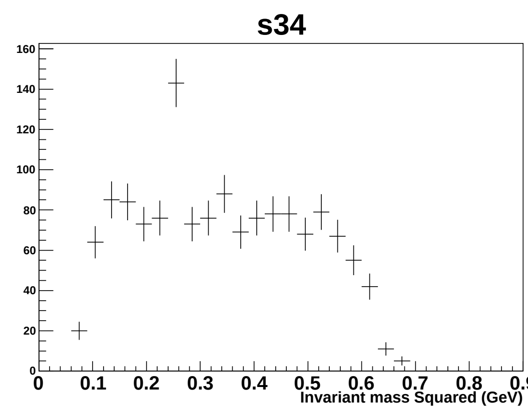

Figure 6.5: $\pi^+\pi^-$ invariant mass squared projection. The narrow peak at $s_{34} \approx 0.25$ GeV^2 is due to the $K_S^0(\pi^+\pi^-)K^+K^-$ background. There is a broad resonant structure spanning most of the mass projection due to the ρ resonance.

All possible decay topologies are therefore categorized into five broad categories:

1. All decay topologies which include a $\phi(1020)$ resonance,

2. All decay topologies which include a $\rho(770)$ resonance,

3. All decay topologies which include a $K^*(892)$ resonance,
4. All decay topologies which include a $K_1^-(1270)$, $K_1^-(1400)$ or a $K^-(1680)$ resonance,
5. All entirely non-resonant topologies,
6. All other decay topologies.

Some of the decay topologies are self conjugate (for example $D \to \phi(1020)\pi^+\pi^-$) however all those which are not self conjugate are considered alongside their conjugate decay topology. For example if the decay topology $K_1(1270)^+(\to \rho(770)K^+)K^-$ is included in the fit model the conjugate decay $\overline{K_1}(1270)^-(\to \rho(770)K^-)K^+$ is also included.

Some decay topologies fell into more than one category; for example the decay $K_1(1270)^+(\to K^*(892)\pi^+)K^-$ contains both a $K_1(1270)$ resonance and a $K^*(892)$ resonance.

Permutations of isobar components are then formed which contained six decay topologies (including conjugate topologies where applicable) with at least one unique decay topology from each of the first four categories.

Combined fits are carried out on all datasets with each of these permutations. Each fit that is carried out is ranked according to its χ^2_{DOF}. The best five models are then considered further. For each of the five best models new models are formed by adding one decay topology (which is not already present in the model) from the first five categories to the model one at a time, discarding any repetitions. The new models formed in this way are then fit to the data.

After each new set of models are fit, all of the models (from each iteration of fits) are again ranked according to their χ^2_{DOF}. This process is repeated iteratively until the best five models remained the same from one iteration to the next.

At this stage, for each of the five best models a decay topology from the sixth category is added, one at a time, to form a new set of models which are then fit.

In the final stage the best 50 models are considered. For each of these models any decay topology which has a fit fraction of less than 5% is removed, one at a time from the model. In the case of models with more than one component with a fit fraction of less than 5%, models are formed with all possible permutations of the small components removed. (In the case of a model with n components with fit fractions of less than 5%, n new models are formed with each of these components removed in turn, then ${}^nC_2$ new models would be formed by removing two of the small components at a time etc.). The resulting models are then fit to the data samples.

All of the fits that had been carried out during this process are then ranked according to the χ^2_{DOF}. The fit fractions for the best 8 models are illustrated in table 6.2. From table 6.2 it may be noted that a number of configurations of resonances produce a similarly good level of agreement with the data. However these best 8 models showed a good qualitative agreement in the components which they contain and the levels (as described by their fit fractions) to which each resonant and non resonant components contributed to the signal PDF. In particular the first and second columns agree entirely to within errors except for the inclusion of the component $\overline{K_1}(1270)^-(\rightarrow \overline{K_0}^*(892), \pi^-), K^+$ for the model in column 2. Since the χ^2_{DOF} of model 2 is not significantly worse than that of the first model, but had the advantage of including a conjugate decay mode for each decay model that contributed to the model, it is decided to adopt model 2 as the final choice.

	1	2	3	4	5	6	7	8
$K_1(1270)^+(\to K^*(892),\pi^+),K^-$	0.073±0.008	0.073±0.008	0.070±0.008	0.070±0.008	0.070±0.008	0.070±0.008	0.087±0.009	0.067±0.008
$\overline{K_1}(1270)^-(\to \overline{K_0}^*(892),\pi^-),K^+$	-	0.009±0.003	0.007±0.003	0.008±0.003	0.008±0.003	0.009±0.003	0.017±0.005	0.008±0.003
$K_1(1270)^+(\to \rho(770),K^+),K^-$	0.047±0.008	0.047±0.008	0.047±0.007	0.048±0.007	0.046±0.007	0.060±0.008	0.051±0.007	0.068±0.011
$\overline{K_1}(1270)^-(\to \rho(770),K^-),K^+$	0.058±0.007	0.060±0.008	0.058±0.007	0.059±0.007	0.060±0.008	0.037±0.008	0.063±0.008	0.035±0.008
$K^+(1410)(\to K^*(892),\pi^+),K^-$	0.044±0.008	0.042±0.007	0.042±0.007	0.034±0.007	0.042±0.007	0.042±0.007	-	0.041±0.007
$\overline{K^-}(1410)(\to \overline{K^*}(892),\pi^-),K^+$	0.052±0.007	0.047±0.007	0.045±0.006	0.029±0.006	0.045±0.006	0.047±0.006	-	0.045±0.006
$K^*(892),(K^-,\pi^+)_P$ P wave	-	-	-	-	-	-	0.039±0.007	-
$\overline{K^*}(892),(K^+,\pi^-)_P$ P wave	-	-	-	-	-	-	0.030±0.005	-
$K^*(892)\overline{K^*}(892)$ S wave	0.058±0.008	0.061±0.008	0.061±0.008	0.061±0.008	0.061±0.008	0.063±0.008	0.042±0.006	0.063±0.008
$K^*(892)\overline{K^*}(892)$ P wave	-	-	-	0.009±0.003	-	-	-	-
$\phi(1020),(\pi^+,\pi^-)_S$ P wave	0.101±0.010	0.103±0.010	0.090±0.009	0.091±0.009	0.096±0.010	0.101±0.009	-	0.089±0.009
$\phi(1020),(\pi^+,\pi^-)_P$ D wave	-	-	-	-	0.020±0.011	-	-	-
$\phi(1020),(\pi^+,\pi^-)_P$ P wave	-	-	-	-	-	-	0.047±0.006	-
$\phi(1020),(\pi^+,\pi^-)_P$ S wave	-	-	0.063±0.011	0.061±0.011	0.114±0.025	-	-	0.059±0.011
$\phi(1020)\rho(770)$ S wave	0.396±0.020	0.383±0.025	0.210±0.020	0.212±0.019	0.159±0.026	0.380±0.020	0.268±0.013	0.209±0.019
$\phi(1020)\rho(770)$ D wave	0.033±0.007	0.034±0.007	0.037±0.007	0.037±0.007	0.011±0.006	0.035±0.007	-	0.038±0.007
$\rho(770)(K^+,K^-)_S$ S wave	-	-	-	-	-	0.012±0.006	-	0.012±0.006
$(\pi^+K^-)_P,(\pi^-K^+)_S$ P wave	0.114±0.011	0.109±0.012	0.109±0.011	0.11±0.011	0.108±0.011	0.093±0.011	-	0.091±0.011
$(\pi^+K^-)_P,(\pi^-K^+)_P$ D wave	-	-	-	-	-	-	0.138±0.012	-
$(\pi^+\pi^-)_P,(K^+K^-)_P$ D wave	-	-	-	-	-	-	0.026±0.007	-
Sum	**0.976±0.023**	**0.967±0.026**	**0.84±0.02**	**0.829±0.02**	**0.84±0.02**	**0.949±0.023**	**0.809±0.014**	**0.825±0.02**
χ^2 **per DOF**	**1.627**	**1.633**	**1.642**	**1.648**	**1.648**	**1.658**	**1.659**	**1.659**
3770 χ^2 **per BIN**	**1.285**	**1.284**	**1.233**	**1.261**	**1.229**	**1.328**	**1.322**	**1.275**
4170 χ^2 **per BIN**	**1.195**	**1.196**	**1.283**	**1.336**	**1.316**	**1.221**	**1.259**	**1.303**
III χ^2 **per BIN**	**1.537**	**1.495**	**1.491**	**1.381**	**1.429**	**1.429**	**1.523**	**1.412**
II.V χ^2 **per BIN**	**2.002**	**1.93**	**1.675**	**1.644**	**1.656**	**1.881**	**1.565**	**1.629**

Table 6.2: Table of fit fractions for the 8 best models in a combined fit to all flavour and CP tagged data sets. The orbital angular momentum of pairs of non resonant particles is illustrated in brackets. The baseline model is number 2.

6.5 Fit Results for the Final Model

The fit results for the final model (as described in the previous section) are presented in table 6.3. This table gives the fitted results for all the parameters that are allowed to float during the fit. The complex amplitude corresponding to the component $K_1(1270)^+(\rightarrow K^*(892), \pi^+), K^-$ is fixed to be unity during the fit. It is the real and imaginary parts (as opposed to the modulus and phase) of the complex amplitude which are fitted. However it is also useful to consider the amplitude and phase of each of the components since these are more easy to interpret physically; these values are given in table 6.4. The χ^2 value per degree of freedom for the final model is 1.63 for 22 degrees of freedom. The fact that this value is greater than one indicates that the model does not describe the data fully. Nonetheless, this value for the goodness of fit is quite acceptable for an amplitude study.

The mass projections for the combined fit to each flavour tagged data set are illustrated in figures 6.6 - 6.10 and for the CP tagged data in figures 6.11 - 6.15. The mass projections illustrate the full PDF which described each particular dataset. The lines representing the signal distributions are slightly "wiggly" due to limited normalisation statistics. The full PDF is a sum of the signal distribution in addition to the relevant background distributions (in the appropriate proportions) for each dataset. The mass projections illustrate a reasonable agreement between the fitted PDF and the data for each of the datasets indicating a consistency between the datasets. The data and fitted PDF are expected to be identical for the four flavour tagged datasets except for efficiency, background and mistagging effects. For the CP tagged datasets however this is not the case due to the fundamentally different nature of the signal PDF.

The most striking feature of figures 6.6 and 6.11 is the ϕ peak (at around 1 $\frac{\mathrm{GeV}}{c^2}$) which is well described by the model for each dataset. Figures 6.7 and 6.12 also shows good agreement between all four flavour tagged datasets and the fit model. Figures 6.8 and 6.13 show good agreement between each dataset and the model except in the region of the $K^*(892)$ resonance (which is at around 900 $\frac{\mathrm{MeV}}{c^2}$) for the CLEO-II dataset in which the signal model underestimates the peak in the data. Since this effect is only found in one dataset it is assumed to be as a result of an efficiency or background effect which hasn't been completely accounted for in the model. Figures 6.9 and 6.14 again show good agreement between the signal and data for all datasets. The peak due to the $K^1(1270)$ resonance (which overlaps with the higher end of the allowed mass range at this Dalitz variable) is well described by the signal model. Figures 6.10 and 6.15 show the model in good agreement with data in all regions of this Dalitz variable. The two CLEO-c datasets and the four CP tagged datasets show that the K_S peaking background is reasonably well measured, and there is no ecvidence of a similar vackground for the CLEO-II.V and CLEO-III datasets, as predicted. The broad ρ(770 resonance appears to be well accounted for by the model.

	Fitted Value
$K_1(1270)^+(\rightarrow K^*(892), \pi^+), K^-$ Real	1.0±0.0
$K_1(1270)^+(\rightarrow K^*(892), \pi^+), K^-$ Imaginary	0.0±0.0
$\overline{K_1}(1270)^-(\rightarrow \overline{K_0}^*(892), \pi^-), K^+$ Real	0.157±0.078
$\overline{K_1}(1270)^-(\rightarrow \overline{K_0}^*(892), \pi^-), K^+$ Imaginary	-0.306±0.060
$K_1(1270)^+(\rightarrow \rho(770), K^+), K^-$ Real	4.067±0.640
$K_1(1270)^+(\rightarrow \rho(770), K^+), K^-$ Imaginary	4.219±0.886
$\overline{K_1}(1270)^-(\rightarrow \rho(770), K^-), K^+$ Real	6.897±0.593
$\overline{K_1}(1270)^-(\rightarrow \rho(770), K^-), K^+$ Imaginary	0.196±1.095
$K^+(1410)(\rightarrow K^*(892), \pi^+), K^-$ Real	4.617±0.561
$K^+(1410)(\rightarrow K^*(892), \pi^+), K^-$ Imaginary	-4.102±0.717
$\overline{K^-}(1410)(\rightarrow \overline{K^*}(892), \pi^-), K^+$ Real	2.609±0.926
$\overline{K^-}(1410)(\rightarrow \overline{K^*}(892), \pi^-), K^+$ Imaginary	-6.253±0.587
$K^*(892)\overline{K^*}(892)$ S wave Real	0.317±0.035
$K^*(892)\overline{K^*}(892)$ S wave Imaginary	0.130±0.043
$\phi(1020)\rho(770)$ S wave Real	-0.324±0.149
$\phi(1020)\rho(770)$ S wave Imaginary	0.985±0.094
$\phi(1020)\rho(770)$ D wave Real	0.204±0.326
$\phi(1020)\rho(770)$ D wave Imaginary	-1.428±0.183
$\phi(1020), (\pi^+, \pi^-)_S$ P wave Real	-1.698±0.834
$\phi(1020), (\pi^+, \pi^-)_S$ P wave Imaginary	-5.932±0.482
$(\pi^+ K^-)_P, (\pi^- K^+)_S$ P wave Real	82.601±6.820
$(\pi^+ K^-)_P, (\pi^- K^+)_S$ P wave Imaginary	11.400±9.744
K_S^0 Background Fraction 3770	0.028±0.005
K_S^0 Background Fraction 4170	0.019±0.006

Table 6.3: Fitted parameters for the combined fit to all datasets for the baseline model. The complex amplitude of the component $K_1(1270)^+(\rightarrow K^*(892), \pi^+), K^-$ is fixed to (1,0) during the fit so as to avoid fitting a redundant number of parameters.

6.5.1 Impact of the CP tagged Data

The combined fit involves a fit to both flavour and CP tagged data sets where the majority of data is flavour tagged and the CP tagged data sets are modeled in terms of the appropriate amplitudes which are dependent on the flavour tagged amplitudes as described in section 6.3. A combined fit has also been carried out to the flavour tagged data sets only. A comparison can then be made between the fit to all data samples and the fit to only flavour tagged data samples. The results of this comparison is given in table 6.5. The comparison illustrates that while the central fitted values for all parameters are consistent to within errors, the precision

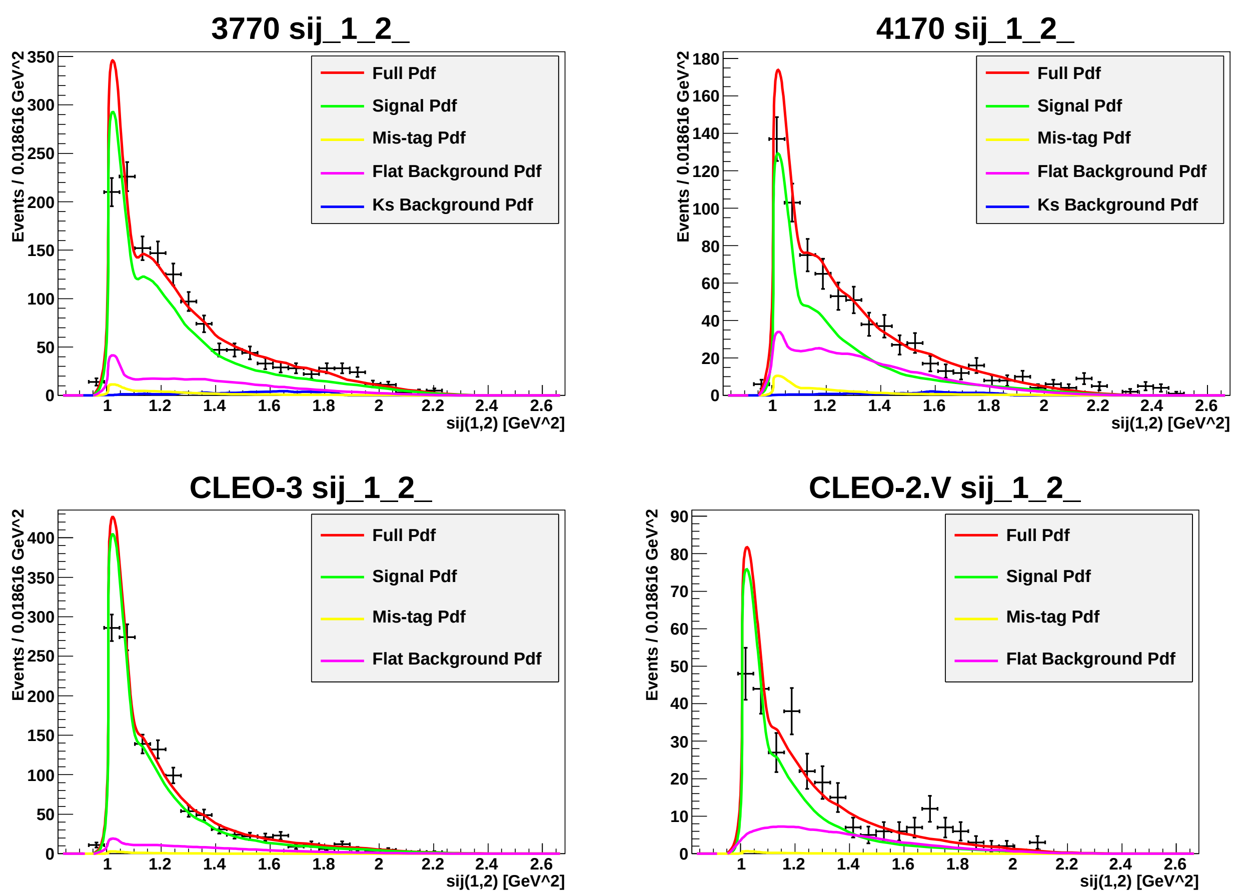

Figure 6.6: Mass projections of fitted result(red) against selected data(black) for all the flavour tagged samples; the 3770, 4170 CLEO-3 and CLEO-2 datasets. Mass projections for $S_{K^+K^-}$.

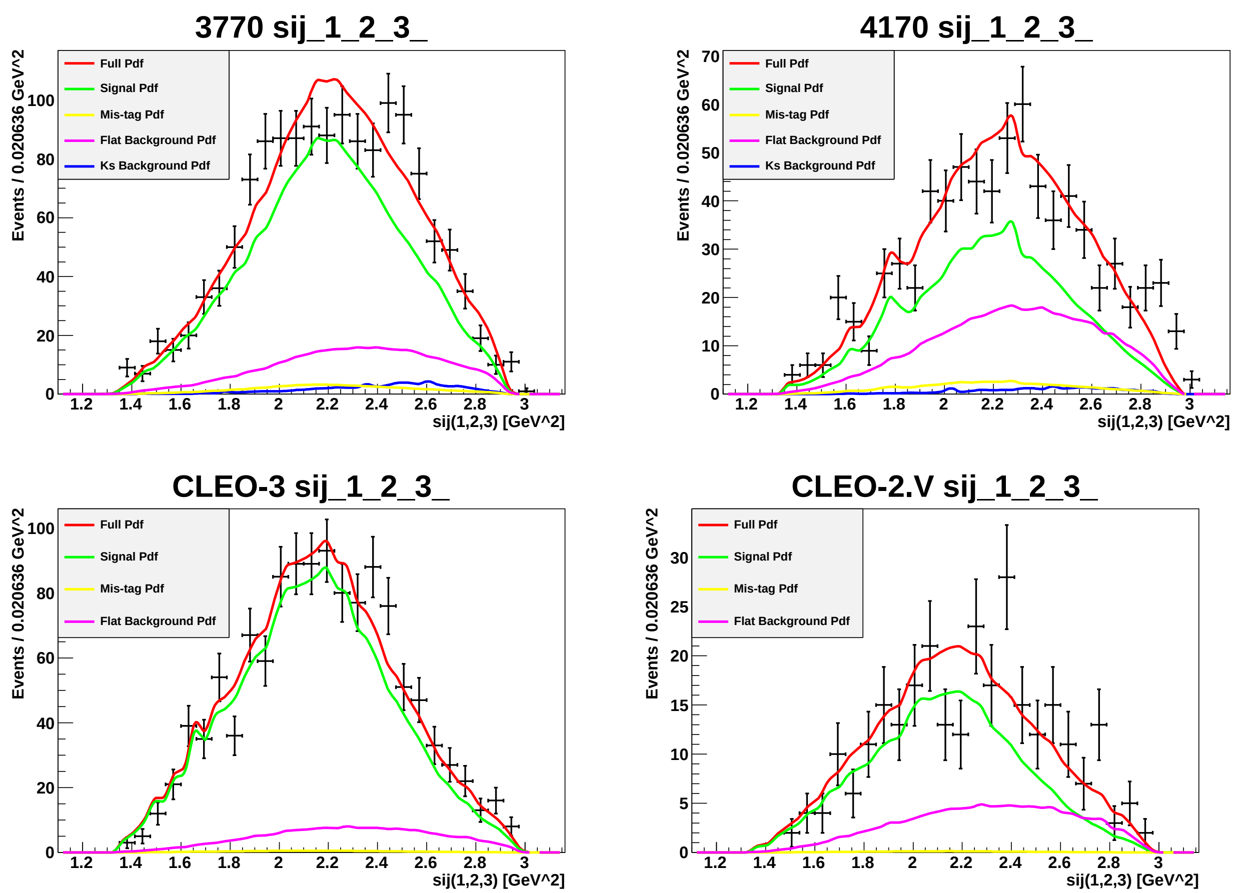

Figure 6.7: Mass projections for $S_{K^+K^-\pi^+}$

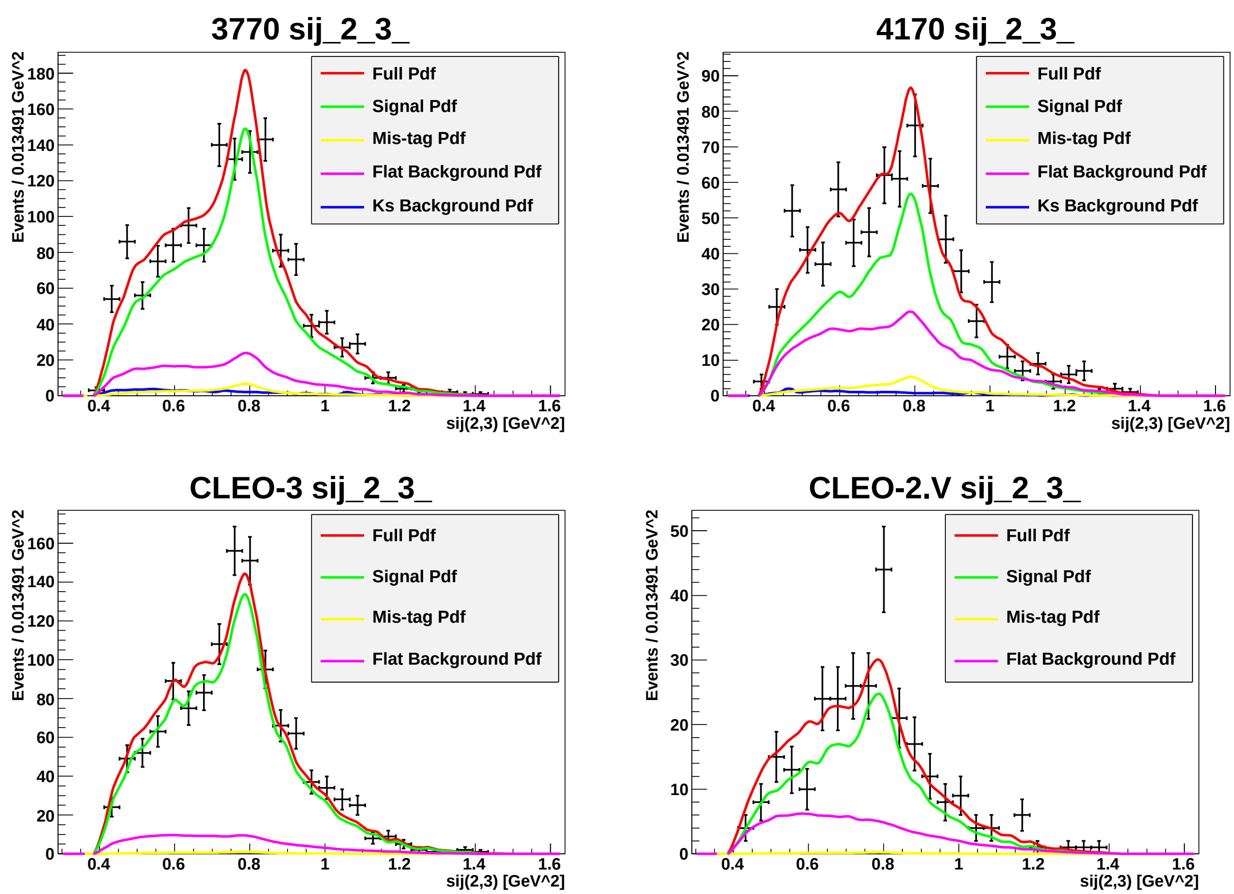

Figure 6.8: Mass projections for $S_{K^-\pi^+}$

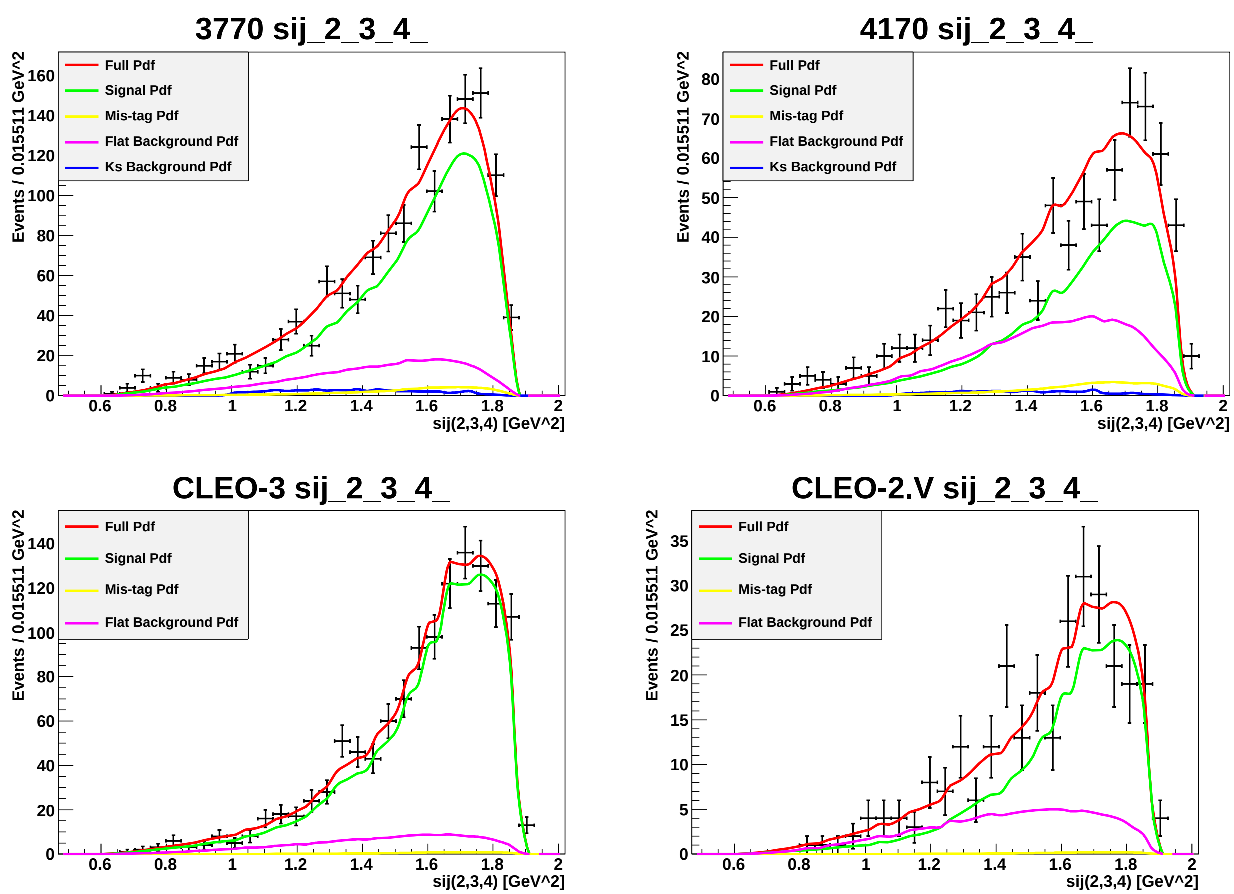

Figure 6.9: Mass projections for $S_{K^-\pi^+\pi^-}$.

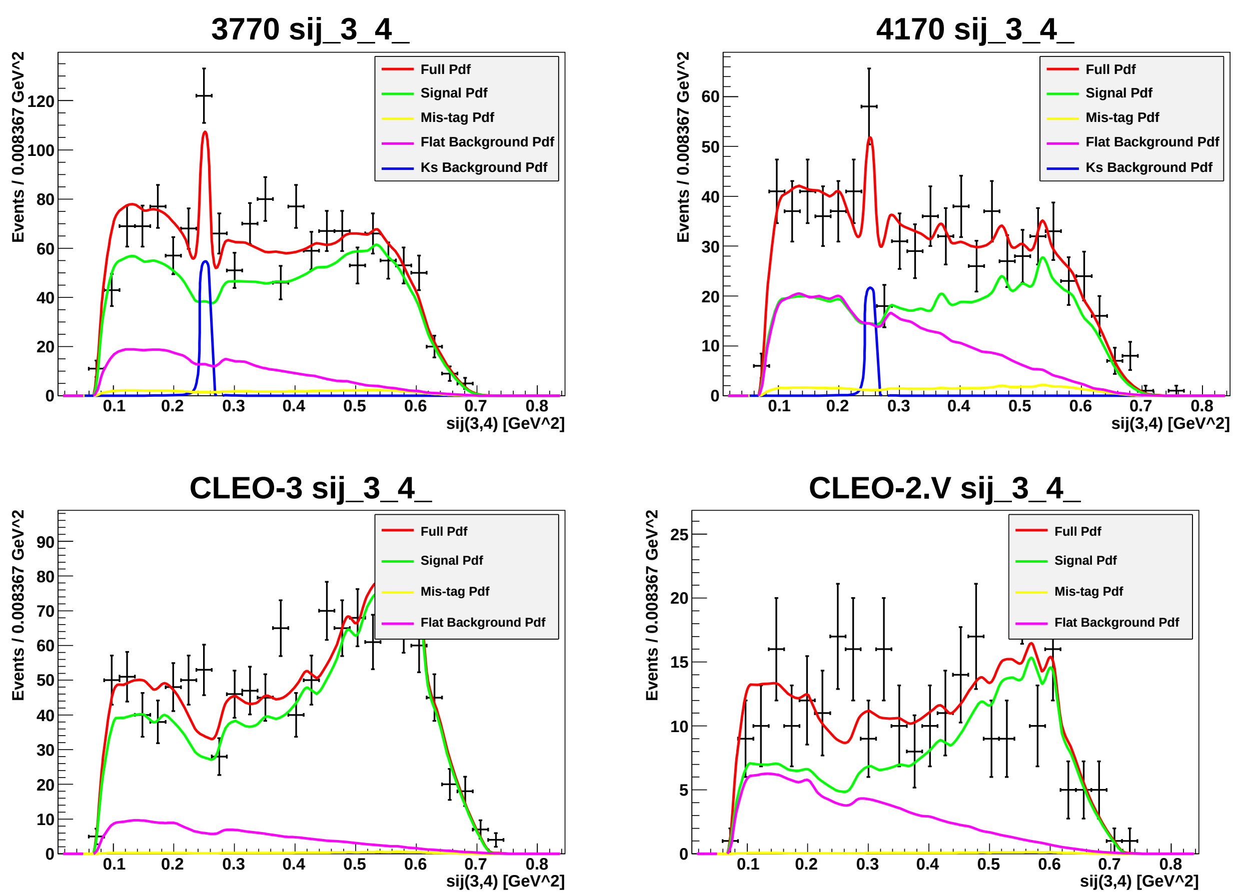

Figure 6.10: Mass projections for $S_{\pi^+\pi^-}$

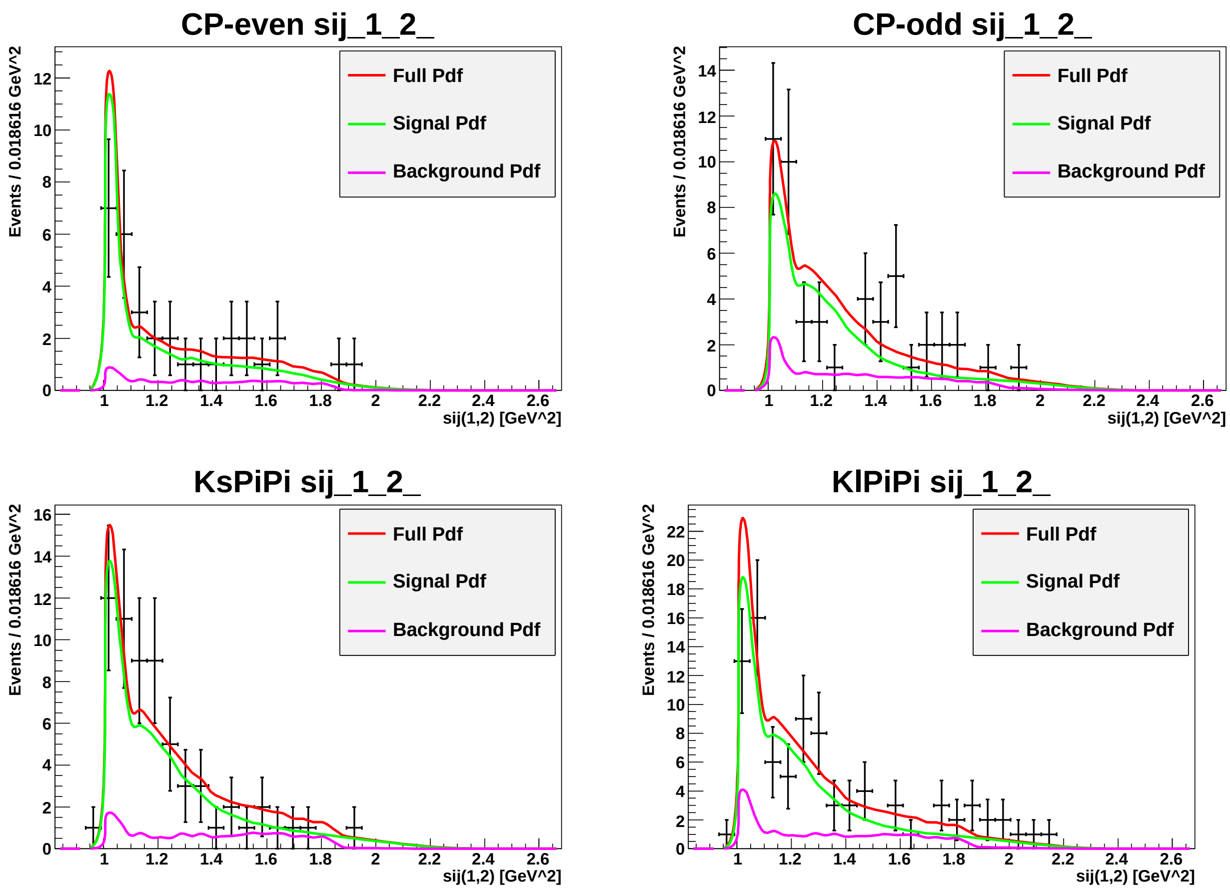

Figure 6.11: Mass projections of fitted result(red) against selected data(black) for all the CP tagged samplesl; the CP even, CP odd $K^0_S\pi^+\pi^-$ and $K^0_L\pi^+\pi^-$ datasets. Mass projections for $S_{K^+K^-}$.

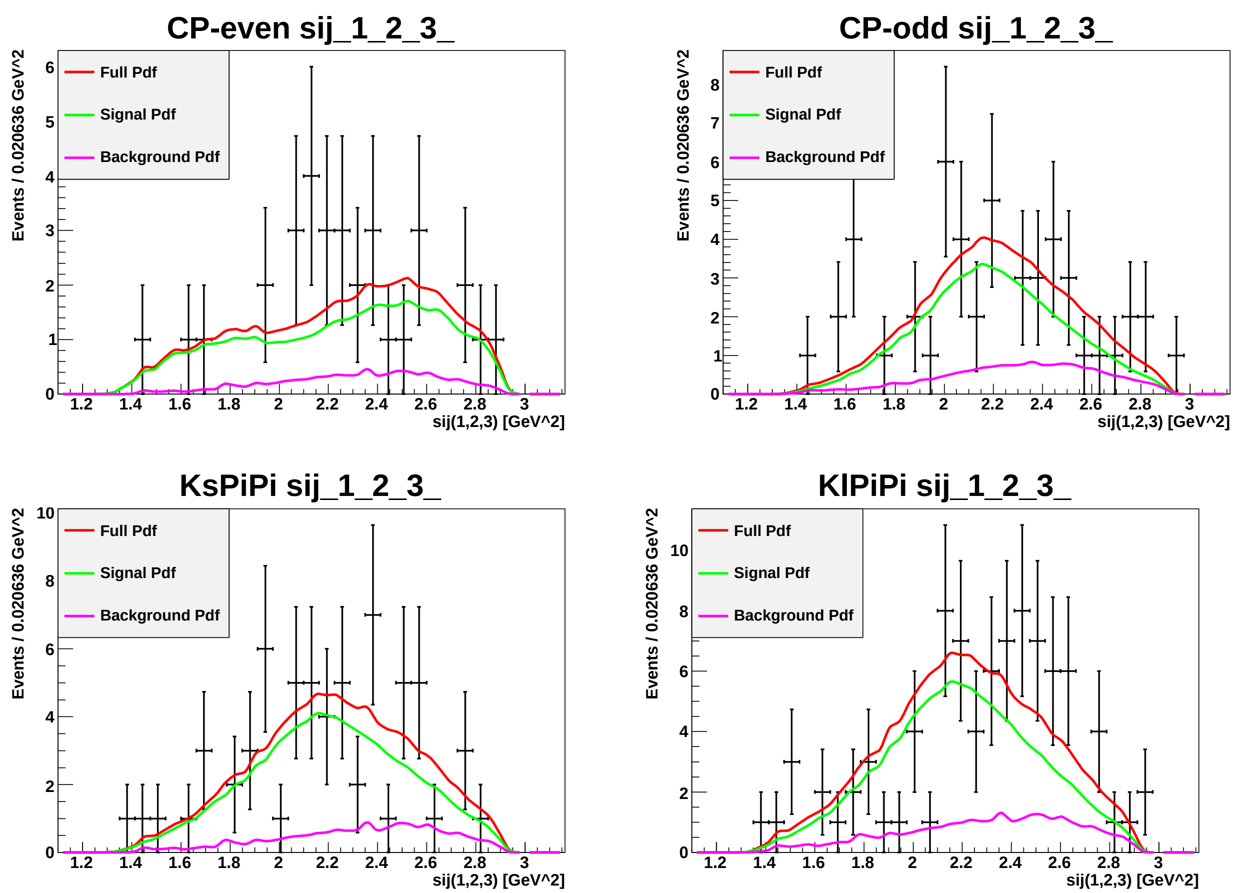

Figure 6.12: Mass projections for $S_{K^+K^-\pi^+}$

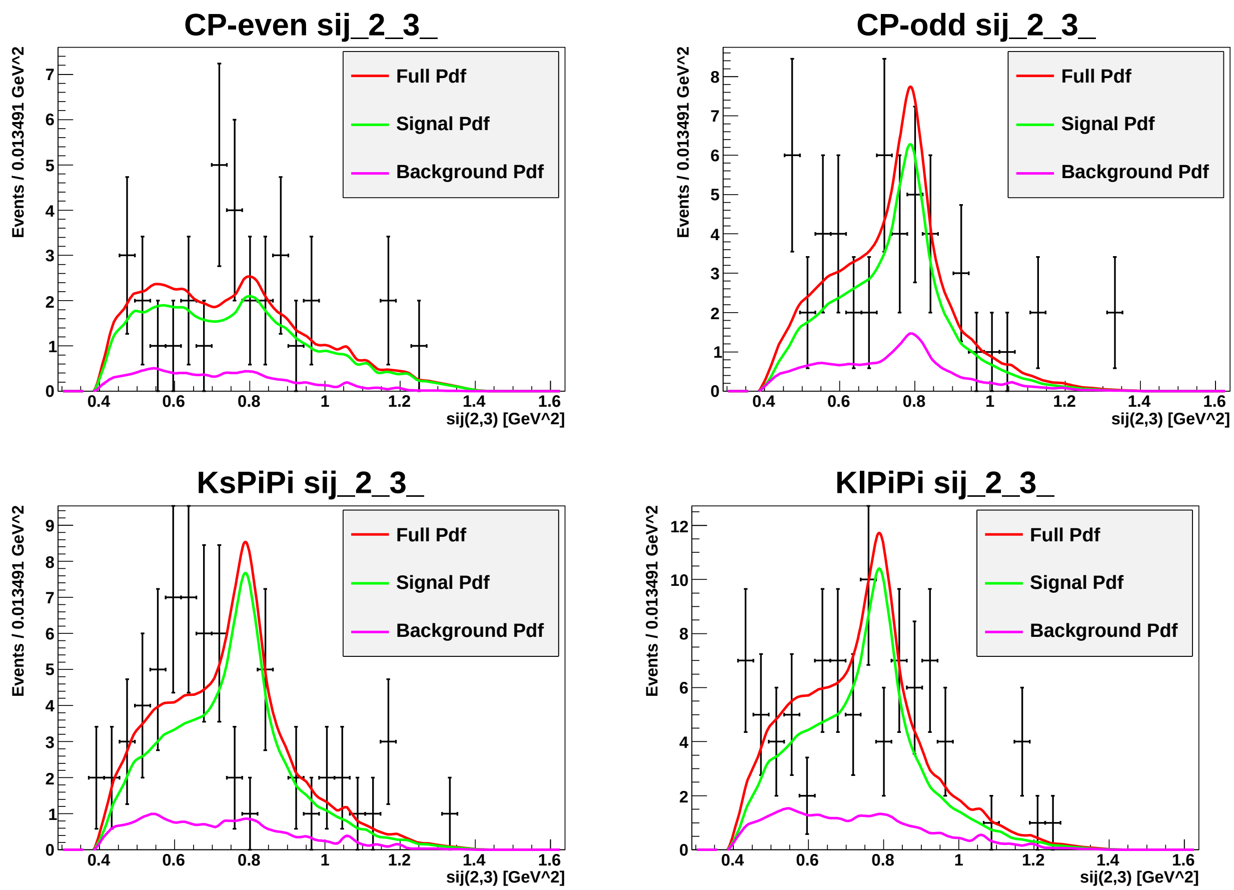

Figure 6.13: Mass projections for $S_{K^-\pi^+}$

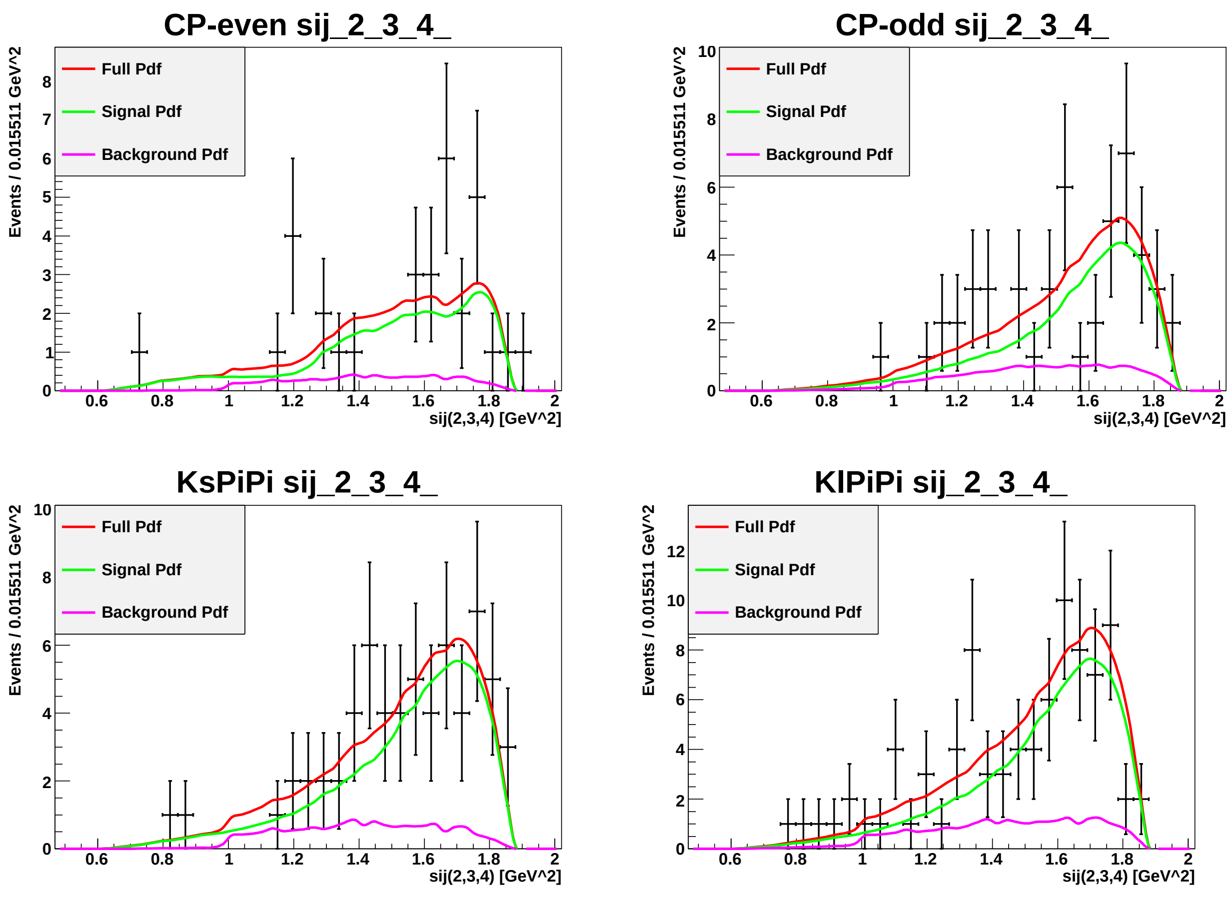

Figure 6.14: Mass projections for $S_{K^-\pi^+\pi^-}$.

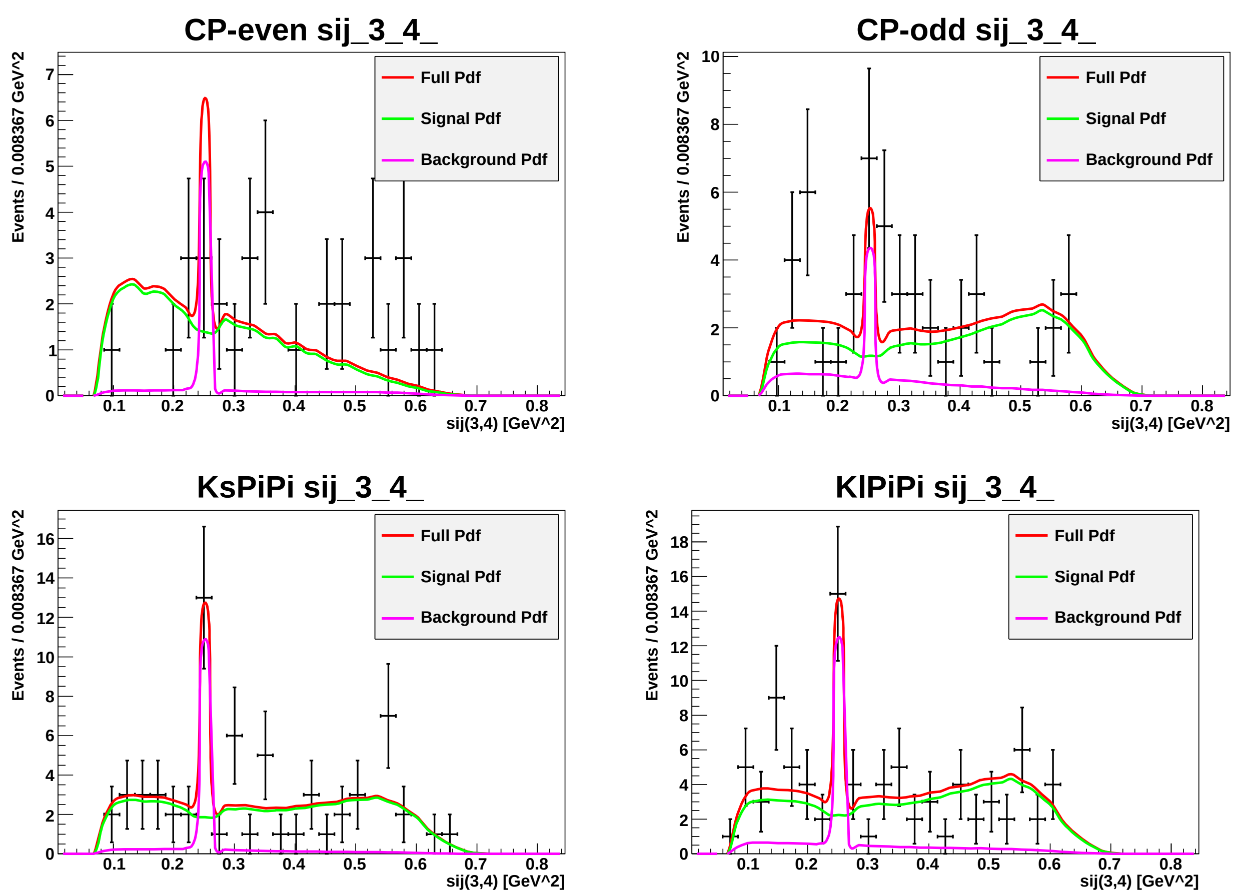

Figure 6.15: Mass projections for $S_{\pi^+\pi^-}$

	Fitted Value
$K_1(1270)^+(\rightarrow K^*(892), \pi^+), K^-$ Phase	0.0±0.0
$K_1(1270)^+(\rightarrow K^*(892), \pi^+), K^-$ Amplitude	0.0±0.0
$\overline{K_1}(1270)^-(\rightarrow \overline{K_0}^*(892), \pi^-), K^+$ Phase	1.098±0.215
$\overline{K_1}(1270)^-(\rightarrow \overline{K_0}^*(892), \pi^-), K^+$ Amplitude	0.345±0.064
$K_1(1270)^+(\rightarrow \rho(770), K^+), K^-$ Phase	0.804±0.131
$K_1(1270)^+(\rightarrow \rho(770), K^+), K^-$ Amplitude	5.86±0.78
$\overline{K_1}(1270)^-(\rightarrow \rho(770), K^-), K^+$ Phase	0.028±0.159
$\overline{K_1}(1270)^-(\rightarrow \rho(770), K^-), K^+$ Amplitude	6.90±0.59
$K^+(1410)(\rightarrow K^*(892), \pi^+), K^-$ Phase	0.726±0.106
$K^+(1410)(\rightarrow K^*(892), \pi^+), K^-$ Amplitude	6.177±0.635
$\overline{K^-}(1410)(\rightarrow \overline{K^*}(892), \pi^-), K^+$ Phase	1.176±0.130
$\overline{K^-}(1410)(\rightarrow \overline{K^*}(892), \pi^-), K^+$ Amplitude	6.776±0.649
$K^*(892)\overline{K^*}(892)$ S wave Phase	0.390±0.123
$K^*(892)\overline{K^*}(892)$ S wave Amplitude	0.342±0.036
$\phi(1020)\rho(770)$ S wave Phase	1.889±0.139
$\phi(1020)\rho(770)$ S wave Amplitude	1.037±0.100
$\phi(1020)\rho(770)$ D wave Phase	1.429±0.224
$\phi(1020)\rho(770)$ D wave Amplitude	1.444±0.187
$\phi(1020), (\pi^+, \pi^-)_S$ P wave Phase	1.85±0.130
$\phi(1020), (\pi^+, \pi^-)_S$ P wave Amplitude	6.172±0.518
$(\pi^+ K^-)_P, (\pi^- K^+)_S$ P wave Phase	0.137±0.116
$(\pi^+ K^-)_P, (\pi^- K^+)_S$ P wave Amplitude	83.4±6.8

Table 6.4: Fitted Parameters in polar coordinates for combined fit to all data set. The complex amplitude of the component $K_1(1270)^+(\rightarrow K^*(892), \pi^+), K^-$ is fixed to (1,0) during the fit. The phases are given in radians.

of the measured complex phases in general improves. This is expected since the CP tagged data sets provide a 6% increase in the quantity of data available. The CP tagged data are expected to improve the precision of the measured parameters to a greater extent than the equivelent sized flavour tagged data set. This is because the CP tagged amplitudes (as described in section 6.3) contain terms of the form $A^*\overline{A}$. Such terms provide greater access to the complex phases of the isobar model (shown in expression 5.1) which are obtained in the fitting procedure.

In order to understand how the impact of the CP-tagged data compares to a flavour-tagged sample of similar size, a comparison is performed in which the flavour-tagged fit is repeated with the CLEO II.V dataset included. The CLEO-II.V data set contains 279 events with an estimated purity of 74.0%, whereas the CP-tagged datasets contain 231 events with an estimated purity of 77.9%. Therefore the two datasets are very similar in size and purity. The effects of removing the CLEO-II.V dataset on the combined fit is shown in table 6.6. In tables 6.6 and 6.5 the average fractional error on the measured parameters is calculated. Any parameters for which the error greatly exceeds the measured value ($err_i > 5 \times V_i$) are omitted in calculating the averagre fractional error. The inclusion of the CLEO-II.V data leads to a 4% improvement on the precision of the measured parameters whereas the inclusion of the CP-tagged dataset lead to a 9% improvement despite the fact that the CP tagged datasets contains fewer events. This suggests that as predicted the CP-tagged data increases the precision on the measured parameters to a greater extent would have been expected from the same number of flavour tagged events.

The χ^2_{DOF} value increases very slightly when the CP tagged data is included in the combined fit. This is not unexpected since the calculation of the χ^2_{DOF} uses only the flavour tagged data sets and the inclusion of the CP tagged data sets represents an additional constraint on the fitted parameters but does not enter the χ^2_{DOF} calculation.

	All Data Sets	**Flavour Tagged Data Sets**	**Relative Shift**
$K_1(1270)^+(\rightarrow K^*(892), \pi^+), K^-$ Real	1.0±0.0	1.0±0.0	0.0
$K_1(1270)^+(\rightarrow K^*(892), \pi^+), K^-$ Imaginary	0.0±0.0	0.0±0.0	0.0
$\overline{K_1}(1270)^-(\rightarrow \overline{K_0}^*(892), \pi^-), K^+$ Real	0.157±0.078	0.156±0.079	0.010
$\overline{K_1}(1270)^-(\rightarrow \overline{K_0}^*(892), \pi^-), K^+$ Imaginary	-0.306±0.060	-0.315±0.061	0.141
$K_1(1270)^+(\rightarrow \rho(770), K^+), K^-$ Real	4.067±0.640	4.252±0.657	0.289
$K_1(1270)^+(\rightarrow \rho(770), K^+), K^-$ Imaginary	4.219±0.886	4.045±0.954	0.197
$\overline{K_1}(1270)^-(\rightarrow \rho(770), K^-), K^+$ Real	6.897±0.593	6.672±0.613	0.379
$\overline{K_1}(1270)^-(\rightarrow \rho(770), K^-), K^+$ Imaginary	0.196±1.095	0.875±1.188	0.620
$K^+(1410)(\rightarrow K^*(892), \pi^+), K^-$ Real	4.617±0.561	4.511±0.624	0.189
$K^+(1410)(\rightarrow K^*(892), \pi^+), K^-$ Imaginary	-4.102±0.717	-4.402±0.744	0.418
$\overline{K^-}(1410)(\rightarrow \overline{K^*}(892), \pi^-), K^+$ Real	2.609±0.926	2.708±0.963	0.107
$\overline{K^-}(1410)(\rightarrow \overline{K^*}(892), \pi^-), K^+$ Imaginary	-6.253±0.587	-6.338±0.619	0.146
$K^*(892)\overline{K^*}(892)$ S wave Real	0.317±0.035	0.332±0.036	0.425
$K^*(892)\overline{K^*}(892)$ S wave Imaginary	0.130±0.043	0.129±0.046	0.028
$\phi(1020)\rho(770)$ S wave Real	-0.324±0.149	-0.242±0.156	0.546
$\phi(1020)\rho(770)$ S wave Imaginary	0.985±0.094	1.039±0.087	0.584
$\phi(1020)\rho(770)$ D wave Real	0.204±0.326	0.055±0.321	0.456
$\phi(1020)\rho(770)$ D wave Imaginary	-1.428±0.183	-1.451±0.180	0.123
$\phi(1020), (\pi^+, \pi^-)_S$ P wave Real	-1.698±0.834	-2.191±0.827	0.590
$\phi(1020), (\pi^+, \pi^-)_S$ P wave Imaginary	-5.932±0.482	-5.724±0.530	0.431
$(\pi^+K^-)_P, (\pi^-K^+)_S$ P wave Real	82.6±6.766	85.3±6.765	0.397
$(\pi^+K^-)_P, (\pi^-K^+)_S$ P wave Imaginary	11.4±9.744	10.1±10.3	0.134
Average Fractional Error	**0.203**	**0.223**	
χ^2 **per DOF**	**1.633**	**1.632**	

Table 6.5: A comparison of fit results using only flavour tagged data sets and using both flavour and CP tagged data sets. The shift between the two is calculated in units of the error on the fitted value for the combined fit to all data sets. The fractional error for each fitted value is calculated as $\frac{err_i}{V_i}$, where V_i gives the ith measured value. The average fractional value for each fit is then given by: $\frac{1}{N}\sum_i |\frac{err_i}{V_i}|$ where N is the number of fitted parameters. The imaginary component of $\overline{K_1}(1270)^-(\rightarrow \rho(770), K^-), K^+$, $(\pi^+K^-)_P, (\pi^-K^+)_S$ P wave imaginary component and the real component of the $\phi(1020)\rho(770)$ D wave resonant contributions have been omitted from the calculation of the average fractional error since these components are not well measured and therefore contribute disproportionately to the average.

	All Data Sets	Cleo-II.V dataset removed	Relative Shift
$K_1(1270)^+(\rightarrow K^*(892),\pi^+),K^-$ Real	1.0±0.0	1.0±0.0	0.0
$K_1(1270)^+(\rightarrow K^*(892),\pi^+),K^-$ Imaginary	0.0±0.0	0.0±0.0	0.0
$\overline{K_1}(1270)^-(\rightarrow \overline{K_0}^*(892),\pi^-),K^+$ Real	0.157±0.078	0.101±0.074	0.725
$\overline{K_1}(1270)^-(\rightarrow \overline{K_0}^*(892),\pi^-),K^+$ Imaginary	-0.306±0.060	-0.272±0.060	0.562
$K_1(1270)^+(\rightarrow \rho(770),K^+),K^-$ Real	4.067±0.640	4.000±0.638	0.105
$K_1(1270)^+(\rightarrow \rho(770),K^+),K^-$ Imaginary	4.219±0.886	4.073±0.864	0.165
$\overline{K_1}(1270)^-(\rightarrow \rho(770),K^-),K^+$ Real	6.897±0.593	6.560±0.593	0.568
$\overline{K_1}(1270)^-(\rightarrow \rho(770),K^-),K^+$ Imaginary	0.196±1.095	-0.469±1.051	0.609
$K^+(1410)(\rightarrow K^*(892),\pi^+),K^-$ Real	4.617±0.561	4.365±0.561	0.450
$K^+(1410)(\rightarrow K^*(892),\pi^+),K^-$ Imaginary	-4.102±0.717	-3.588±0.705	0.717
$\overline{K^-}(1410)(\rightarrow \overline{K^*}(892),\pi^-),K^+$ Real	2.609±0.926	2.519±0.914	0.097
$\overline{K^-}(1410)(\rightarrow \overline{K^*}(892),\pi^-),K^+$ Imaginary	-6.253±0.587	-5.987±0.584	0.453
$K^*(892)\overline{K^*}(892)$ Real	0.317±0.035	0.294±0.034	0.636
$K^*(892)\overline{K^*}(892)$ Imaginary	0.130±0.043	0.130±0.041	0.0
$\phi(1020)\rho(770)$ Real	-0.324±0.149	-0.345±0.141	0.144
$\phi(1020)\rho(770)$ Imaginary	0.985±0.094	0.909±0.093	0.808
$\phi(1020)\rho(770)$ D wave Real	0.204±0.326	0.223±0.315	0.055
$\phi(1020)\rho(770)$ D wave Imaginary	-1.428±0.183	-1.304±0.184	0.680
$\phi(1020),(\pi^+,\pi^-)_S$ P wave Real	-1.698±0.834	-1.41±0.811	0.346
$\phi(1020),(\pi^+,\pi^-)_S$ P wave Imaginary	-5.932±0.482	-5.841±0.456	0.190
$(\pi^+K^-)_P,(\pi^-K^+)_S$ P wave Real	82.6±6.766	75.8±6.313	0.998
$(\pi^+K^-)_P,(\pi^-K^+)_S$ P wave Imaginary	11.4±9.744	10.4±8.84	0.105
Average Fractional Error	**0.203**	**0.212**	
χ^2 **per DOF**	**1.633**	**1.614**	

Table 6.6: A comparison of fit results using all datasets and the results obtained by ommitting the CLEO-II.V dataset. The shift between the two is calculated in units of the error on the fitted value for the combined fit to all data sets. The fractional error for each fitted value is calculated as $\frac{err_i}{V_i}$, where V_i gives the ith measured value. The average fractional value for each fit is then given by: $\frac{1}{N}\sum_i|\frac{err_i}{V_i}|$ where N is the number of fitted parameters. The imaginary component of $\overline{K_1}(1270)^-(\rightarrow \rho(770),K^-),K^+$, $(\pi^+K^-)_P,(\pi^-K^+)_S$ P wave imaginary component and the real component of the $\phi(1020)\rho(770)$ D wave resonant contributions have been omitted from the calculation of the average fractional error since this component is not well measured and therefore contributes disproportionately to the average.

6.6 Fitter validation tests

In order to validate the method for accounting for the efficiency effects imposed by the event selection, and to check for any biases coming from the detector reconstruction, a pull study is conducted. This is an extension to the study reported in section 5.4.1 where the integrity of MINT was tested, but in an environment without detector effects.

The CLEO-c Monte Carlo system was used to produce the $e^+e^- \to \psi(3770) \to D^0\overline{D}^0$ events. One hundred sets of 40000 $D^0 \to K^+K^-\pi^+\pi^+$ events are generated in MINT according to an amplitude model consisting of the eleven resonant components which are present in the final amplitude model. The MINT generated events are then boosted into the CLEO-c D^0 frame and inserted into the decay while the $\overline{D}^0$ was allowed to decay generically. These Monte Carlo events are then passed through the detector and reconstruction simulation. The event selection was then applied to the reconstructed Monte-Carlo events. The efficiency of selecting the reconstructed events was $\approx 10\%$. Therefore after selection 100 sets of ~ 4000 events remained.

For each event set the complex amplitudes are fitted with one complex component fixed to avoid fitting redundant parameters. The efficiency effects are accounted for via the efficiency corrected Monte Carlo method described in section 4.4. The fitted complex amplitudes are then compared to the input values. For each event set the "pull" from the input value (pull $= \frac{\text{fitted}-\text{Input}}{\text{Error on fitted result}}$) was calculated for each fitted parameter and fit fraction. The distribution of these pull values for each parameter are then fit to a Gaussian distribution. In the absence of any systematic bias the pull values would be expected to be distributed according to a Gaussian function centred around 0 with a width of 1. In order to distinguish fitter bias from shifts due to reconstruction effects the above validation study was carried out twice. In one case Monte Carlo truth information was used to describe the particles four momenta and on the second occasion the reconstructed values for the particles four momenta are used in the fit.

The results of these fits are shown in table 6.7. The pull distributions for the fitted parameters for the fits which used the Monte Carlo truth information are

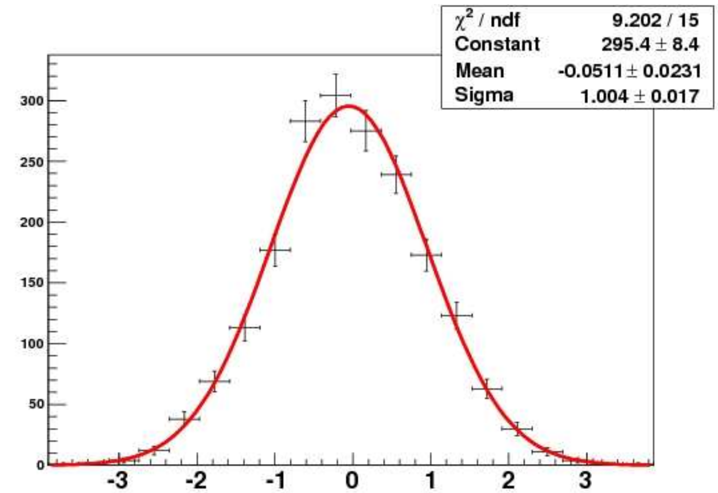

Figure 6.16: Pull study using Monte Carlo truth momenta. Pulls of all fitted parameter

shown in aappendix D in figure D.1, and for the fits which used reconstructed momenta in figure D.2. The sum of the pulls for all parameters for all fits are illustrated in figures 6.17 and 6.16 for the reconstructed and Monte Carlo truth fits respectively. The fitted and generated values for the fits which used the Monte Carlo truth information are also illustrated, in the complex plane for the reconstructed momenta in figure 6.18. The fit fractions are also compared to those that are input. These results are given in table 6.8 and for the fits which used the Monte Carlo truth information the distributions are shown in figure D.3 and for the fits which used reconstructed momenta in figure D.4. The fitted PDF can also be plotted in comparison to the generated data for the five independent mass projections for one randomly selected fit, these results are shown in plots 6.19.

From these results it is apparent that small biases exist for some of the fitted parameters (for example the $(\phi\rho)_S$ real component). The biases are most likely to be due to correlations between parameters. There is no large difference in behaviour observed between the studies with truth and reconstructed data. In the final result these biases are accounted for in the assignment of systematic uncertainties, described in section 6.7.

	Monte Carlo Truth Data		Reconstructed Data	
	Fitted Mean	**Fitted Width**	**Fitted Mean**	**Fitted Width**
$K_1(1270)^+(\rightarrow K^*(892), \pi^+), K^-$ Real	0.0±0.0	0.0±0.0	0.0±0.0	0.0±0.0
$K_1(1270)^+(\rightarrow K^*(892), \pi^+), K^-$ Imaginary	0.0±0.0	0.0±0.0	0.0±0.0	0.0±0.0
$\overline{K_1}(1270)^-(\rightarrow \overline{K_0}^*(892), \pi^-), K^+$ Real	-0.427±0.125	1.020±0.140	-0.36±0.120	0.986±0.126
$\overline{K_1}(1270)^-(\rightarrow \overline{K_0}^*(892), \pi^-), K^+$ Imaginary	0.027±0.133	1.140±0.121	-0.104±0.143	1.130±0.125
$K_1(1270)^+(\rightarrow \rho(770), K^+), K^-$ Real	0.083±0.119	1.060±0.115	0.155±0.187	1.350±0.188
$K_1(1270)^+(\rightarrow \rho(770), K^+), K^-$ Imaginary	-0.145±0.091	0.845±0.073	-0.286±0.104	0.826±0.097
$\overline{K_1}(1270)^-(\rightarrow \rho(770), K^-), K^+$ Real	-0.006±0.105	0.880±0.104	-0.028±0.115	1.010±0.113
$\overline{K_1}(1270)^-(\rightarrow \rho(770), K^-), K^+$ Imaginary	-0.241±0.143	1.170±0.142	-0.218±0.123	1.080±0.120
$K^+(1410)(\rightarrow K^*(892), \pi^+), K^-$ Real	-0.316±0.127	1.110±0.120	-0.409±0.106	0.976±0.093
$K^+(1410)(\rightarrow K^*(892), \pi^+), K^-$ Imaginary	0.084±0.139	1.080±0.116	0.111±0.109	0.885±0.100
$\overline{K^-}(1410)(\rightarrow \overline{K^*}(892), \pi^-), K^+$ Real	-0.047±0.107	0.908±0.099	-0.076±0.132	0.956±0.114
$\overline{K^-}(1410)(\rightarrow \overline{K^*}(892), \pi^-), K^+$ Imaginary	-0.348±0.112	0.948±0.121	-0.230±0.128	1.060±0.117
$K^*(892)\overline{K^*}(892)$ S wave Real	0.278±0.105	0.943±0.091	0.210±0.138	1.130±0.115
$K^*(892)\overline{K^*}(892)$ S wave Imaginary	-0.151±0.113	0.989±0.095	-0.018±0.099	0.831±0.089
$\phi(1020)\rho(770)$ S wave Real	-0.292±0.114	0.871±0.147	-0.256±0.101	0.896±0.115
$\phi(1020)\rho(770)$ S wave Imaginary	-0.018±0.104	0.852±0.086	0.166±0.104	0.861±0.099
$\phi(1020)\rho(770)$ D wave Real	0.196±0.128	1.051±0.113	0.310±0.131	1.112±0.121
$\phi(1020)\rho(770)$ D wave Imaginary	-0.062±0.112	0.963±0.093	-0.014±0.121	0.907±0.099
$\phi(1020), (\pi^+, \pi^-)_S$ P wave Real	-0.201±0.139	1.140±0.123	-0.125±0.135	1.160±0.116
$\phi(1020), (\pi^+, \pi^-)_S$ P wave Imaginary	-0.163±0.090	0.846±0.095	-0.237±0.132	1.080±0.121
$(\pi^+K^-)_P, (\pi^-K^+)_S$ P wave Real	0.169±0.101	0.865±0.096	0.009±0.119	0.977±0.105
$(\pi^+K^-)_P, (\pi^-K^+)_S$ P wave Imaginary	0.025±0.155	1.150±0.211	-0.068±0.124	0.864±0.110
All Real Components	-0.008±0.034	1.032±0.026	-0.021±0.034	1.030±0.024
All Imaginary Components	-0.106±0.031	0.960±0.022	-0.113±0.032	0.953±0.023

Table 6.7: Table of the mean and width of the pull distributions for all of the fitted parameters in order to test fitter validity.

	Monte Carlo Truth Data		Reconstructed Data	
	Fitted Mean	**Fitted Width**	**Fitted Pull**	**Fitted Width**
$K_1(1270)^+(\rightarrow K^*(892), \pi^+), K^-$	-0.038±0.102	0.959±0.088	-0.025±0.103	0.963±0.081
$\overline{K_1}(1270)^-(\rightarrow \overline{K_0}^*(892), \pi^-), K^+$	-0.282±0.112	1.030±0.097	-0.364±0.136	1.100±0.123
$K_1(1270)^+(\rightarrow \rho(770), K^+), K^-$	-0.028±0.082	0.758±0.094	-0.088±0.101	0.844±0.134
$\overline{K_1}(1270)^-(\rightarrow \rho(770), K^-), K^+$	0.055±0.140	1.09±0.126	0.098±0.117	0.965±0.090
$K^+(1410)(\rightarrow K^*(892), \pi^+), K^-$	-0.341±0.139	1.140±0.133	-0.437±0.126	1.050±0.107
$\overline{K^-}(1410)(\rightarrow \overline{K^*}(892), \pi^-), K^+$	-0.046±0.088	0.745±0.098	-0.241±0.175	0.995±0.257
$K^*(892)\overline{K^*}(892)$ S wave	0.057±0.116	0.997±0.106	0.051±0.150	1.150±0.135
$\phi(1020)\rho(770)$ S wave	0.214±0.110	0.976±0.096	0.318±0.112	0.956±0.083
$\phi(1020)\rho(770)$ D wave	0.098±0.113	1.020±0.095	0.136±0.108	0.950±0.114
$\phi(1020), (\pi^+, \pi^-)_S$ P wave	0.190±0.108	0.853±0.088	0.166±0.1	0.893±0.078
$(\pi^+K^-)_P, (\pi^-K^+)_S$ P wave	-0.258±0.113	0.837±0.100	0.060±0.117	0.877±0.099
All Fractions	0.022±0.029	0.922±0.018	0.007±0.030	0.941±0.019
Mean χ^2 per DOF	**0.947±0.009**		**0.959±0.009**	

Table 6.8: Table of fitted results for pull distributions for fit fractions to test fitter validity.

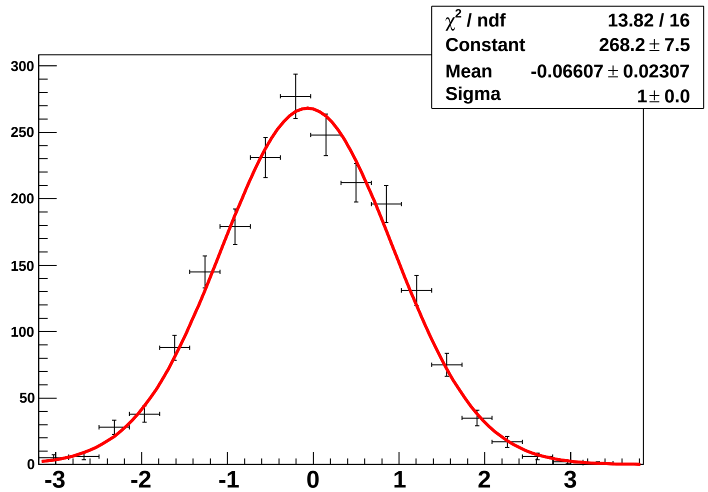

Figure 6.17: Pulls of all fitted parameters. For pull study using reconstructed momenta.

6.7 Systematic Uncertainties

It is necessary to consider sources of systematic uncertainty or effects that could bias the results. The systematical errors which are considered consist of those that relate to the description of backgrounds and the treatment of efficiencies and those which result from assumptions in the description of the signal model. In general, in order to determine the shift resulting from each systematic uncertainty the treatment of the relevant effect was shifted according to its expected variation, a new fit was carried out, and the shift on each of the measured parameters was taken as an estimate of the systematic uncertainty due to this effect. Each independent systematic effect was considered in isolation and the shifts added in quadrature to give an estimate of the total systematic shift on each of the parameters. A summary of all systematics is given in tables 6.14 - 6.16.

6.7.1 Breit Wigner Model Assumptions

The isobar model as constructed in this study, with Breit-Wigner terms as described in chapter 1, uses Blatt-Weisskopf penetration factors in order to describe the form factors of the resonant decays. The systematic uncertainty which can be attributed to this assumption was determined by setting the form factors to 1 in the fit. This is a conservative approach to assign this systematic component. The effect is nonetheless

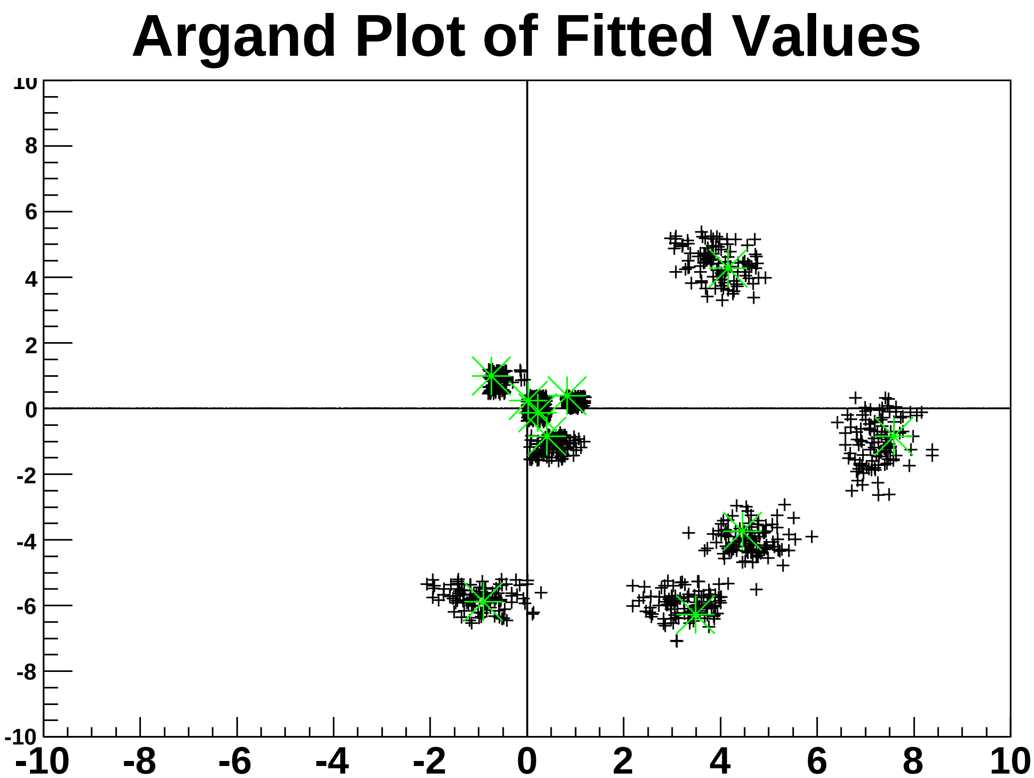

Figure 6.18: Argand diagram of fitted complex amplitudes (black) and generated amplitudes (green). For pull study using reconstructed momenta.

found to be reasonably small, and in general significantly smaller than the statistical uncertainty.

6.7.2 Resonance Masses and Widths

In this study the masses and measured widths of the resonances which appear in the Breit-Wigner term of expression 1.36 are taken as quoted in [22] and are displayed in table 6.9. In order to calculate the systematic effect due to the uncertainty on each of these masses and widths, each measured value was shifted up and down by one sigma and the magnitude of the shift on each of the fitted variables was averaged. The resulting systematic shifts on the measured parameters resulting from each shift in the mass or width of a resonance are added in quadrature to give the total systematic error resulting from the uncertainties on these quantities.

In considering this category of systematic, the decay $D^0 \to \overline{K_1}(1270)^{\pm}(\to \rho(770), K^-), K^{\mp}$ is a special case. The lower mass limit of the $K_1(1270)$ is below threshold for $K\rho$ pro-

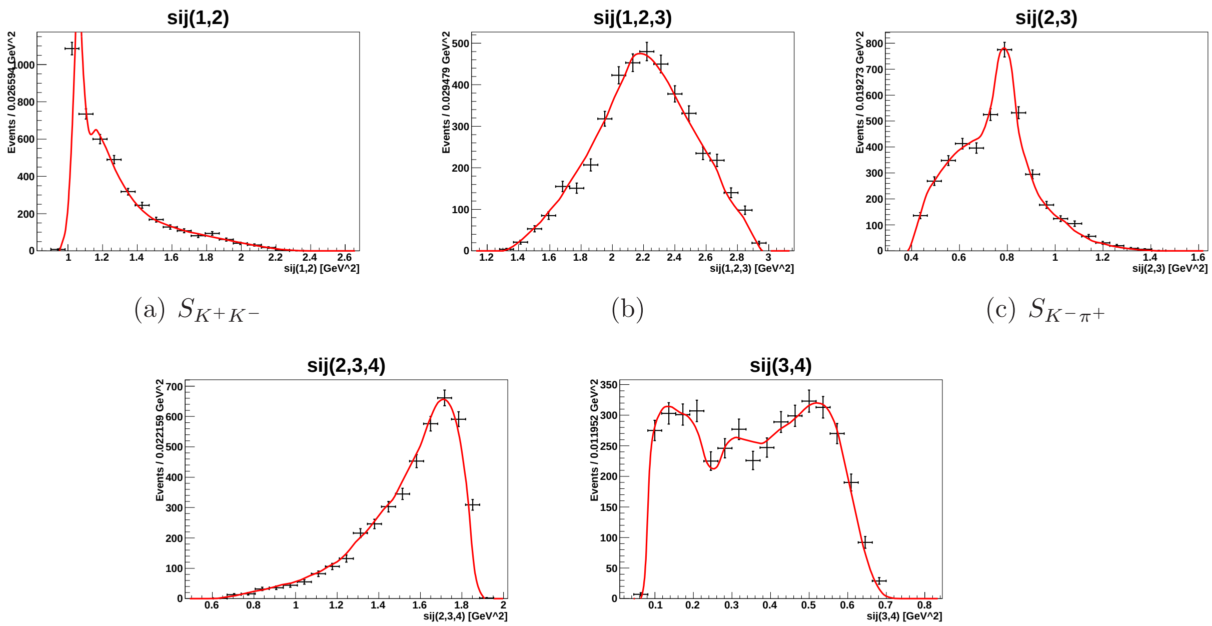

(a) $S_{K^+K^-}$ (b) (c) $S_{K^-\pi^+}$

(d) $S_{K^-\pi^+\pi^-}$ (e) $S_{\pi^+\pi^-}$

Figure 6.19: Projections of fitted result(red) against selected Monte Carlo data(black)

duction. In fact the decay can still proceed due to the non zero width of the $K_1(1270)$ resonance. However the mass of the $K_1(1270)$ resonance would have crossed the threshold condition and the Breit-Wigner description of the decay amplitude may therefore break down. In order to estimate the uncetainty in this case the mass of the $K_1(1270)$ was lowered to the edge of the physical region (1269.2 MeV) and the shift this caused, denoted shift$_{PR}$, is calculated. This mass shift represents a fraction of $\frac{2.8}{7}$ of the full error on the mass (since the full error on the mass measurement is 7 MeV but a shift of only 2.8 MeV takea the mass to the limit of the physical region). Thus to obtain an estimate of the shifts at the true lower bound of the resonance, shift$_{LB}$ the shifts for each parameter are scaled: shift$_{LB,i} = \frac{7}{2.8} \times$ shift$_{PR,i}$.

From tables 6.16, 6.15 and 6.14 it is clear that the precision on the measurements of all parameters are particularly limited by the knowledge on the measurements of the masses and widths of the resonances. Tables 6.10 and 6.11 illustrate how much the uncertainties on the measured mass and widths of each resonance contribute to the total systematic. From these tables it may be noted that the largest of these contributions is from the $K_1(1270)$ resonance. The contributions towards this shift

Resonance	**Mass** (MeV)	**Width** (MeV)
ϕ	1019.455 ± 0.020	4.26 ± 0.04
ρ	775.49 ± 0.34	146.2 ± 0.7
$K^*(892)$	891.66 ± 0.26	50.8 ± 0.9
$K(1410)^{\pm}$	1414 ± 15	232 ± 15
$K_1(1270)^{\pm}$	1272 ± 7	$90 \pm 20^*$

Table 6.9: Measured masses and fixed widths for resonances used in the final model of this study as taken from [22]. *This large error on the width of the $K_1(1270)^{\pm}$ is described as an "educated guess", and is larger than the average error of the published values. It is used in this study as a conservative estimate.

from uncertainties on the mass and width of this resonance are illustrated in tables 6.12 and 6.13. From these tables it may be noted that large shifts result from both the mass and width uncertainties of this resonance. As described in table 6.9, the uncertainty on the $K_1(1270)$ width is very large. The sensitivity to the mass of the $K_1(1270)$ resonance is most likely to be due to the fact that the mass of the resonance lies close to the threshold condition for the decay $D^0 \to K^{\mp}K_1(1270)^{\pm}(\to \rho(770)K^{\pm})$, so the fit results are particularly sensitive to this mass.

6.7.3 Background Uncertainties

The level of flat background for each of the flavour tagged datasets (listed in table 4.3) is shifted up and down by one sigma from the measured values. The magnitude of the shift was averaged between the upward and downward changes in order to provide an estimate of the total systematic due to each background fraction. In order to account for uncertainties in the models used to describe the flavour tagged flat and peaking background, any component listed in tables 5.2 and 5.3 which had a fit fraction within 3 sigmas of 0 was omitted, one at a time. In the case of CP tagged backgrounds the background description was omitted entirely from each of the four CP tagged data sets, one at a time. As can be seen in tables 6.16, 6.15 and 6.14, uncertainties in the background descriptions provide a relatively small contribution to the total systematic error on the results.

Component	$K_1(1270)$	$K^*(892)$	$\rho(770)$	$K^*(1410)$	$\phi(1020)$	**Total**
$K_1(1270)^+(\to K^*(892),\pi^+),K^-$ Real	0.0	0.0	0.0	0.0	0.0	0.0
$K_1(1270)^+(\to K^*(892),\pi^+),K^-$ Imaginary	0.0	0.0	0.0	0.0	0.0	0.0
$\overline{K_1}(1270)^-(\to \overline{K_0}^*(892),\pi^-),K^+$ Real	0.397	0.283	0.283	0.282	0.283	0.691
$\overline{K_1}(1270)^-(\to \overline{K_0}^*(892),\pi^-),K^+$ Imaginary	0.301	0.201	0.199	0.194	0.200	0.499
$K_1(1270)^+(\to \rho(770),K^+),K^-$ Real	2.458	0.376	0.456	0.375	0.376	2.583
$K_1(1270)^+(\to \rho(770),K^+),K^-$ Imaginary	1.140	0.252	0.302	0.256	0.252	1.258
$\overline{K_1}(1270)^-(\to \rho(770),K^-),K^+$ Real	4.891	0.400	0.835	0.397	0.401	5.01
$\overline{K_1}(1270)^-(\to \rho(770),K^-),K^+$ Imaginary	0.897	0.553	0.544	0.545	0.553	1.417
$K^+(1410)(\to K^*(892),\pi^+),K^-$ Real	1.470	0.044	0.042	0.788	0.019	1.669
$K^+(1410)(\to K^*(892),\pi^+),K^-$ Imaginary	2.077	0.756	0.756	0.738	0.756	2.564
$\overline{K^-}(1410)(\to \overline{K^*}(892),\pi^-),K^+$ Real	1.332	1.162	1.160	1.159	1.162	2.677
$\overline{K^-}(1410)(\to \overline{K^*}(892),\pi^-),K^+$ Imaginary	2.849	0.926	0.925	0.943	0.925	3.402
$K^*(892)\overline{K}^*(892)$ S wave Real	3.193	0.776	0.777	0.778	0.776	3.551
$K^*(892)\overline{K}^*(892)$ S wave Imaginary	0.700	0.903	0.901	0.902	0.903	1.935
$\phi(1020)\rho(770)$ S wave Real	1.300	0.761	0.762	0.77	0.761	2.006
$\phi(1020)\rho(770)$ S wave Imaginary	3.414	0.953	0.959	0.964	0.954	3.914
$\phi(1020)\rho(770)$ D wave Real	1.155	0.639	0.641	0.648	0.639	1.726
$\phi(1020)\rho(770)$ D wave Imaginary	2.312	0.474	0.479	0.480	0.474	2.501
$\phi(1020),(\pi^+,\pi^-)_S$ P wave Real	1.739	1.041	1.041	1.048	1.041	2.716
$\phi(1020),(\pi^+,\pi^-)_S$ P wave Imaginary	2.548	0.142	0.139	0.143	0.148	2.564
$(\pi^+K^-)_P,(\pi^-K^+)_S$ P wave Real	3.551	0.804	0.806	0.808	0.805	3.9
$(\pi^+K^-)_P,(\pi^-K^+)_S$ P wave Imaginary	0.927	1.172	1.169	1.173	1.171	2.52

Table 6.10: Table of combined systematic shifts, resulting from uncertainties on the measured masses and widths of each resonance. All shifts are quoted in units of statistical uncertainty.

Component	$K_1(1270)$	$K^*(892)$	$\rho(770)$	$K^*(1410)$	$\phi(1020)$	**Total**
$K_1(1270)^+(\to K^*(892),\pi^+),K^-$	1.931	0.552	0.556	0.555	0.567	2.23
$\overline{K_1}(1270)^-(\to \overline{K_0}^*(892),\pi^-),K^+$	1.064	0.185	0.19	0.194	0.19	1.13
$K_1(1270)^+(\to \rho(770),K^+),K^-$	0.534	0.3	0.304	0.302	0.306	0.808
$\overline{K_1}(1270)^-(\to \rho(770),K^-),K^+$	0.395	0.039	0.066	0.03	0.041	0.406
$K^+(1410)(\to K^*(892),\pi^+),K^-$	0.481	0.349	0.353	0.345	0.339	0.844
$\overline{K^-}(1410)(\to \overline{K^*}(892),\pi^-),K^+$	0.455	0.317	0.336	0.332	0.35	0.808
$K^*(892)\overline{K}^*(892)$ S wave	0.796	0.105	0.062	0.176	0.064	0.826
$\phi(1020)\rho(770)$ S wave	1.159	0.339	0.336	0.339	0.34	1.342
$\phi(1020)\rho(770)$ D wave	0.422	0.006	0.075	0.016	0.012	0.429
$\phi(1020),(\pi^+,\pi^-)_S$ P wave	0.201	0.188	0.185	0.187	0.18	0.421
$(\pi^+K^-)_P,(\pi^-K^+)_S$ P wave	0.919	0.208	0.205	0.207	0.196	1.005

Table 6.11: Table of combined systematic shifts, on the fit fractions for each resonance, resulting from uncertainties on the measured masses and widths of each resonance. All shifts are quoted in units of statistical uncertainty.

Component	$K_1(1270)$ **Mass Shift**	$K_1(1270)$ **Width Shift**	**Total**
$K_1(1270)^+(\to K^*(892),\pi^+),K^-$ Real	0.0	0.0	0.0
$K_1(1270)^+(\to K^*(892),\pi^+),K^-$ Imaginary	0.0	0.0	0.0
$\overline{K_1}(1270)^-(\to \overline{K_0}^*(892),\pi^-),K^+$ Real	0.327	0.226	0.397
$\overline{K_1}(1270)^-(\to \overline{K_0}^*(892),\pi^-),K^+$ Imaginary	0.27	0.133	0.301
$K_1(1270)^+(\to \rho(770),K^+),K^-$ Real	2.347	0.729	2.458
$K_1(1270)^+(\to \rho(770),K^+),K^-$ Imaginary	1.11	0.26	1.14
$\overline{K_1}(1270)^-(\to \rho(770),K^-),K^+$ Real	4.889	0.141	4.891
$\overline{K_1}(1270)^-(\to \rho(770),K^-),K^+$ Imaginary	0.658	0.61	0.897
$K^+(1410)(\to K^*(892),\pi^+),K^-$ Real	0.309	1.437	1.47
$K^+(1410)(\to K^*(892),\pi^+),K^-$ Imaginary	0.425	2.033	2.077
$\overline{K^-}(1410)(\to \overline{K^*}(892),\pi^-),K^+$ Real	1.073	0.79	1.332
$\overline{K^-}(1410)(\to \overline{K^*}(892),\pi^-),K^+$ Imaginary	0.642	2.776	2.849
$K^*(892)\overline{K^*}(892)$ S wave Real	0.766	3.1	3.193
$K^*(892)\overline{K^*}(892)$ S wave Imaginary	0.465	0.523	0.7
$\phi(1020)\rho(770)$ S wave Real	1.158	0.592	1.3
$\phi(1020)\rho(770)$ S wave Imaginary	0.595	3.362	3.414
$\phi(1020)\rho(770)$ D wave Real	0.902	0.721	1.155
$\phi(1020)\rho(770)$ D wave Imaginary	0.337	2.288	2.312
$\phi(1020),(\pi^+,\pi^-)_S$ P wave Real	1.09	1.356	1.739
$\phi(1020),(\pi^+,\pi^-)_S$ P wave (S) P wave Imaginary	0.311	2.529	2.548
$(\pi^+K^-)_P,(\pi^-K^+)_S$ P wave Real	0.863	3.445	3.551
$(\pi^+K^-)_P,(\pi^-K^+)_S$ P wave Imaginary	0.681	0.63	0.927

Table 6.12: Table of systematic shifts, on the fitted parameters, resulting from uncertainties on the measured mass and width of the $K_1(1270)$ resonance. All shifts are quoted in units of statistical uncertainty.

Component	$K_1(1270)$ **Mass Shift**	$K_1(1270)$ **Width Shift**	**Total**
$K_1(1270)^+(\to K^*(892),\pi^+),K^-$	0.698	1.801	1.931
$\overline{K_1}(1270)^-(\to \overline{K_0}^*(892),\pi^-),K^+$	0.644	0.847	1.064
$K_1(1270)^+(\to \rho(770),K^+),K^-$	0.479	0.236	0.534
$\overline{K_1}(1270)^-(\to \rho(770),K^-),K^+$	0.231	0.32	0.395
$K^+(1410)(\to K^*(892),\pi^+),K^-$	0.404	0.26	0.481
$\overline{K^-}(1410)(\to \overline{K^*}(892),\pi^-),K^+$	0.404	0.21	0.455
$K^*(892)\overline{K^*}(892)$ S wave	0.175	0.776	0.796
$\phi(1020)\rho(770)$ S wave	0.943	0.673	1.159
$\phi(1020)\rho(770)$ D wave	0.36	0.219	0.422
$\phi(1020),(\pi^+,\pi^-)_S$ P wave	0.174	0.099	0.201
$(\pi^+K^-)_P,(\pi^-K^+)_S$ P wave	0.571	0.72	0.919

Table 6.13: Table of systematic shifts, on the fit fractions, resulting from uncertainties on the measured mass and width of the $K_1(1270)$ resonance. All shifts are quoted in units of statistical uncertainty.

6.7.4 Mistag Rate Uncertainties

The expected mistag rate of each flavour tagged sample is also shifted from its measured value by one sigma and the shift was calculated in the same way as that of the background fractions. This component provides a very small contribution to the total systematic error.

6.7.5 Quantum Correlations

The analysis of the flavour tagged datasets at 3770 and 4170 can suffer from possible biases brought about by the correlated quantum production mechanism at these energies. Consider first the 3770 data. In this study it is assumed that (apart from the proportion of events that are mistagged) this sample would constitute a pure flavour tagged sample. However since the $D^0\overline{D}^0$ pair result from the decay of the $J^{PC} = 1^{--}$ $\psi(3770)$ particle, the D meson pair is produced in a correlated state and therefore the $D^0 \to K^+K^-\pi^+\pi^-$ decay rate will suffer interference from a contribution from the conjugate decay; $\overline{D}^0 \to K^+K^-\pi^+\pi^-$, and vice versa. The antisymmetric matrix which describes this correlated decay is shown in equation 6.4. In this equation, the state i may be defined as the final state of interest, $K^+K^-\pi^+\pi^-$ so that:

$$\begin{aligned} A_i &= A(D^0 \to K^+K^-\pi^+\pi^-) = A(x) \\ \overline{A}_i &= A(\overline{D}^0 \to K^+K^-\pi^+\pi^-) = \overline{A}(x) \end{aligned} \tag{6.14}$$

where x denotes a particular point in $K^+K^-\pi^+\pi^-$ Dalitz space. In the current analysis the flavour tagging is provided by tagging the other side D in its inclusive decay to kaons under the assumption of a Cabibbo favoured decay. For example $D^0 \to K^- + X$ and $\overline{D}^0 \to K^+ + X$. Therefore it is useful to consider the case where state j of equation 6.4 is defined to be a specific tag, labeled by the subscript t, so that:

$$A_j = A(D^0 \to K^-X_t) = K_t \tag{6.15}$$

$$\overline{A}_j = A(\overline{D}^0 \to K^-X_t) = K_t k_t e^{i\delta_t} \tag{6.16}$$

where δ_t, K_t and k_t are real numbers. Therefore from equation 6.4 the full decay rate for the decay of interest against the specific tag defined by equation 6.15 is given by:

$$\begin{aligned}\Gamma_t &\propto K_t^2(|A(x)|^2 + k_t^2|\overline{A}(x)|^2 \\ &- 2k_t[Re[A(x)\overline{A}(x)]\cos\delta_t + Im[A(x)\overline{A}(x)]\sin\delta_t]).\end{aligned} \tag{6.17}$$

Summing over all possible tags t, which will all in general have different values for k_t, K_t and δ_t, the full decay rate will therefore be given by:

$$\begin{aligned}\Gamma &\propto (\Sigma_t K_t^2)[|A(x)|^2 + \left(\frac{\Sigma_t K_t^2 k_t^2}{\Sigma_t K_t^2}\right)|\overline{A}(x)|^2 \\ &- 2(Re[A(x)\overline{A}(x)]\left(\frac{\Sigma_t K_t^2 k_t\cos\delta_t}{\Sigma_t K_t^2}\right) + Im[A(x)\overline{A}(x)]\left(\frac{\Sigma_t K_t^2 k_t\sin\delta_t}{\Sigma_t K_t^2}\right))]\end{aligned} \tag{6.18}$$

Therefore defining:

$$< k^2 > = \left(\frac{\Sigma_t K_t^2 k_t^2}{\Sigma_t K_t^2}\right) \tag{6.19}$$

$$< k\cos\delta > = \left(\frac{\Sigma_t K_t^2 k_t\cos\delta_t}{\Sigma_t K_t^2}\right) \tag{6.20}$$

$$< k\sin\delta > = \left(\frac{\Sigma_t K_t^2 k_t\sin\delta_t}{\Sigma_t K_t^2}\right) \tag{6.21}$$

equation 6.18 may be rewritten as:

$$\begin{aligned}\Gamma &\propto (\Sigma_t K_t^2)[|A(x)|^2 + |\overline{A}(x)|^2 < k^2 > \\ &- 2\left(Re[A(x)\overline{A}(x)] < k\cos\delta > + Im[A(x)\overline{A}(x)] < k\sin\delta >\right)].\end{aligned} \tag{6.22}$$

Since the tags in question are dominated by Cabibbo favoured and doubly Cabibbo suppressed decays it may be noted that $k_t \approx 0.05$, therefore the term $|\overline{A}(x)|^2 < k^2 >$ will be very small and can be neglected leaving the expression:

$$\begin{aligned}\Gamma &\propto (\Sigma_t K_t^2)[|A(x)|^2 + \\ &- 2\left(Re[A(x)\overline{A}(x)] < k\cos\delta > + Im[A(x)\overline{A}(x)] < k\sin\delta >\right)].\end{aligned} \tag{6.23}$$

It may also be assumed that the parameters relating to the tags; $(\Sigma_t K_t^2)$, $< k\cos\delta >$ and $< k\sin\delta >$ will not vary over the $K^+K^-\pi^+\pi^-$ Dalitz space. Therefore the term

$(\Sigma_t K_t^2)$ may be absorbed into the normalization. To assess the potential effect of the quantum correlations, a study is conducted in which the signal PDF is modified to the form given in expression 6.23. This is used to fit the 3770 flavour tagged dataset. Note there are now two additional free parameters, $< k\cos\delta >$ and $< k\sin\delta >$. The results of this fit are used to estimate the systematic shift on the measured parameters due to the quantum correlations present in this sample.

Quantum correlations are also present at the 4170 flavour tagged dataset. However since the D^0 and $\overline{D}^0$ particles are generally not produced directly at this energy but via various production mechanisms, as described in section 4.3.2, the interference effects, are expected to be diluted with respect to the 3770 case.

The quantum correlation parameters obtained from these fits are $< k\cos\delta >= 0.061 \pm 0.042$ and $< k\sin\delta >= 0.029 \pm 0.007$ for the 3770 dataset and $< k\cos\delta >= 0.051 \pm 0.032$ and $< k\sin\delta >= 0.037 \pm 0.011$ for the 4170 dataset. For both datasets the $< k\sin\delta >$ values are around three sigmas away from zero indicating the presence of quantum correlations.

The systematic shifts due to quantum correlations at the $\psi(3770)$ and $\psi(4170)$ centre of mass energies are added in quadrature in order to give the total systematic shift due to these effects. The combined effects of the quantum correlation present in these two datasets offered a small contribution to the total systematic uncertainty, being in all cases less than 0.35 that of the statistical uncertainty, as shown in tables 6.16, 6.15 and 6.14.

6.7.6 Efficiency Uncertainties

In order to estimate any possible systematic bias due to the description of the efficiency in the case of the flavour tagged CLEO-II.V dataset, the efficiency description was removed entirely from the analysis for this dataset. In practice this involved replacing the efficiency corrected Monte Carlo events with MINT Generated Monte Carlo events which had not been efficiency corrected.

In the case of the 3770, 4170 and CLEO-III datasets an alternative approach is employed to determine the efficiency systematic. An explicit function is developed to account for the efficiency. The magnitude of the three momentum of each of the final state particles is calculated. The kaon and pion with the highest three momentum are labeled as the fast kaon and fast pion respectively, the remaining particles are labeled as the slow kaon and slow pion. The efficiency corrected Monte Carlo events and the initially generated Monte Carlo sample (including events which are not selected after the detector and reconstruction simulation) are then used to produce histograms of efficiency in terms of the fast kaon momentum, slow kaon momentum, fast pion momentum and slow pion momentum, which are treated as independent variables. An efficiency function ϵ is then applied to the PDF, as explained in expression 5.30, where ϵ is given by:

$$\epsilon \;=\; \epsilon_{F\pi}(P_{F\pi}) \times \epsilon_{FK}(P_{FK}) \times \epsilon_{S\pi}(P_{S\pi}) \times \epsilon_{SK}(P_{SK}) \times \epsilon_{K_s}(s_{\pi^+\pi^-}). \quad (6.24)$$

Here $\epsilon_{F(S),K(\pi)}(P_{F(S)K(\pi)})$ gives the efficiency value as a function of the momentum of the fast (slow) kaon (pion) and $\epsilon_{K_s}(S_{\pi^+\pi^-})$ is a function which describes the effect of the K_S^0 veto cuts on the acceptance of $D \to K^+K^-\pi^+\pi^-$ events.

The K_S^0 veto cuts only affects events for which the $\pi^+\pi^-$ invariant mass fall within a certain range of the mass of the K_S^0 particle (0.22 GeV^2 < $\mathrm{S}_{\pi^+\pi^-}$ < 0.3 GeV^2) so the function $\epsilon_{K_S^0}$ is defined to be 1 outside of this range. In the case of the CLEO-III dataset, the function $\epsilon_{K_S^0}$ is defined to be 1 throughout since the K_S^0 veto cuts did not have a large effect on the signal for this dataset. A function is then developed in order to model the effects of the K_S^0 veto cuts within the appropriate range for each of the CLEO-c datasets. The efficiency as a function of $S_{\pi^+\pi^-}$ close to but outside of the range for which the K_S^0 veto cuts are applicable can be modelled with a linear functon. This is illustrated for the 3770 flavour tagged dataset in figure 6.20(a). Defining the function describing this straight line as ϵ_{line}, the acceptance in the region of the K_S^0 veto cuts, as a function of $S_{\pi^+\pi^-}$, is then assumed to be given by $\epsilon_{line}\epsilon_{K_s}$. The function ϵ_{K_s} is modelled as a quadratic function in terms of $S_{\pi^+\pi^-}$ as illustrated in figure 6.20(b) in which the ratio of selected events to generated events as a function of invariant mass squared are shown.

The shift on the measured parameters using this efficiency method compared to the method used in this study is taken as the systematic shift due to the efficiency treatment of these datasets. The total systematic error resulting from uncertainties in the way the efficiencies are handled is generally $0.2 - 0.3$ that of the statistical uncertainty, as shown in tables 6.16, 6.15 and 6.14.

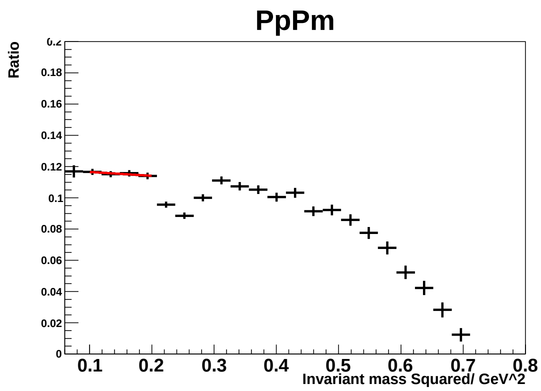

(a) Linear fit to acceptance in terms of $S_{\pi^+\pi^-}$ outside of the region for which the K_S^0 veto cuts are applicable. The K_S^0 veto cuts are applied between 0.2 and 0.35 GeV^2.

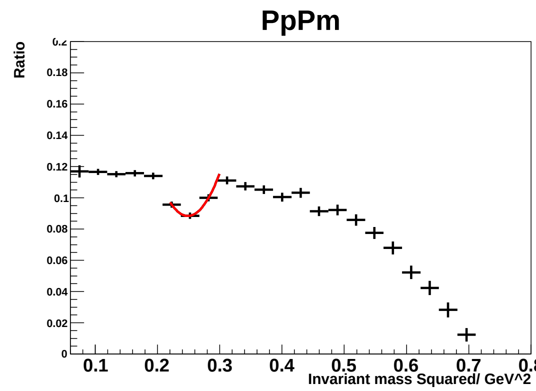

(b) Fit to acceptance in terms of $S_{\pi^+\pi^-}$ within the region for which the K_S^0 veto cuts are applicable. The K_S^0 veto cuts are applied between 0.2 and 0.35 GeV^2.

6.7.7 Fitter Bias

Studies which looked for evidence of fitter bias were described in section 6.6. These find small but significant effects. In order to estimate the systematic shift due to any biases in the fitter the shift on each variable, i is taken to be

$$\begin{aligned} \text{shift}_i &= \text{Mean of pull distribution, for parameter i} \\ &\times \text{ Statistical error on parameter, i} \end{aligned} \tag{6.25}$$

where the pull distributions are those described in section 6.6 in which Monte Carlo truth information is used for the particle's four momenta.The systetamtic uncertanties due to the fitter bias is in all cases less than 0.3 times that of the statistical uncertainty.

6.7.8 Reconstruction Effects

It is also necessary to estimate the shift on each of the variables due to the fact that the momenta of the particles, which are the inputs to the fit, are not reconstructed with perfect accuracy. The shift is calculated for each variable as described in equation 6.25 in this case using the pull study, described in section 6.6, in which the reconstructed four momenta are used as an input to the fit. The shift on each of the variables calculated in this way is assumed to result from a combination of the fitter bias and the reconstruction effects. Therefore, in order to estimate the shift due only to the reconstruction effects, shift_{Rec}, the shift due to the fitter bias, shift_{FB} is subtracted in quadrature from the total shift, shift_{tot}: $\text{shift}_{Rec} = \sqrt{(\text{shift}_{tot})^2 - (\text{shift}_{FB})^2}$. The reconstruction effects calculated in this way offered a relatively small contribution (is in all cases less than 0.3 times that of the statistical uncertainty) towards the total systemtic uncertainty.

6.7.9 Combined Systematic Results

Each of the systematic shifts which have been described are added in quadrature in order to calculate the total systematic shift on each variable. The systematic effects due to each of the effects described, are given in tables 6.14 and 6.15. Table 6.16 shows the systematic shifts on the fitted parameters which have been converted into polar coordinates.

From tables 6.14, 6.15 and 6.16 it is clear that the precision on the measurements of all parameters are limited by systematics rather than statistical precision. The dominant component contributing to the systematic comes from the knowledge of the masses and widths of the resonances in particular that of the $K_1(1270)$. The large systematics in this case are therefore considered to be unavoidable.

Component	**1**	**2**	**3**	**4**	**5**	**6**	**7**	**8**	**9**	**10**	**Total**	**Fitted Value ± Stat ± Syst**
$K_1(1270)^+(\to K^*(892),\pi^+),K^-$ Real	0.0	0.0	0.0	0.0	0.0	0.0	0.0	0.0	0.0	0.0	0.0	1.0±0.0±0.0
$K_1(1270)^+(\to K^*(892),\pi^+),K^-$ Imaginary	0.0	0.0	0.0	0.0	0.0	0.0	0.0	0.0	0.0	0.0	0.0	0.0±0.0±0.0
$\overline{K_1}(1270)^-(\to \overline{K_0}^*(892),\pi^-),K^+$ Real	0.375	0.691	0.044	0.201	0.216	0.026	0.035	0.218	0.423	0.0	0.967	0.157±0.078±0.075
$\overline{K_1}(1270)^-(\to \overline{K_0}^*(892),\pi^-),K^+$ Imaginary	0.059	0.499	0.074	0.104	0.332	0.049	0.023	0.341	0.027	0.0	0.706	-0.306±0.06±0.043
$K_1(1270)^+(\to \rho(770),K^+),K^-$ Real	0.311	2.583	0.071	0.149	0.531	0.021	0.045	0.362	0.071	0.138	2.69	4.067±0.64±1.721
$K_1(1270)^+(\to \rho(770),K^+),K^-$ Imaginary	0.062	1.258	0.029	0.281	0.162	0.009	0.175	0.278	0.14	0.278	1.378	4.219±0.886±1.22
$\overline{K_1}(1270)^-(\to \rho(770),K^-),K^+$ Real	0.346	5.01	0.014	0.208	0.443	0.026	0.037	0.79	0.003	0.029	5.107	6.897±0.593±3.028
$\overline{K_1}(1270)^-(\to \rho(770),K^-),K^+$ Imaginary	0.404	1.417	0.043	0.07	0.352	0.04	0.071	0.522	0.232	0.219	1.638	0.196±1.095±1.794
$K^+(1410)(\to K^*(892),\pi^+),K^-$ Real	0.621	1.669	0.027	0.104	0.11	0.045	0.222	0.401	0.31	0.267	1.891	4.617±0.561±1.061
$K^+(1410)(\to K^*(892),\pi^+),K^-$ Imaginary	0.156	2.564	0.097	0.207	0.189	0.019	0.044	0.172	0.09	0.0	2.593	-4.102±0.717±1.86
$\overline{K^-}(1410)(\to \overline{K^*}(892),\pi^-),K^+$ Real	1.155	2.677	0.092	0.235	0.2	0.011	0.098	0.196	0.046	0.062	2.942	2.609±0.926±2.725
$\overline{K^-}(1410)(\to \overline{K^*}(892),\pi^-),K^+$ Imaginary	0.029	3.402	0.065	0.175	0.222	0.015	0.141	0.515	0.345	0.227	3.481	-6.253±0.587±2.043
$K^*(892)\overline{K^*}(892)$ S wave Real	0.565	3.551	0.08	0.233	0.24	0.004	0.222	0.467	0.271	0.0	3.659	0.317±0.035±0.129
$K^*(892)\overline{K^*}(892)$ S wave Imaginary	0.464	1.935	0.096	0.223	0.261	0.019	0.069	0.445	0.134	0.0	2.075	0.13±0.043±0.09
$\phi(1020)\rho(770)$ S wave Real	0.388	2.006	0.121	0.143	0.419	0.018	0.183	0.384	0.337	0.0	2.163	-0.324±0.149±0.322
$\phi(1020)\rho(770)$ S wave Imaginary	0.414	3.914	0.134	0.139	0.585	0.02	0.341	0.368	0.012	0.0	4.016	0.985±0.094±0.376
$\phi(1020)\rho(770)$ D wave Real	0.322	1.726	0.115	0.119	0.376	0.019	0.134	0.319	0.196	0.24	1.863	0.204±0.326±0.608
$\phi(1020)\rho(770)$ D wave Imaginary	0.241	2.501	0.051	0.126	0.269	0.005	0.304	0.529	0.06	0.0	2.604	-1.428±0.183±0.477
$\phi(1020),(\pi^+,\pi^-)_S$ P wave Real	0.651	2.716	0.143	0.086	0.494	0.028	0.169	0.312	0.204	0.0	2.87	-1.698±0.834±2.393
$\phi(1020),(\pi^+,\pi^-)_S$ P wave Imaginary	0.245	2.564	0.083	0.244	0.262	0.01	0.163	0.518	0.204	0.122	2.669	-5.932±0.482±1.288
$(\pi^+K^-)_P,(\pi^-K^+)_S$ P wave Real	0.415	3.9	0.087	0.272	0.225	0.019	0.012	0.437	0.207	0.0	3.968	82.6±6.766±26.9
$(\pi^+K^-)_P,(\pi^-K^+)_S$ P wave Imaginary	0.989	2.52	0.104	0.187	0.186	0.018	0.082	0.162	0.03	0.0	2.728	11.4±9.744±26.6
K_S^0 Background Fraction 3770	0.002	0.0	0.01	0.394	0.072	0.006	0.011	0.106	0.0	0.0	0.415	0.028±0.005±0.002
K_S^0 Background Fraction 4170	0.002	0.0	0.005	0.19	0.014	0.002	0.019	0.142	0.0	0.0	0.238	0.019±0.006±0.001

Table 6.14: Table of all systematic uncertainties. The systematic shifts are given in terms of the statistical uncertainty for the parameter in question. The number of the head of each column refers to the following systematics: 1) BW Model 2) Masses and Widths of Resonances 3) CP backgrounds 4) Flavour Backgrounds 5) Flavour Backgrounds Fractions 6) Mistag Fractions 7) Quantum Correlations 8) Efficiencies 9) Fitter Bias 10) Reconstruction Effects.

Component	1	2	3	4	5	6	7	8	9	10	Total	Fitted Value ± Stat ± Syst
$K_1(1270)^+(\rightarrow K^*(892),\pi^+),K^-$	0.566	2.23	0.059	0.268	0.291	0.011	0.163	0.569	0.049	0.0	2.409	0.073±0.008±0.019
$\overline{K_1}(1270)^-(\rightarrow \overline{K_0}^*(892),\pi^-),K^+$	0.409	1.13	0.086	0.112	0.429	0.036	0.053	0.152	0.281	0.234	1.344	0.009±0.003±0.004
$K_1(1270)^+(\rightarrow \rho(770),K^+),K^-$	0.297	0.808	0.013	0.32	0.176	0.015	0.132	0.343	0.032	0.083	1.009	0.047±0.008±0.008
$\overline{K_1}(1270)^-(\rightarrow \rho(770),K^-),K^+$	0.317	0.406	0.06	0.087	0.598	0.034	0.075	0.505	0.048	0.085	0.951	0.06±0.008±0.008
$K^+(1410)(\rightarrow K^*(892),\pi^+),K^-$	0.159	0.844	0.046	0.281	0.151	0.017	0.138	0.334	0.353	0.258	1.079	0.042±0.007±0.008
$\overline{K^-}(1410)(\rightarrow \overline{K^*}(892),\pi^-),K^+$	0.335	0.808	0.035	0.13	0.263	0.013	0.048	0.471	0.046	0.238	1.065	0.047±0.007±0.007
$K^*(892)\overline{K^*}(892)$ S wave	0.223	0.826	0.064	0.266	0.191	0.008	0.201	0.641	0.051	0.006	1.14	0.061±0.008±0.009
$\phi(1020)\rho(770)$ S wave	0.345	1.342	0.099	0.054	0.67	0.023	0.414	0.22	0.225	0.225	1.644	0.383±0.025±0.041
$\phi(1020)\rho(770)$ D wave	0.278	0.429	0.026	0.04	0.142	0.018	0.277	0.656	0.092	0.1	0.9	0.034±0.007±0.006
$\phi(1020),(\pi^+,\pi^-)_S$ P wave	0.57	0.421	0.1	0.087	0.18	0.045	0.187	0.191	0.19	0.0	0.813	0.103±0.01±0.008
$(\pi^+K^-)_P,(\pi^-K^+)_S$ P wave	0.232	1.005	0.055	0.204	0.543	0.039	0.166	0.904	0.219	0.0	1.516	0.109±0.012±0.018
Fit Fraction Sum	0.078	3.757	0.046	0.072	0.303	0.029	0.376	0.42	0.081	0.46	3.841	0.967±0.026±0.099

Table 6.15: Table of all systematic uncertainties for the fit fractions of each component. Each of the systematic shifts are given in terms of the statistical error for the parameter in question. The number of the head of each column refers to the following systematics: 1) BW Model 2) Masses and Widths of Resonances 3) CP backgrounds 4) Flavour Backgrounds 5) Flavour Backgrounds Fractions 6) Mistag Fractions 7) Quantum Correlations 8) Efficiencies 9) Fitter Bias 10) Reconstruction Effects.

Component	**1**	**2**	**3**	**4**	**5**	**6**	**7**	**8**	**9**	**10**	**Total**	**Fitted Value ± Stat ± Syst**
$K_1(1270)^+(\to K^*(892), \pi^+), K^-$ Phase	0.0	0.0	0.0	0.0	0.0	0.0	0.0	0.0	0.0	0.0	0.0	0.0±0.0±0.0
$K_1(1270)^+(\to K^*(892), \pi^+), K^-$ Amplitude	0.0	0.0	0.0	0.0	0.0	0.0	0.0	0.0	0.0	0.0	0.0	1.0±0.0±0.0
$\overline{K_1}(1270)^-(\to \overline{K_0}^*(892), \pi^-), K^+$ Phase	0.359	0.827	0.024	0.183	0.095	0.042	0.041	0.304	0.402	0.0	1.055	1.098±0.215±0.227
$\overline{K_1}(1270)^-(\to \overline{K_0}^*(892), \pi^-), K^+$ Amplitude	0.174	0.034	0.083	0.153	0.391	0.027	0.005	0.225	0.236	0.0	0.568	0.345±0.064±0.036
$K_1(1270)^+(\to \rho(770), K^+), K^-$ Phase	0.141	0.455	0.06	0.174	0.428	0.017	0.111	0.065	0.156	0.135	0.709	0.804±0.131±0.093
$K_1(1270)^+(\to \rho(770), K^+), K^-$ Amplitude	0.227	2.516	0.033	0.297	0.215	0.011	0.17	0.43	0.073	0.308	2.614	5.86±0.777±2.031
$\overline{K_1}(1270)^-(\to \rho(770), K^-), K^+$ Phase	0.421	1.274	0.043	0.07	0.339	0.04	0.07	0.511	0.126	0.218	1.501	0.028±0.159±0.238
$\overline{K_1}(1270)^-(\to \rho(770), K^-), K^+$ Amplitude	0.299	5.097	0.013	0.208	0.426	0.024	0.041	0.758	0.007	0.047	5.184	6.9±0.593±3.077
$K^+(1410)(\to K^*(892), \pi^+), K^-$ Phase	0.468	3.036	0.091	0.221	0.197	0.041	0.089	0.294	0.106	0.15	3.108	0.726±0.106±0.329
$K^+(1410)(\to K^*(892), \pi^+), K^-$ Amplitude	0.306	1.036	0.062	0.109	0.119	0.017	0.18	0.267	0.272	0.178	1.186	6.177±0.635±0.753
$\overline{K^-}(1410)(\to \overline{K^*}(892), \pi^-), K^+$ Phase	1.037	3.461	0.106	0.22	0.249	0.009	0.13	0.227	0.129	0.12	3.644	1.176±0.13±0.475
$\overline{K^-}(1410)(\to \overline{K^*}(892), \pi^-), K^+$ Amplitude	0.761	1.663	0.013	0.219	0.082	0.017	0.065	0.445	0.264	0.154	1.922	6.776±0.649±1.247
$K^*(892)\overline{K^*}(892)$ S wave Phase	0.638	1.198	0.105	0.261	0.232	0.018	0.005	0.366	0.209	0.0	1.467	0.39±0.123±0.181
$K^*(892)\overline{K^*}(892)$ S wave Amplitude	0.266	3.859	0.066	0.174	0.278	0.008	0.229	0.547	0.185	0.0	3.932	0.342±0.036±0.143
$\phi(1020)\rho(770)$ S wave Phase	0.471	2.416	0.145	0.13	0.507	0.021	0.243	0.354	0.328	0.0	2.578	1.889±0.139±0.359
$\phi(1020)\rho(770)$ S wave Amplitude	0.164	3.042	0.066	0.164	0.389	0.011	0.222	0.433	0.157	0.0	3.118	1.037±0.1±0.313
$\phi(1020)\rho(770)$ D wave Phase	0.347	2.052	0.119	0.113	0.388	0.019	0.153	0.269	0.188	0.237	2.167	1.429±0.224±0.486
$\phi(1020)\rho(770)$ D wave Amplitude	0.131	1.89	0.026	0.14	0.221	0.005	0.266	0.591	0.114	0.07	2.024	1.444±0.187±0.378
$\phi(1020), (\pi^+, \pi^-)_S$ P wave Phase	0.684	2.636	0.155	0.116	0.514	0.029	0.194	0.38	0.164	0.02	2.816	1.85±0.132±0.371
$\phi(1020), (\pi^+, \pi^-)_S$ P wave Amplitude	0.02	3.009	0.023	0.196	0.202	0.007	0.067	0.365	0.276	0.11	3.059	6.172±0.518±1.583
$(\pi^+K^-)_P, (\pi^-K^+)_S$ P wave Phase	1.037	2.137	0.112	0.164	0.166	0.02	0.082	0.166	0.048	0.0	2.397	0.137±0.116±0.279
$(\pi^+K^-)_P, (\pi^-K^+)_S$ P wave Amplitude	0.126	4.245	0.064	0.299	0.255	0.016	0.016	0.431	0.197	0.0	4.291	83.4±6.834±29.3

Table 6.16: Table of all systematic uncertainties for the fitted parameters expressed in polar coordinates. Each of the systematic shifts are given in terms of the statistical error for the parameter in question. All phases are measured in radians. The number of the head of each column refers to the following systematics: 1) BW Model 2) Masses and Widths of Resonances 3) CP backgrounds 4) Flavour Backgrounds 5) Flavour Backgrounds Fractions 6) Mistag Fractions 7) Quantum Correlations 8) Efficiencies 9) Fitter Bias 10) Reconstruction Effects.

6.8 Robustness Test

In addition to the ensemble study a further robustness test is carried out. In order to test the consistency of the individual datasets the data are separated into two samples: those collected at centre of mass energies around that of the Υ resonances (this consisted of the CLEO-III and CLEO-II.V datasets) and those collected at the lower centre of mass energies of CLEO-c (the 3770 and 4170 datasets). The selection techniques used for each of these datasets is distinct and so the comparison provides a particularly convincing test of consistency. Separate fits are carried out using each of these datasets. The fit fractions obtained for each dataset are then compared. The uncorrelated systematic errors (for example the systematic errors associated with the handling of the efficiency and bacgrounds in the fit but not the systematic errors associated with the Breit Wigner descriptions or masses and widths of the resonances) are included in comparing the fit fractions of the two datasets. The comparison is shown in table 6.17. This shows that the amplitude model produced from the lower energy CLEO-c datasets is consistent with that produced by the CLEO-II.V and CLEO-III datasets to within the stated uncertainties.

Decay	**CLEO-II.V/III Datasets**	**CLEO-c Datasets**	**Relative Shift**
$K_1(1270)^+(\rightarrow K^*(892), \pi^+), K^-$	$4.4 \pm 0.9 \pm 0.9$	$9.8 \pm 1.2 \pm 4.6$	1.1
$\overline{K_1}(1270)^-(\rightarrow \overline{K_0}^*(892), \pi^-), K^+$	$3.6 \pm 0.9 \pm 1.1$	$0.2 \pm 0.2 \pm 2.3$	1.2
$K_1(1270)^+(\rightarrow \rho(770), K^+), K^-$	$2.6 \pm 0.8 \pm 0.5$	$8.5 \pm 1.4 \pm 4.2$	1.3
$\overline{K_1}(1270)^-(\rightarrow \rho(770), K^-), K^+$	$7.9 \pm 1.2 \pm 1.1$	$3.5 \pm 1.1 \pm 3.4$	1.1
$K^+(1410)(\rightarrow K^*(892), \pi^+), K^-$	$4.5 \pm 0.9 \pm 0.6$	$4.5 \pm 1.1 \pm 1.2$	0.0
$\overline{K^-}(1410)(\rightarrow \overline{K^*}(892), \pi^-), K^+$	$5.5 \pm 1.0 \pm 0.8$	$4.6 \pm 0.9 \pm 1.1$	0.4
$K^*(892)\overline{K^*}(892)$	$7.5 \pm 1.8 \pm 2.0$	$5.2 \pm 1.0 \pm 2.0$	0.7
$\phi(1020)\rho(770)$	$39.8 \pm 2.7 \pm 3.1$	$36.9 \pm 3.2 \pm 4.0$	0.5
$\phi(1020)\rho(770)$ D wave	$4.7 \pm 1.0 \pm 1.1$	$1.7 \pm 0.8 \pm 2.3$	1.0
$\phi(1020), (\pi^+, \pi^-)_S$ P wave	$8.3 \pm 1.2 \pm 0.7$	$10.9 \pm 1.7 \pm 3.0$	0.7
$(\pi^+K^-)_P, (\pi^-K^+)_S$ P wave	$14.7 \pm 1.8 \pm 4.5$	$7.8 \pm 1.4 \pm 5.3$	1.1

Table 6.17: Fit fractions for the separate fits to the CLEO II.V and CLEO-III datasets and to the CLEO-c datasets. The relative shift is given in terms of the number of standard deviations. The systematic effects were larger for the CLEO-c sample, this was presumably due to acceptance and background effects that affected particularly sensitive regions of phase space for this dataset.

6.9 Summary

In this chapter the final model for the signal decay has been presented. The systematic effects have been described and were determined to dominate the error on the final result, due mainly to large uncertainties on the masses and widths of the resonant particles. A further discussion of the results is given in chapter 7.

Chapter 7

Discussion of the results and a Search for CP Violation

7.1 Discussion of the Final Amplitude Model

The fit fractions for the final model for the amplitude fit are shown in table 7.1. The dominant contribution is from the $D \to VV$ mode $D \to \phi(1020)\rho(770)$ where the ϕ and ρ resonances are in a relative S wave. The total contribution from the $D \to \phi\rho$ modes is found to be $\approx 40\%$. The next largest contribution is the $D \to AP$ mode $D \to K_1(1270)^+(\to K^*(892)\pi^+)K^-$. In total the $D \to VP$ modes make up $\approx 30\%$ of the final amplitude model. There are also contributions from a non resonant decay and the quasi three body decay mode $D \to \phi(1020)\pi^+\pi^-$ (in which the $\pi\pi$ system and ϕ resonance are in a relative S wave) which are both $\approx 10\%$. There is also a small contribution from the $D \to VV$ mode $D \to K^{*+}(892)\overline{K^{*-}}(892)$ of $\approx 5\%$.

The fact that the dominant contributions are from the $D \to \phi\rho$ and the $D \to AP$ modes can be understood physically because such decays can proceed via tree level processes involving a W meson which couples strongly to vector and axial vector particles. Similarly the three body decay $D \to \phi\pi^+\pi^-$ can proceed via tree level process and so the significant contribution of this mode is expected. Conversely the $D \to VV$ mode $D \to K^*(892)\overline{K^*}(892)$ cannot occur via a tree level process and is expected to proceed dominantly via rescattering, therefore the relatively small contribution of this mode to the final model is also expected. The final model does not contain any contribution from the mode $D \to f_0(980)\pi^+\pi^-$ despite the fact that the $f_0(980)$ resonance couples strongly to K^+K^- channel.

Component	**Fit Fraction**	**Total Fit Fraction**
$K_1(1270)^+(\rightarrow K^*(892), \pi^+), K^-$	0.073±0.008±0.019	**0.278±0.017±0.025**
$\overline{K_1}(1270)^-(\rightarrow \overline{K_0}^*(892), \pi^-), K^+$	0.009±0.003±0.004	
$K_1(1270)^+(\rightarrow \rho(770), K^+), K^-$	0.047±0.008±0.008	
$\overline{K_1}(1270)^-(\rightarrow \rho(770), K^-), K^+$	0.06±0.008±0.008	
$K^+(1410)(\rightarrow K^*(892), \pi^+), K^-$	0.042±0.007±0.008	
$\overline{K^-}(1410)(\rightarrow \overline{K^*}(892), \pi^-), K^+$	0.047±0.007±0.007	
$K^*(892)\overline{K^*}(892)$ S wave	0.061±0.008±0.009	**0.061±0.008±0.009**
$\phi(1020)\rho(770)$ S wave	0.383±0.025±0.041	**0.417±0.026±0.041**
$\phi(1020)\rho(770)$ D wave	0.034±0.007±0.006	
$\phi(1020), \pi^+, \pi^-$ (V) S wave	0.103±0.010±0.008	**0.103±0.010±0.008**
$(\pi^+K^-)_P, (\pi^-K^+)_S$ P wave	0.109±0.012±0.018	**0.109±0.012±0.018**

Table 7.1: The fit fractions for the final amplitude model. Errors are quoted as stat ± sys. The third column gives the fit fractions for the corresponding rows added.

Table 7.2 illustrates the change in fit parameters and fit quality when the baseline model is modified in various ways (which were not previously shown in table 6.2). This is shown in order to justify the presence of certain components in the final model while other similar components have not been included. Table 7.2 shows that if the decay mode $D \rightarrow f_0(980)\pi^+\pi^-$ is included in the fit, either in addition (column two) or instead of (column three) the non resonant component the resulting fit fraction of this component is very small and the quality of the fit (according to the χ^2_{DOF}) is reduced.

It may also be noted that certain angular momentum states are preferred over others in the final model. In the case of the non resonant component neutral pion-kaon pairs exist in a P wave state. Table 7.2 also shows a comparison between the final model and models in which other angular momentum states are included. For example the final model contains a component $D^0 \rightarrow K^*(892)\overline{K^*}(892)$, where the K^* and $\overline{K}^*$ resonances exist in a relative S wave, columns six to eight of Table 7.2 also shows models for which the resonances are in a relative P or D wave. In each case the quality of the fit is decreased and the additional angular momentum states only offer small contributions. This justifies the decision not to include these contributions in the final signal model.

	1	2	3	4	5	6	7	8
$K_1(1270)^+(\to K^*(892),\pi^+),K^-$	0.073±0.008	0.072±0.008	0.07±0.008	0.062±0.008	0.076±0.008	0.077±0.008	0.076±0.008	0.073±0.008
$\overline{K_1}(1270)^-(\to \overline{K_0}^*(892),\pi^-),K^+$	0.009±0.003	0.009±0.003	0.018±0.004	0.011±0.004	0.009±0.003	0.009±0.003	0.008±0.003	0.009±0.003
$K_1(1270)^+(\to \rho(770),K^+),K^-$	0.047±0.007	0.053±0.008	0.049±0.008	0.054±0.008	0.047±0.007	0.045±0.007	0.044±0.007	0.048±0.007
$\overline{K_1}(1270)^-(\to \rho(770),K^-),K^+$	0.06±0.008	0.05±0.008	0.09±0.012	0.044±0.007	0.059±0.007	0.057±0.007	0.056±0.007	0.061±0.008
$K^+(1410)(\to K^*(892),\pi^+),K^-$	0.042±0.007	0.042±0.007	0.049±0.008	0.047±0.007	0.047±0.007	0.039±0.008	0.05±0.007	0.034±0.008
$\overline{K^-}(1410)(\to \overline{K^*}(892),\pi^-),K^+$	0.047±0.006	0.046±0.006	0.055±0.007	0.038±0.007	0.046±0.007	0.029±0.006	0.047±0.007	0.03±0.007
$K^*(892)\overline{K^*}(892)$ S wave	0.061±0.008	0.063±0.008	0.081±0.009	0.089±0.01	0.06±0.008	0.019±0.006	0.018±0.006	0.061±0.008
$K^*(892)\overline{K^*}(892)$ P wave	-	-	-	-	-	0.01±0.003	-	0.009±0.004
$K^*(892)\overline{K^*}(892)$ D wave	-	-	-	-	-	0.041±0.008	0.046±0.009	-
$\phi(1020)\rho(770)$ S wave	0.383±0.022	0.38±0.022	0.33±0.02	0.43±0.024	0.39±0.021	0.397±0.021	0.398±0.021	0.381±0.021
$\phi(1020)\rho(770)$ P wave	-	-	-	-	0.008±0.004	-	-	-
$\phi(1020)\rho(770)$ D wave	0.034±0.007	0.035±0.007	0.033±0.007	0.03±0.007	0.035±0.007	0.033±0.006	0.033±0.006	0.034±0.006
$\phi(1020),(\pi^+,\pi^-)_S$ P wave	0.103±0.01	0.1±0.009	0.089±0.009	0.079±0.009	0.101±0.01	0.099±0.01	0.098±0.01	0.104±0.01
$(\pi^+K^-)_P,(\pi^-K^+)_S$ P wave	0.109±0.012	0.104±0.011	-	-	0.112±0.012	0.1±0.011	0.098±0.011	0.109±0.011
$(\pi^+K^-)_S,(\pi^-K^+)_S$	-	-	-	0.131±0.014	-	-	-	-
$f(0)(980),\pi^+,\pi^-$	-	0.006±0.003	0.025±0.006	-	-	-	-	-
Sum	**0.967±0.026**	**0.96±0.026**	**0.889±0.022**	**1.015±0.026**	**0.991±0.024**	**0.955±0.025**	**0.974±0.025**	**0.955±0.025**
χ^2 **per DOF**	**1.633**	**1.665**	**2.131**	**2.069**	**1.665**	**1.699**	**1.707**	**1.675**

Table 7.2: The fit fractions and χ^2 values for the final model (column 1) compared with the fit fractions for some similar models.

7.1.1 Comparison to the FOCUS model

Table 7.3 shows a comparison between the fit fractions obtained in the best fit to the CLEO data and the model produced by the analysis of data collected at the FOCUS experiment [77]. The study carried out at FOCUS did not distinguish between conjugate decays modes. For example $K_1(1270)^+K^-$ and $K_1(1270)^+K^-$. Therefore for the purpose of this comparison these modes are amalgamated in the CLEO model.

Both models show sizable contributions from $K_1(1270)^{\pm}K^{\mp}$ and $\phi\rho$ decay modes, although the former is more abundant in the FOCUS model while the latter dominates in the CLEO model. In both models the $K_1(1270)$ decays in equal proportions (to within the calculated uncertainties) via $K^*(892)$ and ρ to the final state. Both models show a small contribution from the $K^*(892)\overline{K^*}(892)$ decay mode. FOCUS finds a large ($\approx 20\%$) contribution from the $D \rightarrow AP$ mode $K_1^{\pm}(1400)K^{\mp}$, which is not present in the final CLEO model. The CLEO model contains a significant contribution ($\approx 9\%$) from the mode $K^{\pm}(1410)(\rightarrow K^*(892)\pi^{\pm})K^{\mp}$ which is not included in the FOCUS model. Another significant difference between the two models is the contribution ($\approx 10\%$) of a non-resonant decay mode in the CLEO model which is not present in the FOCUS model. Finally the FOCUS model includes a sizable ($\approx 15\%$) contribution from the decay mode $f_0(980)\pi^+\pi^-$, which is not present in the CLEO model (the inclusion of this mode in the CLEO model is disfavored as described in the previous section). However the quoted error on this component is high (13%) and so the models agree to within errors. The CLEO and FOCUS models both show significant contributions ($\approx 10\%$ and $\approx 30\%$ respectively) from three body intermediate states. The FOCUS model does not consider differing angular momentum states between final state particles so no comparison of these can be made of these contributions.

7.2 Sensitivity to γ From $B^{\pm} \rightarrow D(\rightarrow K^+K^-\pi^+\pi^-)K^{\pm}$

As discussed in chapter 1, measurements of γ may be made from a single decay of the form $B^{\pm} \rightarrow D(\rightarrow f)K^{\pm}$, where f is accessible from both D^0 and $\overline{D}^0$. A measurement of γ via this method requires independent knowledge of the resonant

Component	**CLEO model**	**FOCUS Model**
$K_1(1270)^{\pm}(\to K^*(892), \pi^{\pm}), K^{\mp}$	0.082±0.009±0.019	0.16±0.04±0.05
$K_1(1270)^{\pm}(\to \rho(770), K^{\pm}), K^{\mp}$	0.107±0.011±0.011	0.18±0.06±0.03
$K_1(1270)^{\pm}(\to K^*(1430), \pi^{\pm}), K^{\mp}$	-	0.02±0.01±0.00
Sum of $K_1(1270)^{\pm}K^{\mp}$ modes	0.189±0.014±0.022	0.33±0.06±0.04
$K^{\pm}(1410)(\to K^*(892), \pi^{\pm}), K^{\mp}$	0.089±0.010±0.011	-
$K_1^{\pm}(1400)K^{\mp}$	-	0.22±0.03±0.04
$K^*(892)\overline{K^*}(892)$	0.061±0.008±0.009	0.03±0.02±0.01
$K^*(892)K^{\pm}\pi^{\mp}$	-	0.11±0.02±0.01
$\phi(1020)\rho(770)$	0.417±0.026±0.041	0.29±0.02±0.01
ρ, K^+K^-	-	0.02±0.02±0.02
$\phi(1020), \pi^+, \pi^-$	0.103±0.010±0.008	0.01±0.01±0.00
$f_0(980)\pi^+\pi^-$	-	0.15±0.13±0.02
Non resonant	0.109±0.012±0.018	-

Table 7.3: The fit fractions for the final amplitude model presented in this thesis compared to the model obtained in a previous study on this decay mode performed by the FOCUS collaboration [77].The first uncertainty is statistical, the second systematic.

substructure of the decay $D^0 \to f$. The four body decay $D \to K^+K^-\pi^+\pi^-$ is a potential candidate for a γ measurement using this approach.

The model developed in this thesis (that shown in the first column of table 7.2) is used in a toy MC study to assess the potential of the mode $D \to K^+K^-\pi^+\pi^-$ in a γ measurement.

A previous study had been carried out [85] into the sensitivity to γ which is achievable through this channel, based on the FOCUS model. As the FOCUS analysis did not distinguish between D^0 and $\overline{D}^0$ decays, this study had to make assumptions about the respective D^0 and $\overline{D}^0$ contributions to different states. The sensitivity to the angle γ determined by this study was $14.4 \pm 0.7°$ based on samples of 1000 events, but this conclusion is dependent on the assumptions made.

In order to determine the sensitivity to γ via this channel, sets of 1000 B^+ and 1000 B^- events (corresponding to 1 fb^{-1}) are generated. The amplitudes for these decays are as described in chapter 1 and are given by:

$$A(B^+ \to D(K^+K^-\pi^+\pi^-)K^+) = A_B(A_D + \overline{A}_D r_B \exp i(\delta_B + \gamma) \quad (7.1)$$

$$A(B^- \to D(K^+K^-\pi^+\pi^-)K^-) = A_B(A_D + \overline{A}_D r_B \exp i(\delta_B - \gamma)) \quad (7.2)$$

where the amplitude A_D is given by one of the models for the $D^0 \to K^+K^-\pi^+\pi^-$ decay as presented in 6.2. Initial values for the parameters γ, δ_B and r_B are taken as 70°, 130° and 0.1 respectively. The likelihood functions for the B^+ and B^- events are defined as:

$$P(B^+) = N|A^+|^2 \frac{d^4\phi}{dt_{01}ds_{12}ds_{23}ds_{34}dt_{04}} \tag{7.3}$$

$$P(B^-) = N|A^-|^2 \frac{d^4\phi}{dt_{01}ds_{12}ds_{23}ds_{34}dt_{04}} \tag{7.4}$$

where N is a normalization constant which is obtained through numerical integration and $A^{\pm}$ are the amplitudes for the B^+ and B^- decays defined in equations 7.1 and 7.2 respectively. Having generated B^+ and B^- events according to these likelihood functions, the events are then fitted for the three parameters γ, δ_B and r_B, with all other parameters fixed. Detector and background effects are neglected in the generation and fitting of these events. A log-likelihood fit is carried out, in the same way as was described in Chapter 5 for the fitting of the parameters associated with the $D^0 \to K^+K^-\pi^+\pi^-$ decay. The log-likelihood function in this case is defined as:

$$\log(\mathcal{L}) = \sum_{B^+ \text{ events}} \log(P(B^+)) + \sum_{B^- \text{ events}} \log(P(B^-)). \tag{7.5}$$

The negative log-likelihood function is minimized in terms of the parameters; γ, δ_B and r_B for each set of events. Many such "toy experiments" are generated and fit (typically 60 due to computational limitations), and pull distributions are constructed for each of the three free parameters. Gaussians are fit to these distributions to obtain a mean and width.

The results of these fits are illustrated in Table 7.4 when using model one to generate the $D^0 \to K^+K^-\pi^+\pi^-$ decay. The results are all consistent to within two standard deviations of Gaussians with mean values of 0 and widths of 1. Therefore it was assumed that the log-likelihood fit was unbiased. The errors obtained for each variable are averaged over each of the fits and are displayed in table 7.4. The sensitivity to γ which is obtained was 11°.

	Initial Value	**Error**	**Pull Mean**	**Pull Width**
r_B	0.10	0.020±0.0001	-0.13 ±0.17	0.97±0.16
δ_B	130 deg	11.3±0.3 deg	0.03±0.17	0.88±0.26
γ	70 deg	11.3±0.3 deg	0.43±0.25	1.23±0.44

Table 7.4: The results of the fits of each of the pull distributions to Gaussians.

The sensitivity test as described above is repeated using each of the 8 models described in Table 6.2, these being the models which gave satisfactory agreement with the CLEO data. The results of this test are shown in Table 7.5. It is apparent from these results that most models give a very consistent sensitivity to γ with the exception of model 7 which is 50% worse.

Model Number	**Sensitivity to γ deg.**
1	11.3 ± 0.3
2	11.3 ± 0.3
3	11.7 ± 0.3
4	12.2 ± 0.3
5	11.2 ± 0.3
6	10.7 ± 0.3
7	18.9 ± 0.8
8	10.9 ± 0.3

Table 7.5: The sensitivity to γ when each of the models in table 6.2 is used to describe the $D^0 \to K^+K^-\pi^+\pi^-$ decay. The numbering convention is the same as that used in table 6.2.

This channel contains only charged particles in the final state and is therefore a good candidate for measurements at hadron experiments such as LHCb. In order to make a more accurate estimation of the level of precision achievable at LHCb a more detailed study taking into account detector specific background and efficiency information is required. However it would appear from this preliminary study that this channel provides a promising candidate with which to make a γ measurement.

7.3 Search for CP Violation

In order to carry out the amplitude analysis which has been described in this thesis it is assumed that CP violation can be neglected in the $D \to K^+K^-\pi^+\pi^-$ decay.

As described (in Chapter 1) the Standard Model predictions for CP violation in the charm sector are very small, however some new physics effects could lead to observable direct CP violation in this sector. Recently, interest has been raised by the LHCb experiment reporting evidence for CP violation in $D^0 \to K^+K^-$ and $\pi^+\pi^-$ decays [86].

In the absence of CP violation the D^0 and $\overline{D}^0$ decay would show the same resonant substructure. Therefore by performing separate fits to flavour tagged $D^0 \to K^+K^-\pi^+\pi^-$ and $\overline{D}^0 \to K^+K^-\pi^+\pi^-$ decay data and comparing the amplitude model produced for each, a search for CP violation may be performed. Such a test for CP violation has the advantage of providing information about the region of the Dalitz plot in which any CP asymmetry occurs. This can provide information about the underlying operators involved in generating CP violation in the decay.

In order to carry out this test the D^0 and $\overline{D}^0$ flavour tagged data used in this study are separated for each flavour tagged sample (CLEO-II.V, CLEO-III, 3770 and 4170). A combined fit to all four flavour tagged samples is then carried out for both the D^0 and $\overline{D}^0$ data. The background and efficiency descriptions used for each flavour specific dataset is the same as that described for the fit to the combined D^0 and $\overline{D}^0$ datasets, taking the baseline model but allowing the D^0 and $\overline{D}^0$ decays to have independent parameters. As described in Chapter 4 each of the flavour tagged datasets has a finite level of mistagging. Since a certain proportion of the D^0 ($\overline{D}^0$) dataset events are therefore in fact $\overline{D}^0$ (D^0) events, the D^0 ($\overline{D}^0$) amplitude model has a dependence on the $\overline{D}^0$ (D^0) amplitude model. The fit to both the D^0 and $\overline{D}^0$ datasets are therefore carried out simultaneously but with independent parameters for the D^0 and $\overline{D}^0$ amplitude models. The small proportion of the D^0 ($\overline{D}^0$) PDF which accounts for mistagged events is described by the $\overline{D}^0$ (D^0) amplitude model. The result of this fit is presented in tables 7.6, 7.7 and 7.8. The mass projections for the fits to each of the flavour tagged datsets are shown in figure 7.1.

The comparisons between amplitude models fitted separately to the D^0 and $\overline{D}^0$ decays shows no significant evidence for CP violation. The fitted parameters shown in table 7.7 all agree to within three standard deviations, with over half of the parameters agreeing to within less than one standard deviation. The fit fractions (which provide a convention free description of the amplitude model) obtained for these amplitude models (shown in table 7.8), all agree to within two standard deviations. For nine out of the eleven parameters considered the fit fractions for the D^0 and $\overline{D}^0$ amplitude models lie within one standard deviations of each other. Thus no evidence for CP violation in this decay was found. The fits are plotted for both the D^0 and $\overline{D}^0$ decays in figures 7.1- 7.5.

D^0 Decay Mode	**Combined Flavour tagged Fit**	D^0 **Decays**	$\overline{D}^0$ **Decays**	**Pull**
$K_1(1270)^+(\to K^*(892),\pi^+),K^-$ Phase	0.0 ± 0.0	0.0 ± 0.0	0.0 ± 0.0	0.0
$K_1(1270)^+(\to K^*(892),\pi^+),K^-$ Amplitude	1.0 ± 0.0	1.0 ± 0.0	1.0 ± 0.0	0.0
$\overline{K_1}(1270)^-(\to \overline{K_0}^*(892),\pi^-),K^+$ Phase	1.111 ± 0.215	1.519 ± 0.334	0.981 ± 0.237	1.317
$\overline{K_1}(1270)^-(\to \overline{K_0}^*(892),\pi^-),K^+$ Amplitude	0.353 ± 0.065	0.352 ± 0.084	0.385 ± 0.087	0.266
$K_1(1270)^+(\to \rho(770),K^+),K^-$ Phase	0.76 ± 0.141	0.858 ± 0.169	0.707 ± 0.153	0.664
$K_1(1270)^+(\to \rho(770),K^+),K^-$ Amplitude	5.869 ± 0.812	5.579 ± 0.983	5.956 ± 0.837	0.292
$\overline{K_1}(1270)^-(\to \rho(770),K^-),K^+$ Phase	0.13 ± 0.175	0.414 ± 0.193	0.302 ± 0.179	0.423
$\overline{K_1}(1270)^-(\to \rho(770),K^-),K^+$ Amplitude	6.729 ± 0.627	7.032 ± 1.033	6.394 ± 0.817	0.484
$K^+(1410)(\to K^*(892),\pi^+),K^-$ Phase	0.773 ± 0.109	0.989 ± 0.175	0.678 ± 0.129	1.435
$K^+(1410)(\to K^*(892),\pi^+),K^-$ Amplitude	6.303 ± 0.685	5.387 ± 0.913	6.511 ± 0.862	0.895
$\overline{K^-}(1410)(\to \overline{K^*}(892),\pi^-),K^+$ Phase	1.167 ± 0.133	1.384 ± 0.198	0.949 ± 0.154	1.731
$\overline{K^-}(1410)(\to \overline{K^*}(892),\pi^-),K^+$ Amplitude	6.893 ± 0.683	6.693 ± 0.821	6.746 ± 0.923	0.042
$K^*(892)\overline{K^*}(892)$ S wave Phase	0.37 ± 0.125	0.472 ± 0.165	0.237 ± 0.14	1.086
$K^*(892)\overline{K^*}(892)$ S wave Amplitude	0.356 ± 0.038	0.363 ± 0.052	0.328 ± 0.044	0.505
$\phi(1020)\rho(770)$ S wave Phase	1.801 ± 0.143	2.079 ± 0.189	1.769 ± 0.071	1.536
$\phi(1020)\rho(770)$ S wave Amplitude	1.068 ± 0.092	1.02 ± 0.164	1.048 ± 0.078	0.155
$\phi(1020)\rho(770)$ D wave Phase	1.533 ± 0.221	1.18 ± 0.362	1.481 ± 0.137	0.777
$\phi(1020)\rho(770)$ D wave Amplitude	1.453 ± 0.18	1.136 ± 0.3	1.693 ± 0.228	1.48
$\phi(1020),(\pi^+,\pi^-)_S$ P wave Phase	1.936 ± 0.13	1.745 ± 0.189	1.982 ± 0.089	1.131
$\phi(1020),(\pi^+,\pi^-)_S$ P wave Amplitude	6.131 ± 0.577	5.764 ± 0.651	6.224 ± 0.647	0.501
$(\pi^+K^-)_P,(\pi^-K^+)_S$ P wave Phase	0.118 ± 0.12	0.159 ± 0.157	0.129 ± 0.103	0.157
$(\pi^+K^-)_P,(\pi^-K^+)_S$ P wave Amplitude	85.9 ± 6.827	84.7 ± 9.296	81.7 ± 8.33	0.236

Table 7.6: The comparison on flavour tagged D^0 and $\overline{D}^0$ decays. The column headed "$\overline{D}^0$ Decays" refers to the CP conjugate version of the listed D^0 decay mode. The column headed "Pull" gives the difference between the D^0 and $\overline{D}^0$ decays in terms of statistical uncertainty.

D^0 Decay Mode	**Combined Flavour tagged Fit**	**D^0 Decays**	**$\overline{D}^0$ Decays**	**Pull**
$K_1(1270)^+(\to K^*(892),\pi^+),K^-$ Real	1.0 ± 0.0	1.0 ± 0.0	1.0 ± 0.0	0.0
$K_1(1270)^+(\to K^*(892),\pi^+),K^-$ Imaginary	0.0 ± 0.0	0.0 ± 0.0	0.0 ± 0.0	0.0
$\overline{K_1}(1270)^-(\to \overline{K_0}^*(892),\pi^-),K^+$ Real	0.156 ± 0.079	0.018 ± 0.118	0.214 ± 0.094	1.3
$\overline{K_1}(1270)^-(\to \overline{K_0}^*(892),\pi^-),K^+$ Imaginary	-0.315 ± 0.061	-0.351 ± 0.084	-0.319 ± 0.084	0.274
$K_1(1270)^+(\to \rho(770),K^+),K^-$ Real	4.252 ± 0.657	3.649 ± 0.803	4.529 ± 0.598	0.878
$K_1(1270)^+(\to \rho(770),K^+),K^-$ Imaginary	4.045 ± 0.954	4.22 ± 1.098	3.868 ± 1.081	0.229
$\overline{K_1}(1270)^-(\to \rho(770),K^-),K^+$ Real	6.672 ± 0.613	6.439 ± 0.939	6.105 ± 0.773	0.275
$\overline{K_1}(1270)^-(\to \rho(770),K^-),K^+$ Imaginary	0.875 ± 1.188	2.826 ± 1.425	-1.902 ± 1.175	2.56
$K^+(1410)(\to K^*(892),\pi^+),K^-$ Real	4.511 ± 0.624	2.959 ± 0.961	5.072 ± 0.899	1.606
$K^+(1410)(\to K^*(892),\pi^+),K^-$ Imaginary	-4.402 ± 0.744	-4.5 ± 0.891	-4.081 ± 0.803	0.35
$\overline{K^-}(1410)(\to \overline{K^*}(892),\pi^-),K^+$ Real	2.708 ± 0.963	1.242 ± 1.342	3.928 ± 1.152	1.519
$\overline{K^-}(1410)(\to \overline{K^*}(892),\pi^-),K^+$ Imaginary	-6.338 ± 0.619	-6.576 ± 0.797	-5.483 ± 0.781	0.98
$K^*(892)\overline{K^*}(892)$ S wave Real	0.332 ± 0.036	0.323 ± 0.049	0.319 ± 0.044	0.06
$K^*(892)\overline{K^*}(892)$ S wave Imaginary	0.129 ± 0.046	0.165 ± 0.062	0.077 ± 0.046	1.133
$\phi(1020)\rho(770)$ S wave Real	-0.242 ± 0.156	-0.495 ± 0.205	-0.205 ± 0.074	1.333
$\phi(1020)\rho(770)$ S wave Imaginary	1.039 ± 0.087	0.892 ± 0.149	1.028 ± 0.078	0.813
$\phi(1020)\rho(770)$ D wave Real	0.055 ± 0.321	0.432 ± 0.43	0.152 ± 0.231	0.574
$\phi(1020)\rho(770)$ D wave Imaginary	-1.451 ± 0.18	-1.049 ± 0.271	-1.686 ± 0.228	1.794
$\phi(1020),(\pi^+,\pi^-)_S$ P wave Real	-2.191 ± 0.827	-1.0 ± 1.102	-2.487 ± 0.531	1.216
$\phi(1020),(\pi^+,\pi^-)_S$ P wave Imaginary	-5.724 ± 0.53	-5.675 ± 0.631	-5.703 ± 0.667	0.031
$(\pi^+K^-)_P,(\pi^-K^+)_S$ P wave Real	85.3 ± 6.765	83.6 ± 9.167	81.0 ± 8.329	0.206
$(\pi^+K^-)_P,(\pi^-K^+)_S$ P wave Imaginary	10.1 ± 10.3	13.4 ± 13.4	10.5 ± 8.422	0.181

Table 7.7: The comparison of decay parameters of flavour tagged D^0 and $\overline{D}^0$ decays. The column headed "$\overline{D}^0$ Decays" refers to the CP conjugate version of the listed D^0 decay mode. The column headed "Pull" gives the difference between the D_0 and $\overline{D}_0$ decays in terms of statistical uncertainty.

D^0 Decay Mode	**Combined Flavour tagged Fit**	**D^0 Decays**	**$\overline{D}^0$ Decays**	**Pull**
$K_1(1270)^+(\to K^*(892),\pi^+),K^-$	0.072 ± 0.008	0.074 ± 0.011	0.075 ± 0.011	0.066
$\overline{K_1}(1270)^-(\to \overline{K_0}^*(892),\pi^-),K^+$	0.009 ± 0.003	0.009 ± 0.004	0.011 ± 0.005	0.293
$K_1(1270)^+(\to \rho(770),K^+),K^-$	0.042 ± 0.007	0.043 ± 0.011	0.049 ± 0.011	0.377
$\overline{K_1}(1270)^-(\to \rho(770),K^-),K^+$	0.055 ± 0.007	0.063 ± 0.011	0.052 ± 0.01	0.708
$K^+(1410)(\to K^*(892),\pi^+),K^-$	0.041 ± 0.007	0.032 ± 0.009	0.048 ± 0.01	1.129
$\overline{K^-}(1410)(\to \overline{K^*}(892),\pi^-),K^+$	0.049 ± 0.007	0.046 ± 0.009	0.047 ± 0.009	0.091
$K^*(892)\overline{K^*}(892)$ S wave	0.062 ± 0.008	0.069 ± 0.012	0.057 ± 0.012	0.711
$\phi(1020)\rho(770)$ S wave	0.399 ± 0.023	0.379 ± 0.029	0.4 ± 0.029	0.516
$\phi(1020)\rho(770)$ D wave	0.037 ± 0.008	0.022 ± 0.008	0.048 ± 0.012	1.893
$\phi(1020),(\pi^+,\pi^-)_S$ P wave	0.102 ± 0.01	0.09 ± 0.014	0.107 ± 0.015	0.856
$\pi K,\pi K$ (VS) P wave	0.111 ± 0.011	0.113 ± 0.017	0.107 ± 0.016	0.274
Sum	0.979 ± 0.027	0.939 ± 0.033	1.001 ± 0.033	
χ^2 per DOF	**1.632**	**1.896**	**1.95**	
3770 χ^2 per BIN	**1.297**	**0.996**	**1.258**	
4170 χ^2 per BIN	**1.194**	**1.586**	**1.165**	
3 χ^2 per BIN	**1.48**	**1.294**	**1.379**	
2 χ^2 per BIN	**1.919**	**1.455**	**1.455**	

Table 7.8: The comparison of the fit fractions on flavour tagged D^0 and $\overline{D}^0$ decays.The column headed "$\overline{D}^0$ Decays" refers to the CP conjugate version of the listed D^0 decay mode. The column headed "Pull" gives the difference between the D_0 and $\overline{D}_0$ decays in terms of statistical uncertainty.

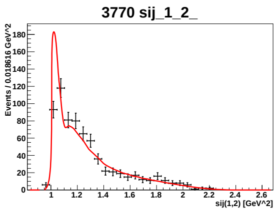

(c) 3770, D^0 decays.

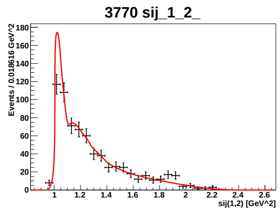

(d) 3770, $\overline{D}^0$ decays.

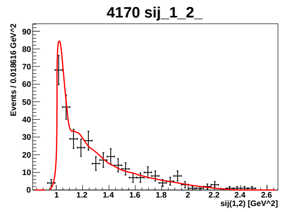

(e) 4170, D^0 decays.

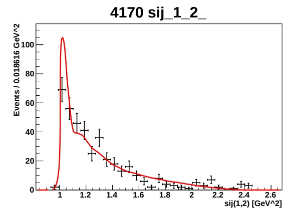

(f) 4170, $\overline{D}^0$ decays.

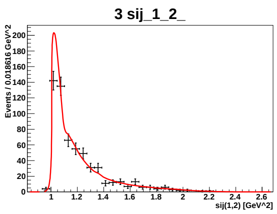

(g) CLEO-III, D^0 decays.

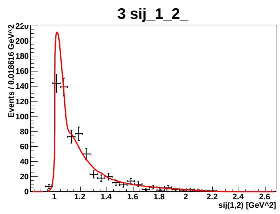

(h) CLEO-III, $\overline{D}^0$ decays.

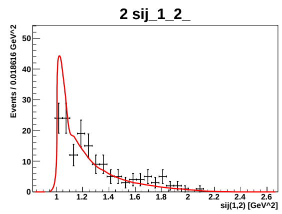

(i) CLEO-II.V, D^0 decays.

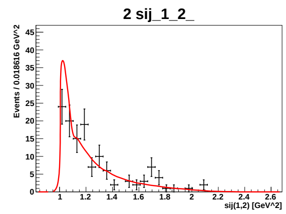

(j) CLEO II.V, $\overline{D}^0$ decays.

Figure 7.1: Mass projections of fitted result(red) against selected data(black) for the flavour tagged datasets for the $S_{K^+K^-}$ projection.

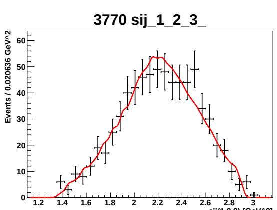

(a) 3770, D^0 decays.

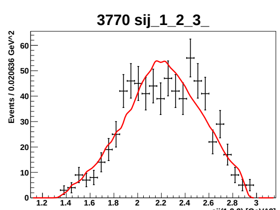

(b) 3770, $\overline{D}^0$ decays.

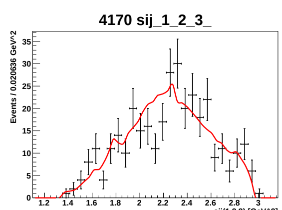

(c) 4170, D^0 decays.

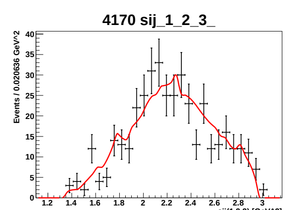

(d) 4170, $\overline{D}^0$ decays.

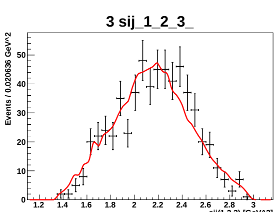

(e) CLEO-III, D^0 decays.

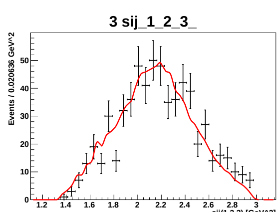

(f) CLEO-III, $\overline{D}^0$ decays.

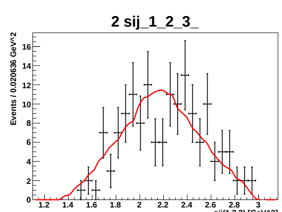

(g) CLEO-II.V,D^0decays.

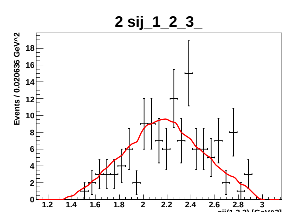

(h) CLEO II.V, $\overline{D}^0$ decays.

Figure 7.2: Mass projections of fitted result(red) against selected data(black) for the $S_{K^+K^-\pi^+}$ projection.

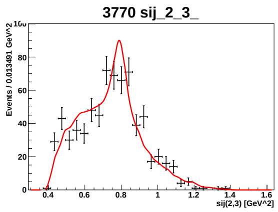

(a) 3770 , D^0 decays.

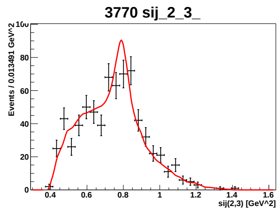

(b) 3770, $\overline{D}^0$ decays.

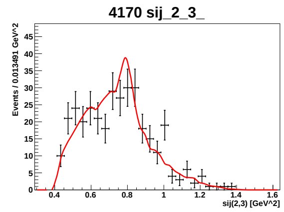

(c) 4170, D^0 decays.

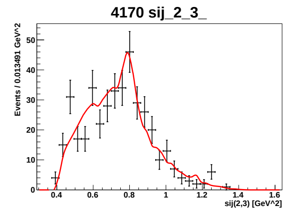

(d) 4170, $\overline{D}^0$ decays.

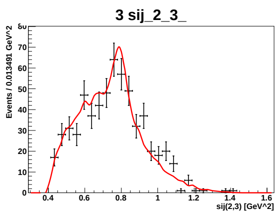

(e) CLEO-III set, D^0 decays.

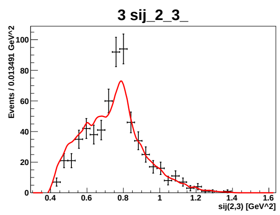

(f) CLEO-III, $\overline{D}^0$ decays.

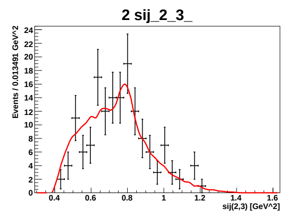

(g) CLEO-II.V,D^0decays.

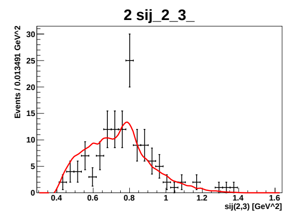

(h) CLEO II.V, $\overline{D}^0$ decays.

Figure 7.3: Mass projections of fitted result(red) against selected data(black) for the $S_{K^-\pi^+}$ projection.

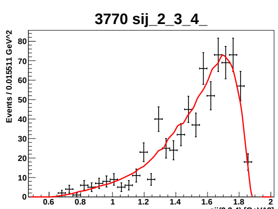

(a) 3770, D^0 decays.

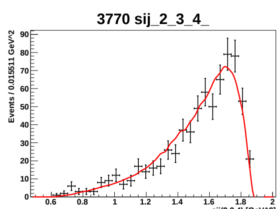

(b) 3770, $\overline{D}^0$ decays.

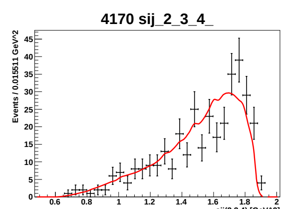

(c) 4170, D^0 decays.

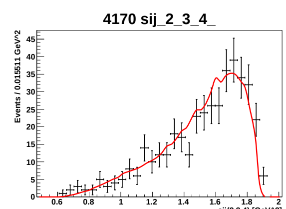

(d) 4170, $\overline{D}^0$ decays.

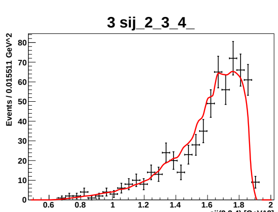

(e) CLEO-III, D^0 decays.

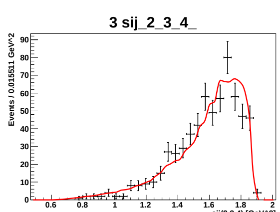

(f) CLEO-III, $\overline{D}^0$ decays.

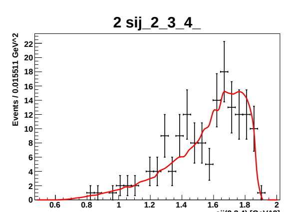

(g) CLEO-II.V,D^0decays.

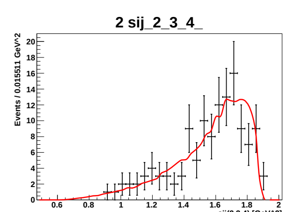

(h) CLEO II.V, $\overline{D}^0$ decays.

Figure 7.4: Mass projections of fitted result(red) against selected data(black) for the $S_{K^-\pi^+\pi^-}$ projection.

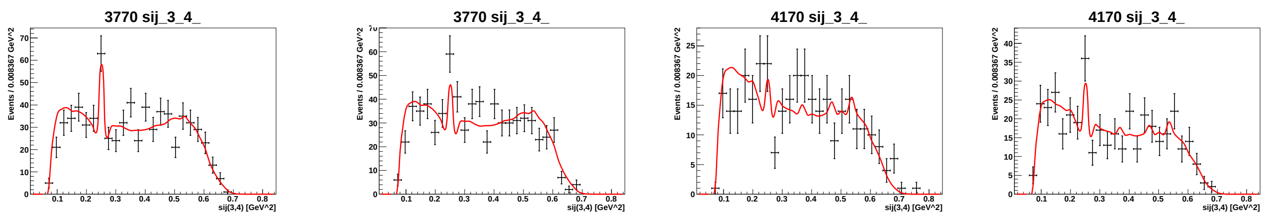

(a) 3770, D^0 decays. (b) 3770, $\overline{D}^0$ decays. (c) 4170, D^0 decays. (d) 4170, $\overline{D}^0$ decays.

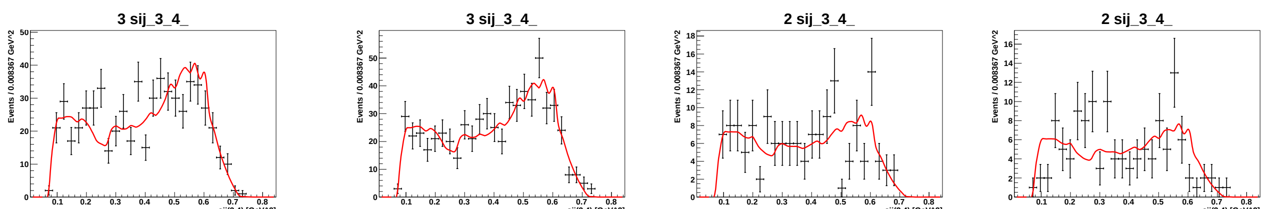

(e) CLEO-III, D^0 decays. (f) CLEO-III, $\overline{D}^0$ decays. (g) CLEO-II.V, D^0 decays. (h) CLEO II.V, $\overline{D}^0$ decays.

Figure 7.5: Mass projections of fitted result(red) against selected data(black) for the $S_{\pi^+\pi^-}$ projection.

Chapter 8

Conclusions

The decay $D^0 \to K_S^0\pi^+\pi^-$, which is a decay mode which when reconstructed in the decay chain $B^\pm \to DK^\pm$, has a high sensitivity to the CKM angle γ was discussed in Chapter 3. In particular the modelling of the $\pi^+\pi^-$ S wave component was described. The more common Breit-Wigner parametrization is not ideal in describing the $\pi^+\pi^-$ S wave which is dominated by broad overlapping resonance. A more physically realistic K-matrix model was implemented to describe this component of the decay. The size of the systematic associated with the $\pi^+\pi^-$ S wave component was investigated. The scale of this systematic effect was found to be large compared to the expected statistical precision of LHCb.

A model had been developed to describe the $D^0 \to K^+K^-\pi^+\pi^-$ decay using CLEO data. This model is in qualitative agreement with a previous analysis which has been carried out on this decay, and the general features of the decay model can be justified physically. The study described in this thesis is the first analysis on this mode to distinguish between conjugate decays and consider higher orbital angular momentum states between the decay particles. The errors on the measured parameters are dominated by systematic effects. In order to reduce the systematic errors improved precision on the measured masses and widths of the resonances, in particular that of the $K_1(1270)$ resonance, would be required. In the future higher statistical samples of $D^0 \to K^+K^-\pi^+\pi^-$ from B-factories or LHCb combined with improved knowledge of particle widths and masses could allow for a more accurate knowledge of this decay.

The amplitude model presented in this thesis has also been used to perform a search for CP violation in the decay. No significant difference was found between the parameters of the D^0 and $\overline{D}$ decays and therefore no CP violation is observable at this level of precision in the decay.

The $D^0 \to K^+K^-\pi^+\pi^-$ decay is a candidate mode for making a γ measurement via $B^\pm \to DK^\pm$ decays. A study has been performed, using the amplitude model determined in this thesis, to determine the precision with which γ could be measured via this decay channel. This study indicates that a good precision on γ (11 deg) could be obtained through such a measurement.

Appendix A

CP Tagged Background Models

Decay Mode	Modes not involving a K_L	Modes involving a K_L
$K_1(1270)^+(\to K^*(892), \pi^+), K^-$	0.176 ± 0.083	0.098±0.037
$K_1(1270)^+(\to \rho(770), K^+), K^-$	0.111 ± 0.090	0.093±0.057
$\overline{K_1}(1270)^-(\to \rho(770), K^-), K^+$	0.0661 ± 0.068	0.164±0.088
$K^+(1410)(\to K^*(892), \pi^+), K^-$	0.111 ± 0.064	0.013±0.016
$\overline{K^-}(1410)(\to \overline{K^*}(892), \pi^-), K^+$	0.043 ± 0.031	0.044±0.024
$K^*(892)\overline{K^*}(892)$	0.012 ± 0.022	0.015±0.016
$\phi(1020)\rho(770)$	0.194 ± 0.150	0.119±0.061
$\phi(1020), \pi^+, \pi^-$	0.162 ± 0.102	0.135±0.036
Non Resonant	0.208 ± 0.091	0.424±0.069

Table A.1: The background fractions for the tagged flat background for the CP tagged and ad-mixture background samples. The samples were sit separately for modes involving K_L particles.

Decay Mode	Fit Fraction
$K^*(892)\pi^+K^-$	0.271 ± 0.0936
$\overline{K}^*(892)\pi^-K^+$	0.233 ± 0.083
$K^*(892)\overline{K^*}(892)$	0.204 ± 0.083
$K_1(1270)^+(\to \rho(770), K^+), K^-$	0.072 ± 0.0483
$\phi(1020), \pi^+, \pi^-$	0.131 ± 0.048
Non Resonant	0.062 ± 0.078

Table A.2: The background fractions for the continuim background for the CP tagged and ad-mixture background samples.

Appendix B

Spin Factors

The spin factors used in this analysis are taken from [70] and the relevant spin factors will be outlined briefly here.

The four body spin factors relevant to this thesis are listed in table B.1. The following abreviations have been made in describing the spin factors:

$$\begin{aligned} P^{\mu\alpha}(p, m^2) &= g^{\mu\alpha} - \frac{p^\mu p^\alpha}{m^2} \\ Z_1(q, pm^2)^\alpha &= q_\mu P^{\mu\alpha}(p, m^2) \end{aligned} \tag{B.1}$$

where p_R is the four momentum of the resonance R, so that if resonance R decays to particles A and B then $p_R = p_A + p_B$ and q_R represents the difference of the four momentua between the decay products of R: $q_R \equiv p_A - p_B$. The ordering of the particles is important; the momentum of the second daughter as listed in the decay chain is always subtracted from that of the first. With reference to the resonance R the following shorthand is used:

$$\begin{aligned} P^{\mu\alpha}(R) &= P^{\mu\alpha}(p_R, m_R^2) \\ Z_1(R) &= Z_1(q_R, p_R m^2). \end{aligned} \tag{B.2}$$

In the case of pairs of non resonant particles m_R^2 is replaced by p^2.

Decay Chain	**Spin Factor**
$D \to AP_1$, $A[S] \to VP_2$, $V \to P_3P_4$	$p_1^{\mu} P(A_{\mu\nu}) Z_1(A)^{\nu}$
$D[S] \to V_1V_2$, $V_1 \to P_1P_2$, $V_2 \to P_1P_2$	$Z_1(V_1)^{\nu} Z_1(V_2)_{\nu}$
$D[P] \to V_1V_2$, $V_1 \to P_1P_2$, $V_2 \to P_1P_2$	$\epsilon_{\alpha\beta\gamma\delta} p_D^{\alpha} q_D^{\beta} q_{V_1}^{\gamma} q_{V_2}^{\delta}$
$D[D] \to V_1V_2$, $V_1 \to P_1P_2$, $V_2 \to P_1P_2$	$Z_1(V_1)_{\alpha} p_{V_2}^{\alpha} Z_1(V_2)_{\beta} p_{V_1}^{\beta}$
$D \to VS$, $V \to P_1P_2$, $S \to P_1P_2$	$p_S^{\mu} Z_1(V)_{\mu}$
$D \to V_1P_1$, $V_1 \to V_2P_2$, $V_2 \to P_1P_2$	$\epsilon_{\alpha\beta\gamma\delta} p_{V_1}^{\alpha} p_{V_1}^{\beta} p_{P_1}^{\gamma} p_{V_2}^{\delta}$

Table B.1: The spin factors for the various four body decay topologies involved in this analysis. Where S represents a scalar particle, P represents a pseudoscalar particle, V represents a vector particle and A an axial vector particle.Symbols within square brackets represents the orbital angular momentum between decay products. When no angular momentum is specified the lowest angular momentum consistent with angular momentum and parity conservation is assumed.

Appendix C

All Considered Resonances

The following is a list of all $D^0 \to K^+K^-\pi^+\pi^-$ decay channels which were considered when developing the final decay model.

In the case of final states that are not self conjugate the conjugate state was also tested but is not included in the following list.

1) Cascade amplitudes containing a higher K^* resonance.

$K_1(1270)^+K^-$, $K_1(1270)^+(K_0^*(1430)\pi^+)K^-$, $K_1(1270)^+(\rho^0\pi^+)K^-$, $K_1(1270)^+(\omega K^+)K^-$

$K_1(1400)^+(K^{*0}\pi^+)K^-$,

$K_2(1430)^+(K^{*0}\pi^+)K^-$, $K_2(1430)^+(\rho^0\pi^+)K^-$,

$K^*(1680)^+(K^{*0}\pi^+)K^-$, $K^*(1680)^+(\rho^0K^+)K^-$.

2) Quasi-two-body amplitudes.

$K^{*0}\overline{K}^{*0}$ S, P and D wave,

$\phi\rho^0$ S, P and D wave,

$\phi\omega$ S wave,

$\phi f_2(1270)^0$ P and D wave.

3) Single-resonance amplitudes.

$\rho\{K^+K^-\}_S$; $\rho\{K^+K^-\}_P$ S, P and D wave, $\rho\{K^+K^-\}_D$ P and D wave, $K^{*0}\{K^-\pi^+\}_S$;

$K^{*0}\{K^-\pi^+\}_P$ S, P and D wave, $K^{*0}\{K^-\pi^+\}_D$ P and D wave,

$\phi\{\pi^+\pi^-\}_S$; $\phi\{\pi^+\pi^-\}_P$ S, P and D wave, $\phi\{\pi^+\pi^-\}_D$ P and D wave,

$f_0(980)^0\{\pi^+\pi^-\}_S$, $f_0(980)^0\{K^+K^-\}_S$,

$f_2(1270)^0\{K^+K^-\}_S$,

$\omega\{K^+K^-\}_S$.

4) Non-resonant amplitudes.

$\{K^+K^-\}_S\{\pi^+\pi^-\}_S$; $\{K^+K^-\}_S\{\pi^+\pi^-\}_P$; $\{K^+K^-\}_P\{\pi^+\pi^-\}_S$; $\{K^+K^-\}_P\{\pi^+\pi^-\}_P$ S, P and D wave,

$\{K^+K^-\}_S\{\pi^+\pi^-\}_D$; $\{K^+K^-\}_D\{\pi^+\pi^-\}_S$; $\{K^+K^-\}_D\{\pi^+\pi^-\}_P$; $\{K^+K^-\}_P\{\pi^+\pi^-\}_D$; P and D wave,

$\{K^+\pi^-\}_S\{K^-\pi^+\}_P$; $\{K^+\pi^-\}_P\{K^-\pi^+\}_S$; $\{K^+\pi^-\}_P\{K^-\pi^+\}_P$ S, P and D wave,

$\{K^+\pi^-\}_S\{K^-\pi^+\}_D$; $\{K^+\pi^-\}_D\{K^-\pi^+\}_S$; $\{K^+\pi^-\}_P\{K^-\pi^+\}_D$; $\{K^+\pi^-\}_S\{K^-\pi^+\}_P$ P and D wave.

Where $\{XY\}_{S,P,D}$ represents a particle X and a particle Y with orbital angular momentum in a S, P or D wave respectively.

Appendix D

Pull Study Plots for Fitted Parameters

Figure D.1: Pull distributions for fitted parameters in the Monte Carlo verification study in which Monte Carlo truth information was used to describe particle's four momenta.

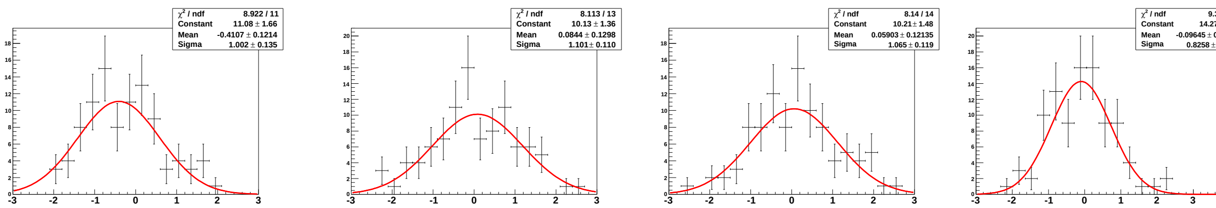

From left to right: Fit fractions for $\overline{K_1}(1270)^-(\rightarrow \overline{K_0}^*(892), \pi^-), K^+$ Real, $\overline{K_1}(1270)^-(\rightarrow \overline{K_0}^*(892), \pi^-), K^+$ Imaginary, $K_1(1270)^+(\rightarrow \rho(770), K^+), K^-$ Real, $K_1(1270)^+(\rightarrow \rho(770), K^+), K^-$ Imaginary

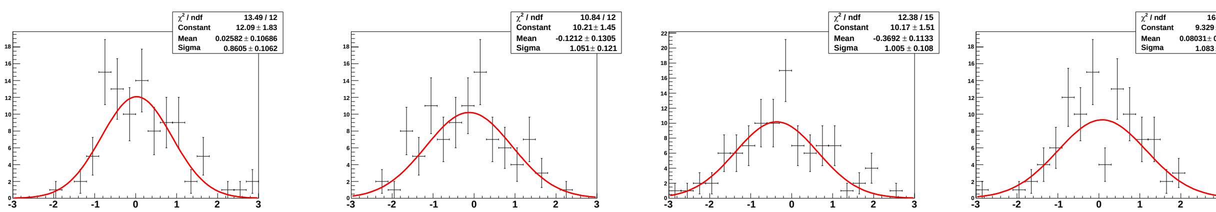

$\overline{K_1}(1270)^-(\rightarrow \rho(770), K^-), K^+$ Real, $\overline{K_1}(1270)^-(\rightarrow \rho(770), K^-), K^+$ Imaginary, $K^+(1410)(\rightarrow K^*(892), \pi^+), K^-$ Real, $K^+(1410)(\rightarrow K^*(892), \pi^+), K^-$ Imaginary

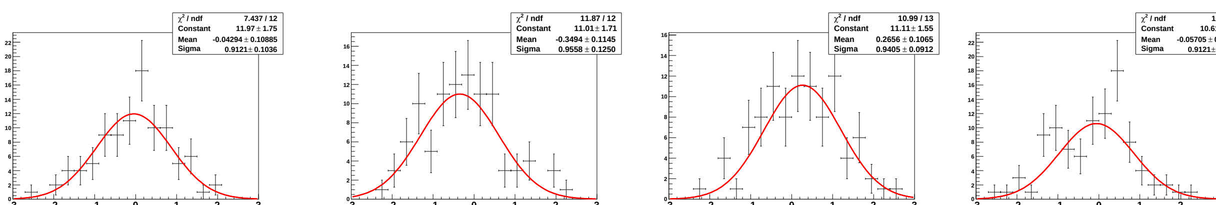

$\overline{K^-}(1410)(\rightarrow \overline{K^*}(892), \pi^-), K^+$ Real, $\overline{K^-}(1410)(\rightarrow \overline{K^*}(892), \pi^-), K^+$ Imaginary, $K^*(892)\overline{K^*}(892)$ Real, $K^*(892)\overline{K^*}(892)$ Imaginary

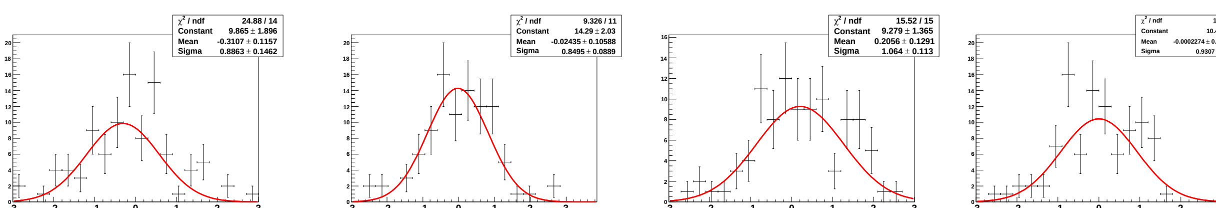

$\phi(1020)\rho(770)$ Real, $\phi(1020)\rho(770)$ Imaginary, $\phi(1020)\rho(770)$ D wave Real, $\phi(1020)\rho(770)$ D wave Imaginary

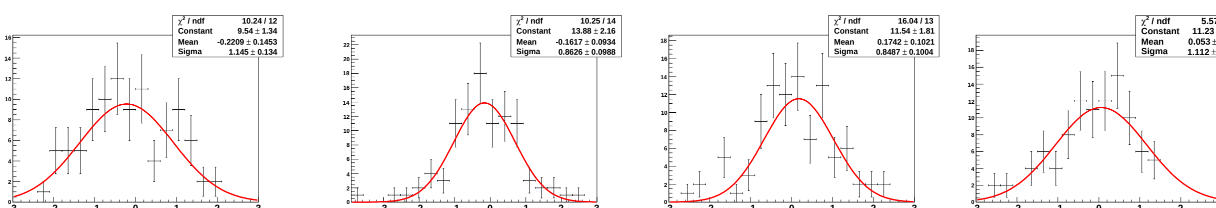

$\phi(1020), (\pi^+, \pi^-)_S$ P wave Real, $\phi(1020), (\pi^+, \pi^-)_S$ P wave Imaginary, $(\pi K)_P, (\pi K)_S$ P wave Real, $(\pi K)_P, (\pi K)_S$ P wave Imaginary

Figure D.2: Pull distributions for fitted parameters in the Monte Carlo verification study in which Monte Carlo reconstructed information was used to describe particle's four momenta.

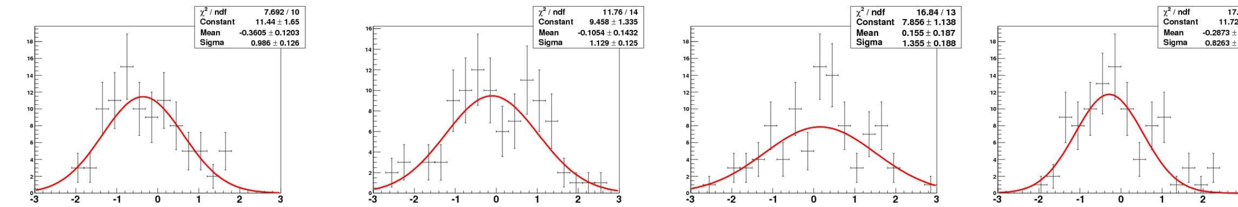

From left to right $\overline{K_1}(1270)^-(\rightarrow \overline{K_0}^*(892), \pi^-), K^+$ Real, $\overline{K_1}(1270)^-(\rightarrow \overline{K_0}^*(892), \pi^-), K^+$ Imaginary, $K_1(1270)^+(\rightarrow \rho(770), K^+), K^-$ Real, $K_1(1270)^+(\rightarrow \rho(770), K^+), K^-$ Imaginary

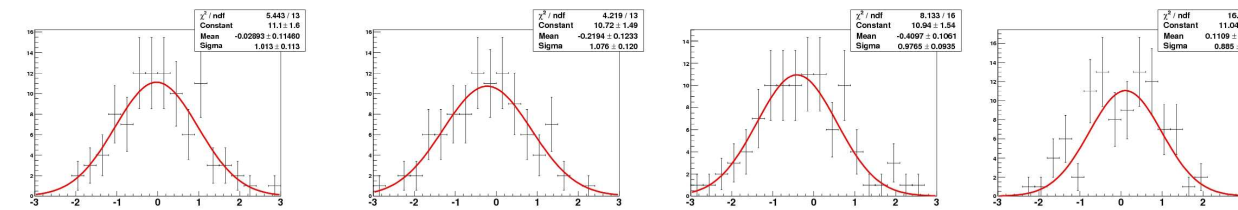

$\overline{K_1}(1270)^-(\rightarrow \rho(770), K^-), K^+$ Real, $\overline{K_1}(1270)^-(\rightarrow \rho(770), K^-), K^+$ Imaginary, $K^+(1410)(\rightarrow K^*(892), \pi^+), K^-$ Real, $K^+(1410)(\rightarrow K^*(892), \pi^+), K^-$ Imaginary

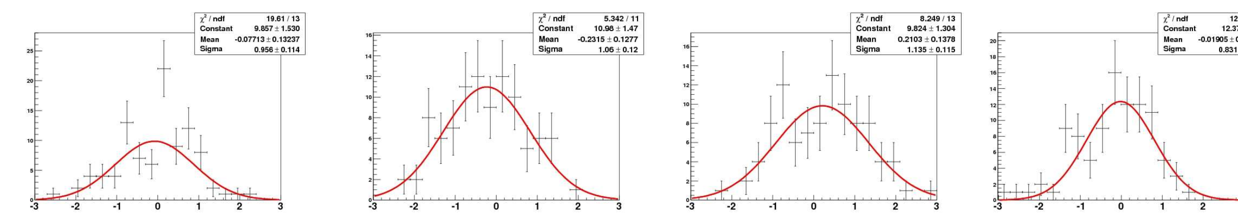

$\overline{K^-}(1410)(\rightarrow \overline{K^*}(892), \pi^-), K^+$ Real, $\overline{K^-}(1410)(\rightarrow \overline{K^*}(892), \pi^-), K^+$ Imaginary, $K^*(892)\overline{K^*}(892)$ Real, $K^*(892)\overline{K^*}(892)$ Imaginary

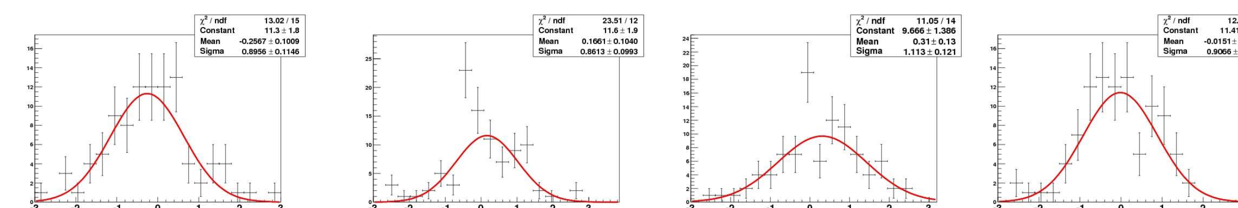

$\phi(1020)\rho(770)$ Real, $\phi(1020)\rho(770)$ Imaginary, $\phi(1020)\rho(770)$ D wave Real, $\phi(1020)\rho(770)$ D wave Imaginary

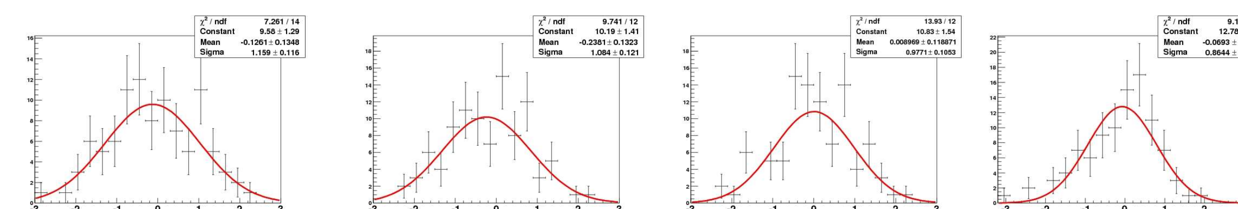

$\phi(1020), \pi^+, \pi^-$ Real, $\phi(1020), \pi^+, \pi^-$ Imaginary, $(\pi K)_P, (\pi K)_S$ P wave Real, $(\pi K)_P, (\pi K)_S$ P wave Imaginary

Figure D.3: Pull distributions for the fit fraction in the Monte Carlo verification study in which Monte Carlo truth information was used to describe particle's four momenta.

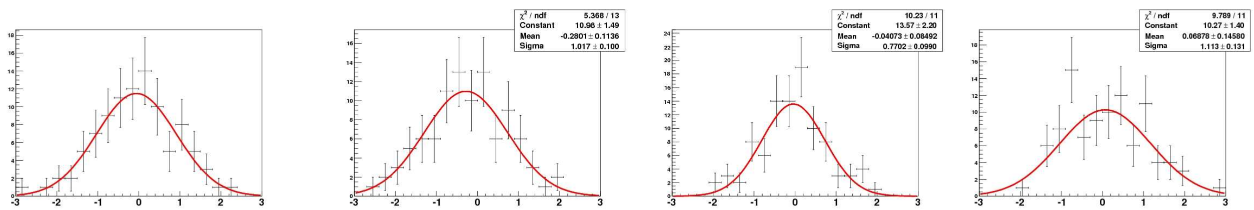

From left to right $K_1(1270)^+(\to K^*(892), \pi^+), K^-$, $\overline{K_1}(1270)^-(\to \overline{K_0}^*(892), \pi^-), K^+$, $K_1(1270)^+(\to \rho(770), K^+), K^-$, $\overline{K_1}(1270)^-(\to \rho(770), K^-), K^+$

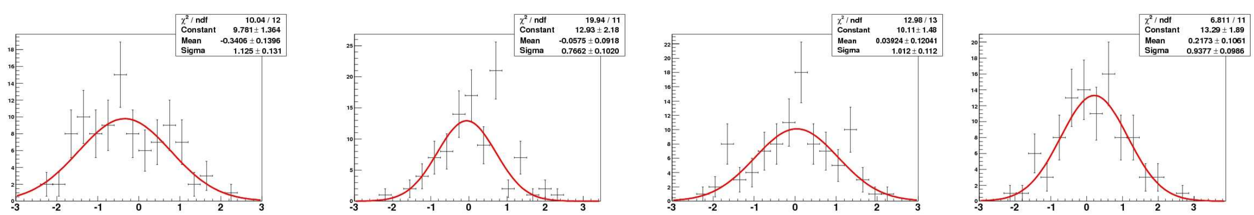

$K^+(1410)(\to K^*(892), \pi^+), K^-$, $\overline{K^-}(1410)(\to \overline{K^*}(892), \pi^-), K^+$, $K^*(892)\overline{K^*}(892)$, $\phi(1020)\rho(770)$

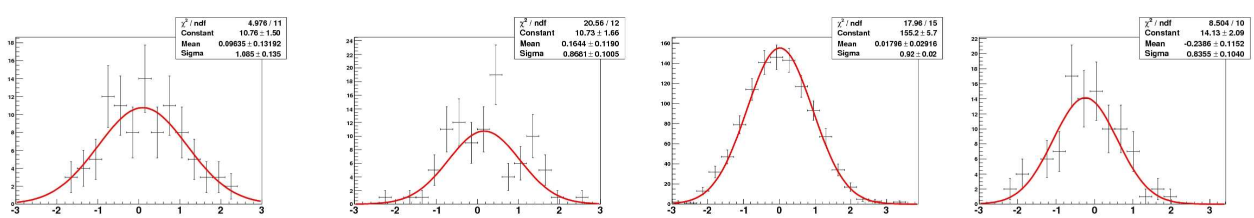

$\phi(1020)\rho(770)$ D wave, $\phi(1020), (\pi^+, \pi^-)_S$ P wave, $(\pi K)_P, (\pi K)_S$ P wave, All Fit Fractions

Figure D.4: Pull distributions for the fit fraction in the Monte Carlo verification study in which Monte Carlo reconstructed information was used to describe particle's four momenta.

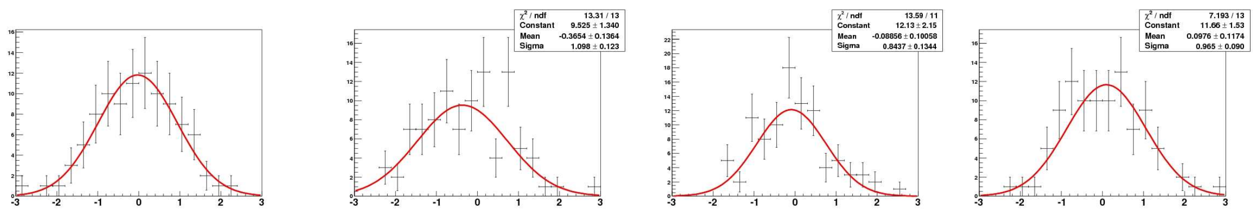

From left to right Fit fractions for $K_1(1270)^+(\rightarrow K^*(892), \pi^+), K^-$, $\overline{K_1}(1270)^-(\rightarrow \overline{K_0}^*(892), \pi^-), K^+$, $K_1(1270)^+(\rightarrow \rho(770), K^+), K^-$, $\overline{K_1}(1270)^-(\rightarrow \rho(770), K^-), K^+$

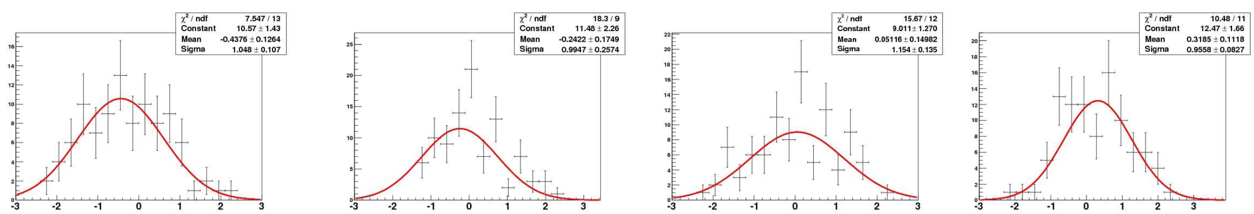

$K^+(1410)(\rightarrow K^*(892), \pi^+), K^-$, $\overline{K^-}(1410)(\rightarrow \overline{K^*}(892), \pi^-), K^+$, $K^*(892)\overline{K^*}(892)$, $\phi(1020)\rho(770)$

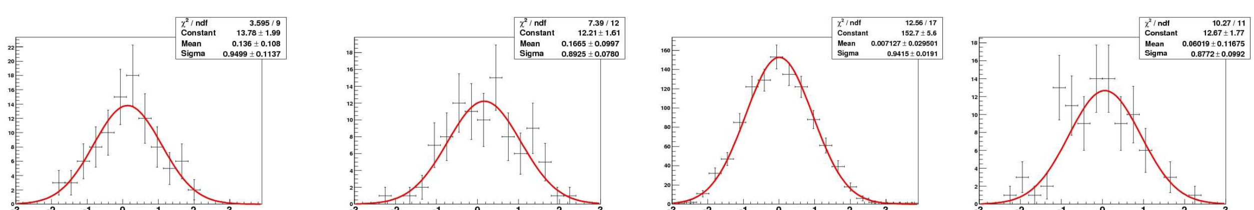

$\phi(1020)\rho(770)$ D wave, $\phi(1020), (\pi^+, \pi^-)_S$ P wave, $(\pi K)_P, (\pi K)_S$ P wave, All Fit Fractions

Bibliography

[1] Phys. Rev. D 85, 122002 (2012).

[2] N. Cabibbo, L. Maiani, G. Parisi, and R. Petronzio. Bounds on the fermions and Higgs boson masses in grand unifed theories. Nuc. Phys., B158:295-X305, 1979.

[3] J. Christenson, J. Cronin, V. Fitch and R. Turlay, Evidence for the Decay of the K^0 meson, Phys. Rev. Lett. 13(138) (1964).

[4] The BaBar Collaboration (B. Aubert et. al.). Observation of CP violation in the B^0 meson system. Phys.Rev.Lett., 87:091801, 2001

[5] The Belle Collaboration (Y. Chao et. al.). Evidence for Direct CP Violation in B^0 and $K\pi$ decays. Phys.Rev.Lett., 93:191802, 2004.

[6] A. Sakharov. Violation of CP invariance, C asymmetry, and baryon asymmetry of the universe. Soviet Physics Journal of Experimental and Theoretical Physics(JETP), 5:24-27, 1967.

[7] E. Noether, Invariante Variationsprobleme, Nachr. v. d. Ges. d. Wiss. zu Gottingen , 235257 (1918).

[8] H. P. Strapp, Derivation of the CPT Theorem and the Connection between Spin and Statistics from Postulates of the S-Matrix Theory, Phys. Rev.Lett. 125, 21392162 (1962).

[9] C. S. Wu, Parity Experiments in Beta Decays, Rev. Mod. Phys. 31,783790 (1959).

[10] CP violation in beauty decays, Michael Gronau, 2007

[11] CP Violation in the Renormalizable Theory of Weak-Interactions, Makoto Kobayashi and Toshihide Maskawa, 1972

[12] The BaBar Physics Book, Eds. P.F. Harrison and H.R. Quinn, SLAC-R-504 (1998).

[13] Evidence for CP violation in time integrated $D^0 \to h^+h^-$ decay Rates, Phys. Rev. Lett. 108, 111602 (2012)

[14] S.L. Glashow, Nucl. Phys. 22, 579 (1961).

[15] CP Violation and the CKM Matrix Annual Review of Nuclear and Particle Science Vol. 56: 501-567 Andreas Hocker, Zoltan Ligeti.

[16] Chau LL, Keung WY. Phys. Rev. Lett. 53:1802 (1984).

[17] L. Wolfenstein, Parameterization of the Kobayashi-Maskawa Matrix, Phys. Rev. Lett. 51(1945) (1983).

[18] C. Jarlskog, Communtator of the Quark Mass Matrices in the Standard Electroweak Model and a Measure of Maximal CP violation, Phys. Rev. Lett 55(1039) (1985).

[19] CKMfitter Group (J. Charles et al.), Eur. Phys. J. C41, 1-131 (2011) [hep-ph/0406184].

[20] Gronau and London, How to Determine all the Angles of the Unitarity Triangle from B_d^0, and B_s^0, Phys. Lett. B 253(483) (1991).

[21] M. Gronau and D. Wyler, On Determing a Weak Phase from Charged B Decay Asymmetries, Phys. Lett. B(265), 172 (1991).

[22] C. Amsler et al., (Particle Data Group), Phys. Lett. B667, 1 (2008),http://pdg.lbl.gov.

[23] A. Giri, Y. Grossman, A. Soffer, and J. Zupan, Phys. Rev.D 68, 054018 (2003).

[24] Y. Grossman, A. L. Kagan and Y. Nir, Phys. Rev. D 75, 036008 (2007).

[25] Y. Nir and N. Seiberg, Phys. Lett. B 309, 337 (1993).

[26] B. Aubert et al. (BaBar collab.), PRL 100, 061803 (2008).

[27] M. Staric et al. (Belle collab.), arXiv:hep-ex/0807.0148v1 (2008).

[28] http://www.slac.stanford.edu/xorg/hfag/.

[29] E687 Collaboration, P.L. Frabetti et al., Nucl. Instrum. Meth. A 329 (1993) 62.

[30] Link, J. et al. (2005), Search for T violation in charm meson decays, Phys. Lett. B, vol. 622, p. 239248.

[31] Maurizio Martinelli, Search for CP violation using T-odd correlations in $D^0 \to K^+K^-\pi^+\pi^-$ decays at BaBar, arXiv:1005.4211v1 [hep-ex].

[32] R.H. Dalitz, Phil. Mag. 44, 1068 (1953).

[33] Review on page 713 of W.-M. Yao et al. [Particle Data Group], Journal of Physics G 33, 1 (2006).

[34] A. Giri, Y. Grossman, A. Soffer and J. Zupan, Phys. Rev. D 68 (2003) 054018.

[35] M Bauer, B. Stech, and M. Wirbel, Z. Phys. C 34, 103 (1987); P. Bedaque, A. Das, and V.S. Mathur, Phys. Rev.D 49, 269 (1994); L.-L. Chau and H.-Y. Cheng, Phys.Rev. D 36, 137 (1987); K. Terasaki, Int. J. Mod. Phys.A 10, 3207 (1995); F. Buccella, M. Lusignoli, and A.Pugliese, Phys. Lett. B 379, 249 (1996).

[36] D. Atwood, I.Dunietz and A. Soni, Phys. Rev. D 63 (2001) 036005.

[37] MARK-III Collaboration, D. Coffman et al., Resonant substructure in $K\pi\pi\pi$ decays of D mesons, Phys. Rev. D 45(7), 21962211 (Apr 1992).

[38] S. U. Chung, Heliciity-Coupling Amplitudes in Tensor Formalism, Phys.Rev. D 48, 12251239 (Aug 1993).

[39] Coffman D, et al (Mark III Collaboration). Phys. Rev. D 45:2196 (1992).

[40] D. Asner arXiv:hep-ex/0410014v3.

[41] S.M. Flatte, Phys. Lett. B63 (1976) 228.

[42] Peterson, D. (1998). "Construction of the CLEOIII tracking system: Silicon vertex detector and drift chamber". Nuclear Instruments and Methods in Physics Research.

[43] CLEO Collaboration, The CLEO III Detector: Design and Physics Goals, CLNS 94/1277, http://www.lns.cornell.edu/public/CLNS/ (1994).

[44] Vontoerne, E et al. (2003). ”Status of the CLEO III silicon tracker”. Nuclear Instruments and Methods in Physics Research.

[45] Ehrlich, R.; et al. (1983). ”Particle identification by ionization measurements: Description of the CLEO dE/dx system”. Nuclear Instruments and Methods in Physics Research 211: 17.

[46] CLEO Collaboration, CLEO-c and CESR-c: A New Frontier of Weak and Strong Interactions, CLNS 01/1742, http://www.lns.cornell.edu/public/CLNS/ (2001).

[47] Artuso, M.; et al. (2005). ”The CLEO RICH Detector”. Nuclear Instruments and Methods in Physics Research Section A 554: 147194.

[48] I. M. Frank and I. E. Tamm, C. R. Ac. Sci. U.S.S.R 14, 109 (1937).

[49] Ross, W. (1997). ”The CLEO II.V silicon vertex detector”. Nuclear Instruments and Methods in Physics Research.

[50] D. J. Lange, Nucl. Instrum. Meth. A 462, 152 (2001).

[51] P. Avery et al., QQ: The CLEO Event Generator, (unpublished), URL http: //www.lns.cornell.edu/public/CLEO/soft/QQ.

[52] S. Agostinelli et al., Nucl. Instrum. Methods Phys. Res. A 506,250 (2003).

[53] J.Libby and L.Martin, “An investigation of the $\pi\pi$ S-wave model for measurements of γ with $B^{\pm} \rightarrow (K^0_S\pi^+\pi^-)_D K^{\pm}$ at LHCb,” CERN-LHCB-2007-142.

[54] P. del Amo Sanchez *et al.* (BABAR collaboration), Phys. Rev. Lett. **105**, 121801 (2010).

[55] A.Giri, Y. Grossman, A. Soffer, J.Zupan, Phys Rev D68 054018 (2003).

[56] A. Poluektov *et al.* (Belle Collaboration), Phys. Rev. D **81**, 112002 (2010).

[57] I. Adachi *et al.* (Belle Collaboration), arXiv:1106.4046v1 [hep-ex].

[58] B.Aubert *et al*. (BABAR collaboration) hep-ex/0607104.

[59] A.Poluektov *et al.* (BELLE collaboration) Phys. Rev. D73 112009 (2006).

[60] V. Gibson, C Lazzeroni, J. Libby, LHCb-48-2007.

[61] D.Asner J. Phys. G 33, 1 (2006).

[62] S.U. Chung *et al.*, Ann. Physik. 4 (1995) 404.

[63] V.Anisovich, A.Sarantsev, Eur. Phys Journal A16 229 (2005).

[64] I.J.R.Aitchison, Nucl Phys. A189, 417 (1972).

[65] B. Aubert *et al.* hep-ex/0507101.

[66] CKMfitter Group, (A. Höcker *et al.*), *Eur. Phys. J. C* **21**, 225 (2001); CKMfitter Group (J. Charles *et al.*), *Eur. Phys. J. C.* **41**, 1 (2005), and updates at http://ckmfitter.in2p3.fr/; M. Ciuchini *et al.*, *J. High Energy Phys.* 0107 (2001) 013; UTFit Collaboration (M. Bona *et al.*), *J. High Energy Phys.* 081 (2006) 10, and updates at http://www.utfit.org/.

[67] J. Charles *et al.* (CKMfitter group) Eur. Phys J C41 1 (2005).

[68] D. Aston *et al.* (LASS Collaboration) Nucl. Phys. B2296 493 (1988).

[69] E. Byckling and K. Kajantie, Particle Kinematics, John Wiley & Sons, New York, 1973.

[70] MARK-III Collaboration, D. Coffman *et al.*/ Phys Rev. D 45 (1992) 2196.

[71] J.M. Blatt and V.F Weisskopf, *Theoretical Nuclear Physics*, John Wiley & Sons, New York, (1973)

[72] Jonas Rademacker http:$//www.phy.bris.ac.uk/people/rademacker\_j/documentation_htm$

[73] J.D. Jackson, Nuovo Cimento 34 (6), 1645, (1964).

[74] E. Byckling, K.Kajantie, Phys Rev. 187 5 (1969).

[75] Coles, Stuart An Introduction to Statistical Modeling of Extreme Values. Springer-Verlag, London. (2001).

[76] F. James, MINUIT: function minimization and error analysis, CERN, Geneva (1994).

[77] FOCUS Collaboration, J. Link et al., Phys. Lett. B 610 (2005) 225.

[78] E791 Collaboration, E.M. Aitala et al., Phys. Lett. B 423 (1998) 185.

[79] S. Dobbs et al. (CLEO Collaboration), Phys. Rev. D 76, 112001 (2007).

[80] Dobbs S et al (CLEO collaboration). Phys. Rev. D, 2007,76: 112001.

[81] N. Lowrey et al. (CLEO Collaboration), Phys. Rev. D 80, 031105 (2009).

[82] J. Libby et al.(CLEO Collaboration) .Phys.Rev.D82:112006,2010.

[83] M. Goldhaber and J. L. Rosner, Mixing of Neutral Charmed Mesons and Tests for CP violation in their Decay, Phys. Rev. D 15(5), 12541259 (March 1977).

[84] D. M. Asner et al. (CLEO Collaboration), Phys. Rev. D 78,012001 (2008).

[85] Determining the unitarity triangle angle γ with a four-body amplitude analysis of $B^{\pm}(K^{+}K{-}\pi^{+}\pi^{-})_{D}K^{\pm}$ decays. J. Rademacker1, G. Wilkinson, 2007 (arXiv:hep-ph/0611272v3)

[86] R. Aaij *et al.* [LHCb Collaboration], Evidence for CP violation in time-integrated $D^0 \to h^+h^-$ decay rates. arXiv:1112.0938 [hep-ex].